Straightforward Routes to Hexagonal Boron Nitride Nanomaterials

Ping-Yuan Lee

Wolfson College

University of Oxford

A thesis submitted for the degree of

Doctor of Philosophy

Trinity 2025

To my parents,
for being the reason behind it all.

Acknowledgements

First and foremost, I want to express my deepest gratitude to my supervisors, Professor Nicole Grobert and Dr. Barbara M. Maciejewska. Thank you both for your unwavering encouragement, wisdom, and belief in me. Prof. Grobert, you have been so much more than a supervisor, you've been a mentor and a guiding light, both professionally and personally. Thank you for giving me the opportunity to become part of Oxford and the NbD group. Your trust allowed me to grow not just as a researcher, but as a person. I'll always be grateful for the opportunities you gave me to collaborate across research groups in the UK and beyond. That trust changed everything. Dr. Maciejewska, thank you for being a steady presence since day one. Your patience, insightful advice, and tireless support, especially through the long nights of writing papers, proposals, and finally this thesis, have meant more than I can say. I've always felt that you were in my corner, and that made all the difference.

To the whole NbD group and the big Begbroke family, thank you for making the journey so much more than just work. To past and present members: your help, your kindness, and the laughter we shared meant the world to me. Together we went far beyond colleagues, we became lifelong friends. Special thanks to Kai Ling Ng, Shiling Dong, George T. Tebbutt, Ryan M. Schofield, Tongshan Liu, Nayantara, John Ballentine, Eoin O'Sullivan, Dillon McGurty, Shih-Yun Shen, Yunqing Yang, Jieming Zhang, Ruining Jin, Zheng Wu, and Justin Limkaichong for your support in and outside the lab.

To Professor Andrew S. Weller and Professor Marcel Swart, thank you for your invaluable contributions. Prof. Weller, your chemistry quite literally made the project possible. Prof. Swart, thank you for your generosity in granting access to AMS software, for warmly hosting me during my research visit in Girona, and for your thoughtful insights into the computational work. You helped make the complex parts feel possible. I also want to thank Mathew J. Cross,

Chloe M. van Beek, Claire N. Brodie, and Athul S. Bhaskaran for your collaboration and support along the way.

To the friends I met in Oxford, there are far too many to name, but I'd like to mention a few who made this journey unforgettable. To my OUBaC family: Andrew, Leo, Matthew, Tom, James, Ian, Rob, Benjy, Nathan, Varad, Rash, Jerry, Jack, David, Yuhang, and Chris, badminton wouldn't have been the same without you. I'm so glad we shared memories and achievements on and off the court that we'll be talking about for years to come. To my friends who filled my Oxford life with laughter, support, and late-night conversations: Tim, Albert, Han, Lucus, Blake, Julie, Ismael, Marek, Johnny, and John, thank you for being part of this chapter of my life. Your friendship meant more than I can express.

To my partner, Sherry, there are no words that can fully express how much you mean to me. Your love, patience, and belief in me carried me through the hardest days. Only the two of us truly know what this journey has taken, and I am endlessly grateful to have you walking it with me. I love you. Thank you for everything.

And finally, to my beloved family—my dad Ying-Chieh, my mom Yu-Wei, and my sister Ho-Yun—thank you for your unconditional love and unwavering support in everything I do. Even from afar, I felt your strength with me every step of the way. I would not be here without you.

Abstract

Advanced fibres such as carbon, ceramic, and polymer fibres enable the fabrication of structures and composites for applications reliant on lightweight, oxidation resistant, mechanically strong, and electrically insulating materials, *e.g.* in all forms of land, air and space transportation and in applications within extreme environments. Hexagonal-boron nitride fibres (BNF) harness these advantages, and in addition, offer ultra-high-strength-to-weight ratio and low density. Yet, existing precursors for polymer-derived BNF are limited to insoluble and highly air/moisture sensitive polyborazylenes, hindering fibre production at scale.

The future exploitation of BNF depends on the development of economically accessible and safe production methods. These should also present a scope for BNF microstructural and compositional tunability and output a high purity/crystallinity of BNF. In this thesis, two novel synthesis pathways are proposed that are primarily motivated by the demand to address the scalability challenges of BNF. Both pathways rely on the polymer-derived ceramic route based on the recently developed robust synthesis of the pre-ceramic precursor: *N*-methyl poly(aminoborane) [$(H_2B{\cdot}NHCH_3)_n$, denoted as PMeAB]. The reliable synthesis of PMeAB, when combined with its non-volatility, highly solubility, and high B- N-content, makes it a promising single-source precursor for BN materials.

First, I demonstrate a straightforward synthesis of BNF through solution electrospinning process. Examination of PMeAB solution properties, electro-spinnability, and thermal behaviours, determine, for the first time, the optimal parameters for electrospinning PMeAB solutions into fibres. Subsequent curing and high temperature annealing using ammonolysis demonstrated the formation of cross-linked PMeAB fibres and its gradual transition toward

BNF with ~97 wt.% purity and turbostratic/hexagonal ordering. To my knowledge, the method presented here represents the first instance of using additive-free solution electrospinning process to produce BNF.

Secondly, two template-free synthesis approaches for high-purity, porous, three-dimensional solids constructed from low-dimensional hexagonal-BN (h-BN) nanostructures, including nanosheets (BNNS), nanofibers (BNNF), and/or nanotubes (BNNT) were proposed. The first structure is synthesized via a one-step, template-free, and substrate-free reaction of PMeAB with ammonia gas, resulting in a porous and mechanically stable interconnected BNNS/BNNF hierarchical structure, where the thermal dehydrogenation process, known as "chemical blowing", plays a pivotal role. The second structure utilises the *eee*-isomer of *N,N,N*-trimethylcyclotriborazane [$(H_2BNMeH)_3$, denoted as MeCTB], repurposing a main-group polymer as a precursor for 3D porous BN, constructed from fibrous BN (BNNT/BNNF). Comprehensive microscopic and spectroscopic analyses confirm the high purity and crystallinity of the resulting hexagonal-phase porous BN, marking the first reliable, controllable, and scalable synthesis of BNNS/BNNF and BNNT/BNNF porous structures *via* PMeAB-based chemistry.

Finally, a theoretical model is proposed for the PMeAB-to-h-BN conversion route, based on a combination of density functional theory (DFT) calculations and reactive force field (ReaxFF) molecular dynamics (MD) simulations. The thermal decomposition pathways of PMeAB, its monomer unit MeIB, and its cyclic derivative MeCTB were first systematically investigated through potential energy surface (PES) mapping using DFT. Subsequently, existing ReaxFF parameter sets were evaluated and validated against DFT-derived data for key PMeAB-related chemistries. Large-scale MD simulations were conducted using the validated ReaxFF, coupled with ChemTraYzer2 (CTY2), to enable detailed reaction pathway analysis. The integrated framework of PES mapping and ReaxFF MD provides comprehensive insights

into the fundamental reaction pathways involved in the molecule evolution from precursors to h-BN, *i.e.* (i) bond dissociation, (ii) dehydrogenation, (iii) cyclisation, (iv) carbon removal, and (v) network formation.

This thesis describes the development of new polymer-derived ceramic routes to BN nanomaterials based on PMeAB, a B–N polymer derived from commercially available starting materials. It also provides fundamental, underpinning experimental and theoretical observations that serve as a basis for the further design of other h-BN nanostructures.

Patents/Publications/Conferences

Patents

- Nicole Grobert, Barbara M. Maciejewska, and **Ping-Yuan Lee**, *Boron-nitride fibres*, GB patent number GB2416470.9, filed by Oxford University Innovation Limited on 8th Nov 2024)

Publications

- **Ping-Yuan Lee**, Barbara M. Maciejewska, Mathew J. Cross, Chloe M. van Beek, Claire N. Brodie, Athul S. Bhaskaran, George T. Tebbutt, Ryan M. Schofield, Samuel J. Page, Ed Darnbrough, Marcel Swart, Andrew S. Weller, and Nicole Grobert, *A Straightforward Route to hexagonal-Boron Nitride Fibers*, published on Advanced Composites and Hybrid Materials, 8, 392, **2025**

  The content of this work is partly reproduced in **Chapter 2**.

(In Preparation)

- **Ping-Yuan Lee *et al.*,** *Selective Synthesis of N,N,N-Trimethylcyclotriborazane: A Precursor for hexagonal-Boron Nitride Aerogel*

  The content of this work is partly reproduced in **Chapter 3**.

- **Ping-Yuan Lee *et al.*,** *Mechanistic Insights into the Polyaminoborane-Route to Hexagonal Boron Nitride Nanostructures*

  The content of this work is partly reproduced in **Chapter 4**.

Conferences

- **Ping-Yuan Lee**, Barbara M. Maciejewska, Mathew J. Cross, Andrew S. Weller, and Nicole Grobert, *One-Step Synthesis of Hierarchical Boron Nitride Porous Nanomaterials*, presented in Materials Research Society Fall Meeting, Boston, USA, Dec 2024

  The content of this work is partly reproduced in **Chapter 3**.

- George T. Tebbutt, Barbara M. Maciejewska, **Ping-Yuan Lee**, and Nicole Grobert, *Achieving Carbon Nanotube Encapsulated β-Sn – Direct Observation of the Encapsulation Mechanism by In Situ TEM*, presented in Materials Research Society Fall Meeting, Boston, USA, Dec 2024

Statement of Ownership

The work presented herein was conducted solely by the author. Contributions from other researchers are explicitly acknowledged where appropriate.

Content

List of Abbreviations

1D, 2D, 3D……One-, Two-, Three-Dimensional
AB……....Ammonia Borane
a-BN……...Amorphous Boron Nitride
ADF……Amsterdam Density Functional
AFM……...…Atomic Force Microscopy
AMS……..…Amsterdam Modeling Suite
BCN……..……...Boron Carbonitride
BET……..Brunauer-Emmett-Teller
BN……..Boron Nitride
BNF……Boron Nitride fibre
BNNF……Boron Nitride Nanofibre
BNNS……Boron Nitride Nanosheet
BNNT……Boron Nitride Nanotube
CVD……...Chemical Vapour Deposition
DFT……...Density Functional Theory
DFTB……Density Functional Based Tight Binding
EDX……..Energy-Dispersive X-Ray Spectroscopy
EELS……...Electron Energy Loss Spectroscopy
FFT……..Fast Fourier Transform
FT-IR……Fourier Transform Infrared
h-BN……Hexagonal Boron Nitride
MeAB……Methylamino Borane
MeCTB……..*N,N,N*-Trimethylcyclotriborazane
MD…….……Molecular Dynamics
PAB…….…….....Polyaminoborane
p-BN……...Porous Boron Nitride
PMeAB……...….*N*-Methyl Polyaminoborane
ReaxFF……Reactive Force Field
SEM……Scanning Electron Microscopy
STEM……...Scanning Transmission Electron Microscopy

t-BN……...Turbostratic Boron Nitride

TEM……..…Transmission Electron Microscopy

TGA-MS……..Thermal Gravimetric Analysis With Mass Spectrometer

TPS……..…Transient Plane Source

UV-Vis DRS……..UV-Vis Diffuse Reflectance Spectroscopy

VLS……Vapour-Liquid-Solid Method

XPS……..X-Ray Photoelectron Spectroscopy

XRD……X-Ray Diffraction

Chapter 1

Introduction

Contents

1.1 Thesis Overview

The thesis is structured into five chapters. It opens with an introduction chapter that outlines the background, motivation, research gaps, and aims of the research project. **Chapter 1** also presents a comprehensive literature review covering: (1) BN structures and properties, (2) various synthesis methods for producing BN nanomaterials, particularly BN fibres, (3) computational methodologies used to model the target material system, and (4) potential applications for the synthesized BN nanomaterials. **Chapter 2** introduces a new approach for producing BN micro- to nanoscale fibres with ultra-high purity and minimal porosity, using an additive-free electrospinning process followed by a multistep thermal treatment. **Chapter 3** presents two novel approaches for synthesizing 3D BN porous solids with tuneable morphology and chemical composition, based on one-step thermal treatment. **Chapter 4** integrates theoretical and experimental perspectives on the synthesis of BN nanostructures by correlating empirical observations with results derived from computational approaches, including DFT calculations and ReaxFF MD simulations. Finally, **Chapter 5** presents the conclusions and key new science from the research, along with proposed directions for further development in this field.

1.1.1 Background and Motivation

The rapid integration of next-generation nanomaterials into space technology has sparked a renewed era of innovation in both interplanetary missions and near-Earth exploration.[1] The advantages of nanomaterials and nanostructured systems include substantial mass reduction, enhanced multifunctionality, improved durability under extreme conditions, and increased propulsion efficiency.[2] As a response to this momentum, The National Aeronautics and Space Administration's (NASA) 2015 *Nanotechnology Roadmap*[3] emphasized the need for novel design paradigms that fuse space technology with new nanomaterials and nanostructures to

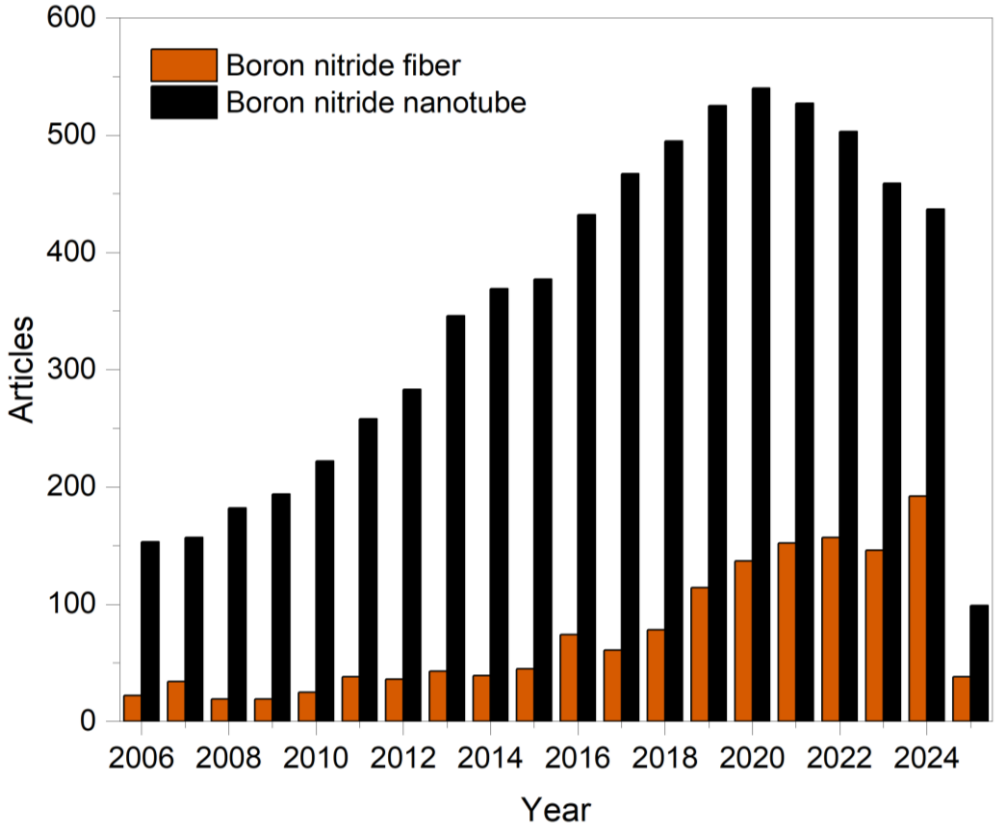

Figure 1.1: Published research papers collected in Web of Science from 2006 to 2025 comparing 'boron nitride fiber' and 'boron nitride nanotube', orange and black column, respectively.

enable the development of advanced, deep-space-capable, and adaptive spacecraft. These nanomaterials are envisioned as critical components in systems such as ultracapacitors, active and passive thermal management layers, nanofiltration membranes for water recovery, high-efficiency energy storage systems, hybrid power generation platforms, advanced proton exchange membrane fuel cells, and next-generation air revitalisation systems.

Over the past decade, the NASA Glenn Research Centre has advanced the development of carbon and BN nanotubes (CNT and BNNT, respectively) for applications in space environments.[4] These 1D nanomaterials are of particular interest due to their low densities (1.7–2.1 g/cm^3),[5,6] high aspect ratios, exceptional thermal conductivity (>300 W·m^{-1}·K^{-1}),[7] and outstanding mechanical properties, including Young's moduli reaching into the TPa magnitude (1–1.25 TPa).[8,9] While CNT can be either metallic or semiconducting depending on their

chirality,[10] BNNT are consistently electrically insulating due to their intrinsic wide bandgap, which originates from the electronic structure of alternating boron and nitrogen atoms, leading to significant orbital splitting.[11] This property, coupled with their superb elastic modulus (~1.3 TPa[62]), makes BNNT the strongest known insulating fibre to date.[12] Moreover, BNNT exhibit the rare dual functionality of being both dielectric and thermally conductive. In terms of thermal stability, BNNT surpass CNT, withstanding oxidative degradation in air up to 800–900 °C[13] and remaining stable up to 1500 °C in inert atmospheres.[14] BNNT also possess a high neutron absorption capacity, attributed to the large neutron absorption cross-section of boron (^{11}B: 7.67 × 10^{-22}; ^{10}B: 3.835 × 10^{-21}; N: 1.9 × 10^{-24} cm^2),[15] a characteristic not exhibited by CNT. Despite these advantages, the current NASA production method for BNNT—relying on high-power lasers and operating under extreme pressures and temperatures—is resource intensive and not amenable to large-scale implementation.[16] Alternative synthesis techniques such as chemical vapor deposition and template-based methods have also been explored; however, these approaches face similar challenges in terms of scalability.[17]

More recently, NASA's attention has turned to spun BN fibres (BNF), which share structural similarities with BNNT but may offer several distinct advantages. Spun BNF demonstrate ultrahigh continuity and aspect ratios, increased flexibility in structural modification, and potentially lower manufacturing costs.[18] Despite these promising features, BNF remain underexplored relative to BNNT (**Figure 1.1**), largely due to the absence of efficient and reliable synthesis methods. For instance, NASA has employed a force-spinning technique using carbon-rich polymer additives to produce BNF.[19,20] However, the excessive carbon content has thus far hindered the formation of high-quality BNF.

The development of a scalable, efficient, and cost-effective synthesis strategy for BNF could offer a viable alternative to the expensive and technically demanding production of

BNNT.[21,22] However, three fundamental questions and concerns highlight the gap between the theoretical promise of BNF and its practical applicability:

(1) **Is BNF production truly low-cost?** Currently, there is no robust or straightforward method available, as the proposed precursors and processing routes are not readily scalable and thus remain confined to laboratory-scale experiments.[23,24]

(2) **Do BNF products meet the quality standards required for advanced technological use?** Existing BNF products often exhibit poor quality, and critical details regarding their BN phase, crystallinity, and purity are frequently lacking or insufficiently characterized.[25–31]

(3) **What are the underlying mechanisms governing BNF formation from various precursors?** Experimental data alone have not been sufficient to elucidate a comprehensive reaction pathway. Further computational studies at the atomic and molecular levels are necessary to map reaction landscapes and provide mechanistic insight, which in turn could guide more rational design and control of BNF synthesis processes.[32,33]

Addressing these limitations is essential to bridge the gap between hypothesis and reality, and to evaluate the true potential and viability of BNF as complementary or alternative materials to BNNT in high-performance space applications.

1.1.2 Aim of the Thesis

The aim of this thesis is to address the questions highlighted in the motivation section. First, I aim to demonstrate that BNF can be produced using a simple, scalable setup, including electrospinning and/or direct thermolysis, with readily available precursors, PMeAB and MeCTB, that are stable in ambient conditions—a key factor for scalability. Second, extensive microscopic and spectroscopic characterisations are performed to confirm the presence of h-

BN in BNF and evaluate the quality of the BN, focusing on purity, crystallinity, and phase. Finally, I seek to understand the underlying mechanisms of the PMeAB-to-h-BN conversion. To achieve this, a combined experimental and computational approach is employed, relying heavily on computational tools such as Density Functional Theory (DFT) calculations and Reactive Force Field (ReaxFF) simulations. These tools will provide atomistic insights that are otherwise inaccessible experimentally. Through the comprehensive theoretical and experimental investigation, this thesis aims to develop potentially scalable methods for producing high-crystallinity and high-purity BNF capable of rivalling BNNT, while also elucidating the mechanisms that govern their structural quality, thereby contributing to the advancement in the field of BN nanomaterials and fibre research.

1.2 Literature Review

1.2.1 Hexagonal Boron Nitride (BN)

Boron nitride is a widely recognized and technologically significant ceramic material that exists in various forms, such as amorphous or crystalline structures with rhombohedral (r-BN), wurtzitic (w-BN), turbostratic (t-BN), cubic (c-BN), or hexagonal (h-BN) configurations.[34] Among them, h-BN has attracted the most attention due to its versatility and ability to form various nanoscale morphologies, including 2D nanosheets, 1D nanotubes, and 0D fullerene-like structures.[35] Crystal structures for each BN polymorph are presented in **Figure 1.2**.[36]

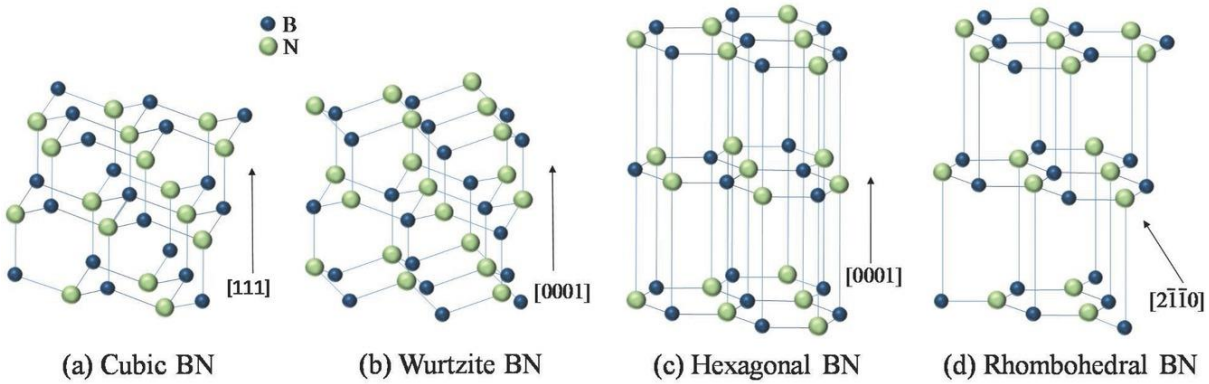

Figure 1.2: Crystal structures of (a) cubic, (b) wurtzite, (c) hexagonal, and (d) rhombohedral BN.[36]

h-BN is the most thermodynamically stable phase among the above-mentioned BN polymorphs and serves as a low-density, sp^2-hybridized counterpart to graphite. Its hexagonal structure consists of borazine (B_3N_3) rings, which are structurally similar to benzene. The lattice constants of h-BN (0.25 nm in-plane and 0.333 nm interlayer spacing) closely resemble those of graphene (0.246 nm and 0.337 nm, respectively).[37] Despite their structural similarity, graphene's delocalized π-electrons and h-BN's localized electrons due to ionic bonding lead to fundamentally different properties. The atomic layers in h-BN primarily exhibit an AA' stacking arrangement, where each boron atom aligns with a nitrogen atom in the adjacent layer, driven by electrostatic interactions.[38] In contrast, graphene typically adopts AB (Bernal) stacking, where half of the carbon atoms in one layer align with the centres of the hexagons in the adjacent layer, minimizing repulsive interactions between identical atoms. h-BN demonstrates high in-plane thermal conductivity (up to 2000 $W \cdot K^{-1} \cdot m^{-1}$), superb mechanical properties [friction coefficient <0.3, elastic modulus ~0.8 TPa, and wear resistance (specific wear rates reported as low as 1–3 × 10^{-6} $mm^3/N \cdot m$ under dry sliding conditions], excellent thermal stability (stable in air up to 1100 °C) and chemical inertness, wide bandgap (5.6 eV), low density (2.3 $g \cdot cm^{-3}$), layered structure, and a negative thermal expansion coefficient (-2.90 × 10^{-6} K^{-1} in the a/b-axis and 4.05 × 10^{-5} K^{-1} in the c-axis).[39] These combined characteristics of h-BN make it suitable for a wide range of applications, including, but not limited to engineered components for space and aerospace vehicles and structures, thermal management materials in

electronic packaging, filler materials for functional composites, high-temperature ceramics and insulators, lubricants and adhesives, corrosion-resistant coatings, water purification systems, and drug delivery platforms.[39]

Bulk h-BN powders have been produced for over a century, and extensive research has led to the development of scalable and cost-effective synthesis methods, including CVD, ball milling followed by annealing, high-temperature solid-state reactions, and mechanochemical synthesis.[40,41] Similar to graphene, obtained by exfoliating bulk graphite powders, exfoliating h-BN into its sheet-like counterpart, BNNS, is highly desirable for various industrial applications. However, h-BN is significantly more resistant to oxidation and intercalation than graphite,[42] making exfoliation and the formation of stable colloidal dispersions particularly challenging, thus limiting its practical applicability in real-world systems.[43]

A promising alternative is the synthesis of 1D BN nanostructures, such as BNNT and BNF. These 1D nanomaterials inherently avoid the strong interlayer van der Waals interactions that cause restacking in 2D BNNS, offering enhanced colloidal stability and dispersion without the need for aggressive intercalation or chemical modification.[44] Their anisotropic morphology and reduced tendency to aggregate make them feasible for uniform integration into various material matrices.[45] BNNT and BNF present a viable route to overcome the limitations associated with BNNS, while preserving the desirable properties of BN at the nanoscale.

1.2.2 BN Fibres: Synthesis, Properties, & Applications

In recent years, 1D nanostructures, including nanofibres, nanotubes, nanorods, nanowires, and nanowhiskers, have garnered significant research interest owing to their unique physical and chemical characteristics,[46] since the groundbreaking discovery of CNT by Iijima.[47] Significant progress has been made in the synthesis of macroscopic assemblies of these 1D nanomaterials through a range of physical and chemical fabrication techniques.[46] 1D nanomaterials have been

extensively used as functional elements or interconnects in the development of nanoscale products, especially in electronic devices,[48] thermal management,[49] multifunctional composites,[50] and environmental remediation.[51]

As mentioned in section **1.2.1**, the layered structure of h-BN enables its malleability to transform into various 1D nanostructures, mainly BNNT and BNF,[52] expanding its applicability in diverse scientific fields. BNNT, though structurally analogous to the well-known CNT and exhibiting comparable mechanical strength, are distinguished by their wide bandgap semiconducting nature. BNNT exhibit remarkable thermal stability, withstanding temperatures up to 900 °C in air, and offer high optical transparency in the visible range. They combine electrical insulation with high thermal conductivity, emit single deep ultraviolet (UV) light, absorb thermal neutrons effectively, and demonstrate piezoelectric behaviour under mechanical deformation. Additionally, the partial ionic character of B–N bonding, arising from the significant electronegativity difference between boron and nitrogen, imparts unique chemical properties distinct from those of CNT.[53] Unlike the nonpolar in-plane C–C bonds in graphene, the polarity of B–N bonds within the h-BN lattice introduces localized charge distribution, influencing surface chemistry and adsorption behaviour. Macroscopic structures composed entirely of BNNT (bulky papers, yarns, mats, and thin films) offer significant potential for the advancement of innovative BNNT-based devices. Their high BNNT content, extensive surface area, efficient carrier transport pathways, and inherent ability to accommodate mechanical strain make them particularly advantageous for functional applications.[54] Although significant attention has been directed toward BNNT, BNF have potential to surpass certain properties of BNNT for its ultrahigh continuity with significantly lower production cost (**Table 1.1** summarises the comparison of the key properties of BNF versus BNNT).[55] Reported BNF products generally exhibit higher electrical resistivity

Table 1.1: A comparison of the properties of BNF versus BNNT.

Properties	BNF	BNNT
Appearance	Light yellow to white[56]	White
Electrical Resistivity (Ω·cm)	3×10^{7}–3×10^{9} [57] 10^{12}–10^{14} [58,59]	300[60] 7.8×10^{4} [61]
Mechanical Properties (Young's Modulus)	27–82 GPa[58] 78 GPa[28]	1.3 TPa[62]
Thermal Conductivity ($W\cdot m^{-1}\cdot K^{-1}$)	-	350[63]
Thermal Stability (in air) (°C)	855[58] 890[56]	700–900[64]

compared to BNNT, but tend to have lower Young's modulus and reduced thermal stability. In addition, the thermal conductivity of individual BNF remains difficult to assess, and reliable, standardised measurements are not yet available. Despite several BNF products have been proposed through various methods in the past decade, the fibres' size, crystal structure, morphology, and quality vary widely.

Among various fabrication techniques, spinning process is the most used method to produce free-standing fibres mats due to the relatively simple setups, the capability of mass production, and the ability to create highly continuous and ultrathin products with controllable diameters, compositions, and orientations.[65] In addition to the well-reported polymer fibres, inorganic fibres made of carbon,[66] carbides,[67] oxides,[68] and nitrides have been synthesized by heat treatment of the polymeric precursor fibres to achieve polymer-to-ceramics conversion. This so-called polymer-derived ceramics (PDC) route is an attractive approach for the design of high-performance ceramics with well-controlled compositional and microstructural homogeneities; especially in nitride compound systems.[69] To date, however, the large-scale production of high-quality BNF *via* PDC route remains a challenge. This is mainly because there is not yet a reliable single B- N-containing precursor system for a simple electrospinning

Table 1.2: Summary of the conditions for the synthesis of BNF by spinning methods.

Precursor[a]	Solvent[b]	Additive[c]	Spinning Voltage/ Temperature	Annealing Temperature (Atmosphere)	Diameter	Ref.
Electrospinning						
PBMABZ	DMF	PAN	4.5kV / RT	1000°C (NH_3) 1800°C (N_2)	100-400nm	29
BN NPs	H_2O	PVA	20kV / RT	1000°C (Ar)	180-550nm	70
B_2O_3	EtOH	PVB	20kV / RT	1100°C (NH_3) 1500°C (N_2)	80-350nm	26
B_2O_3	DMF	PAN	20kV / RT	1100°C (NH_3) 1500°C (N_2)	43-230nm	27
Boric acid Melamine	H_2O	PVP	20kV / RT	600°C (Air) 1400°C (N_2)	avg. 130.1nm	71
Melt-Spinning						
PBMABZ	-	-	0kV / 115-185°C	1000°C (NH_3) 1800°C (N_2)	17.5-21µm	72
P(PMABZ-co-MABZ)	-	-	0kV / 140°C	800°C (NH_3) 1800°C (N_2)	avg. 7.6µm	73
PBMBZ or PBMABZ	-	-	0kV / 130-140°C	600°C (NH_3) 1800°C (N_2)	10-30µm	31
PBMABZ	-	-	0kV / 70°C	1000°C (NH_3) 1800°C (N_2)	5-50µm	57
PBMABZ	-	-	0kV / 200°C	1000°C (NH_3) 1800°C (N_2)	10µm	74
PBMABZ	-	-	0kV / 150-200°C	1000°C (NH_3) 1800°C (N_2)	10-25µm	75
PBMABZ	-	-	0kV / 140-160°C	1000°C (NH_3) 1600°C (N_2)	avg. 9µm	76
PBMABZ	-	-	0kV /	800°C (NH_3)	avg. 12µm	77

[a] PBMABZ, poly[*B*-(methylamino)borazine]s; BN NPs, boron nitride nanoparticles; P(PMABZ-co-MABZ), poly[2-propylamino-4,6-bis(methylamino) borazine-co-tri(methylamino) borazine]; PBMBZ, poly(*B*-methylborazine)s.

[b] DMF, *N,N*-dimethylformamide; H_2O, deionized water; EtOH, ethanol.

[c] PAN, polyacrylonitrile; PVA, polyvinyl alcohol; PVB, polyvinyl butyral; PVP, polyvinylpyrrolidone.

			120-130°C	1600°C (N_2)		
PBMABZ	-	-	Not specified	1200°C (NH_3) 1400°C (Ar)	avg. 13μm	[78]

setup.

The precursors used in previous studies so far can be divided into two categories: (i) colloidal particles with polymer-aid and (ii) polyborazylenes (PBZ)-based single-source precursors. **Table 1.2** summarises the attempted syntheses of BNF reported in the literature. Qiu *et al.*[26,27] have fabricated aligned long BNNF through electrospinning of B_2O_3/PVB mixture followed by high temperature nitridation. However, the obtained BNNF showed porous structure due to low ceramics yield (<20 wt.%) and uneven solid vapor nitridation. PDC route avoids the use of oxygen-containing precursors and offers precise control over the precursor compositions.[29] The borazine (BZ) derivatives, with the potential to yield borazine backbone cyclic polymers, PBZ, have attracted the greatest interest over the past three decades as promising precursors for polymer-derived BN, especially fibrous BN.[28,69,79] PBZ's basal structure units of hexagonal B–N rings limits the occurrence of complex structural rearrangements upon ceramic conversion and giving rise to the highest ceramic yields (up to 90 wt.%),[75] crucial for reaching the ideal performance of final ceramics product.[80] However, PBZ suffer from high toxicity and moisture-sensitivity, poor spinnability and low solubility in common electrospinning solvents (*e.g.* chloroform, dimethylformamide),[73,81,82] requiring specially designed polymer melt processing equipment and strict operation conditions, limiting its further development. Another major challenge for PBZ lies in complex production, primarily due to the use of BZ as a starting material, which itself presents considerable challenges in its synthesis, especially its isolation from the reaction mixture with a typical yield of only 10%, due to the simultaneous formation of significant amounts of by-products.[83]

My primary objective revolves around identifying a family of B- N-rich polymers that possesses sufficient molecular weight to electrospin into fibres (typically with M_w > 10,000

g·mol^{-1} but with considerable variation across diverse polymer categories),[84] exhibits high solubility in common solvents, remains non-volatile under ambient conditions, and can be synthesized from a straightforward route.

1.2.3 *N*-methyl Polyaminoborane (PMeAB): An h-BN Precursor

Pursuant to the objectives, I target B- N-rich polymer with a linear configuration. Linear polymers confer several benefits in comparison to their cyclic counterparts, notably a higher degree of chain entanglement, enhanced processability, and greater control over the molecular weight.[85,86] Most importantly, linear polymers typically demonstrate improved solubility in various solvents, leading to more stable solution states—a critical factor for the uniformity of the electrospinning process.[87] Their intrinsic chain flexibility further facilitates the production of nanoscale fibres.[88] From a mechanical standpoint, chain flexibility results in high tensile strength and elongation at break;[89] thus, particularly suitable for electrospun fibre applications.[90]

Figure 1.3: Molecular structures and abbreviations of PMeAB-related compounds.

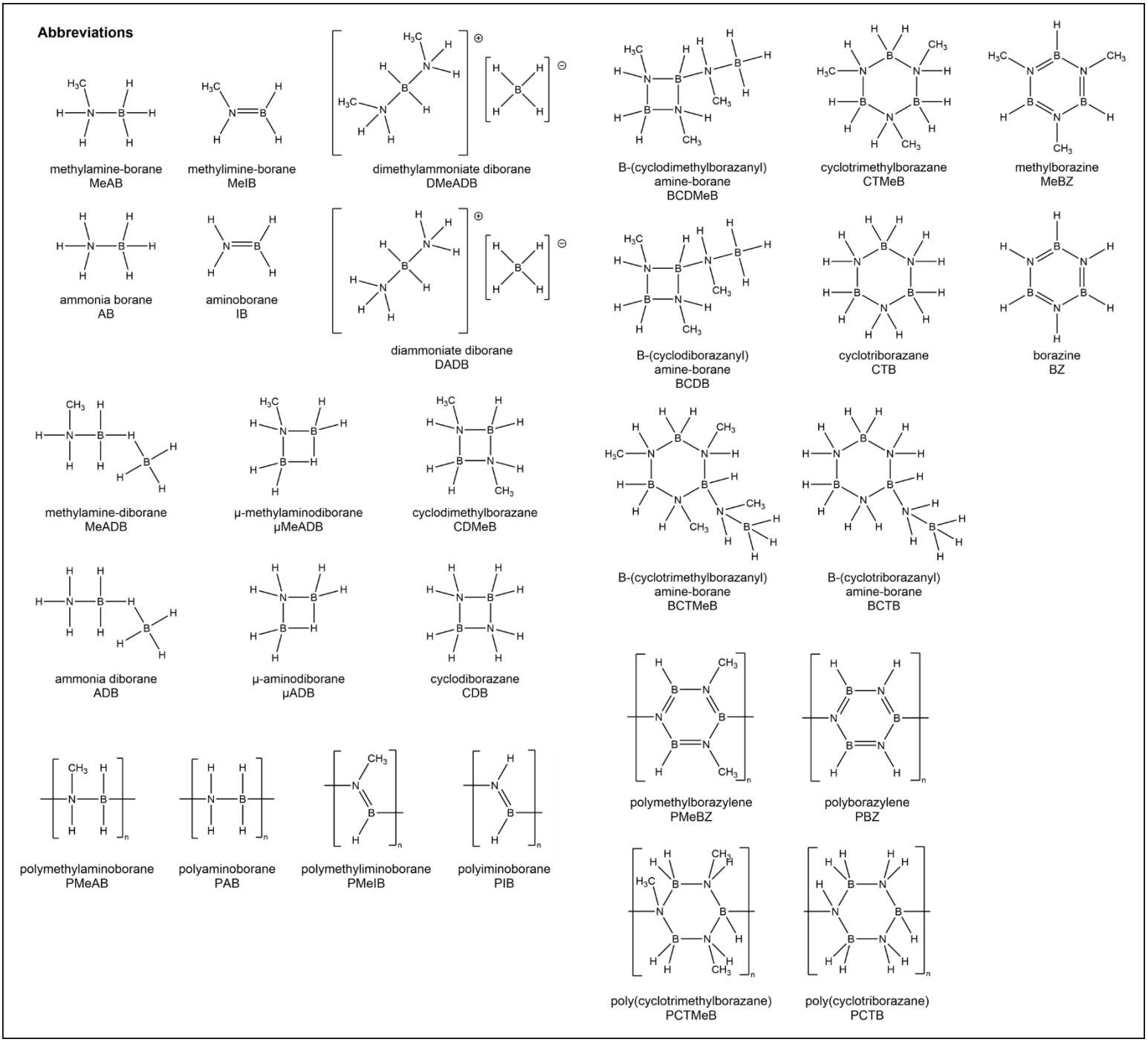

Ammonia borane [($H_3B{\cdot}NH_3$), denoted as AB] (**Figure 1.3**), has been gaining popularity since first discovered by Shore and Parry in 1955,[91] as a single source solid precursor for the synthesis of BN materials because its naturally stoichiometric ratio of N:B.[92–94] Although AB has polymerisation ability to form linear poly(aminoborane)s [($H_2B–NH_2)_n$, denoted as PAB], it has been more commonly utilised for synthesizing two-dimensional h-BN through vapor

phase pyrolysis processes.[95] In contrast, less emphasis has been given to BN production through the direct pyrolytic decomposition of solid AB or PAB. All attempts to understand the underlying mechanism remained speculative and were vaguely described as the combination of two thermodynamically favored pathways, namely the AB-to-BZ-to-PBZ-to-BN pathway and the AB-to-PAB-to-PIB-to-BN pathway, where PIB represent poly(iminoborane)s $(H_2B{=}NH_2)_n$.[96]

Despite being a non-volatile, air-stable, and non-toxic solid, pure PAB exhibits poor solubility in common organic solvents, limiting its processibility toward BN.[97] The introduction of alkyl groups at nitrogen or boron positions enhances PAB's solubility in polar organic solvents, enabling the determination of molecular weights and spectroscopic characterisation, as well as opening up the possibility of using polymer solutions processing techniques.[97] One such variant, *N*-methyl poly(aminoborane)s $[(H_2B{\cdot}NMeH)_n]$, the simplest methyl derivative of poly(aminoborane)s $[(H_2B{-}NH_2)_n]$, can be synthesized by the metal catalysed dehydropolymerisation of methylamine borane $[(H_3B{\cdot}NMeH_2)$, denoted as MeAB].[98] The high B- N-content, linear polymer structure, high solubility in common solvents, air-stable property, and sufficient molecule weight make it a promising precursor for solution electrospun BNF. Latest study from Weller's group[99] revealed a novel way of producing high molecular weight PMeAB (M_n = 37,900–78,100 g·mol^{-1}) using [Rh(L)(NBD)]Cl (**[1]Cl**) [L = κ^3-(^{i}Pr$_2$PCH$_2$CH$_2$)$_2$NH, NBD = norbornadiene] precatalytic system with very low catalyst

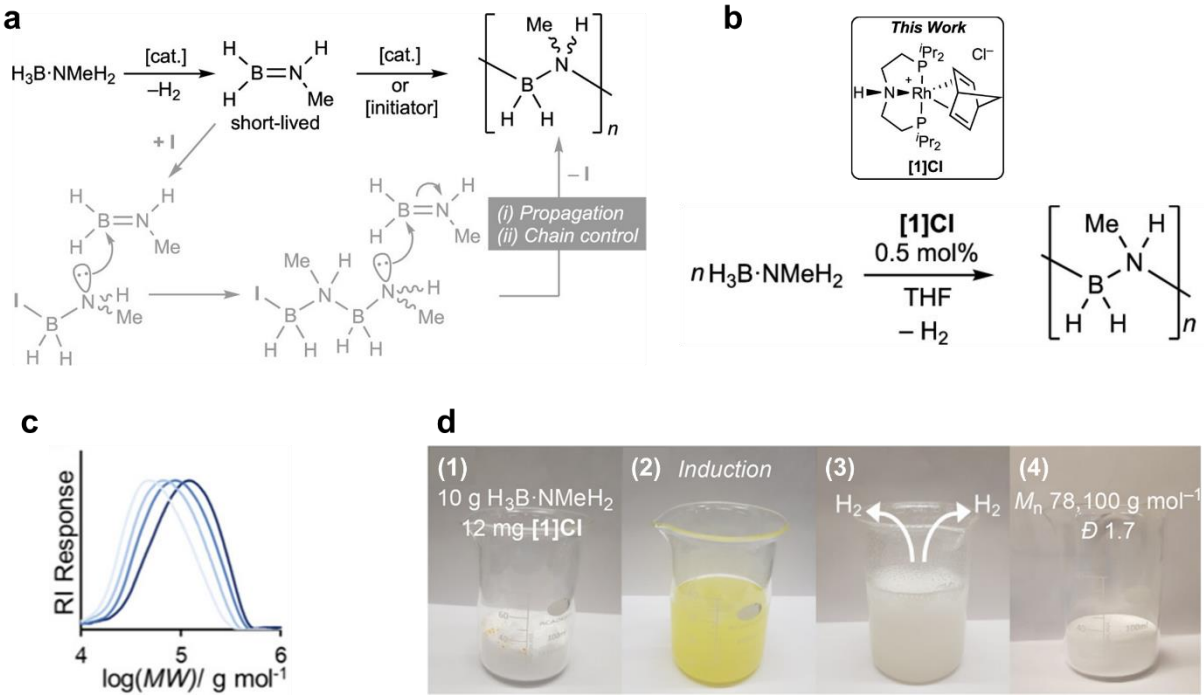

Figure 1.4: (a) Generic dehydropolymerisation process using MeAB. (b) The proposed simple, easy to assemble, tolerant-to-air, precatalyst [Rh{(^{i}Pr$_2$PCH$_2$CH$_2$)$_2$NH}(NBD)]Cl, **[1]Cl**, for the dehydropolymerisation of commercial, as supplied, MeAB in THF solvent. (c) The overlaid GPC traces of isolated PMeAB samples with various well-defined molecular weights. (d) Air-tolerant dehydropolymerisation of 10 g MeAB and 12 ppm **[1]Cl** to produce PMeAB.[99]

loadings (0.01 mol %) under ambient condition (**Figure 1.4**). The underlying mechanism follows a ligand-cooperative dehydrogenation pathway, initiated by the formation of an active Rh(III) hydride species (Rh(L)H$_3$), which interacts with H$_3$B·NMeH$_2$ through outer-sphere dihydrogen bonding. This triggers N–H activation and H$_2$ release via a turnover-limiting step, generating the reactive H$_2$B═NMeH. Subsequent head-to-tail B–N coupling propagates the polymer chain with very low barriers, while boronium salts act as chain-transfer agents, enabling well control over molecular weight. The controlled synthesis of well-defined PMeAB on a 10 g scale paves the way for mass production of high quality BNF (*e.g.* high purity, crystallinity, homogeneity, continuity, etc.). To date, however, little information has been published detailing the processing and thermolysis of PMeAB.[99–102]

Among the few examples, Brodie *et al.*[99] briefly explored the processibility of PMeAB either in solutions or the molten state, and were exemplified by melt-extruded fibres, drop-

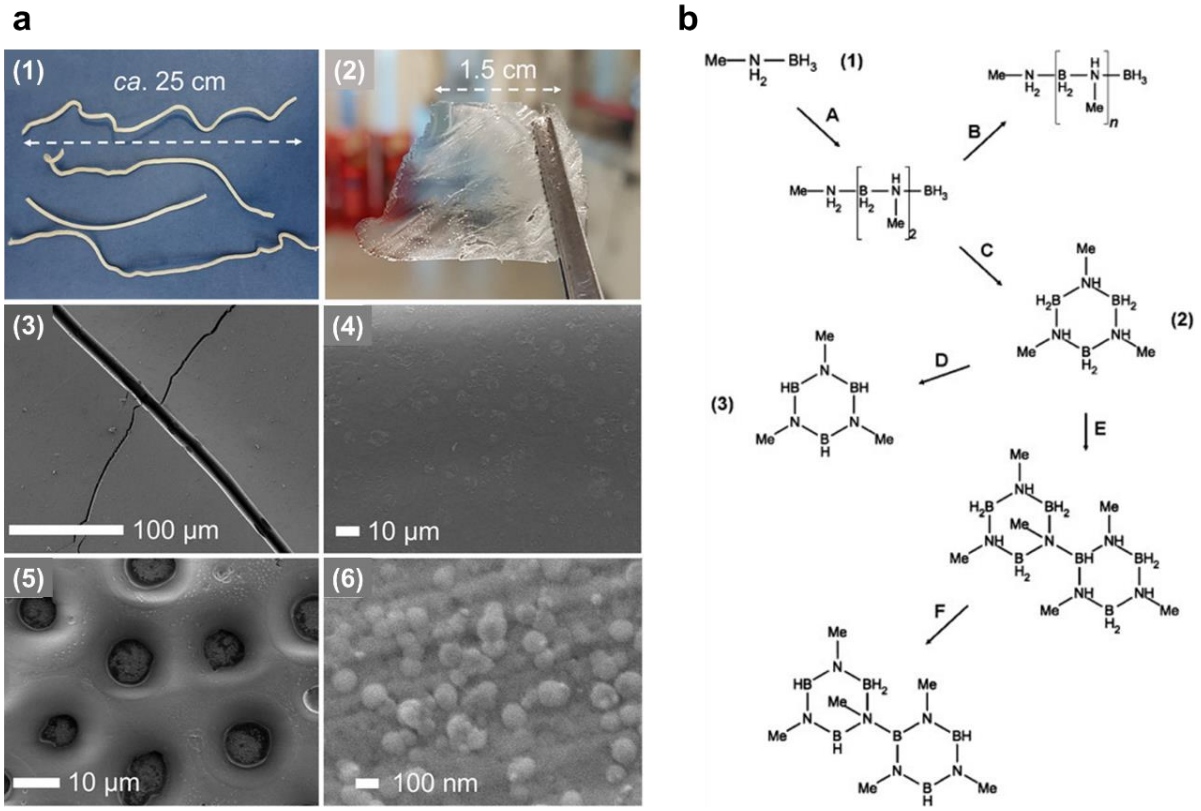

Figure 1.5: (a) Examples of processed PMeAB: (1) melt-extruded; (2) drop-cast thin film; (3) SEM image of drop-cast thin film; (4) electrosprayed thin film SEM image; (5) porous film SEM image; (6) polymer beads SEM image.[99] (b) Schematic of thermolysis reactions of MeAB. Path A→B: dehydropolymerisation. Path A→C→D: cyclisation. Path A→C→E→F: cross-linked network formation.[100]

casted thin films, and electrosprayed porous films (**Figure 1.5a**). Studies on the thermolysis of PMeAB proposed by Bowden *et al.*[100] highlighted the significance of the potential thermal dehydrogenation pathways of MeAB in both monomeric and polymeric forms (**Figure 1.5b**). The results, however, were limited to the low temperature region (below 250 °C) and conducted under inert atmosphere. No data on the thermal cross-linking phenomenon, thermal behaviours occurring at high temperatures, including pyrolysis, annealing, and crystallisation was presented. The presence of methyl group in PMeAB introduces an additional complication into the system: the presence of carbon impurities. Finding the way of controlling and removing carbon becomes a crucial step in achieving high-purity BN materials. Another equally important challenge is the preserve the fibre morphology and structure because MeAB is

known to melt at temperature as low as 55 – 58 °C and suffer from excessive weight reduction (>80 wt.%) upon heating, if not cross-linked.[100] In order to preserve the desired morphology of the final product, it is critical to include a curing step to form a non-volatile cross-linked intermediate before subjecting the material to high-temperature annealing.[69]

To fully utilise PMeAB as a precursor for h-BN materials, a comprehensive understanding of its reaction mechanisms is essential for any meaningful technological advancement. The integration of experimental and computational approaches is expected to provide complementary insights, bridging existing knowledge gaps and advancing the understanding and potential of PMeAB.

1.2.4 Density Functional Theory for H/B/C/N Chemistry

Computational modelling has emerged as a vital tool in materials science, particularly for exploring the structure, dynamics, and reactivity of complex chemical systems. For multicomponent systems such as my hydrogen, boron, carbon, and nitrogen system (H/B/C/N), experimental investigation is often limited by resolution, cost, and timescale constraints. In this context, atomistic simulations serve as a powerful complement to experimental methods, enabling the study of material behaviour at the electronic, atomic, and molecular levels.

Figure 1.6 presents a hierarchical overview of computational methods. Quantum mechanical (QM) approaches, such as ab initio and DFT,[103,104] offer high accuracy in predicting material properties but are limited to small systems due to their high computational costs. On the other end, general-purpose force fields (FF) like DREIDING[105] and UFF[106] can handle much larger systems efficiently, but they are unable to model chemical reactions because their bond potentials are fixed. The development of approximation methods such as ReaxFF[107] was driven by the need to bridge this gap, offering a balance between the accuracy of QM methods and the scalability of classical FF.

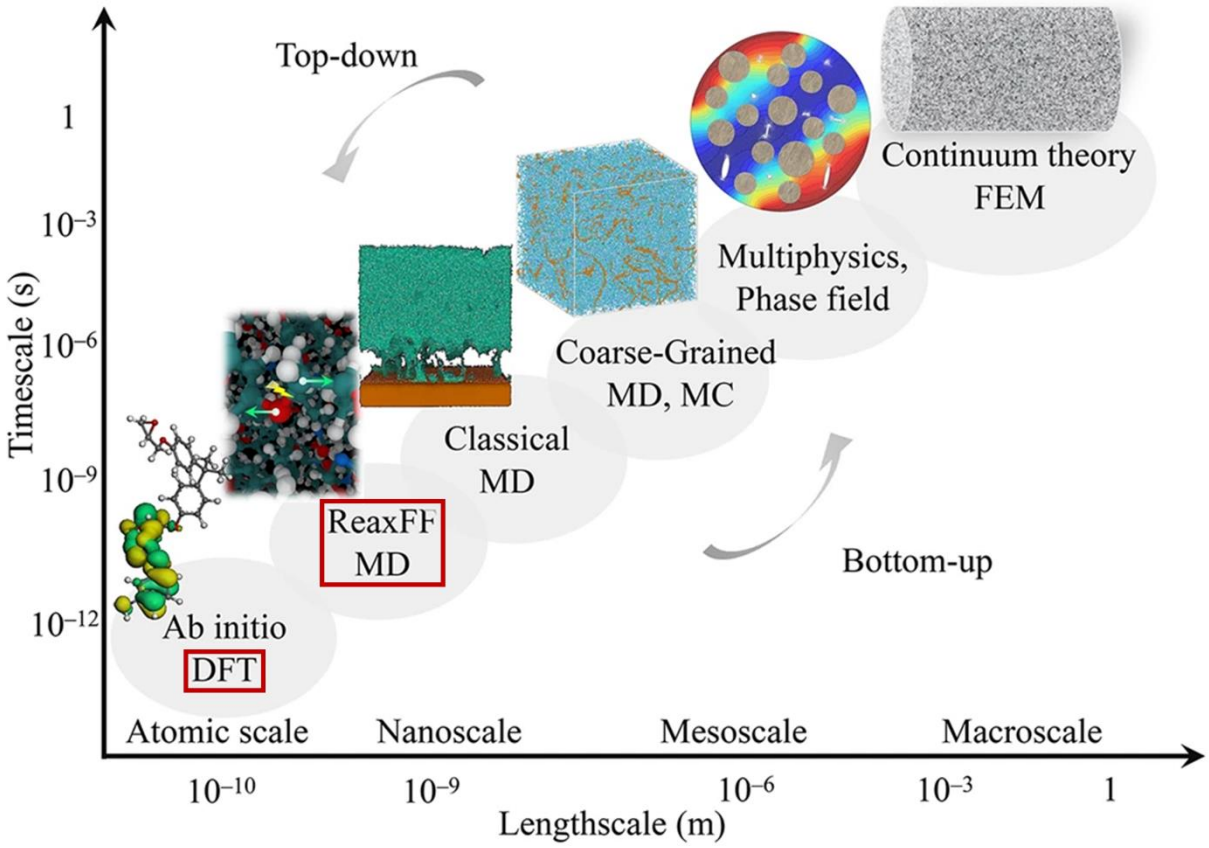

Figure 1.6: Multiscale simulation framework.[122,319]

Computational studies using DFT to investigate the thermal chemistry of H/B/C/N systems remain limited compared to those focused on the H/B/N system, particularly AB. However, findings from AB thermal decomposition simulations can serve as a valuable reference for the H/B/C/N compounds due to their structural similarities and experimentally observed mechanistic parallels.[100] Thermal decomposition pathways of AB, as proposed in the literature,[96] can be broadly classified into four categories: (1) dehydrogenation, (2) dissociation, (3) polymerisation, and (4) cyclisation. Among these, dehydrogenation has been the most extensively studied,[108] owing to AB's potential as a hydrogen storage material. More recent studies, however, have highlighted the significant roles of dissociation and cyclisation reactions.[109–111] Dissociation yielding small molecular fragments have been shown to facilitate dehydrogenation, while cyclisation, often following polymerisation, leads to the formation of

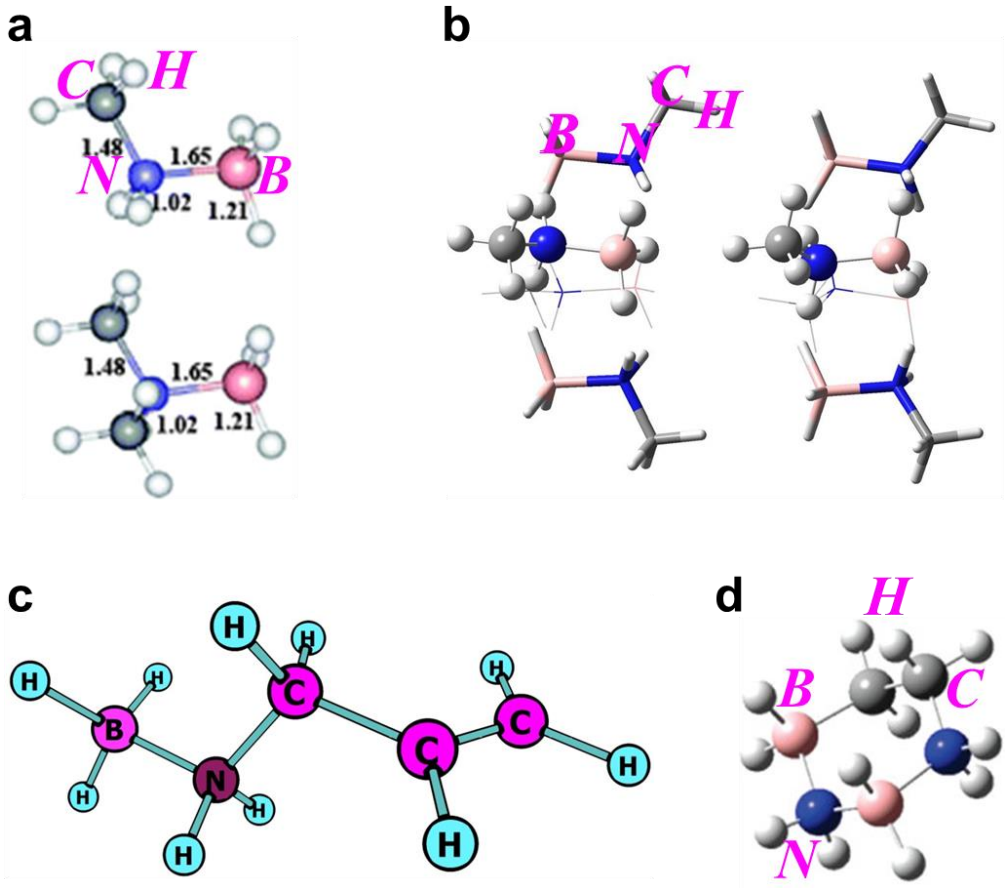

Figure 1.7: Molecular structures of representative H/B/C/N compounds investigated in the literature using DFT methods. (a) MeAB and dimethylamine–borane [$BH_3NH(CH_3)_2$];[115] (b) Methylamine–borane octamer [$(BH_3NH_2CH_3)_8$];[116] (c) Allylamine–borane ($CH_2CHCH_2NH_2BH_3$);[117] and (d) Cyclic compounds $C_2B_2N_2H_{12}$ and C_4BNH_{12}.[118]

CTB, BZ, and other cyclic species. These reaction pathways are interdependent, with each influencing the kinetics and overall decomposition mechanism of AB.

Among the limited DFT studies on H/B/C/N systems, most have focused primarily on the crystal structures of the resulting compounds.[112–114] Of the few that address reaction mechanisms, nearly all concentrate solely on the first dehydrogenation step. Sun *et al.*[115], using the B3LYP functional, reported that MeAB and dimethylamine-borane [$BH_3NH(CH_3)_2$] (**Figure 1.7a**) exhibit slightly higher activation barrier for the first H_2 release compared to pure AB, suggesting that methyl substitution enhances reversibility and suppresses BH_3/NH_3 formation, though it does not improve the H_2 release rate. Liu *et al.*[116] studied the dihydrogen-

bonded methylamine–borane octamers [$(BH_3NH_2CH_3)_8$] (**Figure 1.7b**) using B3LYP, revealing that stepwise release of six equivalents of H_2 leads to the formation of a six-membered B–N ring. The process is exothermic, with increasing enthalpy along the dehydrogenation pathway. Yaya *et al.*[117] employed B3LYP, M06-2X, and wB97XD3 functionals to investigate allylamine-borane ($CH_2CHCH_2NH_2BH_3$) (**Figure 1.7c**), identifying the second dehydrogenation step as rate-limiting, though the overall H_2-release pathway requires minimal energy. Matus *et al.*[118] explored the dehydrogenation energetics of $C_2B_2N_2H_{12}$ and C_4BNH_{12} cycles (**Figure 1.7d**) using B3LYP functional and found that dehydrogenation across the B−N bond is energetically more favourable as compared to dehydrogenation across the B−C, N−C, and C−C bonds.

Overall, there remains a significant knowledge gap regarding the complete dehydrogenation, as well as the dissociation and cyclisation mechanisms in larger H/B/C/N systems such as PMeAB and MeCTB, let alone their reactivity with other molecules or potential structural evolution toward BN-like frameworks. Addressing these gaps is essential for developing a comprehensive mechanistic understanding of H/B/C/N thermal chemistry and advancing the rational design of BN-based materials from H/B/C/N precursors.

1.2.5 Reactive Force Field for H/B/C/N Chemistry

When simulating systems with timescales significantly greater than 100 ps and/or containing more than 100 atoms, the computational cost becomes prohibitively high using the DFT method. To address this limitation, the ReaxFF reactive force field has been developed, which retains a level of accuracy that is comparable to QM methods, while substantially lowering computational demands through the use of a FF approximation. In this approach, interatomic interactions are described using parameterized empirical functions rather than solving the Schrödinger equation, enabling efficient simulation of large, reactive systems without

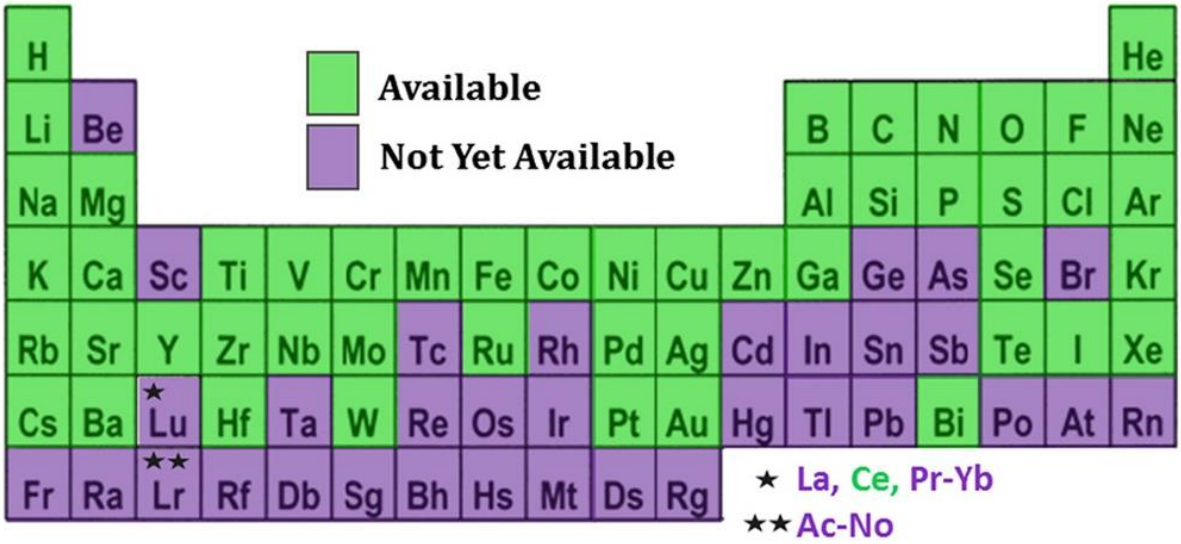

Figure 1.8: Elements currently described in available ReaxFF parameter sets.[120]

sacrificing essential chemical fidelity.[119] Classical FF are capable of modelling large molecular systems; however, they require the explicit definition of all chemical bonds, making them unsuitable for simulating chemical reactions. In contrast, ReaxFF models chemical bonding using bond orders rather than fixed bonds, enabling the dynamic formation and breaking of bonds throughout a simulation.[107]

More specifically, ReaxFF integrates a bond-order formalism with polarizable charge descriptions to capture both reactive and non-reactive interactions among atoms.[120] This framework enables ReaxFF to reliably represent covalent bonding as well as electrostatic forces across a broad spectrum of elements and materials (elements with published ReaxFF parameter set are highlighted in **Figure 1.8**).[120] The total system energy within ReaxFF is expressed as:

$$E_{\text{system}} = E_{\text{bond}} + E_{\text{over}} + E_{\text{angle}} + E_{\text{tors}} + E_{\text{vdWaals}} + E_{\text{Coulomb}} + E_{\text{specific}}$$

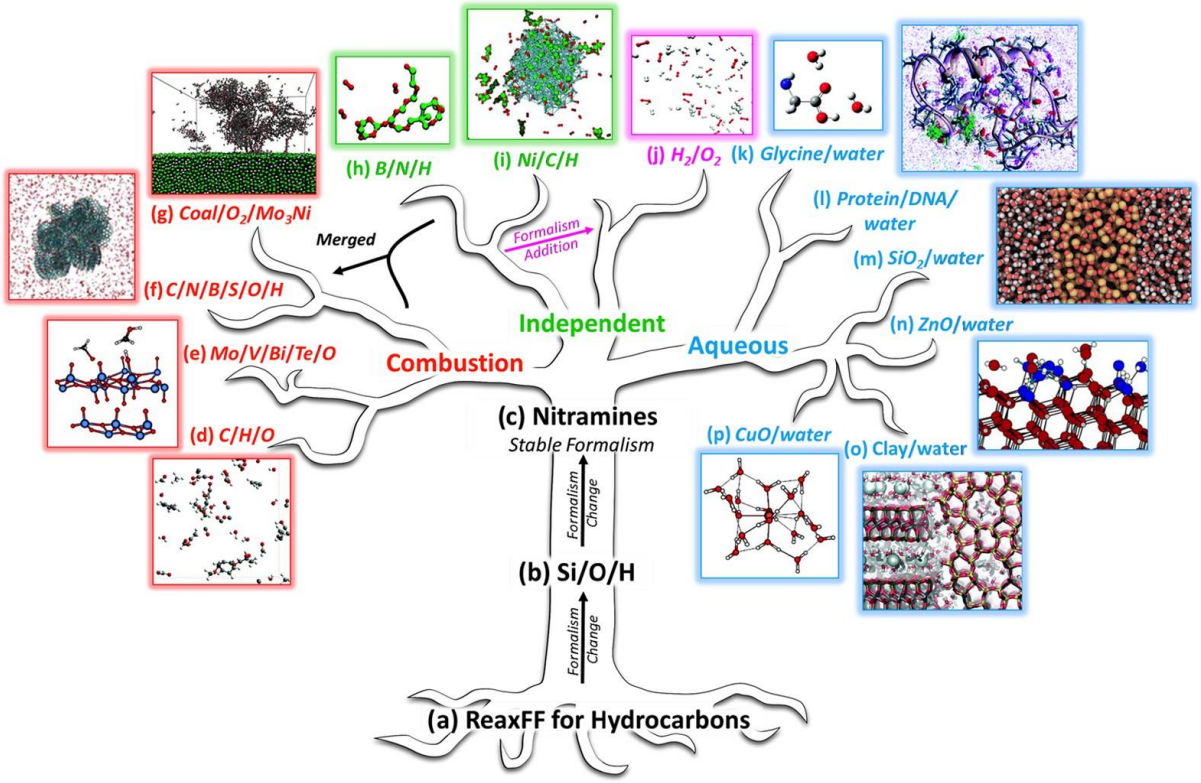

Figure 1.9: ReaxFF development tree, where parameter sets on a common 'branch' are fully transferable with one another.[120]

Here, E_{bond} denotes a continuous function of interatomic distances that accounts for bond formation energies. The terms E_{angle} and E_{tors} represent the energetic contributions arising from valence angle strain (three-body) and torsional strain (four-body), respectively. Valence angle strain occurs when bond angles deviate from their equilibrium values, introducing energy penalties due to geometric distortion of the molecular framework. Torsional strain arises from the rotation around bonds, where eclipsed or non-ideal dihedral angles increase steric and electronic repulsion. E_{over} introduces a penalty for over-coordination based on valence rules—for instance, a high energy cost is imposed when a carbon atom exceeds four bonds, reflecting the severe instability associated with violating fundamental bonding constraints. Electrostatic and van der Waals interactions, represented by $E_{Coulomb}$ and $E_{vdWaals}$, are computed between all atom pairs, independent of their bonding status or bond order. Finally, $E_{specific}$ encompasses

system-dependent terms, which are included only when necessary to account for particular features such as lone pairs, conjugation, hydrogen bonding, or C_2 corrections.[120]

As illustrated in **Figure 1.9**, existing ReaxFF parameter sets can be broadly categorized into two primary branches, each internally transferable: (1) the combustion branch and (2) the aqueous branch.[120] Within the combustion branch, numerous studies have utilised ReaxFF to explore reactive phenomena in systems comprising elements such as C/H/O[119] and C/N/B/S/O/H.[121] The present study is based on the HCONSB.ff force field,[122] which belongs to this branch. Specifically, the $ReaxFF_{HCONSB}$ parameterisation defines all relevant bond dissociation energies, angular distortions, and reaction barriers for systems involving H/B/C/N atoms. Originally developed for studying the dehydrogenation of ammonia borane (B/N/H systems)[123], $ReaxFF_{HCONSB}$ has been subsequently extended and refined through additional parameterisations for C/H/O[121] and C/H/O/N/S[124] systems in two separate studies. Both of these developments fall within the combustion branch, which, owing to its internal transferability,[120] supports the application of $ReaxFF_{HCONSB}$ to simulate a diverse range of atom types present in my system. Therefore, I expect a decent transferability for $ReaxFF_{HCONSB}$ to effectively capture the key steps in the reaction of H/B/C/N systems, including: (i) dissociation, (ii) dehydrogenation, (iii) cyclisation, (iv) carbon removal, and (v) ceramic network formation.

Because ReaxFF parameters are derived from QM calculations, the method can be directly applied to novel systems that have not been extensively studied experimentally. By further integrating them with DFT and experimental observations, it becomes possible to elucidate complex reaction mechanisms, predict material properties, and ultimately inform the rational design of new materials. However, a validated ReaxFF parameter set for the H/B/C/N system has yet to be established.

Chapter 2

Scalable Production of Polymer-Derived Boron Nitride Fibres from Solution Electrospun Polyaminoborane

Contents

2.1 Introduction

BN fibres (BNF) are sought after for ultra-lightweight applications that need to perform in extreme environments, *e.g.*, those encountered in space, aerospace, and other means of transportation.[125–127] BNF are particularly interesting due to their isoelectronic relationship, and closely related structures to carbon-based materials. BNF present certain advantages over carbon fibre counterparts. Compared with carbon fibers, BNF are electrically insulating,[128] and have superior thermal stability and chemical inertness.[129–131] These properties, coupled with high Young's modulus of fibrous BN, make BNF potentially the strongest known insulating material to date.[130] BNF also possess the exceptionally rare combination of being both a dielectric and a thermal conductor.[132] It outperforms carbon fibres in thermal stability in both oxidizing and inert atmospheres and exhibits much greater chemical resistance to extreme conditions.[31] Despite these outstanding properties, and existing demand, the availability of BNF is limited as current synthetic routes are not straightforward. Therefore, very few reports on the synthesis of BNF exist to date. Among the key bottlenecks are the properties of BN precursor systems and their subsequent processability into fibres.[28,69,79] Despite various systems being reported, the resulting BNF have shown considerable variability in terms of fibre diameter, crystal structure, morphology, and overall quality, [25–31] and only minor progress has been made towards their potential for scalable manufacturing.

In the past decade, NASA reported the synthesis of BN nanotubes (BNNT), however, the process requires specialised high-power lasers and operates at high pressures and temperatures, limiting wider adoption of these methods.[133] Chemical vapour deposition and template methods have also been explored.[134] Other dedicated work on the production of BNF has mainly centred around melt-spinning, hot extrusion (combining spinning and thermolysis), and electrospinning of B, C, and N-containing polymer precusors.[69] Precursors employed in these latter studies were either polymer additive-aided colloidal particles, or polyborazylenes (PBZ)-

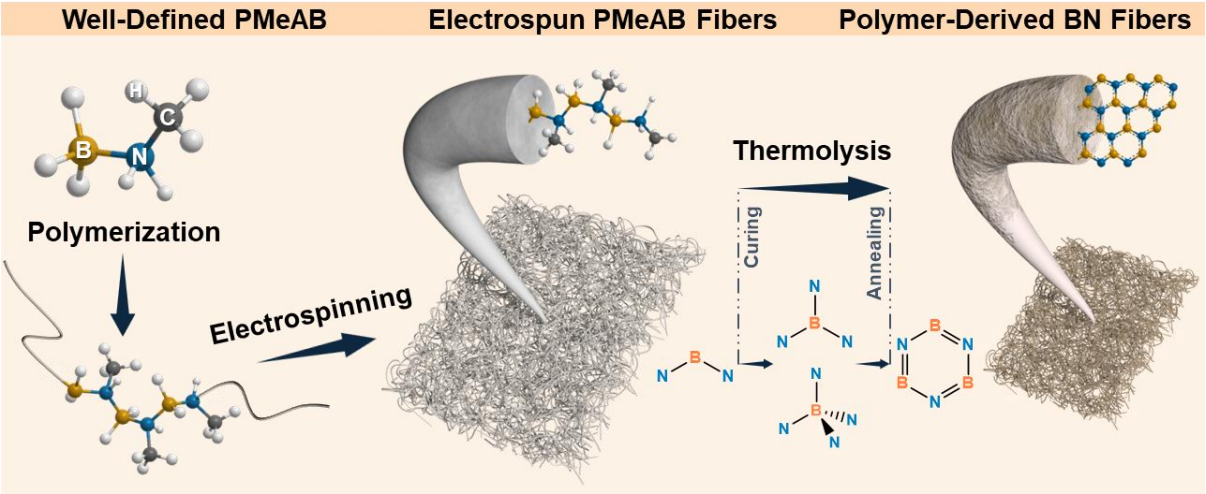

Figure 2.1: Schematic synthetic route toward PMeAB fibres (PMeABF) and BNF.

based single-source precursors. For instance, by electrospinning B_2O_3/PVB mixtures followed by high temperature nitridation, Qiu *et al.* [26,27] produced long, aligned, BN nanofibres (*ca.* 100 nm in diameter and *ca.* 13 cm in length) with a porous structure due to uneven solid vapor nitridation and low ceramic yield (<20 wt.%). The polymer-derived ceramic route, on the other hand, offers precise control over precursor compositions,[29] because polymeric precursors derived from borazine already contain units of hexagonal B-N rings, and therefore leads to the highest ceramic yield (90 wt.%) reported.[28] Yet, PBZ is air-sensitive,[23,24,57,135–137] and has low solubility in common solvents and therefore requires specially designed polymer melt processing equipment and strict operation conditions, limiting its further development.[73,81,82] Electrospinning provides a straightforward and efficient way to create continuous polymer and ceramic fibers with diameters ranging from micro- to nanoscale.[21,22] For the generation of high-quality BNF, the design of precursors that are stable and can be dissolved in common solvents is critical, as this will enable the efficient fabrication of ceramic fibres by means of electrospinning.[138]

One such potential precursor is the main-group polymer,[139] *N*-methylpolyaminoborane, $[(H_2BNMeH)_n]$ (PMeAB), which is best prepared by catalytic routes, (although stoichiometric methods are also known[140,141]) as first reported by Manners in 2008, using the catalyst Ir(^{t}Bu-

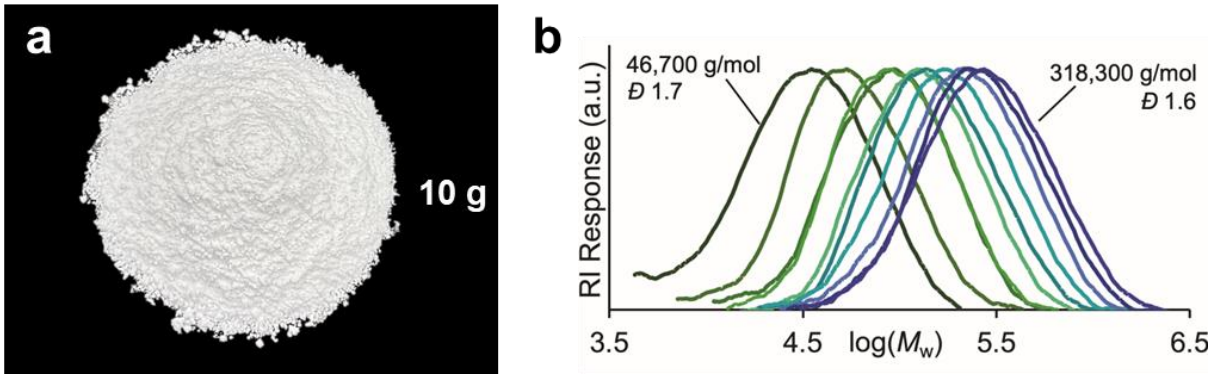

Figure 2.2: (a) As-synthesized PMeAB powder. (b) Overlaid GPC traces of the PMeAB prepared as shown in Figure 2c.

POCOP)H_2, **[Ir]**, (^{t}Bu-POCOP = κ^3-(OP^{t}Bu$_2$)$_2$C$_6$H$_3$).[142,143] With this catalyst (at 0.3 mol% loadings) the commercially available amine-borane pre-monomer, $H_3B{\cdot}NMeH_2$ (MeAB), was reported to undergo an atom-efficient dehydropolymerisation to form PMeAB, where H_2 is the only co-product (M_w = 160,000 g·mol^{-1}, $Đ$ = 2.9).[142–144] Our collaborator, the Weller Group, has recently demonstrated that partial control[145] over the degree of polymerisation (M_w) in PMeAB synthesis can be achieved using the air-tolerant pre-catalyst [Rh(L)(NBD)]Cl, **[Rh]**, [L = κ^3-(^{i}Pr$_2$PCH$_2$CH$_2$)$_2$NH, NBD = norbornadiene], and a boronium chain-control agent, that reduces the M_w from 133,100 g·mol^{-1} to, for example, 64,400 g·mol^{-1} ($Đ$ = 1.7) in a controlled manner.[99] The molecular weight of PMeAB can be modulated through (1) temperature, (2) catalyst loading, (3) catalyst type (structure and element), and (4) the rate of chain elongation. Pre-catalyst **[Rh]** can also be used at low catalyst loadings (0.01 mol%) to produce PMeAB on 10g scale. However, methods to increase M_w in a systematic, controlled and scalable manner above ~160,000 g·mol^{-1}, on a scale suitable for the study of BNF synthesis at low catalyst loadings has not been reported.[146] PMeAB is a promising precursor for the manufacture of BNF by electrospinning methods because of its: (i) high B–N-content, (ii) good solubility in common solvents such as THF or $CHCl_3$, and (iii) its stability at room temperature as an easy to handle solid. However, the electrospinning and subsequent thermolysis of PMeAB have not been reported in any detail,[142,147] and the optimal parameters for these processes with regard to

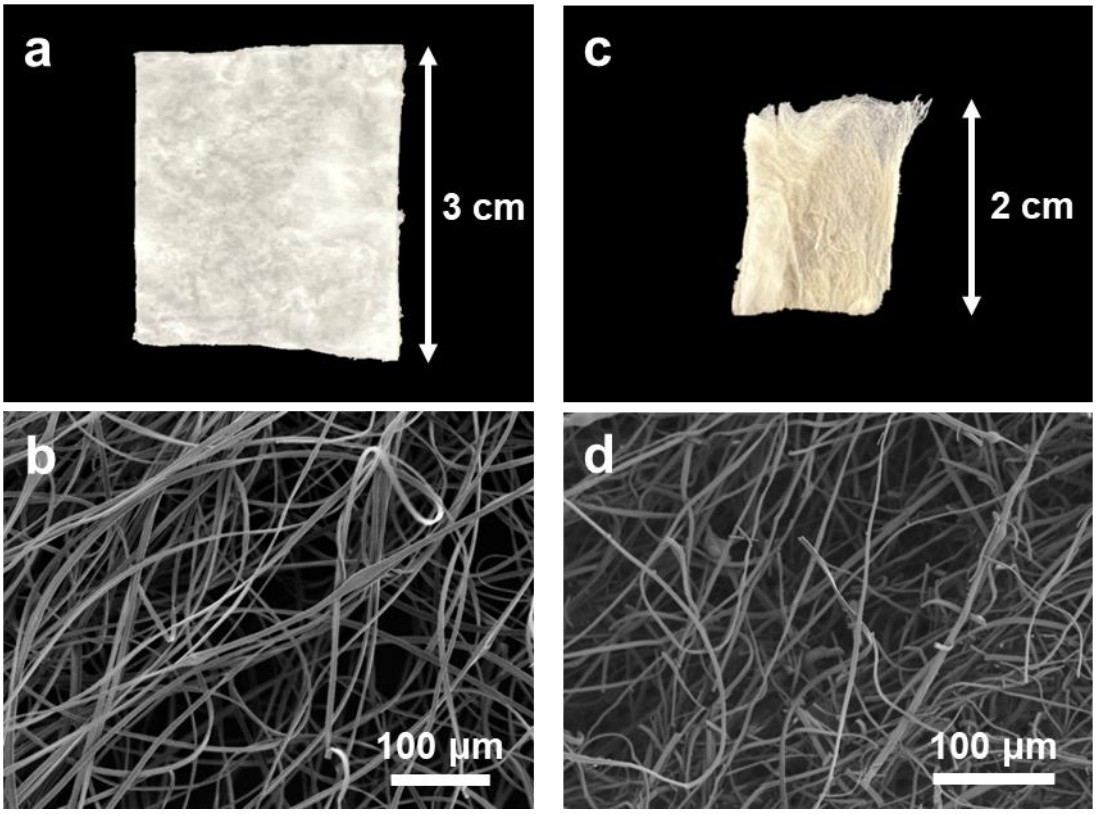

Figure 2.3: Actual photo of (a) PMeABF and (c) BNF. Typical SEM images for (b) PMeABF and (d) BNF.

polymer chain length has yet to be determined. There have been sporadic reports on the use of powdered polyaminoboranes as potential pre-ceramics to BN over the last 25 years. The thermolysis of parent $[H_2BNH_2]_n$ was reported by Kim and co-workers,[148] while Manners and co-workers reported thermolysis of pelletized PMeAB.[142] The pyrolysis of MeAB[100] has been reported to form an ill-defined cross-linked solid. To my knowledge, there have been no reports on the use of PMeAB to generate BNF.

In this chapter, I describe the development of a new polymer-derived ceramic route to BNF using PMeAB (**Figure 2.1**). This approach uses a scalable, and straightforward, polymer pre-ceramic synthesis of PMeAB, with low loadings of catalyst to offer fine control of the polymer over a wide range of M_w (**Figure 2.2**). Subsequent additive-free electrospinning of polymer samples with optimal M_w (**Figure 2.3a, b**), curing (cross-linking), and pyrolysis yields ultra-high purity micro- and nanoscale BNF (**Figure 2.3c, d**). Detailed characterisation provides

composition, phase, microstructure, and morphology characteristics of these BNF. My results offer a straightforward method for producing high purity, solid BNF at scale from commercially available starting materials, as well as fundamental, underpinning, observations that serve as a basis for the further design of other BN-containing structures.

2.2 Materials & Methods

2.2.1 Materials

Table 2.1: Summary of reactants and solvents used in this chapter for synthesis of BNF.

Name	Purity	Supplier
Reactants		
$PMeAB_{(s)}$	>95%	*Weller's Group*[99]
$NH_{3(g)}$	>99.94%	*BOC*
$Ar_{(g)}$	99.998%	*BOC*
Solvents		
$CHCl_{3(l)}$	-	*Fisher Scientific*

2.2.2 Synthesis

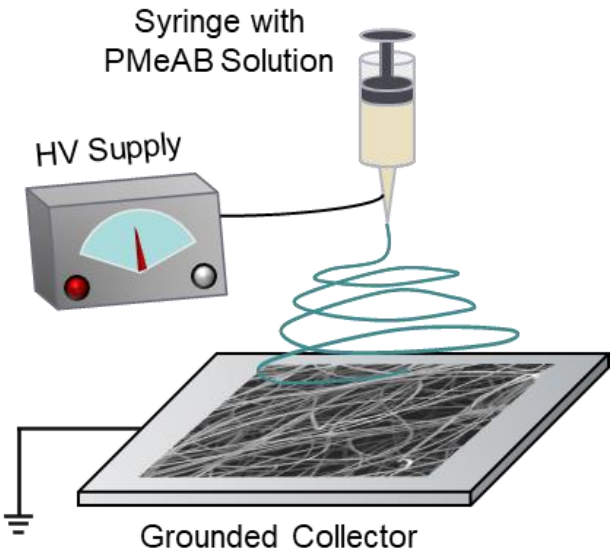

Figure 2.4: Schematic of the electrospinning setup.

The fabrication of BNF can be divided into two main stages: (1) the electrospinning process to produce PMeABF, and (2) the thermal treatment to convert the electrospun PMeABF into BNF.

In the electrospinning stage, the spinning solutions were prepared using PMeAB with average measured molecular weights (M_w) ranging from 110,500 g·mol^{-1} to 290,500 g·mol^{-1} dissolved in 2 mL of $CHCl_3$. The dissolution process involved continuous stirring for 1 hour at room temperature. Once the PMeAB was fully dissolved to form a homogeneous solution, it was transferred immediately to a 1 mL syringe equipped with a 23-gauge stainless steel needle. The syringe was connected to a high voltage supply (Genvolt High Voltage Power Supply). The solution was gravity-fed without the use of a syringe pump. The tip-to-collector distance was maintained at 30 cm throughout the electrospinning experiments. An applied voltage ranging from 20 to 35 kV was used to ensure optimal electrospinning continuity. The electrospinning process was conducted in a glove box with controlled temperature (20±1°C) and humidity (15±1%). Finally, the PMeAB precursor fibres were collected on a piece of aluminium foil attached to a grounded metal substrate and could be easily peeled off into free-standing fibres mat. Although other solvents such as THF, DMF, and DMSO can dissolve PMeAB, they fail to produce spinnable solutions and instead result in electrospraying, primarily due to their higher boiling points compared to chloroform.

The conversion of PMeABF to BNF involved two essential steps: thermal curing followed by high-temperature annealing under an NH_3 atmosphere. The curing process was carried out in a vacuum oven at a temperature of 100°C for 48 h, maintaining a vacuum pressure below 10^{-1} bar. Subsequently, the cured PMeABF were annealed in a high-temperature tube furnace. The fibres were heated directly to 1400°C and held at that temperature for 2 h in an atmosphere consisting of a mixture of NH_3 and Ar gases in a volume ratio of 1:2. The samples were then

allowed to cool naturally to room temperature. The heating rate from room temperature to 1400°C was set at 10°C/min.

2.2.3 Characterisations

All polymeric materials were analysed by gel permeation chromatography (GPC) measured on a Malvern Viskotec GPC_{max} together with a Viskotec TDA 305 RI detector. Polymer M_n is referenced to polystyrene standards between M_n 474 – 476,800 $g \cdot mol^{-1}$. GPC measurements were conducted by the Weller's Group. All samples were passed through 3 columns consisting of a porous styrene divinylbenzene copolymer (2 × T5000 and 1 × T4000 Malvern columns). The eluent used was GPC grade THF containing 0.1% w/w $[NBu_4]Br$ and the flow rate was 1 $cm^3 \cdot min^{-1}$. Each polymer sample was dissolved in GPC grade THF $[NBu_4]Br$ (2 mg mL^{-1}) and filtered through a PTFE filter (pore size: 45 μm). The viscosity of the PMeAB solutions was measured using a Brookfield DV-II viscometer with a cone spindle CP-41. A fixed volume of 2 mL of the solution was loaded into the sample cup, and a ramping of rotation speed was employed from 50 to 120 rpm, corresponding to shear rates of 100−240 s^{-1}. For highly viscous PMeAB solutions, the rotation speed was reduced to 10 rpm to maintain the % torque between 10 and 100%. The viscosity measurement was conducted twice, and the averaged viscosity values were reported. Surface tension measurements were performed using an Ossila contact angle goniometer in ambient conditions and calculated manually by combining Eqs. 1 and 2 proposed by Arashiro and Demarquette,[d] and by referencing the table of H values provided by Andreas et al.[e] as a function of S, allowing γ to be determined from the photograph of a pendant drop.

[d] Arashiro EY, Demarquette NR (1999) Use of the pendant drop method to measure interfacial tension between molten polymers. Mater Res 2:23–32.

[e] Andreas JM, Hauser EA, Tucker WB (1938) Boundary tension by pendant drops1. J Phys Chem 42(8):1001–1019.

$$\gamma = \frac{g \times D_e^2 \times \Delta\rho}{H} \quad (1)$$

where γ is the surface tension, g is the gravitational constant, Δρ is the density difference (in this case, the difference between the density of the polymer solution and the density of air, $\Delta\rho = \rho_{sol} - \rho_{air}$. Since $\rho_{sol} \gg \rho_{air}$, we approximate $\Delta\rho = \rho_{sol} - \rho_{air} \approx \rho_{sol}$), D_e is the equatorial diameter of the drop, H is a correction factor which is related to the shape factor of the pendant drop, S, defined as:

$$S = \frac{D_s}{D_e} \quad (2)$$

where D_s is the drop diameter measured horizontally at a distance D_e away from the apex of the drop. Scanning Electron Microscopy (SEM) images were acquired using a Zeiss Merlin SEM and a JEOL JSM-840F SEM operating at an accelerating voltage of 3 kV. Prior to imaging, the samples were coated with a 10 nm layer of platinum (Pt). Fiber diameters were determined by analysing at least 200 unbiased counts (major diameter of a dumbbell-like cross section) from the SEM images and fitting the resulting histogram. Energy-Dispersive X-ray Spectroscopy (EDX) line scanning and elemental mapping were performed using a Zeiss Merlin SEM operating at an accelerating voltage of 3 kV. Transmission Electron Microscopy (TEM) images were obtained using a JEOL JEM-2100F TEM operating at an acceleration voltage of 200 kV. X-ray Photoelectron Spectroscopy (XPS) analysis was conducted using a Thermo Scientific K-Alpha X-ray Photoelectron Spectrometer System. An ion pumped VG Microtech CLAM 4 MCD analyser system equipped with unmonochromated Mg K_α X-ray radiation of 1253.6 eV was used. Fourier Transform Infrared (FT-IR) Spectroscopy attenuated total reflection (ATR) spectra were recorded using a Varian Excalibur FTS 3500 FT-IR spectrometer in the range of 600 to 4000 cm^{-1}. X-ray Diffraction (XRD) analysis was performed at room temperature using a Siemens D5000 powder diffractometer with copper Kα radiation (λ = 0.15406 nm) and a secondary monochromator. The samples were continuously rotated during data collection, and a step size of 0.05° 2θ was used in the range of 10–100° 2θ

with a count time of 12 s per step. Thermogravimetric analysis coupled with differential scanning calorimetry and mass spectrometry (TGA-DSC-MS) was performed using a STA 449 F3 Jupiter® instrument, integrated with a 403 Aëolos Quadro quadrupole mass spectrometer. The samples were heated in Ar atmosphere from room temperature to 1400°C at a heating rate of 10°C/min. The quadrupole was used to scan all m/z ratios from m/z=1 to m/z=150 approximately every 30 s. ^{11}B magic angle spinning−nuclear magnetic resonance (^{11}BMAS-NMR) measurements were carried out at 128.39 MHz using a Varian VNMRS spectrometer and 4 mm (rotor o.d.) probe. Spectra were acquired at a spin rate of 12 kHz. All direct excitation ^{11}B spectra were acquired with a 1 μs 30° solid pulse which was determined from a 6 μs solution pulse determined on $BF_3{\cdot}OEt_2$. The spectra were acquired with a recycle delay of 1 s determined on the sample. Boron spectral referencing is relative to $BF_3{\cdot}OEt_2$. ^{11}BMAS-NMR measurements were conducted by the Weller's Group. Nanoindentation tests were conducted by Dr. Ed Darnbrough with a standard Berkovich diamond tip using a low load module on a Hysitron TI Premier. The tip shape was calibrated using fused silica and the hardness and reduced modulus measurements from the samples were calculated using the formulas introduced by Oliver and Pharr.[149] Precursor PMeABF were directly electrospun onto single crystal silicon wafers and BNF were dissolved in acetone and drop-cast onto single crystal silicon wafers prior to the measurements.

2.3 Results & Discussion

In this section, I report a reliable, controllable, and scalable synthesis methodology for producing pure micro- and nano-BNF, offering a competitive alternative to NASA's energy-intensive BNNT production. The single-source precursor, PMeAB, plays a pivotal role in this process due to its high B–N content and good solubility in common electrospinning solvents. The catalytic, and scalable, synthesis of PMeAB with controlled molecular weights (M_w =

110,500–290,500 g·mol^{-1}), enables the production of BNF by electrospinning method and thermolysis under ammonia. PMeAB molecular weight and concentration were identified as key factors dictating the viscosity and surface tension, and thus influencing the overall spinnability of the PMeAB solution. I reveal that the subsequent formation of a cross-linked intermediate during PMeAB thermolysis is essential to retain the fibrous morphology during the conversion to BNF. Comprehensive characterisation demonstrated the purity and homogeneity of the BNF, with ~97 at.% of B and N contents combined throughout the fiber body. This newly disclosed route to BNF offers a route to potentially valuable multifunctional material for lightweight composites suitable for applications in extreme environments such as space or aerospace.

2.3.1 Electrospinning PMeAB Solutions

Table 2.2: Dehydropolymerisation conditions and details of resulting polymers (see **Appendix A** for full experimental conditions).

Entry	Cat.	(mol%)	Conditions	Temp (°C)	M_w (g·mol^{-1})	$Đ$	Scale (g)	Code
1	**[Rh]**	(0.01)	Slow	60	46,700	1.7	10	**PMeAB1**
2	**[Rh]**	(0.01)	Slow	40	71,800	1.5	10	**PMeAB2**
3	**[Rh]**	(0.01)	–	20	110,500	1.5	10	**PMeAB3**
4	**[Ir]**	(0.1)	–	20	112,800	1.5	1	**PMeAB4**
5	**[Rh]**	(0.01)	Slow	20	148,600	1.5	50	**PMeAB5**
6	**[Rh]**	(0.01)	Slow	5	172,000	1.5	10	**PMeAB6**
7	**[Rh]**	(0.01)	Slow	0	205,200	1.6	10	**PMeAB7**
8	**[Ru]**	(0.03)	$NMeH_2$	20	250,500	1.5	5	**PMeAB8**
9	**[Ir]**	(0.1)	$NMeH_2$	-15	290,500	1.6	5	**PMeAB9**
10	**[Ir]**	(0.1)	Slow/$NMeH_2$	-15	318,300	1.5	6	**PMeAB10**

The controlled catalytic synthesis of PMeAB with molecular weights ranging from M_w = 46,700 to 318,300 g·mol^{-1} was conducted by my collaborator, the Weller's Group. The

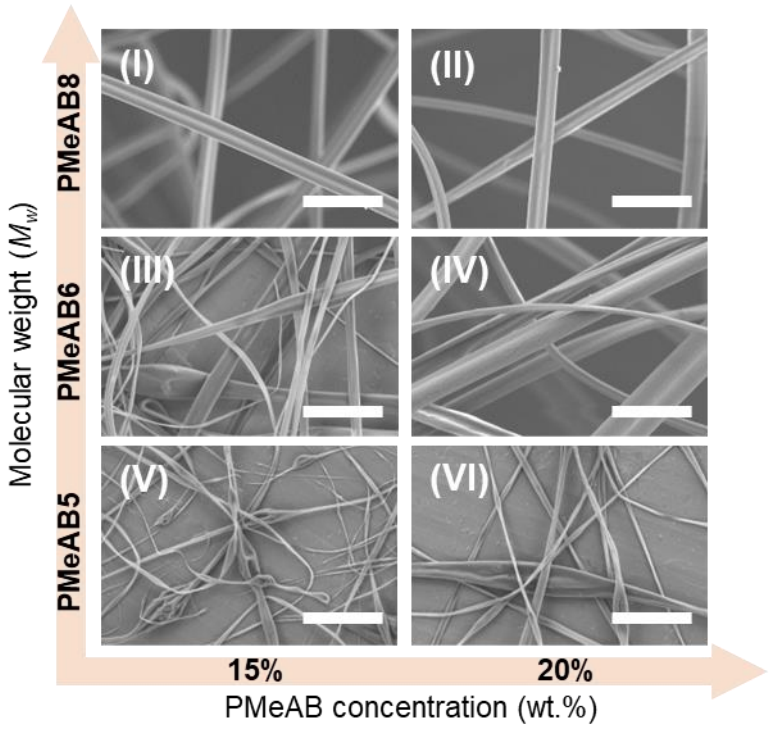

Figure 2.5: Morphology of the electrospun PMeABF using representative PMeAB (M_w = 148,600 g·mol-1; 172,000 g·mol^{-1}; 250,500 g·mol^{-1}) and concentrations ().

resulting PMeAB samples are designated sequentially as **PMeAB1** through **PMeAB10**, where a lower number corresponds to a lower molecular weight, and conversely, a higher number indicates a higher molecular weight (**Table 2.2**).

The key solution parameters necessary for optimal electrospinning conditions were determined using polymer samples **PMeAB1** to **PMeAB9**. The concentration of PMeAB solutions ($CHCl_3$) varied from 5 to 30 wt.%; with the spinning solutions labelled as **PMeABX-Y%**, where Y corresponds to the weight percentage of PMeAB. **Figure 2.5** shows the key results from these studies, that demonstrate that both PMeAB molecular weight and its concentration determine the spinning behaviour and resulting fibre morphology. Electrospinning of PMeAB with lower M_w, i.e. **PMeAB1**, **PMeAB2**, **PMeAB3**, **PMeAB4**, **PMeAB5,**, at concentrations below 10 wt.% typically resulted in the formation of droplets instead of fibres. At polymer concentrations between 15 and 30 wt.%, the solutions became spinnable. This corresponds to the overlap concentration (c*), wherein a sufficient level of

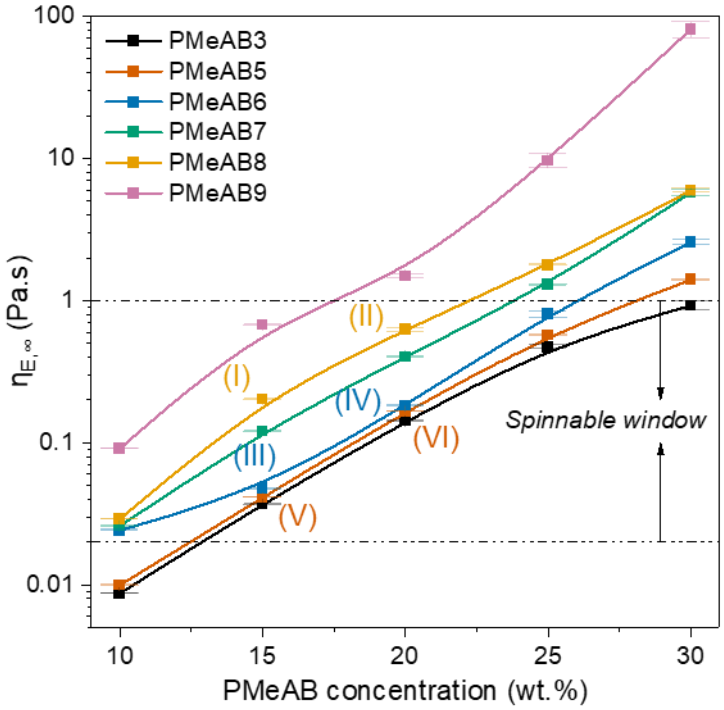

Figure 2.6: Effect of solution viscosity on the spinnability of PMeAB/$CHCl_3$ solutions. The spinnable window indicate the optimal viscosity range for successful electrospinning of PMeABF.

polymer chain entanglement is achieved.[150] While electrospinning of **PMeAB5-15%** led to fibers with beads, **Figure 2.5(V)**, increasing the concentration to **PMeAB5-20%** and **PMeAB5-25%** partially suppressed their formation, *e.g.* **Figure 2.5(VI)**. Further increasing the concentration to **PMeAB5-30%** makes the solution too viscous to be electrospun. Comparing **PMeAB1, 2, 3, 4, and PMeAB5** with higher M_w PMeAB, such as **PMeAB6** and **PMeAB7**, at the same polymer concentration (20% or 25%), revealed that **PMeAB6** and **PMeAB7** form more homogeneous fibres with significantly fewer beads, see **Figures 2.5(III) vs (V)** and **Figure 2.5(IV) vs (VI)**. Notably, electrospinning **PMeAB6-20%** yields fibres without any beads. The further increase of the M_w using **PMeAB8** and **PMeAB9** results in high-quality bead-free fibres, when a concentration of 15 wt.% is used, **Figure 2.5(I)**. PMeAB with molecular weights ranging from M_w = 110,500 (**PMeAB3**) – 250,500 g·mol^{-1} (**PMeAB8**),

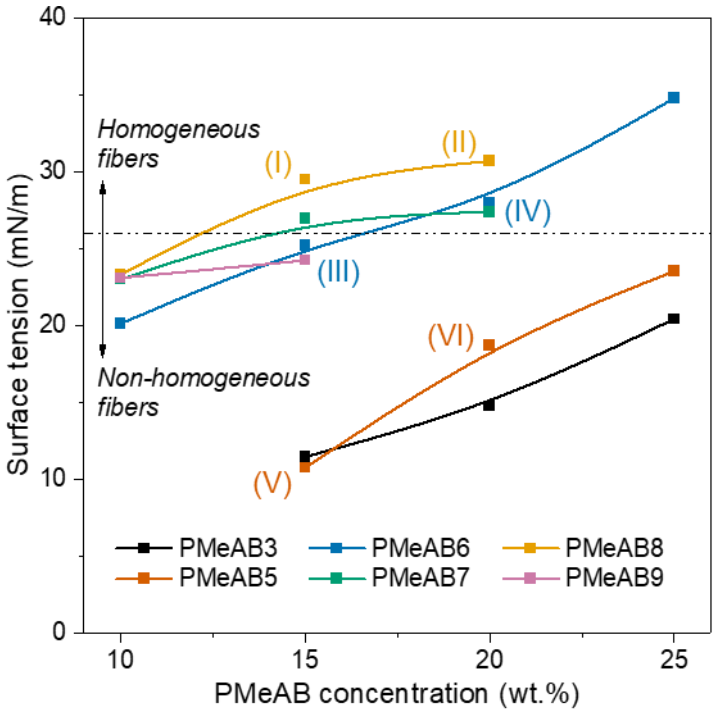

Figure 2.7: Effect of solution surface tension on the spinnability of PMeAB/$CHCl_3$ solutions. The dashed line indicates the threshold surface tension required for producing homogeneous PMeABF.

at concentrations between 15 and 20%, were found to be optimal for the electrospinning in $CHCl_3$ solvent. The very high molecular weight **PMeAB10** was not tested further.

Parametric studies, focusing on the viscosity and surface tension of the PMeAB solutions, have been used to establish optimal conditions for the electrospinning of PMeABF. A viscosity of approximately 0.02 Pa·s is sufficient for the PMeAB/$CHCl_3$ solution to be spinnable (**Figure 2.6**). However, above a viscosity threshold of ~1 Pa·s electrospinning is not possible due to the high cohesion of the solution. Within this spinnable window (0.02 to 1 Pa·s), the morphology of the electrospun fibres vary. This variation is attributed to the surface tension of the spinning solution, which is influenced by its composition and directly impacts the quality of the fibres produced, and is a result of the intermolecular interactions between the polymer chains and the solvent molecules.[151,152] As surface tension increases with an increase in polymer concentration, this allows for an assessment of the lower limit for effective electrospinning, which is shown

to be 26 mN/m (**Figure 2.7**). Above this limit, PMeAB solutions are spinnable, generating fibers of good quality, high homogeneity and continuity. Conversely, when surface tension is too low, the electrostatic forces dominate over capillary forces, causing the jet to break up into droplets rather than forming a continuous filament, which results in beaded fibres. The estimated optimal viscosity of 0.02~1 Pa·s and minimum ST value of 26 mN/m agree well with values reported in literature.[153]

Fibre diameter can be tuned by the selection of solution and/or electrospinning parameters. The electrospun PMeABF here have diameters ranging from several microns to less than 100 nm. Despite a broad diameter distribution within each sample, a general trend is notable: as the concentration or molecular weight of the polymer increases, the average diameter of the fibres tends to increase (**Figure 2.8**). This is consistent with literature precedent for other electrospun fibres and shows that using higher concentrations or molecular weights of polymer results in thicker electrospun fibres, due to increased polymer chain entanglement within the spinning solution.[18,84] Notably, there was no change to the chemical composition of PMeABF after electrospinning, as measured by solution ^{1}H and ^{11}B NMR spectroscopy (**Figures 2.9**, **2.10**). The ^{1}H NMR spectrum for electrospun PMeABF also showed no residual $CHCl_3$ solvent (**Figure 2.9**).

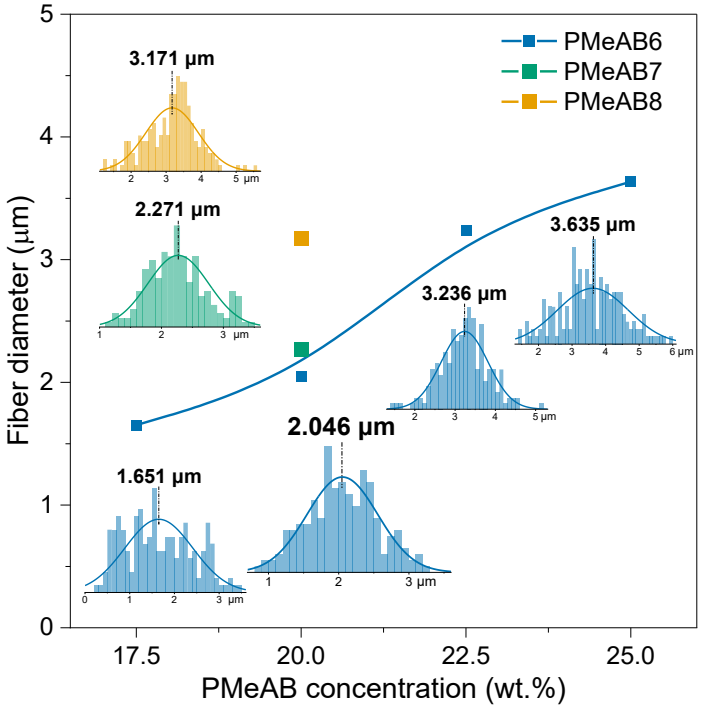

Figure 2.8: Polymer concentration and M_w effects on the diameter of the electrospun PMeABF.

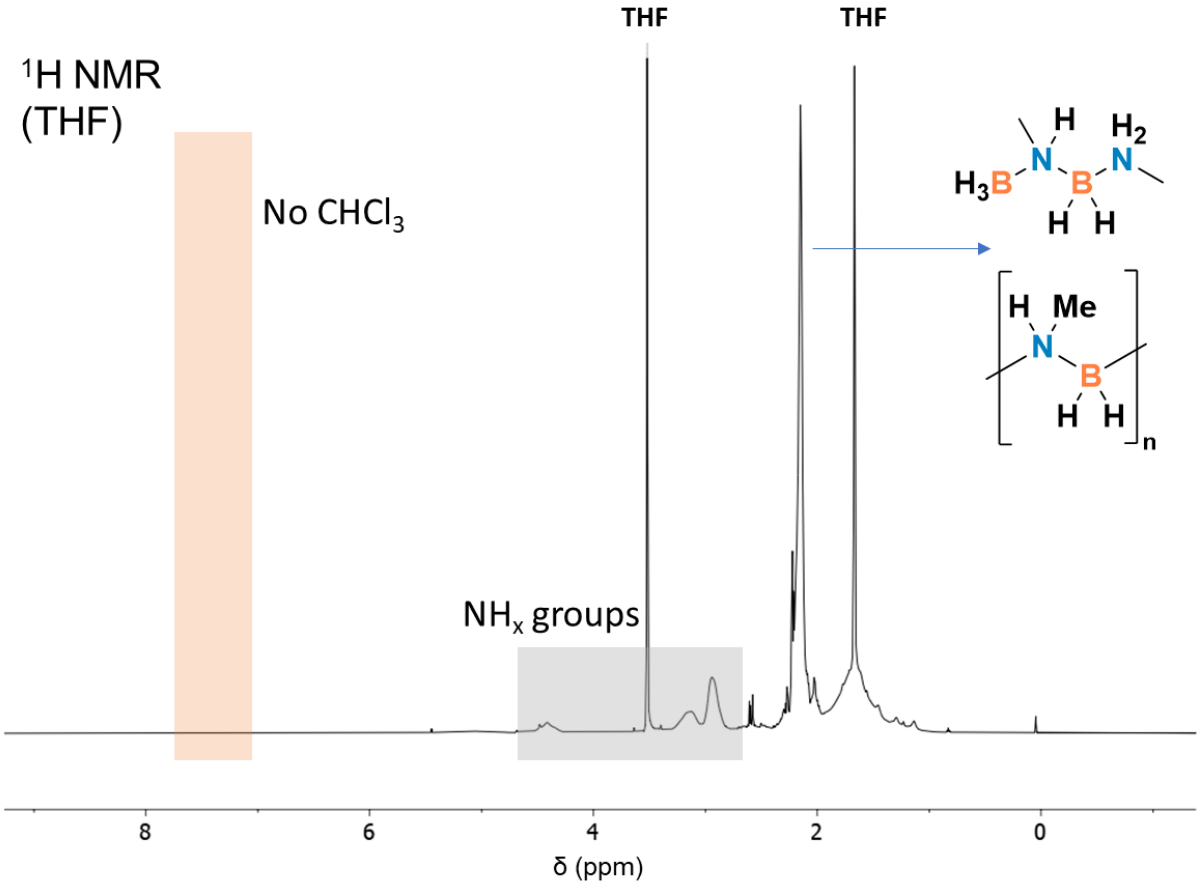

Figure 2.9: ^{1}H NMR spectrum of as-spun PMeABF showing no solvent residue.

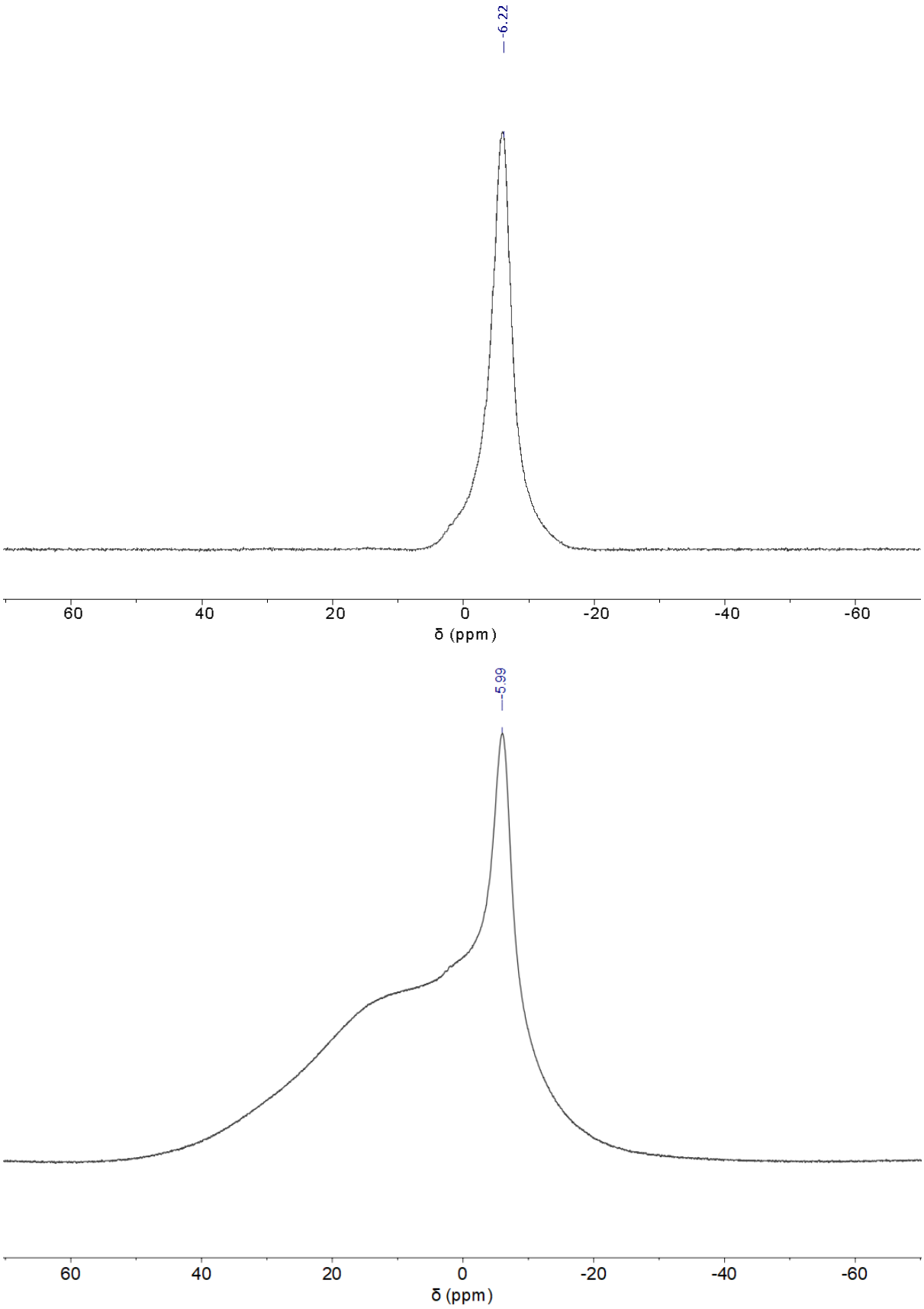

Figure 2.10: ^{11}B NMR spectra of PMeAB7 (baseline corrected and uncorrected, top and bottom respectively): $CDCl_3$, 193 MHz, 298 K.

2.3.2 Conversion of PMeAB Fibres to BN Fibres

Figure 2.11: Actual photo of as-spun PMeABF heating to 300°C in NH_3 without curing process. Direct heating of PMeABF under NH_3 causes the fibers to melt and fail to retain fibrous morphology.

The conversion of PMeABF to the desired BNF product requires two key steps: vacuum curing and subsequent high-temperature annealing under NH_3 (ammonolysis). One of the challenges of any conversion process is preserving the shape of the fibres (**Figure 2.11**). The methodology developed here was a sequential low temperature vacuum curing (100°C for 48h) of as-spun ("raw") PMeABF followed by high-temperature annealing in a NH_3 atmosphere. As shown in **Figure 2.12a** (and **Figure 2.13**), the surface and cross-section of the raw PMeABF are smooth and dense, with an average fibre diameter of 3.64 μm. Following curing (**Figure 2.12b**), the average diameter of PMeABF becomes 3.56 μm and the fibre now exhibit a dense surface with slight roughness observed at the cross-section. After annealing (**Figure 2.12c**), the BNF retains its well-defined fibrous morphology, and the surface remains densely packed and non-hollow, without visible defects or pores (**Figure 2.14**). Crystallisation is observable at the cross-section,

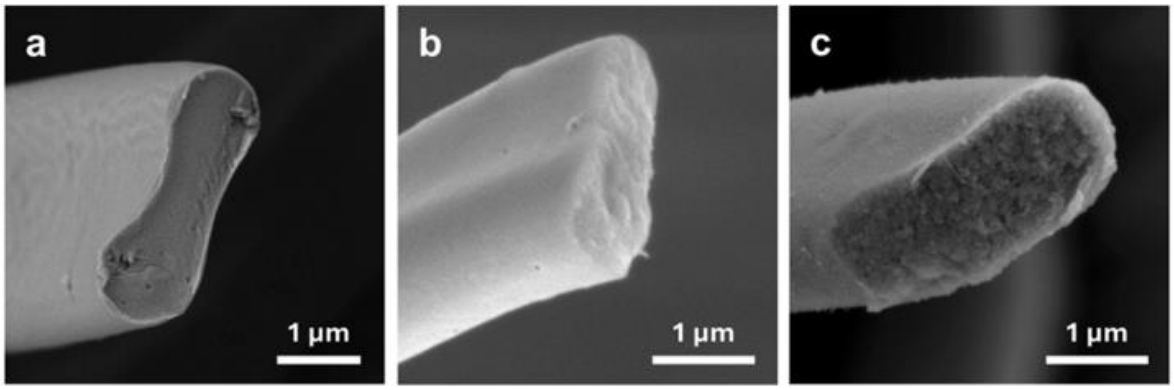

Figure 2.12: SEM images of (a) a PMeABF, (b) a cured PMeABF, and (c) a BNF.

indicating the overall conversion from PMeAB polymer to BN ceramic. The average diameter of the BNF is 3.38 µm, which is not significantly different from PMeABF. Unlike other kinds of polymer-derived ceramics that show notable size reduction,[69] PMeAB-derived BNF exhibit only a small volume shrinkage of 7%.[69] The main difference between raw and cured PMeABF is that the latter is not soluble in solvents such as $CHCl_3$, THF or DMF. Following this electro-spinning and curing process using solid-state ^{11}B NMR spectroscopy showed no difference between PMeAB and precured PMeABF, **Figure 2.15**, with a broad signal observed at δ ~–8, consistent with solution ^{11}B NMR spectra. In contrast the ^{11}B solid-state NMR spectrum of the cured PMeABF shows a decrease in the intensity of this δ ~–8 signal, and new signals at δ ~10 (broad) and δ ~1 (sharp) are observed. The linewidths and chemical shifts of these new signals are characteristic of three-coordinate, trigonal, BN_3 environments, and four coordinate, BN_4, environments respectively; as previously noted for polymers derived from the dehydrocoupling of hydrazineborane.[154,155] Computational ^{11}B NMR calculations based on density functional theory (DFT) using the KT2 functional (COSMO, ZORA) confirms these ^{11}B assignments by assigning the peak positions (details of the computational studies conducted by my collaborators, the Swart's Group, are provided in the **Appendix B**). Collectively, experimental and computational results indicate the cross-linking behaviour toward higher BN coordination numbers, which occurred within the PMeABF during the thermal curing process.

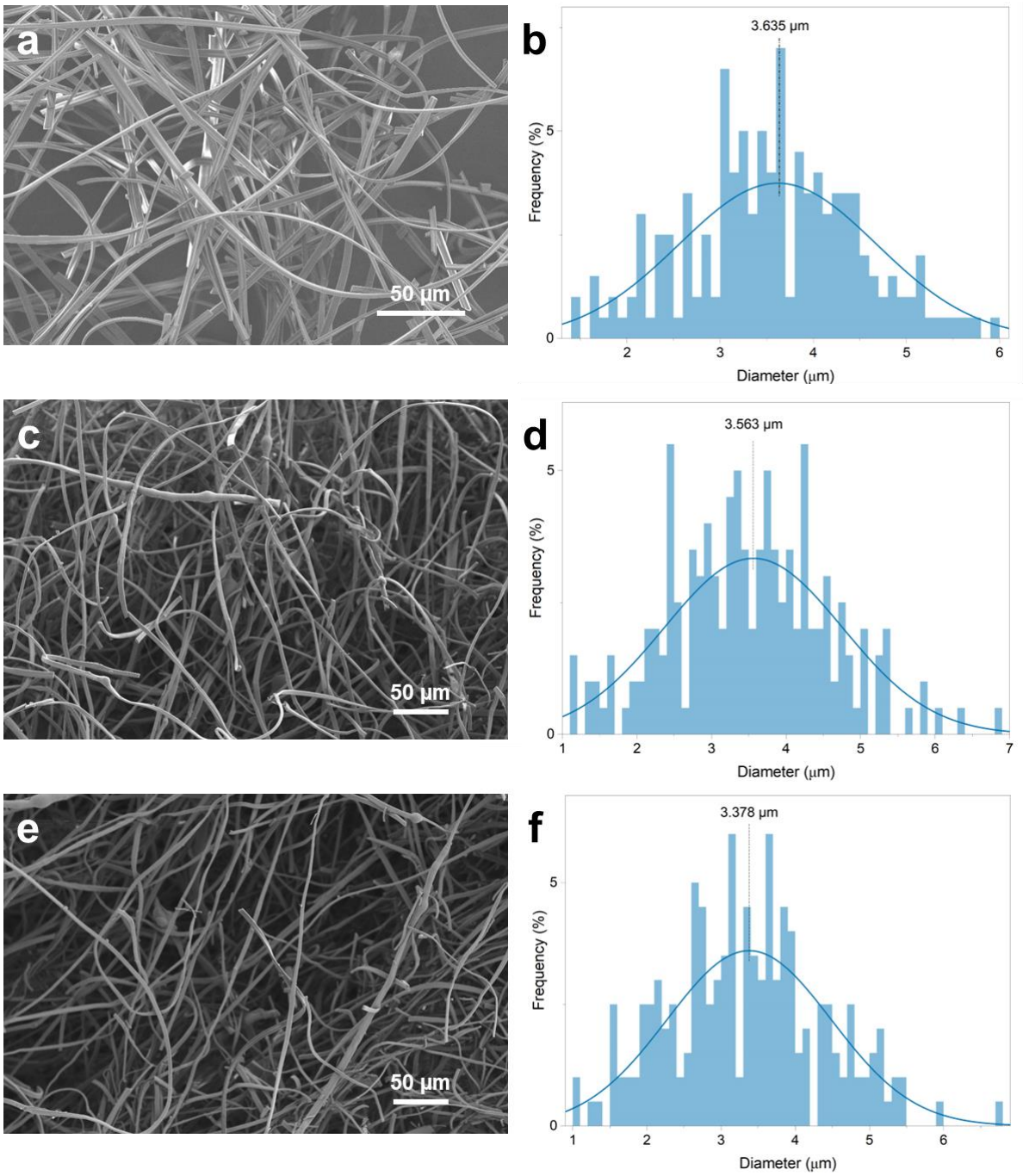

Figure 2.13: SEM image and fibre diameter distribution of (a, b) raw PMeABF with an average fibre diameter of 3.635 µm, (c, d) cured PMeABF with an average fibre diameter of 3.563 µm, and (e, f) BNF with an average fibre diameter of 3.378 µm.

Figure 2.16 and **Figure 3.14** show the TGA-DSC-MS spectra for cured PMeABF and precursor PMeAB samples respectively, as measured under an argon atmosphere. While these TGA-DSC-MS conditions do not replicate the actual conversion process, they give valuable information about the thermal decomposition behaviours of both cured and uncured PMeABF.

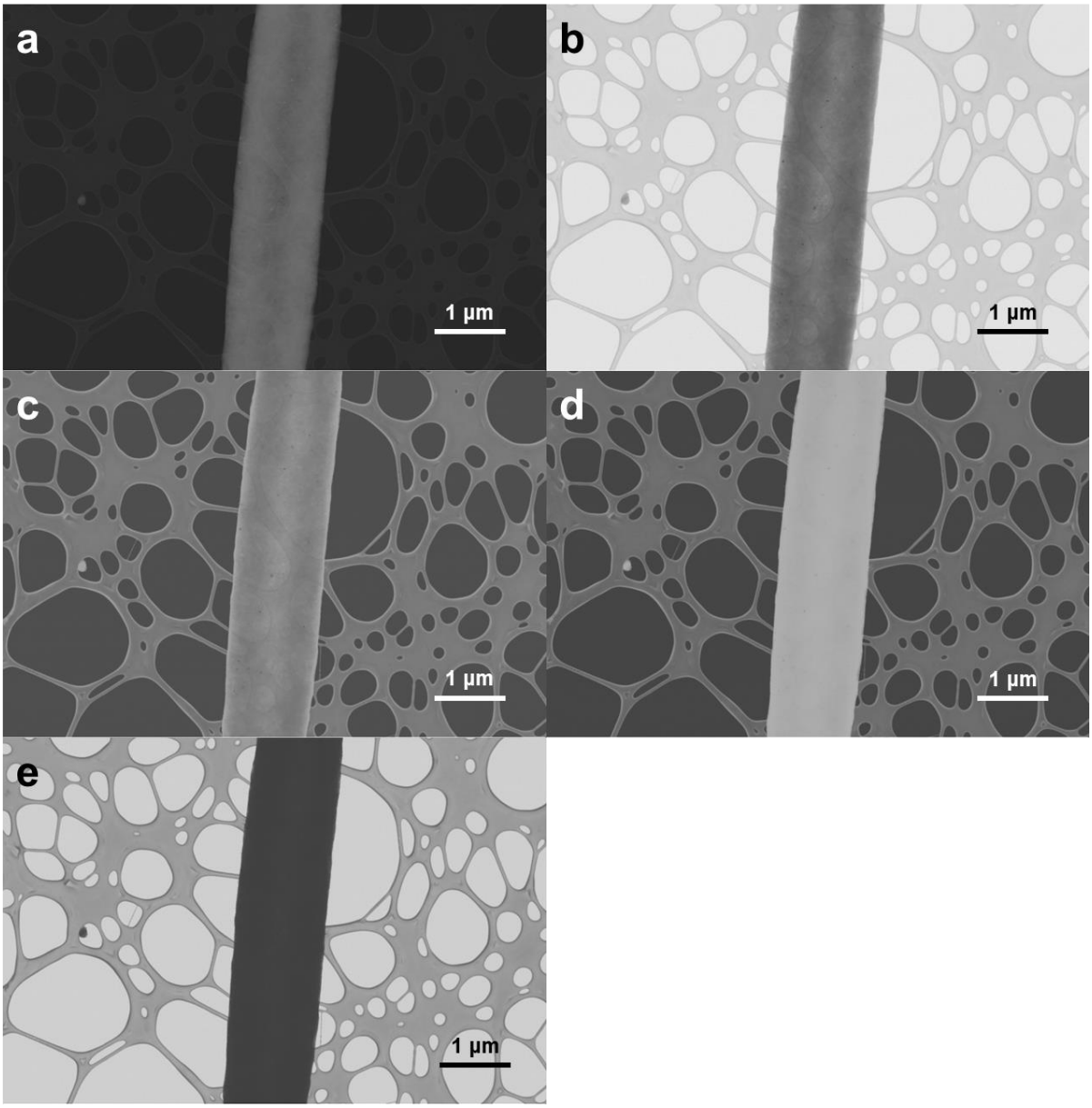

Figure 2.14: Scanning Transmission Electron Microscopy (STEM) images of a single synthesized BNF in (a) HADF mode, (b) BF+DF mode, (c) ADF mode, (d) DF mode, and (e) BF mode.

The TGA of cured PMeABF showed significantly less weight loss, *i.e.* 36.1 wt.%, during thermal decomposition, compared to 81.9 wt.% for the uncured precursor PMeABF. This limited weight loss can be caused by (i) the gradual release of volatile substances during the curing process and (ii) the formation of a stable cross-linked polymer structure in the cured PMeABF, compared to the linear polymer structure of the precursor PMeABF. The curing

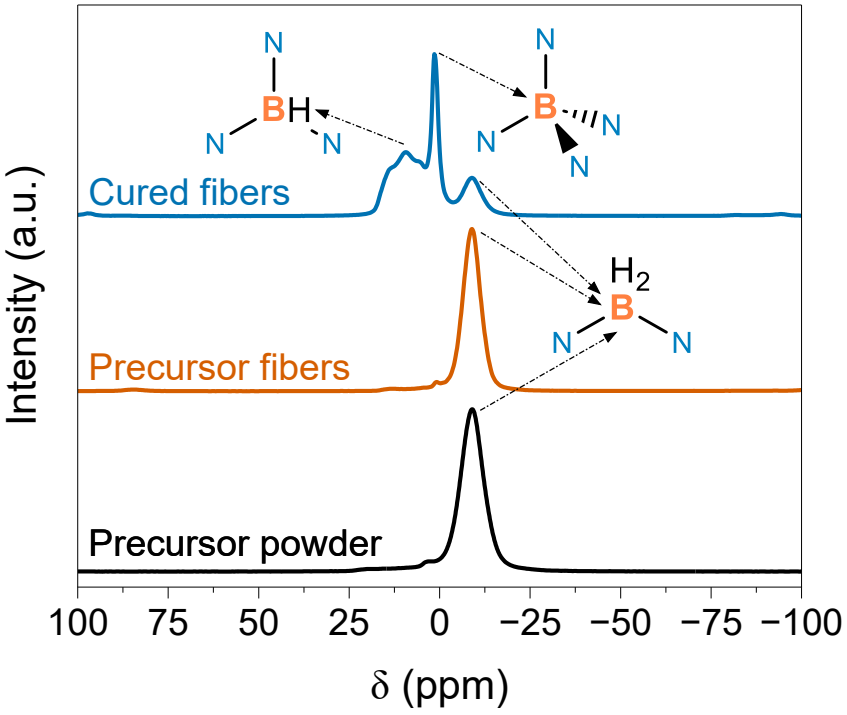

Figure 2.15: Representative solid-state ^{11}B NMR spectra of PMeABF before and after curing process.

process, instead of rapid decomposition reactions during annealing, enables a controlled release of substances, enhancing the thermal stability of PMeABF and reducing the overall weight loss.

The corresponding MS spectra obtained from precursor and cured PMeABF shows that hydrogen, methane, ammonia, $NHCH_3$ (m/z = 30), BNH_2CH_3 (m/z = 42), borazine ($B_3N_3H_6$, m/z = 81), and tri-methyl-substituted borazine ($B_3N_3H_3(CH_3)_3$, m/z = 121} were detected for both samples during thermolysis. These species were initially hypothesised based on decomposition pathways reported in TGA-MS studies of ammonia borane in the literature, which exhibit similar B–N bond cleavage and cyclic borazine formation mechanisms. These compounds are significant for PMeABF, while their relative concentrations were lowered for the cured PMeABF. These observations agree those noted for PBZ under TGA-MS analyses and underscores the importance of the curing step for the efficient conversion of PMeAB to BN.[100] In support of this hypothesis, when uncured PMeABF is exposed to the high tempertaure annealing process in ammonia, melting and rapid release of gases occurs at

relatively low temperatures above 120 °C (**Figure 3.14**). This behaviour has been noted to be observed for PMeAB's monomer MeAB and its close relative AB at temperatures ranging from 100-150°C.[100,156]

Analysis by XPS and FT-IR allows for the evolution of the gross elemental and structural composition of PMeABF to BNF to be determined (**Figure 2.17, 2.18**). **Figure 2.17** shows the

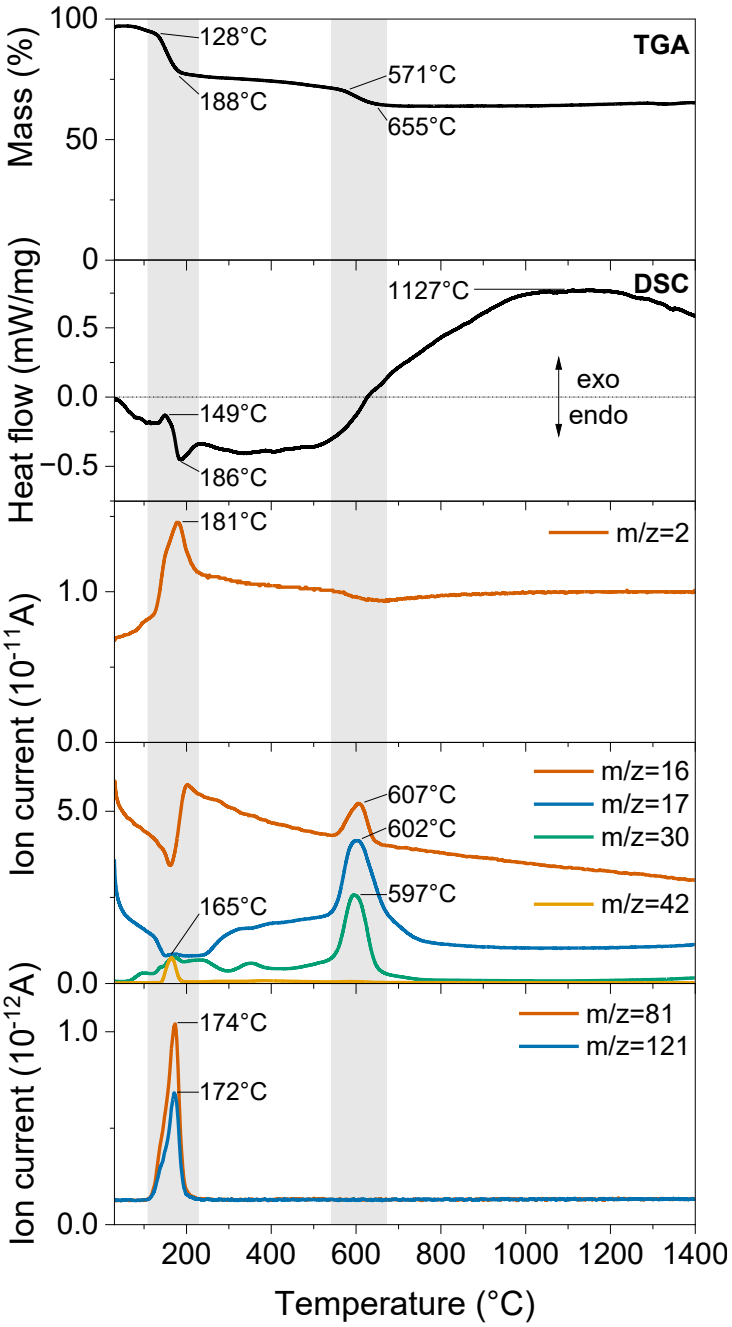

Figure 2.16: Synchronous TG–MS analysis for the released products during heating of cured PMeABF up to 100°C in Ar.

B, C, and N elemental content derived from the corresponding XPS spectra (**Figure 2.19**) for electrospun precursor PMeABF, cured PMeABF, and cured then annealed PMeABF at various temperatures between 150-1400 °C in NH_3. NH_3 is used to eliminate the carbon impurities, introduced from methyl group in PMeAB, which is critical to achieve high-purity h-BN. Guilhon *et al.* studied tris(isopropylamino)borane as the precursor to synthesize BN through

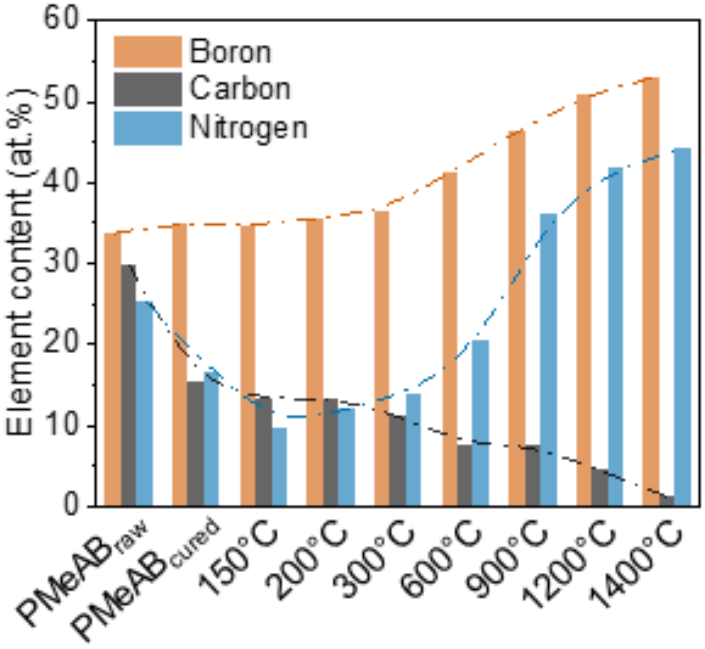

Figure 2.17: Element contents of PMeABF annealed at different temperatures (calculated from XPS spectra).

thermal treatment in NH_3, proposing that NH_3 facilitates the elimination process of methyl amine and CH_4.[79] This observation aligns with my XPS results, in which the C and N contents decrease simultaneously up to 150 °C, while the N content starts to increase at 200 °C onward, with the C content diminishing significantly, to less than 2%. It is proposed that the reducing nature of the NH_3 environment not only facilitates further release of amine and CH_4 from the precursor fibres but also provides an additional N source to react with B-rich intermediates. **Figure 2.18** shows FT-IR spectra for PMeABF, cured PMeABF, and cured PMeABF annealed at temperatures between 150°C to 1400°C. The spectra for cured PMeABF that has been annealed at 150°C, 200 °C, and 300 °C show a gradual increase in intensity of B−N stretching (1320 cm^{-1}) and B−N bending (758 cm^{-1}) modes, while B−H (2342 cm^{-1}) and C−H (1456 cm^{-1} and 2984 cm^{-1}) stretching modes gradually decrease. In the temperature range between 300 °C to 900 °C, N−H and N−C stretching modes disappear due to the removal of N−H terminal group and the C content decreases due to ammonolysis.[26,148,156] The spectra for cured PMeABF annealed at 900 °C and above have only the B−N stretching and B−N bending modes

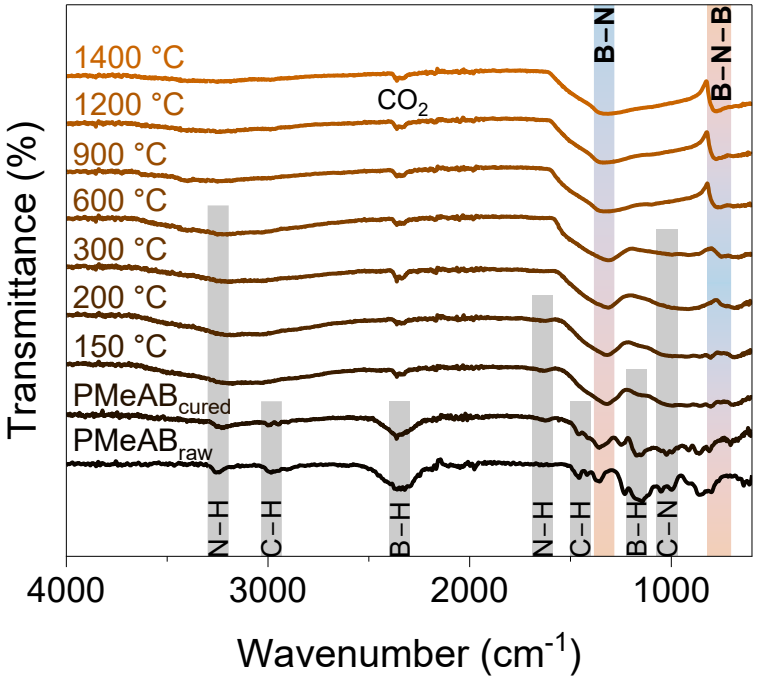

Figure 2.18: FT-IR spectra of PMeABF annealed at different temperatures.

present.[157] The effective removal of C species from B-C-N-rich polymers during the annealing process in NH_3 has been discussed previsouly.[29,78,158–160] This process primarily relies on the evolution of methylamine through transamination reactions, as well as carbothermal reactions between carbon and NH_3.[159,160] The elemental ratio for BNF produced through annealing PMeABF at 1400 °C in NH_3 is 1:1.2, which suggests a nearly stoichiometric composition of B and N elements, with a negligible carbon impurity of 1.31%. In polymer-derived BN materials, such low levels of carbon and oxygen impurities (with both below 2 wt.%) are considered significant, as compared to the impurity levels reported in the literature (**Table 2.3**). As observed, most papers in this field avoid even mentioning the content of carbon and oxygen impurities.

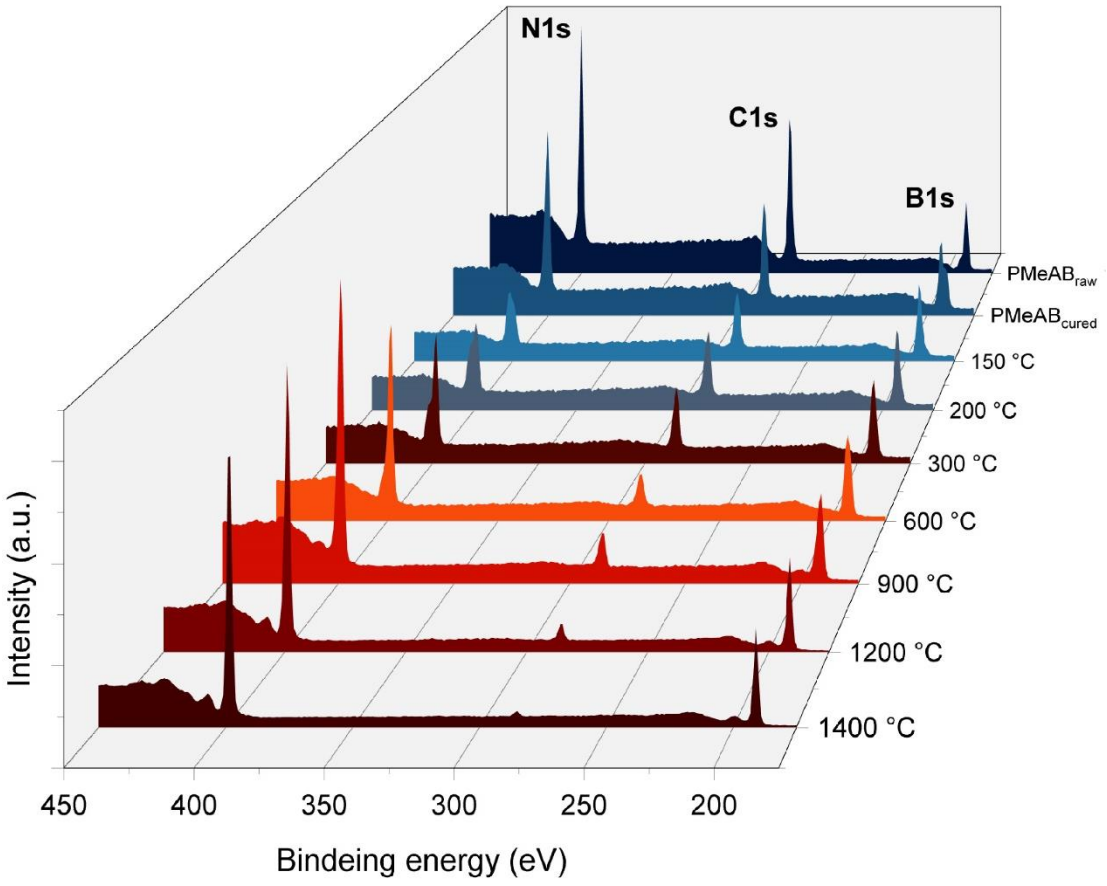

Figure 2.19: Typical XPS spectra of PMeABF heated at different temperatures. Peak intensities are quantified by normalizing the relatively stable boron peak to 1 across all temperatures. B, C, and N elemental contents derived from the XPS spectra show continual reduction of C content as well as an initial decrease and following increase of N content. This indicates that NH_3 serves a dual role, removing carbon while also providing nitrogen at temperatures above 200°C.

Table 2.3: Measured or calculated carbon and oxygen contents in synthesized BNF in literature.

Reference	Carbon Content	Oxygen Content	Thermal Treatment
This work	1.31%	1.61%	1400°C (NH_3)
Thermal behaviour of a series of poly[*B*-(methylamino)borazine] for the preparation of boron nitride fibers[72]	Not specified	~2%	1000°C (NH_3) 1800°C (N_2)
A new class of boron nitride fibers with tunable properties by combining an electrospinning process and the polymer-derived ceramics route[29]	Not specified	Not specified	1000°C (NH_3) 1800°C (N_2)
Design and synthesis of a novel spinnable polyborazine precursor with high ceramic yield via one-pot copolymerization[161]	<1%	<1%	800°C (NH_3) 1800°C (N_2)
Boron Nitride Fibers Prepared from Symmetric and Asymmetric Alkylaminoborazines[31]	2.5–3.2%	Not specified	600°C (NH_3) 1800°C (N_2)
Alkylaminoborazine-based precursors for the preparation of boron nitride fibers by the polymer-derived ceramics (PDCs) route[57]	Not specified	Not specified	1000°C (NH_3) 1800°C (N_2)
High-performance boron-nitride fibers from poly(borazine) preceramics[28]	Not specified	Not specified	1000°C (NH_3) 1800°C (N_2)
High-performance boron nitride fibers obtained from asymmetric alkylaminoborazine[30]	Not specified	Not specified	1000°C (NH_3) 1600°C (N_2)
Preparation and properties of hollow BN fibers derived from polymeric precursors[76]	<1%	Not specified	1000°C (NH_3) 1600°C (N_2)

Nearly stoichiometric BN fiber by curing and thermolysis of a novel poly[(alkylamino)borazine][78]	0.14%	0.53%	1200°C (NH_3) 1400°C (Ar)
Electrospinning of boron nitride nanofibers with high temperature stability[71]	Not specified	Not specified	600°C (Air) 1400°C (N_2)
Boron Nitride Nanofibers by the Electrospinning Technique[25]	Not specified	Not specified	1000°C (Ar)
Large-Scale Production of Aligned Long Boron Nitride Nanofibers by Multijet/Multicollector Electrospinning[56]	Not specified	Not specified	1100°C (NH_3) 1500°C (N_2)
Synthesis of continuous boron nitride nanofibers by solution coating electrospun template fibers[27]	Not specified	Not specified	1100°C (NH_3) 1500°C (N_2)
Crystallinity, Crystalline Quality, and Microstructural Ordering in Boron Nitride Fibers[162]	~2%	Not specified	1000°C (NH_3) 1800°C (N_2)
Controlling the chemistry, morphology and structure of boron nitride-based ceramic fibers through a comprehensive mechanistic study of the reactivity of spinnable polymers with ammonia[163]	2.4–7.6%	<2%	1000°C (NH_3) 1800°C (N_2)
Texture, structure and chemistry of a boron nitride fibre studied by high resolution and analytical TEM[164]	Not specified	Not specified	1800°C (NH_3/N_2)
Effects and Control of Polymer-Converted Carbon Impurity in Synthesizing Continuous Boron Nitride Nanofibers by Electrospinning[165]	0.5–5%	1–3%	1100°C (NH_3) 1500°C (N_2)
Polymer-Derived Boron Nitride: A Review on the Chemistry, Shaping and Ceramic Conversion of Borazine Derivatives[69]	1–5%	2–6%	900–1450°C (NH_3) 1800°C (N_2)

Microstructures and properties of polymer-derived hexagonal boron nitride fibers with initial gradient oxygen contents[77]	Not specified	0.5–5%	800°C (NH_3) 1600°C (N_2)
Pure & crystallized 2D Boron Nitride sheets synthesized via a novel process coupling both PDCs and SPS methods[166]	2.4%	11.5%	1800°C (N_2)

2.3.3 Detailed Characterisation of the BN Fibres

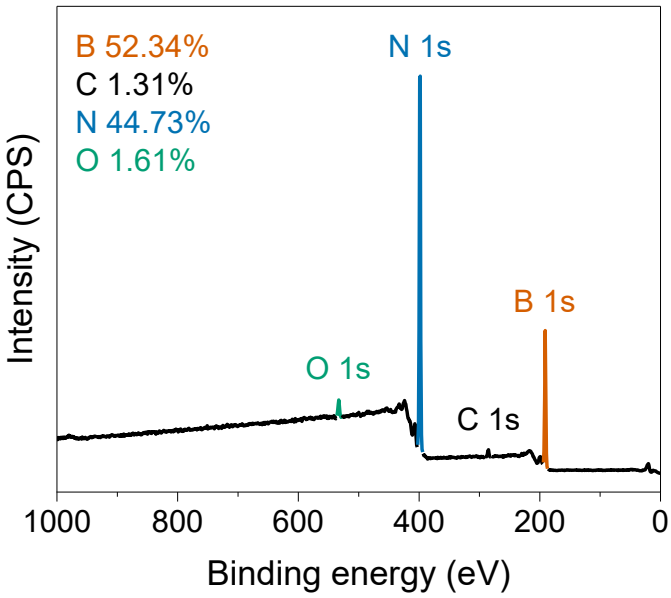

Figure 2.20: XPS survey spectrum, inset shows calculated element content of B, C, N, and O. (g-h) XRD pattern of synthesized BNF (orange) and exfoliated h-BN (black). (h) Enlarged (002) peak. (i) Typical TEM image of a BNF, inset shows FFT's diffraction pattern.

An XPS analysis of the synthesized h-BN fibres shows B 1s (190.4 eV), C 1s (284.8 eV), N 1s (398.0 eV), and O 1s (533.1 eV) peaks confirming the intrinsic BN nature (**Figure 2.20**).[167] The presence of significantly weaker signals at approximately 188.7 eV and 396.6 eV for B−C and N−C, respectively,[168,169] is consistent with less than 2% of these C impurities. B−O (~192.5 eV)[168] and N−O (~400.4 eV)[169] modes for the BNF are present in low intensity (**Figure 2.21**). The presence of minor oxygen impurities in the sample could potentially be attributed to small amounts of oxidation or moisture adsorption occurring during sample preparation under an ambient atmosphere. The atomic percentages of B and N are measured as 52.34% and 44.73%, respectively, which aligns with the B-rich composition indicated by the EDX line profile results (**Figure 2.22**). Elemental mapping analysis (**Figure 2.22**) provides evidence for the homogeneous distribution of B and N within the h-BN fibres. Studies have shown that the presence of oxygen impurities can influence the thermal conductivity of BN materials. For

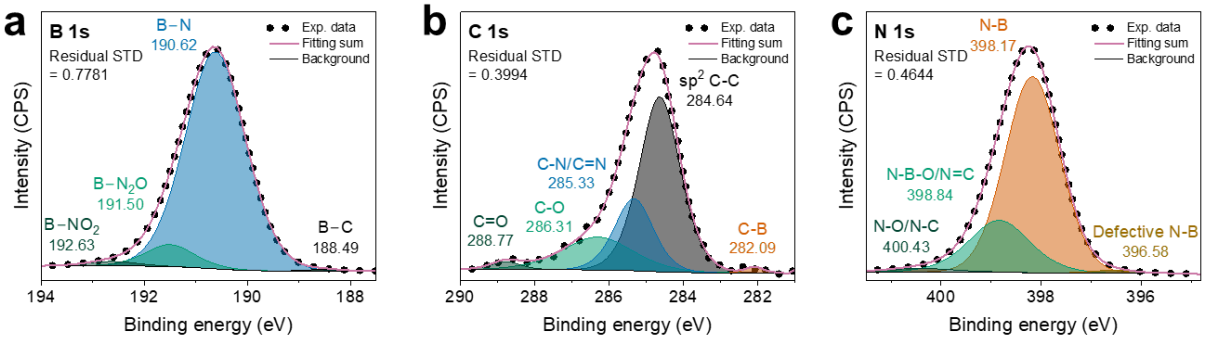

Figure 2.21: High-resolution spectrum of (a) B 1s, (b) C 1s, and (c) N 1s.

example, research on BNNT indicates that oxygen impurities, resulting from partial oxidation, can affect their thermal properties.[131] However, given the minor impurity content in my samples, any effect on the insulation and thermal conductivity is expected to be negligible.

The FT-IR spectra for both synthesized BNF and commercial exfoliated h-BN nanosheets (BNNS) were compared (**Figure 2.23**). For BNNS, two distinct absorption peaks are observed at 1359 and 802 cm^{-1} corresponding to in-plane B−N stretching vibration of sp^2-bonded h-BN and out-of-plane B−N−B bending vibration.[170] The BNF shows two, very similar, sharp absorption peaks at 1354 and 798 cm^{-1} but the relative peak intensity for B−N to B−N−B bending vibration is higher than that for BNNS. This is most likely due to the larger thickness of BNF compared to BNNS.[171] No additional peak between 3000-3500 cm^{-1} was observed for BNF.

The X-ray diffraction (XRD) pattern of the synthesized BNF also aligns with the pattern obtained from BNNS, displaying similar peak positions, and confirms the crystalline structure of BNF (**Figure 2.24**). In the XRD spectrum two broad peaks are observed at 2θ ~ 25° and 43°, corresponding to the (002) and (100) crystal planes of h-BN, respectively.[172] Compared with BNNS, the peaks show broadened width [FWHM: $BNF_{(002)}$ peak = 5.25° and $BNF_{(100)}$ peak = 4.06° *vs* $BNNS_{(002)}$ peak = 0.29° and $BNNS_{(100)}$ peak = 0.29°]. This is suggestive of a turbostratic structure of BN, with less extended/ordered stacking along both a- and c-axes. The calculated $d_{(002)}$ layer spacing for the BNF is 0.352 nm, slightly larger than that of BNNS (0.333

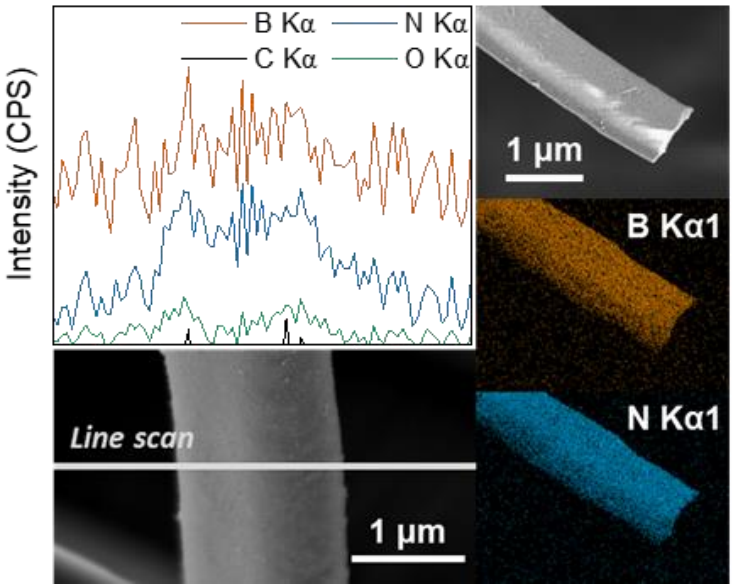

Figure 2.22: EDX line scan profile and elementary mapping of an individual BNF.

nm). This expansion is generally observed in 1D-structured BN materials due to the combination of turbostratic ordering and wall curvature. The calculated average crystallite size of BNF is 2.16 nm, indicating a polycrystalline structure (**Figure 2.25**). While the turbostratic polycrystalline structure is evident, the presence of higher resolved peaks, *e.g.* (101), (102), (004), (110), in the XRD pattern of BNF indicates that a certain level of ordering is still present in the material.

High-resolution transmission electron microscopy (HRTEM) combined with fast Fourier transform patterning (FFT) was used to further quantify degree of crystallinity of the synthesized BNF. The measured d-spacing is 0.334 nm for (002) planes, and 0.214 nm for (100) planes, in agreement with previously reported values (**Figure 2.26, 2.27**).[173] FFT reveals the partially ordered structure, with ring-like diffraction patterns dominating, that correspond to turbostratic or polycrystalline regions, in addition to several visible diffraction spots corresponding to hexagonal or crystalline regions.[174] These diffraction spots were assigned to the (002) and (100) planes, consistent with the results obtained from HRTEM and XRD analyses (**Figure 2.27, 2.28**). Combining both XRD and TEM results, I conclude that t-BN and

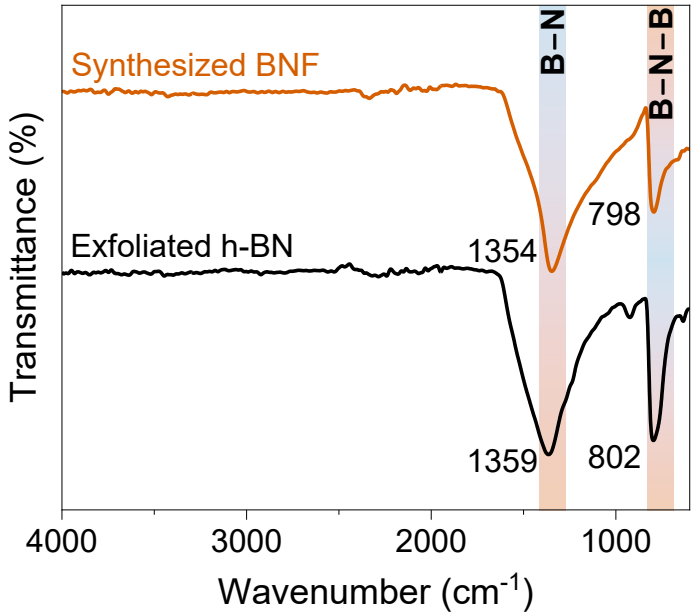

Figure 2.23: FT-IR spectra of synthesized BNF (orange) and exfoliated h-BN (black).

h-BN coexist within the ceramic fibres. This structural disorder is comparable to that observed in turbostratic graphite, where misalignment between layers affects XRD results. In carbon materials, such disorder does not imply the absence of crystalline regions but rather a lack of consistent long-range order.[175] Overall, the detailed characterisation of the annealed PMeABF demonstrate fabrication of high purity polycrystalline hexagonal/turbostratic form of h-BN fibres starting from a readily synthesized pre-ceramic B–N polymer precursor.

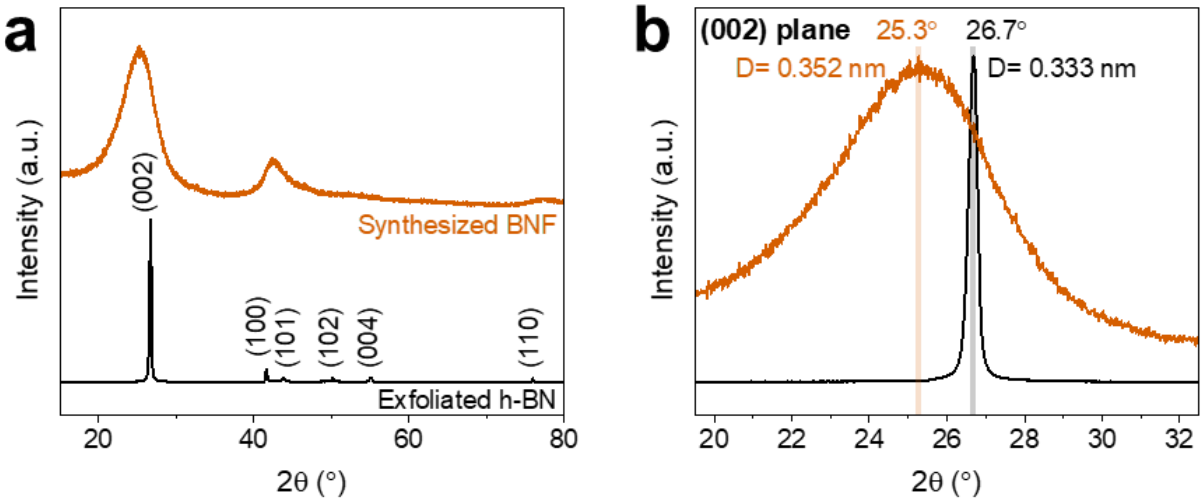

Figure 2.24: (a) XRD pattern of synthesized BNF (orange) and exfoliated h-BN (black). (b) Enlarged (002) peak.

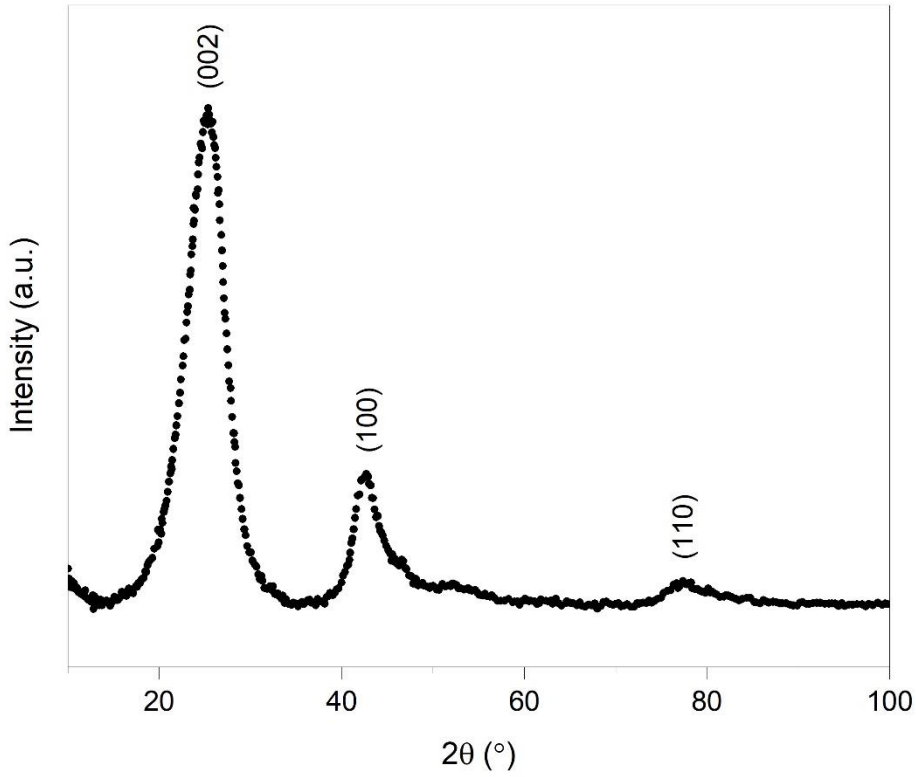

$$D = \frac{K\lambda}{\beta \cos\theta}$$

D= Crystallite size (nm)

K= 0.9 (Scherrer constant)

λ= 0.15406 nm (wavelength of the X-ray source)

β= FWHM (radians)

θ= Peak position (radians)

Position (2θ)	FWHM (β)	Crystallite Size D (nm)	Average D (nm)
25.0882	5.25064	1.550013643	**2.160388727**
42.95612	4.0587	2.103413759	
77.77309	3.60926	2.827738778	

Figure 2.25: Crystallite size D calculation from the XRD pattern by fitting the three dominating peaks *e.g.* (002), (100), and (110). The average crystallite size is calculated to be 2.16 nm, indicating a polycrystalline structure of BN.

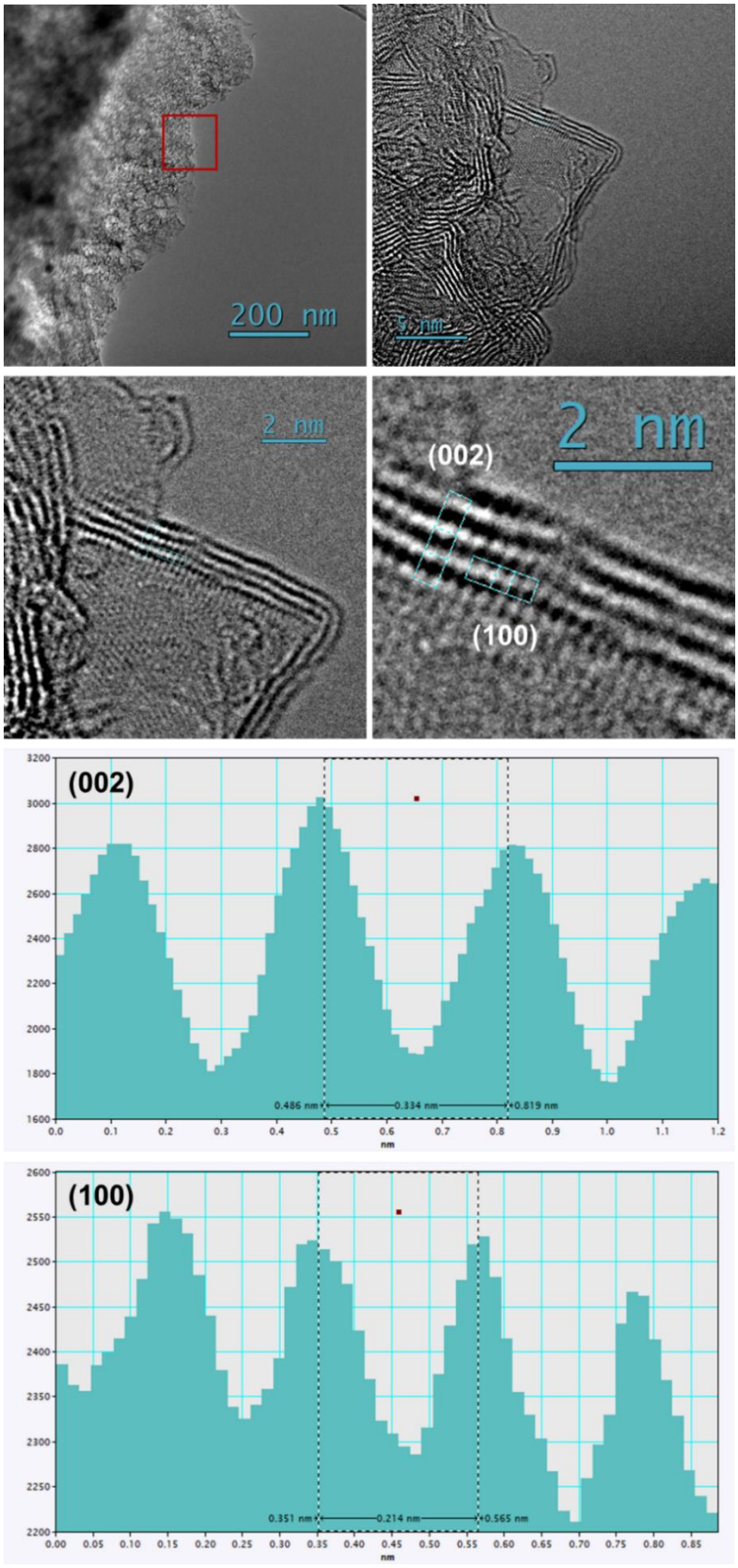

Figure 2.26: HRTEM line profiles of BNF showing d-spacing of 0.334 nm for (002) planes and 0.214 nm for (100) planes.

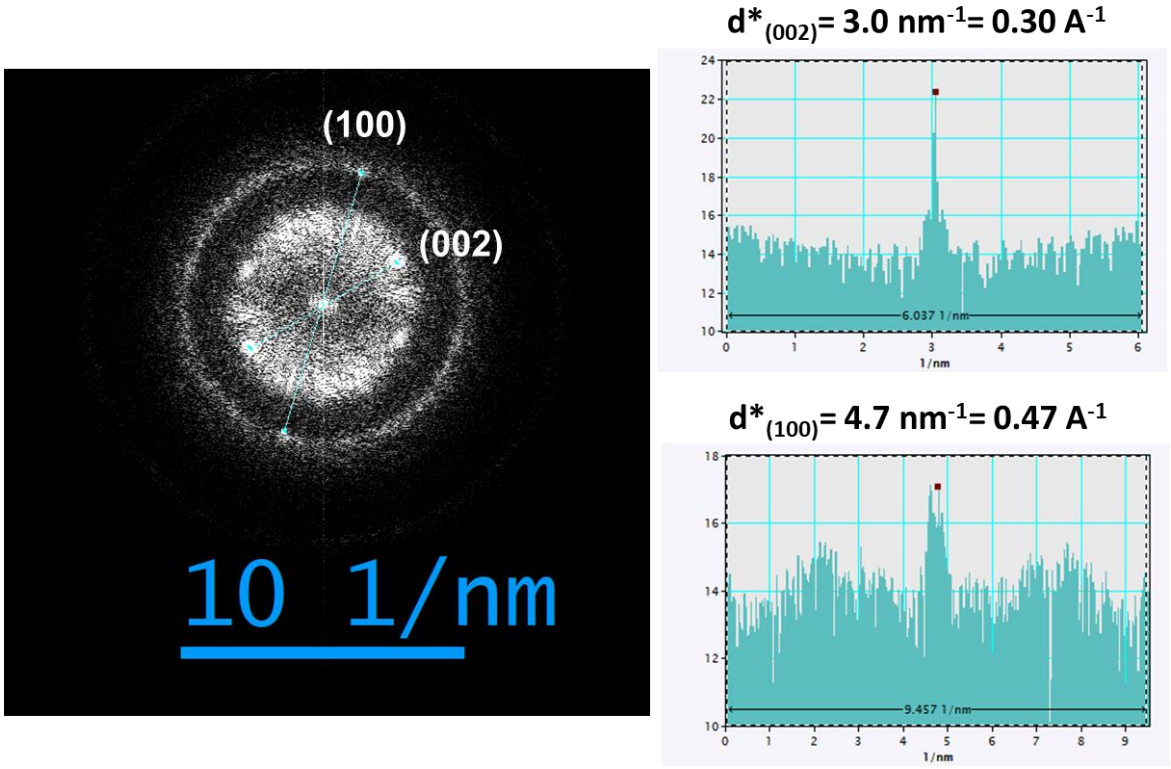

Figure 2.27: Line profiles of FFT derived from the HRTEM image of BNF (**Figure 2.15**) showing d* of 3.0 nm^{-1} for (002) planes and 4.7 nm^{-1} for (100) planes.

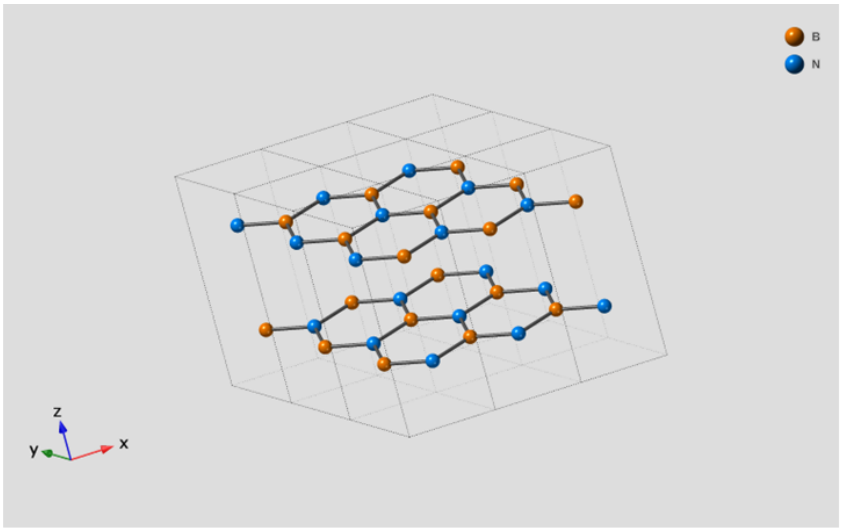

[010] Direction

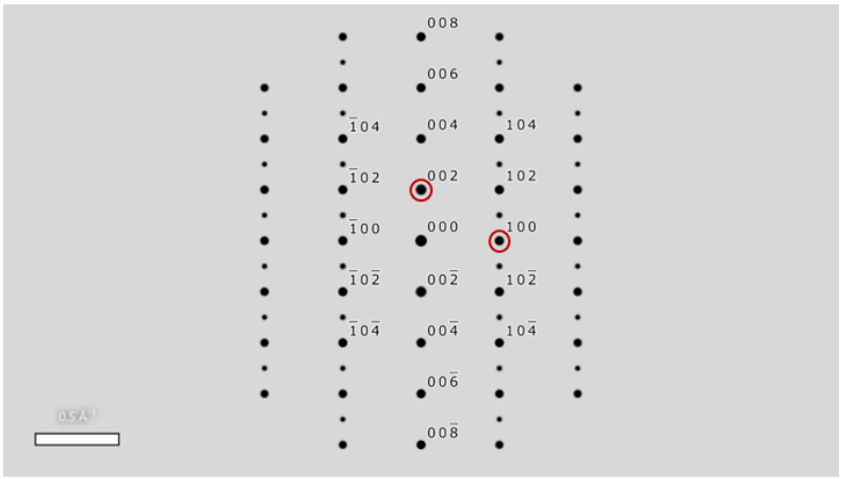

No.	Vis	h	k	l	d [Å]	d* [Å^{-1}]	I/Imax	F(Re)	F(Im)	ϕ	Lp	N
00001	☑	0	0	-2	3.33060	0.30025	100.000%	-3.4640E+1	0.0000E+0	180.00°	1.000	4
00002	☑	0	0	2	3.33060	0.30025	100.000%	-3.4640E+1	0.0000E+0	180.00°	1.000	4
00003	☑	0	0	-4	1.66530	0.60049	6.875%	9.0826E+0	0.0000E+0	0.00°	1.000	16
00004	☑	0	0	4	1.66530	0.60049	6.875%	9.0826E+0	0.0000E+0	0.00°	1.000	16
00005	☑	-1	0	0	2.16852	0.46114	4.202%	-7.1010E+0	0.0000E+0	180.00°	1.000	1
00006	☑	1	0	0	2.16852	0.46114	4.202%	-7.1010E+0	0.0000E+0	180.00°	1.000	1

Figure 2.28: Simulation of a perfect h-BN crystal using SingleCrystal software, showing d-spacing of 0.334 nm for (002) planes and 0.214 nm for (100) planes and d* of 3.0 nm^{-1} for (002) planes and 4.7 nm^{-1} for (100) planes.

2.3.4 Mechanical Properties of BN Fibres

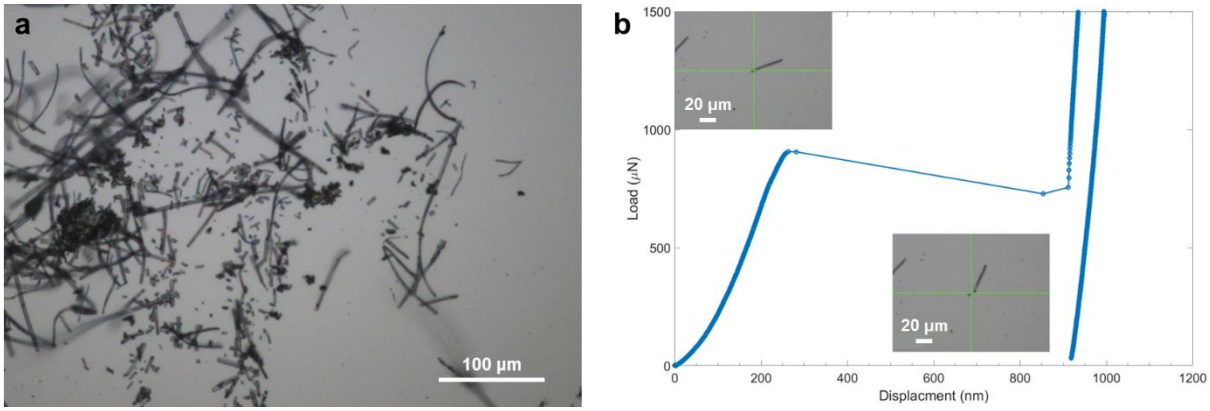

Figure 2.29: (a) Optical image taken using the TI Premier, and (b) example load-displacement data with optical before and after inserts.

Nanoindentation test were conducted in order to give an indication of the mechanical properties of BNF. Precursor PMeABF were directly electrospun onto single crystal silicon wafers and BNF were dissolved in acetone and drop-cast onto single crystal silicon wafers. This dispersed fibres enough to allow individual fibres to be tested via nanoindentation (**Figure 2.29**). Figure **2.29a** shows a low magnification optical image of dispersed fibres and **Figure 2.29b** shows a single targeted indentation on a fibre resulting in fracture as demonstrated by the before and after optical images and the large displacement jump in the load-displacement data. The large increase in load after the displacement jump is indicative of the indenter impacting on the silicon substrate, to avoid this the results collected on fibres have been conducted at low loads (below 800 µN) to avoid fracture and minimize the impact of the substrate.

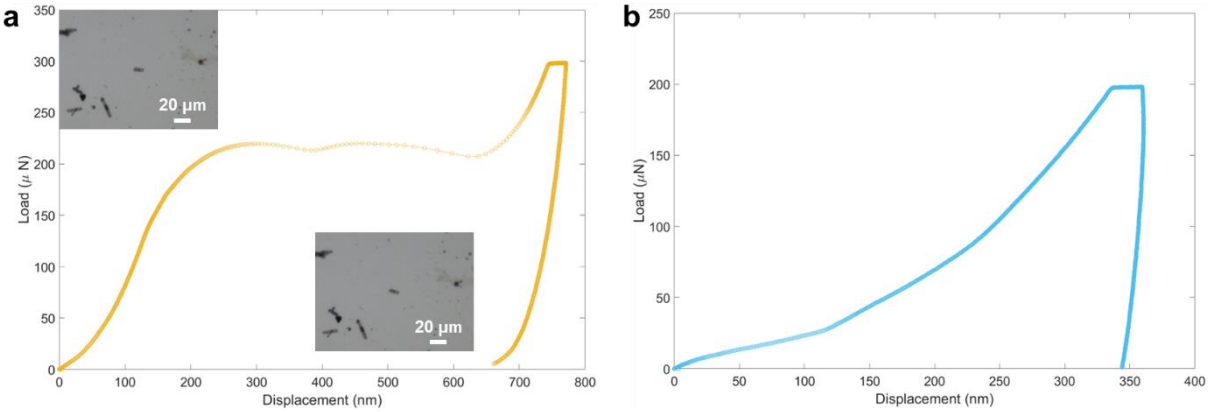

Figure 2.30: (a) Example BNF load-displacement curve, and (b) example PMeABF load-displacement curve.

The elastic reduced modulus of BNF (1.1±0.6 GPa) is in line with those observed in the BNNT fibres (~1.4 GPa)[176] and in the BNNT "buckypaper" (~1.2 GPa).[177] The measured hardness in the BNF (11.1±1.3 MPa) is also in line with the estimated tensile strength of the BNNT fibres (~15.7 MPa)[176] and the BNNT "buckypaper" (~13.8 MPa)[177]

Some BNF showed regions of potential fibre movement/rotation during the test that is distinct from the fracture jump as shown in **Figure 2.30a** where the fibre is still whole after indentation but slightly rotated and there is no large step in displacement within the test. Although this is not ideal and speaks to the difficulty of collecting mechanical properties data from samples of this type the elastic values are calculated on unloading which is unaffected by the rotation observed during loading. PMeABF did not show any movement or rotation during testing and **Figure 2.30b** shows an example load-displacement of a fibre.

The data from BNF results in standard deviation in measurement of the hardness of less than 12% of the mean which can be expected for the relatively small number of measurements from fibres without obvious fracture (from post-test optical image) or impact with the substrate (displacement jump) highlighting the difficulty of conducting this sort of measurement. The PMeABF results have almost 100% standard deviation and results may be affected by the substrate in a more subtle way that is not easily triaged. This suggests that future attempts at

measuring mechanical properties via this method should consider in-situ testing where the impact point of the indenter tip on the sample can be directly observed and guaranteed.

2.4 Summary

A straightforward method for the production of BNF is reported, that uses a combination of solution electrospinning and high temperature annealing, using the well-defined polymer pre-ceramic, PMeAB. This air-stable, as a solid, main-chain B–N polymer is synthesized by a controlled atom efficient catalytic dehydropolymerisation of the readily available premonomer, $H_3B{\cdot}NMeH_2$, using very low loadings of catalysts that are commercially available (*i.e.* **[Ir]**, minimising contamination of the resulting PMeAB, therefore reducing residual metal impurities in the final BN products). The degree of polymerisation of PMeAB is readily controlled, and PMeAB can be synthesized on 50 g scale. This straightforward synthesis of PMeAB, when combined with its non-volatility, highly solubility, and high B–N-content, make it a promising single-source precursor for BN materials. To validate this hypothesis, examination of PMeAB's solution properties, electro-spinnability, and thermal behaviours, determined, for the first time, the optimal parameters for electrospinning PMeAB solutions into fibrous forms of PMeABF. Subsequent curing and high temperature annealing using ammonolysis demonstrated the formation of cross-linked PMeABF and its gradual transition toward BNF with high purity and turbostratic ordering. To my knowledge, the method presented here represents the first instance of using additive-free solution electrospinning process to produce BNF. The other key contribution is the first proposal of a stabilised PMeAB intermediate through curing and the first attempt at ammonia annealing of PMeAB, which together enables the design of complex PMeAB-derived BN structures. My PMeAB-route to BNF by electrospinning precisely controlled polyaminoborane pre-ceramic precursors offer advantages over the current state-of-the art methods. It uses widely available, commercially

accessible, precursors and catalysts to straightforwardly generate PMeAB suitable for electrospinning and then BNF production. These practical improvements now allow for the development of larger scale manufacturing routes, which will allow for the exploration of these technologically important high-performance materials in a wide variety of settings such as fibre reinforced composites.

Chapter 3

Template-Free Synthesis of 3D Boron Nitride Porous Nanostructures from Linear and Cyclic B-N Molecular Precursors

Contents

3.1 Introduction

Low-dimensional materials have displayed unique potential in the fields of environment, energy,[178] catalysis,[179] and electronics[180] due to their reduced dimensions, high specific surface areas, and facile tunability of size, shape, morphology, and microstructure. Among these materials, 1D nanotubes and 2D nanosheets made from carbon and/or BN are notable representatives. h-BN nanosheets and nanotubes are well known for their exceptional chemical inertness and thermal stabilities (up to 1000 °C in air and over 2000 °C in inert atmosphere).[35] In terms of electrically insulating applications, h-BN is preferred over its carbon counterpart owing to its broader band gap, typically around 5~6 eV.[35] Introducing porous structures into BN nanomaterials can further enhance the surface area and offer additional active sites desired for molecular separation and storage.[181] The stability and potentially high porosity of p-BN have prompted several studies in the past decade, focusing on its synthesis and subsequent applications in gas sorption processes. These applications include, but are not limited to, CO_2 capture,[182] CO_2/CH_4 separation,[183] paraffin/olefin separation,[184] and H_2 storage.[185]

Table 3.1 Summary of synthesis methodologies for p-BN.

Methodology	Precursor		Template	Thermolysis Parameters		p-BN Properties			Ref
	B Source	N Source		Temperature (°C)	Atmosphere	Morphology	Structure	Impurity	
Template-Free Synthesis									
Chemical Blowing	H_3BNH_3		-	1200-1400	Ar	Nanosheets	h-BN	O	156,186
Polymer-Derived Ceramic	$(H_3BNH_{\frac{1}{3}})_{\frac{1}{3}}$; $(B_3N_3H_{\frac{1}{3}})_{\frac{1}{3}}$		-	1300-1800	N_2; NH_3	Nanosheets; Flakes	h-BN; t-BN	C; O	187–190
Freeze-Drying	H_3BO_3	$C_3H_6N_6$	-	1050-1500	N_2; NH_3	Microfibres; Nanoribbons	a-BN	C; O	191–193
Solvo-Thermal Reaction	NH_4BF_4	NH_4BF_4; NaN_3	-	260	N_2	Nanosheets; Nanorods	t-BN	C; O	194
Solid-State Reaction	H_3BO_3; B_2O_3	$C_3H_6N_6$; CH_4N_2S·HCl; NH_3·H_2O; $(NH_2)_2CO$; $(H_2NC)_2NH$; NaN_3; NH_4Cl	-	300-1400	N_2; NH_3; H_2	Nanosheets; Microbelts; Flakes; Pellets; Whiskers	h-BN; t-BN; a-BN	C; O	182,185,195,196
Template-Based Synthesis									
Chemical Vapour Deposition	B_2O_3	N_2	C; SiO_2	1700	N_2	Nanosheets; Nanorods; Nanotubes	h-BN	-	173,197
Infiltration	H_3BNH_3; $(B_3N_3H_{\frac{1}{3}})_{\frac{1}{3}}$; $(HNBNHCH_3)_3$		C; SiO_2; Zeolite	1000-1450	O_2; NH_3	Microparticles; Pellets	t-BN; a-BN	O	198–200
Structure Directing Templating	$(HNBNHCH_3)_3$; H_3BNH_3; H_3BO_3; $Na_2B_4O_7$·$10H_2O$; B_2O_3	$(HNBNHCH_3)_3$; H_3BNH_3; $C_3N_6H_6$; $CO(NH_2)_2$	$C_{19}H_{42}BrN$; P123; $C_{16}H_{33}ClN$; Activated C	600-1700	N_2; NH_3	Nanofibres; Pellets; Nanosheets; Nanoribbons	a-BN	C; O	201–206

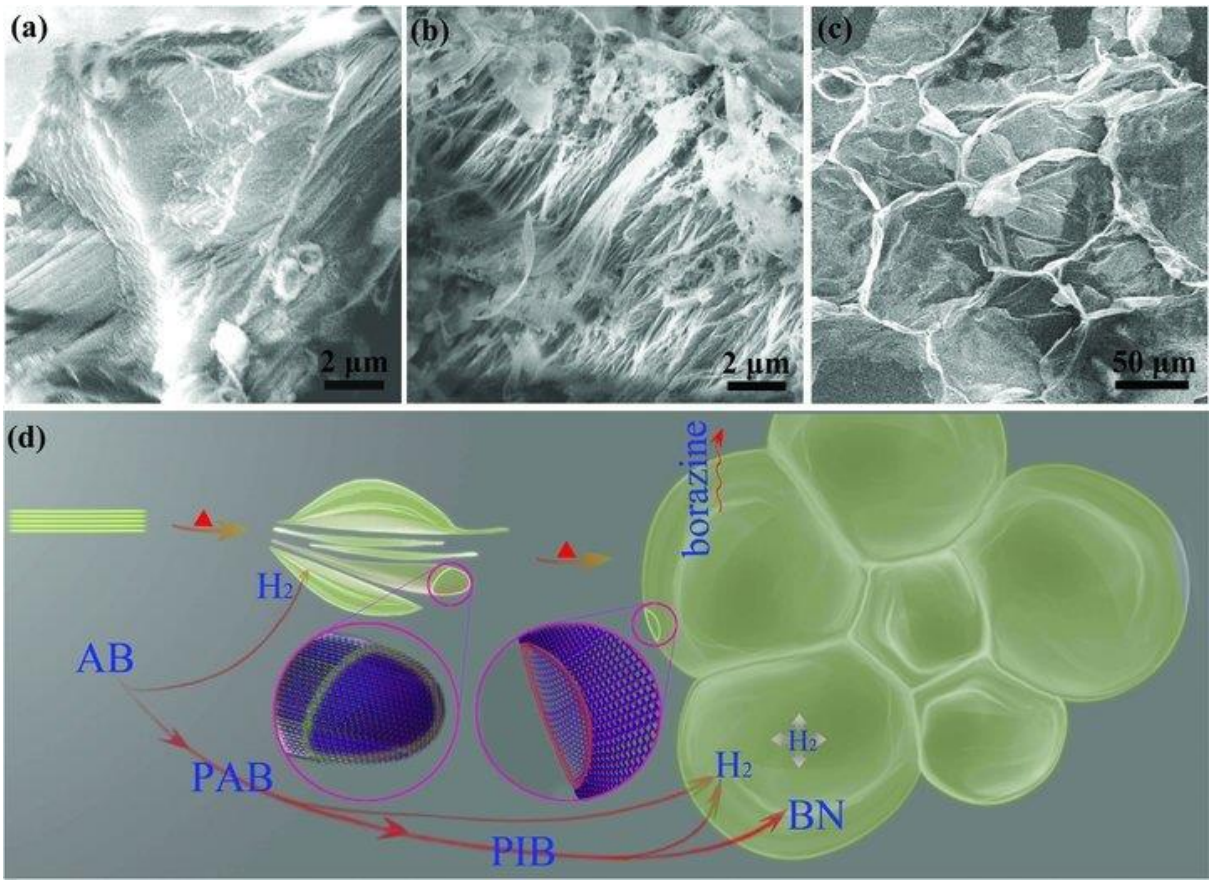

Figure 3.1: Growth process of BN nanosheets using the chemical blowing method proposed by Wang *et al.*[156]

p-BN is typically obtained through high-temperature reactions between single or multiple boron- and nitrogen-containing precursors. This can be carried out with or without the use of a template. **Table 3.1** summarises the synthesis methods, associated precursors, structural/compositional properties, and thermolysis parameters for p-BN presented in the literature. Template-based methods employ preformed porous templates onto which BN is deposited or attached, forming p-BN; the template is subsequently removed by thermal treatment or chemical means. Template-free methods are a better choice than template-based ones, as they require fewer reagents and synthesis steps. Among various template-free methods proposed for p-BN, Wang *et al.*[156] introduced a relatively new strategy, *i.e.* "chemical blowing", which relies on creating bubbles with atomically thin B–N–H polymer walls by releasing H_2 gas from a precursor AB compound, as shown in **Figure 3.1**. This one-step, single-

source approach avoids the use of templates, catalysts, or substrates, enabling fast, simple, and cost-effective production of high-yield BNNSs at an industrial scale. Although it is evident that porosity was introduced into the BNNSs during the H_2 release, the mechanism of porosity formation and its subsequent development were not presented. To ensure the deployment of p-BN at a larger scale, one must be able to tune its porosity and chemistry for a given application, which clearly necessitates an understanding of its formation process.

PMeAB, a linear polymer with alternating boron and nitrogen backbone, can be synthesized by the metal catalysed dehydropolymerisation of methyl-substituted AB, MeAB. In Chapter 2, I described the potential of using PMeAB as the precursor to produce high quality BN in fibrous form through thermolysis in flowing ammonia. Here, I have developed a one-step template-free method to produce p-BN with tunable porosity, chemistry, and surface texture based on the chemical blowing of PMeAB and its reaction with ammonia. This approach relies on the thermal dehydrogenation of PMeAB to induce controllable porosity in the initial stage, along with using ammonia to assist in forming BN nanomorphologies (nanosheets, nanotubes and/or nanofibres).

Recently, Weller's group reported that the addition of sodium bis(trimethylsilyl)amide [$NaN(SiMe_3)_2$] to the synthesized PMeAB induces a selective depolymerisation reaction, resulting in the formation of the *eee*-isomer of *N,N,N*-trimethylcyclotriborazane [$(H_2BNMeH)_3$, denoted as MeCTB] (**Figure 3.2**).[207] Upon sublimation, the resulting MeCTB self-assembles into a 3D sponge-like porous structure. Structurally, MeCTB contains a B–N six-membered ring, analogous to cyclotriborazane [$(H_2BNH_2)_3$, denoted as CTB], the dehydrogenated form of borazine (BZ)—a well-known precursor for h-BN nanomaterials. This structural similarity suggests that MeCTB could potentially exhibit a comparable thermal

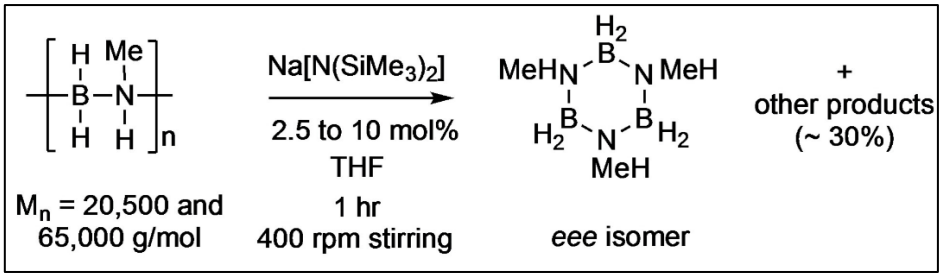

Figure 3.2: Depolymerisation of PMeAB using $Na[N(SiMe_3)_2]$ for the synthesis of MeCTB proposed by the Weller's Group.[207]

decomposition behaviour, wherein the B–N ring structure inherently restricts the occurrence of volatile side reactions, thereby facilitating the formation of h-BN while preserving the original porous morphology of the precursor.

Therefore, MeCTB, as a chemically repurposed derivative of the well-studied main-group polymer PMeAB, presents itself as a promising precursor for fabricating 3D h-BN sponge structures. However, unlike CTB or BZ, MeCTB incorporates methyl groups, introducing carbon into the molecular framework. This additional element complicates the thermal decomposition pathway, making the conversion to h-BN less predictable. In this study, I demonstrate the successful synthesis of a highly porous 3D BN sponge with a large surface area, derived from MeCTB via a straightforward one-step thermolysis process under an ammonia atmosphere.

The integration of h-BN into 3D porous forms is considered to be one of the most effective strategies to resolve the agglomeration issue caused by π-stacking among individual BN components; thus, enabling the full realisation of the intrinsic 2D nature and high surface area of h-BN.[208] In this chapter, I present the development of two novel techniques to construct 3D p-BN: (i) a thermal chemical blowing method utilizing PMeAB, and (ii) a similar but less volatile chemical blowing method based on MeCTB. Through careful control over the thermolysis process, p-BN with high specific surface areas and pore volumes can be produced.

All samples were characterized comprehensively by analytical tools to investigate the porosity, microstructure, composition, and surface texture of materials.

3.2 Materials & Methods

3.2.1 Materials

Table 3.2: Summary of reactants and solvents used in this chapter for synthesis of p-BN.

Name	Purity	Supplier
Reactants		
$PMeAB_{(s)}$	>95%	*Weller's Group*[99]
$MeCTB_{(s)}$	>95%	*Weller's Group*[207]
$NH_{3(g)}$	>99.94%	*BOC*
$Ar_{(g)}$	99.998%	*BOC*
Solvents		
$CHCl_{3(l)}$	-	*Fisher Scientific*
$THF_{(l)}$	-	*Fisher Scientific*
$DMF_{(l)}$	-	*Fisher Scientific*
$DMSO_{(l)}$	-	*Fisher Scientific*

3.2.2 Synthesis

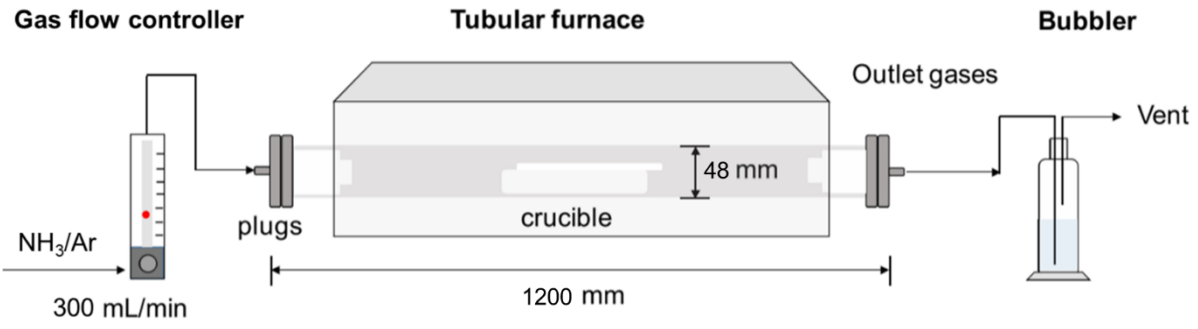

Figure 3.4: Schematic of tubular furnace set-up with gas flow controller and bubbler.

The synthesis setup in this chapter is schematically presented in **Figure 3.2**. The setup includes a tubular furnace (TSH15, *Elite*) with an alumina tube (ALM 5848 OD58mm x ID48mm x

1200mm, *Almath*) connected to the gas inlets controlled by a mass flow controller (Mass-Flo®, *MKS instruments UK ltd*). The other end of the alumina tube was connected to a bubbler filled with water to prevent back flow, filter outgoing gases, and provide visual checking to ensure the absence of leaks in the setup. Inside the alumina tube, 100 mg of PMeAB in either powder or solution form is contained in an alumina boat with an alumina lid placed on top. Prior to the heating of the furnace, 150 sccm of Ar for 10 mins is used to flush the system. The rector furnace is heated up to 1400 ˚C in 300 sccm NH_3/Ar flow with 10 ˚C/min heating rate for 2 hrs. After reaction, the furnace is cooled under Ar flow and the setup is carefully removed for further characterisation.

3.2.3 Characterisations

SEM images were acquired using a Zeiss Merlin SEM and a JEOL JSM-840F SEM operating at an accelerating voltage of 3 kV. Prior to imaging, the samples were coated with a 10 nm layer of platinum. EDX line scanning and elemental mapping were performed using a Zeiss Merlin SEM operating at an accelerating voltage of 3 kV. BNNF diameters were determined by analysing at least 200 unbiased counts from the SEM images and fitting the resulting histogram. TEM images were obtained using a JEOL JEM-2100F TEM operating at an acceleration voltage of 200 kV and a JEOL ARM-200F operating at an accelerating voltage of 80 kV. STEM images and EELS spectra, line-scans and maps were obtained on the JEOL ARM-200F, with beam energy 80kV. The convergence and collection semi-angle were set to 30 and 40 mrad respectively. TGA-MS measurements were conducted using a STA 449 F3 Jupiter® instrument coupled with a 403 Aëolos Quadro quadrupole mass spectrometer. The samples were heated in Ar atmosphere from room temperature to target temperatures at a heating rate of 10°C/min. The quadrupole was used to scan all m/z ratios from m/z = 1 to m/z

= 150 approximately every 30 s. Raman spectra were collected using a JY Horiba Labram Aramis imaging confocal microscope with a 532 nm green light laser. The laser intensity was tuned according to the Raman signal. No prior treatments were done on the product samples for Raman spectroscopy studies. XPS analysis was conducted using a Thermo Scientific K-Alpha X-ray Photoelectron Spectrometer System. An ion pumped VG Microtech CLAM 4 MCD analyser system equipped with unmonochromated Mg K_α X-ray radiation of 1253.6 eV was used. XRD analysis was performed at room temperature using a Siemens D5000 powder diffractometer with copper K_α radiation (λ = 0.15406 nm) and a secondary monochromator. The samples were continuously rotated during data collection, and a step size of 0.05° 2θ was used in the range of 10–100° 2θ with a count time of 12 s per step. FT-IR Spectroscopy attenuated total reflection (ATR) spectra were recorded using a Varian Excalibur FTS 3500 FT-IR spectrometer in the range of 600 to 4000 cm^{-1}. BET surface area analysis was performed based on N_2 adsorption isotherm obtained by a Micromeritics Gemini VII BET surface area analyzer. UV-Vis DRS was conducted on a Varian Carry 5000 UV-Vis-NIR spectrophotometer using a Praying Mantis diffuse reflectance accessory. The powder samples were pressed into non-transparent flat pellets before characterisation. All samples were characterized by ensuring the same equipment calibration, and the results were presented without normalisation.

3.3 Results & Discussion

In this section, the structures of the as-synthesized p-BN were systematically analysed to evaluate the effectiveness of the proposed fabrication methods in introducing a hierarchical porous structure into the BN frameworks and to facilitate comparison of the quality and quantity of p-BN structural/compositional properties with those in the literature. Next, the microstructures and elemental compositions of the p-BN samples were examined in detail.

Based on these observations, the formation mechanisms underlying the various BN morphologies were proposed and will be further integrated with computational studies discussed in Chapter 4. Finally, the controlled carbon doping into the p-BN matrix, resulting in the formation of porous boron carbon nitride (p-BCN), is demonstrated.

3.3.1 Achieving 1D/2D Nano-BN Hybrid Porous Structures

Figure 3.5: Actual image of a drop-cast PMeAB/$CHCl_3$ solution after drying overnight.

PMeAB samples were first dissolved in various solvents, including $CHCl_3$, THF, or DMF, yielding viscous PMeAB solutions. These solutions were subsequently drop-cast into containers and allowed to dry completely prior to undergoing high-temperature annealing, as illustrated in **Figure 3.5**. PMeAB solutions prepared in $CHCl_3$, THF, or DMF with a PMeAB weight percentage above 15% are suitable for drop-casting. A similar PMeAB concentration in THF has been reported in the literature to produce transparent PMeAB thin films.[99]

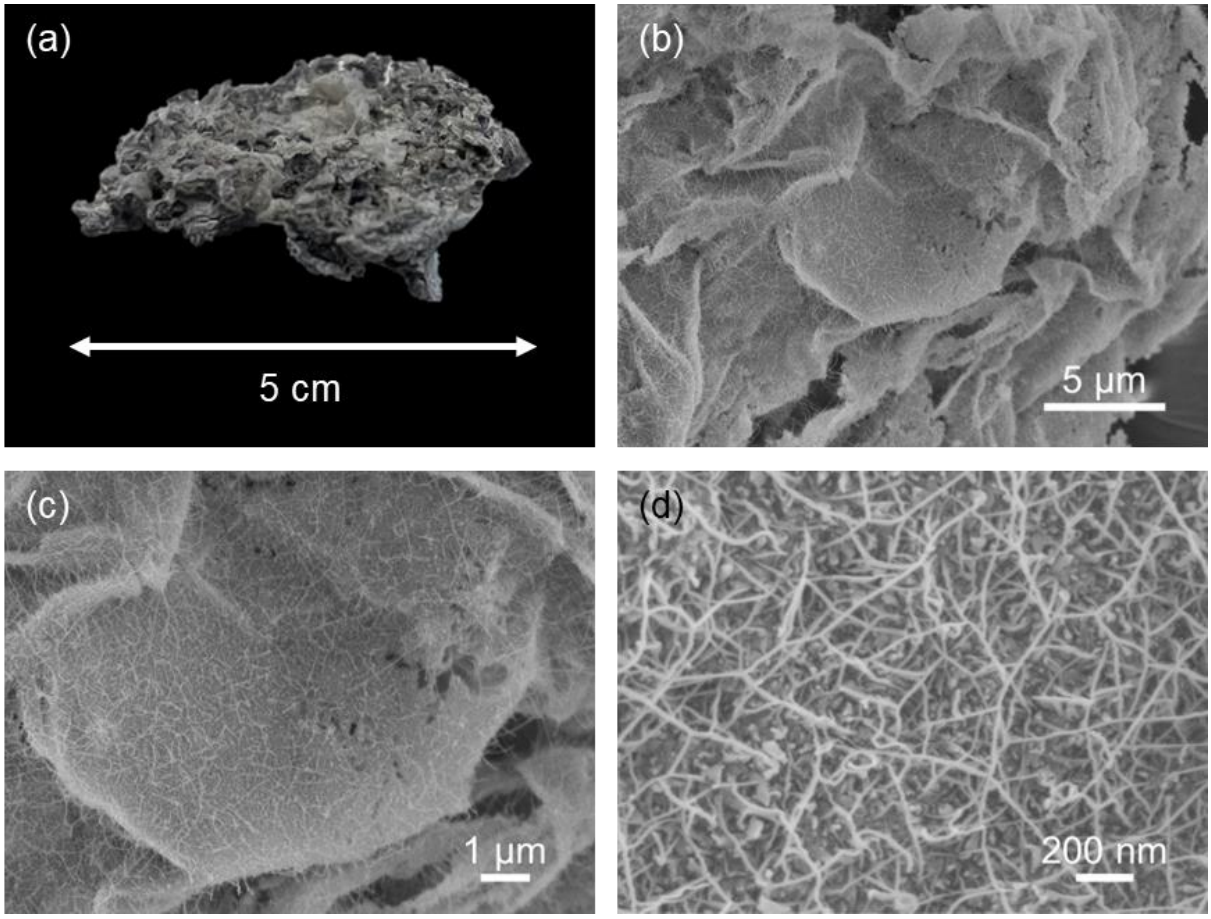

Figure 3.6: Morphology of PMeAB-derived p-BN. (a) Optical image of a 3D p-BN, showing a light-grey BN specimen. (b-d) Typical SEM images of the microstructure of p-BN, revealing a hierarchical 1D/2D nano-BN architecture.

The as-grown p-BN exhibits a crushed, porous shell-like morphology, as shown in **Figure 3.6b**, consisting of numerous randomly stacked, collapsed 2D BNNS, each with a thickness of approximately 150 nm and lateral dimensions often exceeding 10 µm, uniformly distributed across the entire area (**Figure 3.7a**). In addition, as-grown 1D nano-BN structures homogeneously and densely distributed across the surfaces of these BNNS throughout the entire p-BN specimen, as shown in **Figure 3.6c, d**. The diameters of these 1D nano-BN structures are approximately 38 nm, with lengths reaching up to 10 µm (**Figure 3.7b**). This differs from the previously reported chemically blown BNNS by Wang *et al.*[156] As discussed in **Section 3.1**, their method produces BNNS without the 1D nano-BN features observed in my work, and the porosity and surface area of their BNNS were not characterized. Although the

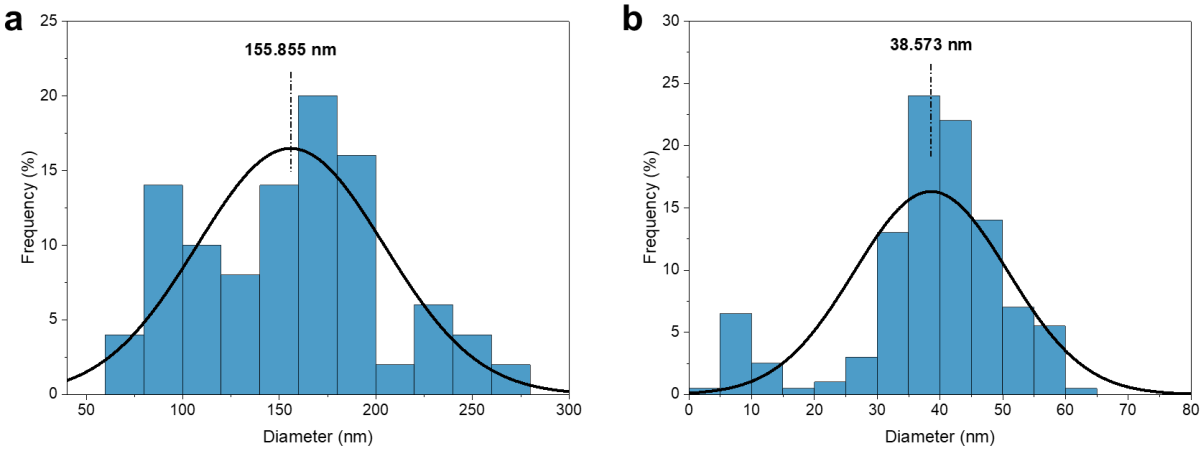

Figure 3.7: (a) Thickness distribution of as-grown BNNS in p-BN. (b) Diameter distribution of as-grown 1D nano-BN in p-BN.

BNNS are thinner (generally ranges from 1 to 5 nm) than those produced in my study, the final product exists as dispersed BN powder, lacking the 3D monolithic structure achieved in my p-BN. The structural coherence of monolithic structure enables easier processing, shaping, and integration into devices. The continuous 3D network facilitates improved mechanical stability against stress, enhanced thermal management, and better chemical resistance compared to dispersed BN powders, which tend to suffer from aggregation, poor structural cohesion, and limited applicability in load bearing or thermally demanding environments.[173,209]

HRTEM results reveal that the BNNS possess a few-layered structure, as shown in **Figure 3.8a, b**. The examined BNNS comprises approximately seven atomic layers, as determined by the number of fringes observed at the folded edge. The interlayer spacing is measured to be 0.334 nm, which agrees well with the value reported for bulk layered h-BN.[173] In **Figure 3.8a**,

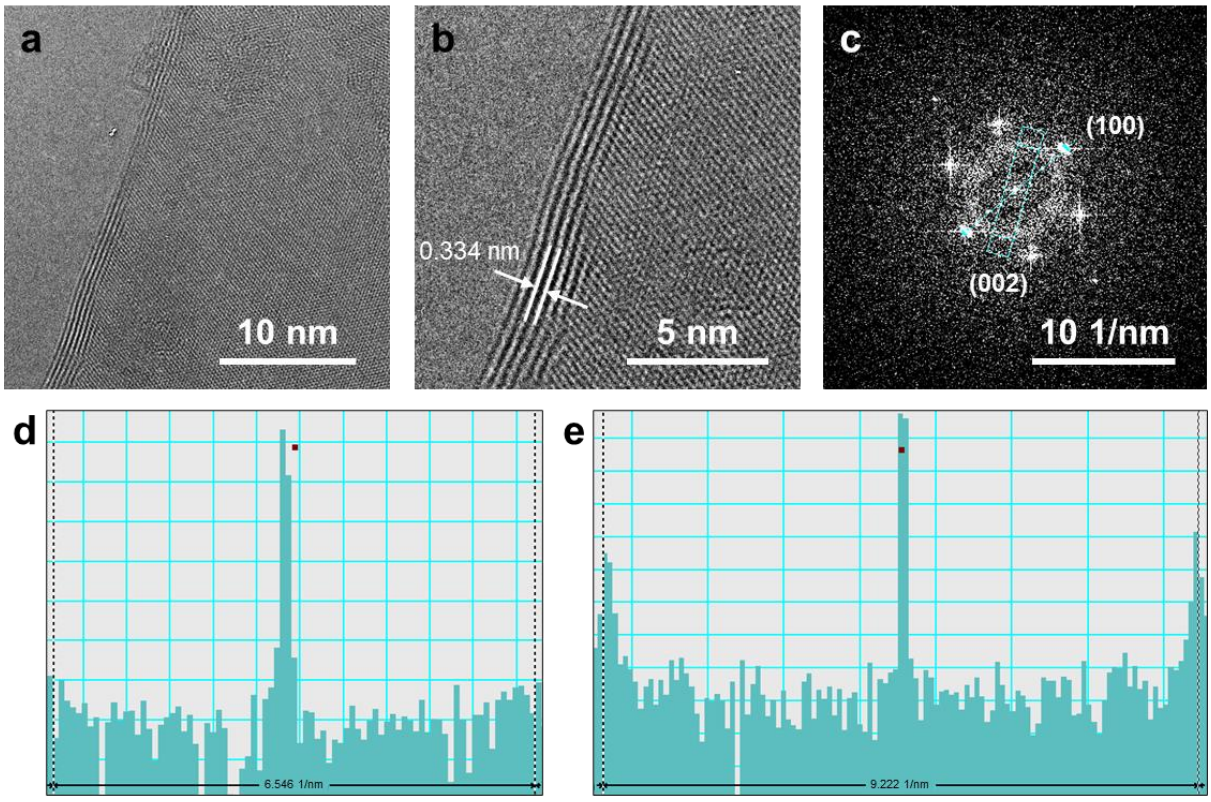

Figure 3.8: TEM characterisation of highly-crystallised BNNS in synthesized p-BN. (a) Low-resolution and (b) High-resolution TEM images, showing the edge of a few-layer BNNS. (c) Corresponding FFT pattern on the BNNS surface. (d, e) Line profiles of FFT, showing d* of 3.273 nm^{-1} for (002) planes and 4.611 nm^{-1} for (100) planes.

a Moiré pattern can be observed in the top right corner, further indicating the presence of stacked few-layer 2D BNNS.[210] FFT analysis shows a six-fold symmetric diffraction pattern, with clearly defined spots corresponding to the (002) and (100) planes of h-BN (**Figure 3.8d, e**), thereby confirming its hexagonal structure and multilayer nature.[211] These results indicate the high crystallinity of the synthesized BNNS.

Some BNNS are found to be more disordered, forming randomly entangled networks that contribute to a polycrystalline structure (**Figure 3.9**). **Figure 3.9a** illustrates the interlaced connections between BNNS. Although the individual few-layer BNNS domains are well-crystallised (**Figure 3.9b**), they lack long-range structural order. In other words, the synthesized 3D p-BN frameworks can be regarded as ensembles of h-BN polycrystals. The

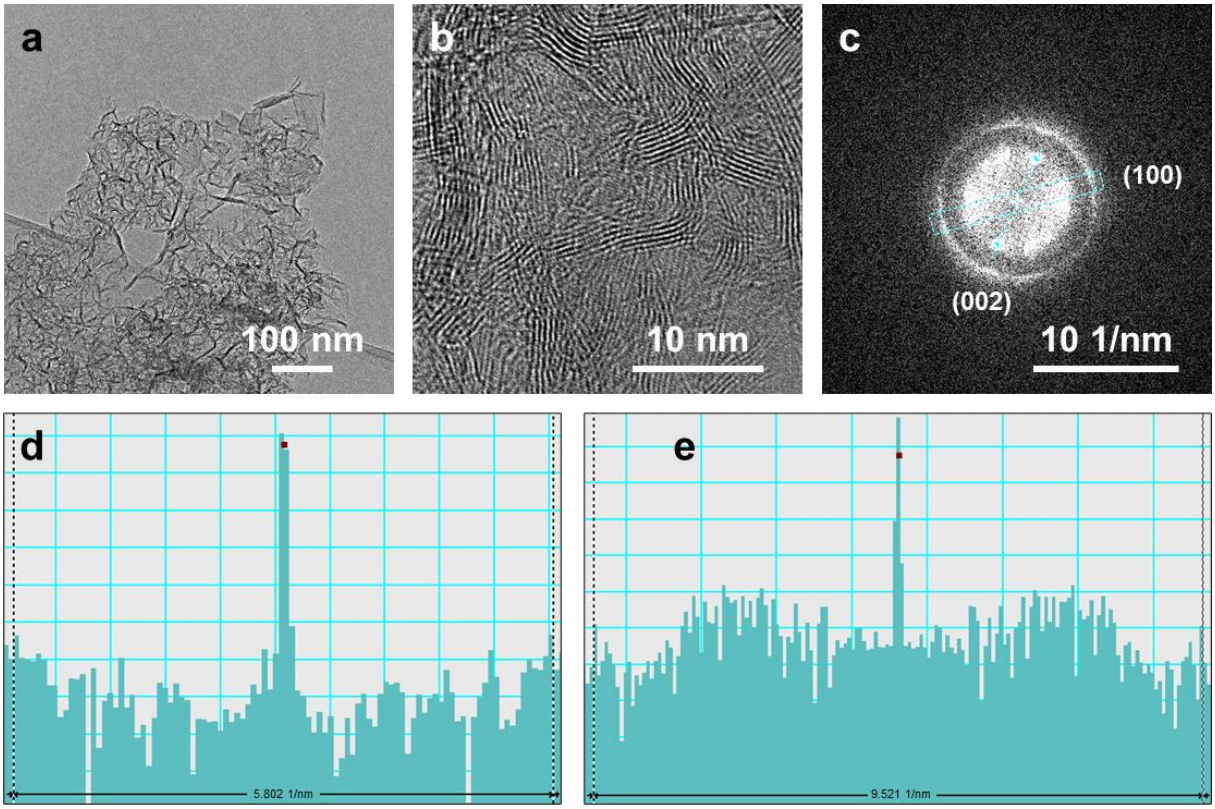

Figure 3.9: TEM characterisation of partially disordered BNNS in synthesized p-BN. (a) Low-resolution and (b) High-resolution TEM images, showing randomly interconnected of few-layer BNNS. (c) Corresponding FFT pattern on the BNNS surface. (d, e) Line profiles of FFT, showing d* of 2.901 nm^{-1} for (002) planes and 4.761 nm^{-1} for (100) planes.

FFT pattern in **Figure 3.9c** displays a ring-like structure corresponding to the (002) and (100) planes of h-BN, with less distinct diffraction spots compared to those in **Figure 3.8c**. This further confirms the polycrystalline nature of the synthesized h-BN.[182]

The 1D nano-BN structures observed on the surface of the BNNS are identified as either hollow boron nitride nanotubes (BNNT) or solid boron nitride nanofibres (BNNF), as shown in **Figure 3.10**. **Figure 3.10a** presents a multi-walled BNNT (MW-BNNT) consisting of approximately seven concentric walls. The outer diameter is measured to be 6.67 nm, which is relatively small compared to the typical MW-BNNT diameter reported in the literature, usually ranging from 20 to 50 nm or larger.[133] The BNNT in the p-BN sample exhibit a highly crystalline structure with well-defined walls and a d-spacing of 0.33 nm. Although some

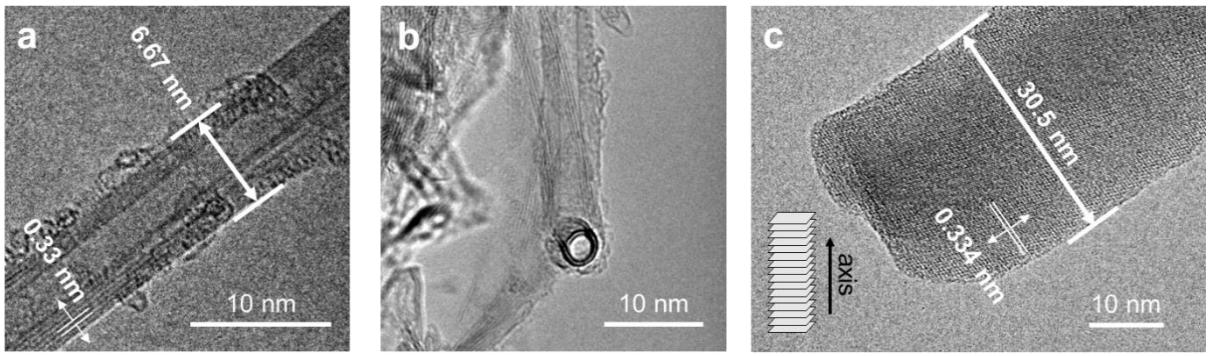

Figure 3.10: TEM characterisation of 1D nano-BN structures in synthesized p-BN. High-resolution TEM image of (a, b) a multi-walled BN nanotube and (c) a platelet BN nanofibre.

nanoparticle-like features are observed attached to the outer walls, I attribute these to 0D BN nanostructures rather than impurities, given the high purity of the p-BN material, as confirmed by XPS analysis (**Figure 3.18a**). **Figure 3.10b** shows a cross-sectional view of another BNNT within the same p-BN specimen, where a clear tubular morphology is evident at the open tube end.

In addition to BNNT, BNNF are also prominently observed (**Figure 3.10c**). These BNNF are notable due to their unique platelet-like structure, in which layers of h-BN are stacked along the rod axis, contrasting with BNNT, where the BN layers are oriented parallel to the tube axis. The BNNF are generally larger than the BNNT (as shown in **Figure 3.7b**, the data exhibit a bimodal distribution with two distinct peaks, indicating the presence of two dominant structural features, i.e. the BNNT and the BNNF), with diameters in the range of 30–40 nm and a consistent d-spacing of 0.334 nm. Similar platelet 1D nanostructures have been reported in carbon systems (*e.g.*, platelet carbon nanofibres),[212] but such structures are rarely observed in BN systems. The formation of these BNNF is likely influenced by the presence of excess hydrogen or other heteroatoms for the stabilisation of the plates during synthesis,[212] a hypothesis that will be further discussed based on the TGA-MS result presented in **Section 3.3.2** combined with the computational studies in **Chapter 4**. Hydrogen tends to passivate the dangling bonds at the edges of h-BN layers. Once passivated, newly arriving B or N atoms

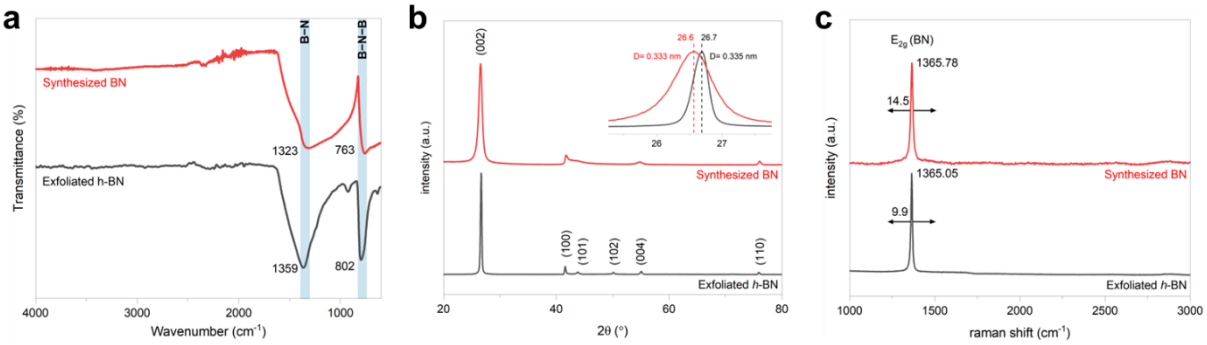

Figure 3.11: (a) FT-IR spectra of synthesized p-BN (red) and exfoliated h-BN (black). (b) XRD pattern of synthesized p-BN (red) and exfoliated h-BN (black), inset shows enlarged (002) peak. (c) Raman spectra of synthesized p-BN (red) and exfoliated h-BN (black).

cannot attach to the same basal plane but instead nucleate a new layer atop the existing one, promoting the vertical stacking of h-BN layers along the growth direction and resulting in the observed platelet morphology.[213]

To further characterize the properties of BN materials, FT-IR, XRD, and Raman spectroscopy were employed, as shown in **Figure 3.11**. The FT-IR spectra of both synthesized p-BN and exfoliated commercial BNNS were analysed over the range of 600–4000 cm^{-1} (**Figure 3.11a**). For the exfoliated BNNS, two prominent absorption peaks were observed at 1359 and 802 cm^{-1}, corresponding to the in-plane B–N stretching vibration of sp^2-bonded h-BN and the out-of-plane B–N–B bending vibration, respectively.[170] Similarly, the synthesized p-BN exhibited two distinct peaks at 1323 and 763 cm^{-1}, indicative of the same characteristic vibrational modes. Additionally, a peak at 1096 cm^{-1} appeared in the spectrum of BNNS, which can be attributed to the C–O stretching of tertiary alcohols, suggesting possible surface adsorption of residual isopropanol used during the sonication process, despite post-treatment removal efforts. Notably, no peaks were observed in the 3000–3500 cm^{-1} region for p-BN, indicating the absence of OH^- impurities commonly associated with hydroxyl groups.[170]

XRD and Raman spectroscopy further confirmed the high crystallinity and hexagonal phase of the synthesized p-BN, with results closely matching those of the exfoliated BNNS.

The XRD pattern revealed four well-defined peaks at approximately 2θ ≈ 26°, 41°, 54°, and 76°, corresponding to the (002), (100)/(101), (004), and (110) crystallographic planes of h-BN, respectively (**Figure 3.11b**).[172] The similarity in peak positions and intensities between p-BN and exfoliated BNNS strongly indicates the preservation of the hexagonal structure. The inset in **Figure 3.11b** highlights the (002) peak, showing near-identical position and a calculated d-spacing of 0.333 nm for p-BN, in agreement with the value obtained from TEM analysis (**Figure 3.8**). Raman spectroscopy also revealed strong correspondence between the synthesized p-BN and exfoliated BNNS (**Figure 3.11c**). Both materials exhibited a single, sharp E_{2g} mode characteristic of h-BN, located at 1365.78 cm^{-1} for p-BN and 1365.05 cm^{-1} for BNNS. The full width at half maximum (FWHM) of the p-BN Raman peak was 14.5 cm^{-1}, only slightly broader than the 9.9 cm^{-1} observed for exfoliated BNNS. A FWHM in the range of ~10 cm^{-1} typically indicates high crystallinity,[214,215] reinforcing the structural quality of the synthesized material.

The overall consistency of FT-IR, XRD, and Raman results between the synthesized p-BN and exfoliated BNNS suggests that the p-BN is primarily composed of 2D BNNS with a slightly greater thickness than that of the exfoliated BNNS. Notably, no carbon-related peaks were detected in any of the characterisation techniques, confirming the high purity of the synthesized BN and the effective exclusion of carbonaceous contaminants, similar to that of commercially exfoliated BNNS.

3.3.2 Chemical Blowing of PMeAB

The fabrication process of BNNS is illustrated in **Figure 3.12**. During the thermal treatment of raw PMeAB (**Figure 3.12a**) under an ammonia atmosphere, the initially ribbon-like morphology progressively becomes disordered and diffuse upon heating above 80 °C (**Figure**

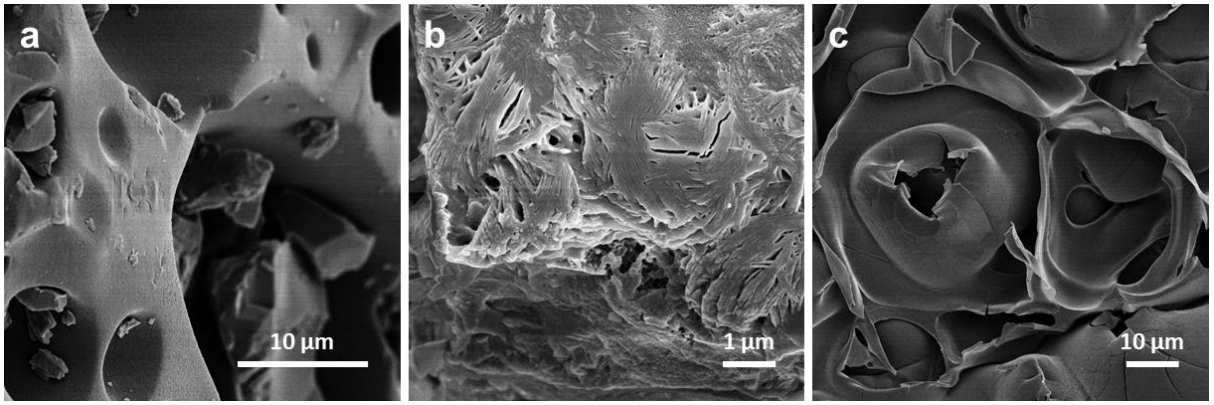

Figure 3.12: Growth process of BNNS under proposed chemical blowing of PMeAB. SEM image of (a) the as-prepared PMeAB at ambient temperature, (b) a moderately disordered ribbon-like structure formed after thermal treatment at 80 °C in an ammonia atmosphere, and (c) an intermediate obtained at 300 °C, displaying a foam-like morphology composed of tightly packed, interconnected bubbles.

3.12b). This structural change is attributed to a phase transition into a more mobile intermediate state, indicative of increased chemical reactivity. The emergence of this mobile phase originates from slight thermal perturbation, which disrupts the hydrogen-bonding network within PMeAB.[156,216] Upon further heating, this intermediate undergoes dehydrogenation and converts into poly(methyliminoborane) (PMeIB), which subsequently transforms into $BNCH_x$ species at approximately 300 °C (**Figure 3.12c**), and finally crystallises into h-BN at 1400 °C (**Figure 3.6**). This sequence aligns with previously reported reaction pathways.[156] Notably, the $BNCH_x$ phase exhibits a bubble-like morphology composed of densely packed spherical domains, suggesting a formation mechanism akin to "chemical blowing." This mechanism draws conceptual inspiration from the known blowing behaviour of ammonia borane (AB).[156] In this process, the activated intermediate phase of PMeAB begins to decompose near 100 °C (**Figure 3.13a**), releasing hydrogen gas and inducing inflation of the soft polymer matrix into gas-filled bubbles. The inherent polarity of B–N bonds may facilitate chain alignment into planar configurations that effectively entrap the evolving gas.[156] Owing to localised exothermic reactions, the conversion from PMeAB to PMeIB and subsequently to $BNCH_x$ proceeds rapidly.

The thermolysis is conducted under an ammonia-rich atmosphere. Ammonia preferentially reacts with methyl groups in PMeAB, generating volatile NCH_x species that aid in the removal of carbon content.[217] Thus, the conversion pathway not only involves the transformation from PMeAB to PMeIB to $BNCH_x$, but also includes side reactions such as the formation of polyaminoborane (PAB) and polyiminoborane (PIB), eventually contributing to the evolution of BNH_x intermediates. Hydrogen evolution effectively inflates the polymeric bubbles until their walls become increasingly thin. In parallel, small volatile species—such as borane, ammonia, methane, borazine, and methylborazine—are released, promoting additional thinning of the bubble walls, as evidenced by TGA-MS spectra in **Figure 3.13**, displaying characteristic peaks of these released species. At elevated temperatures (~1400 °C), the dehydrogenated bubble walls solidify into h-BN. Subsequent bubble collapse or rupture results in the formation of thin BNNS.

To better understand the complex chemical transformations occurring during the thermal decomposition of PMeAB, and to identify the volatile species released at various temperatures, thermogravimetric analysis coupled with *in situ* mass spectrometry (TGA-MS) was conducted. While the actual thermolysis experiments for converting PMeAB to p-BN were carried out under an ammonia atmosphere, the TGA-MS measurements were performed in an argon atmosphere due to equipment constraints. Prior to heating, the system was thoroughly purged with argon for two hours to eliminate residual gases, and the background signal was subtracted to ensure accurate detection of decomposition products.

The mass spectrum recorded at both before (**Figure 3.13b**) and after (**Figure 3.13c**) the point of maximum decomposition, corresponds to the peak observed in the differential scanning calorimetry (DSC) curve (**Figure 3.13a**). This peak indicates the highest rate of heat release, suggesting that the most vigorous, predominantly exothermic, reaction occurs at this temperature. Among the numerous fragments detected, several were identified as well-known

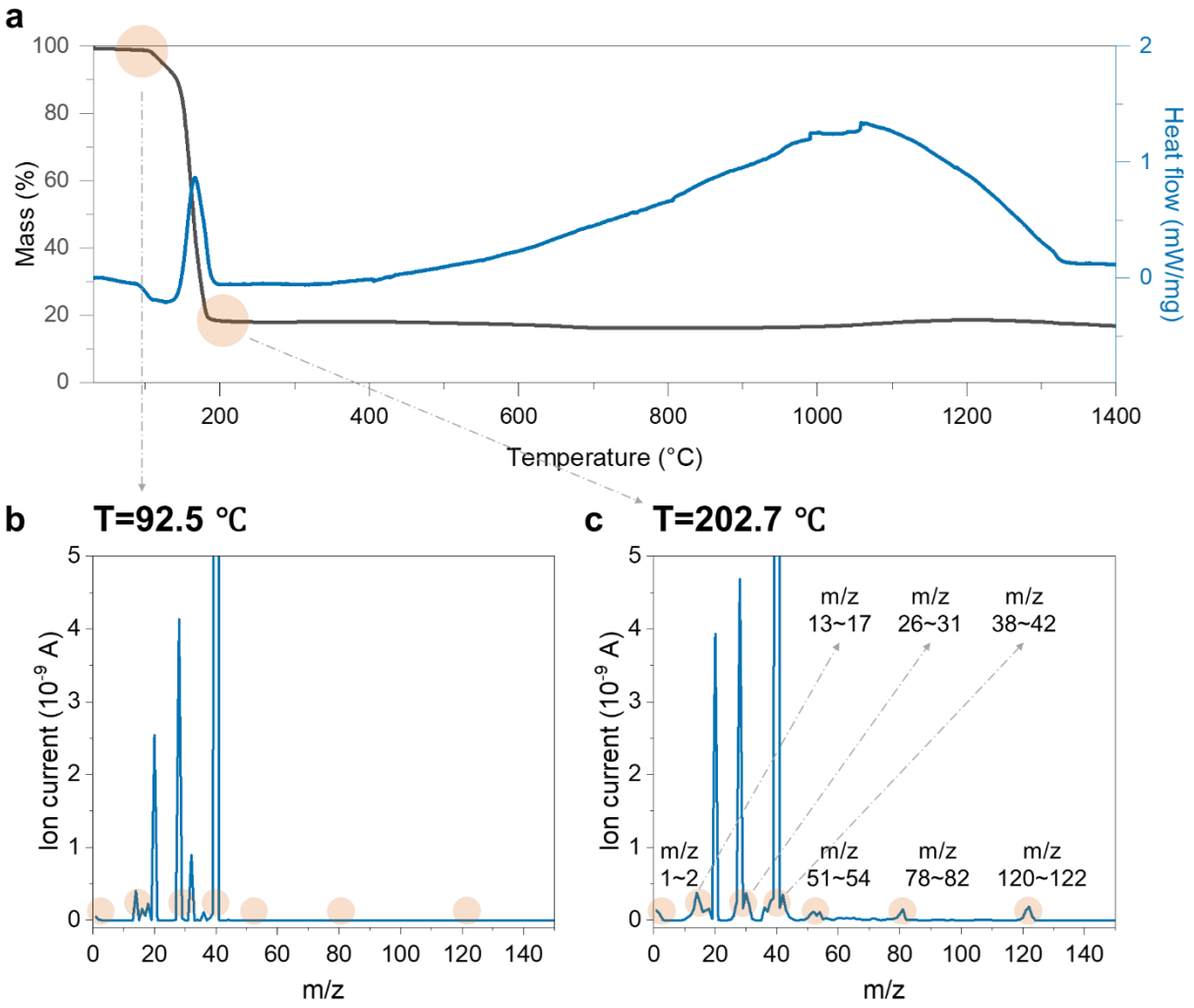

Figure 3.13: (a) TGA (black) and DSC (blue) profiles of PMeAB during heating from room temperature to 1400 °C under an argon atmosphere. (b) Mass spectrum recorded at 92.5 °C, prior to the onset of major decomposition. (c) Mass spectrum recorded at 202.7 °C, after significant decomposition has occurred, with peak profiles assigned to various evolved chemical species.

chemical species based on their characteristic mass-to-charge (m/z) ratios. To date, no reports have documented the simultaneous detection of this broad range of decomposition products or systematically explored their roles in h-BN synthesis from PMeAB. However, studies on AB provide a useful point of reference for interpreting these results and for formulating initial assumptions regarding the PMeAB system.[218]

Identified species include hydrogen (H_2, m/z ~ 2), borane (BH_3, m/z ~ 13),[218] ammonia (NH_3, m/z ~ 17),[218] diborane (B_2H_6, m/z ~ 26),[218] ammonia borane (BH_3NH_3, m/z ~ 30), borazine and cyclotriborazane ($B_3N_3H_x$, m/z ~ 78–82),[100,219,220] and methyl-borazine and

cyclotrimethyl-borazane ($B_3N_3C_3H_x$, m/z ~ 120–122).[100] In addition to these, two prominent but less clearly assigned fragments appear in the m/z ~ 26–31 and m/z ~ 38–42 ranges. The signal at m/z ~ 16 is likely attributable to methane (CH_4), derived from the decomposition of the methyl group in PMeAB. The fragment cluster in the m/z ~ 26–31 range is consistent with monomeric aminoborane (BNH_x),[219,220] as reported in earlier studies, or possibly with NCH_x-type complexes, considering the presence of methyl groups in the system. The m/z ~ 38–42 range appears to reflect a more complex mixture of species, potentially including hydrogen-rich triborane (B_3H_x),[221] aminodiborane (B_2NH_x),[222,223] and dehydrogenated methylamine borane derivatives ($BH_xNH_xCH_x$). Further, signals in the m/z ~ 51–54 range may correspond to species such as B_2NCH_x and cyclodiborazane ($B_2N_2H_x$). However, the exact molecular structures of these fragments remain uncertain. **Chapter 4** will address this through computational modelling, aiming to predict the most probable structures and assess their relevance to the overall decomposition and BN formation pathway. It is worth noting that while secondary decomposition or deposition during the transfer of species to the mass spectrometer may occur, such effects are expected to be minimal, as most of the detected species are stable within the timescale of the measurement.

Once the key chemical species were identified, subsequent measurements were carried out to track their evolution during heating. The release profiles of all significant species were monitored from room temperature up to 1400 °C, as shown in **Figure 3.14**. Notably, several expected decomposition products of PMeAB, including H_2 (m/z = 2), dehydrogenated MeAB (m/z = 42), BZ (m/z = 81), and MeBZ (m/z = 121), first appear at approximately 200 °C. These signals suggest that PMeAB undergoes a series of concurrent reactions: dehydrogenation to generate H_2, dissociation to form MeAB-type species ($BH_xNH_xCH_x$), and cyclisation to yield BZ and MeBZ. From around 250 °C, the evolution of H_2, dehydrogenated MeAB, BZ, and MeBZ continues. However, the signals for BZ and MeBZ diminish and disappear by 400 °C,

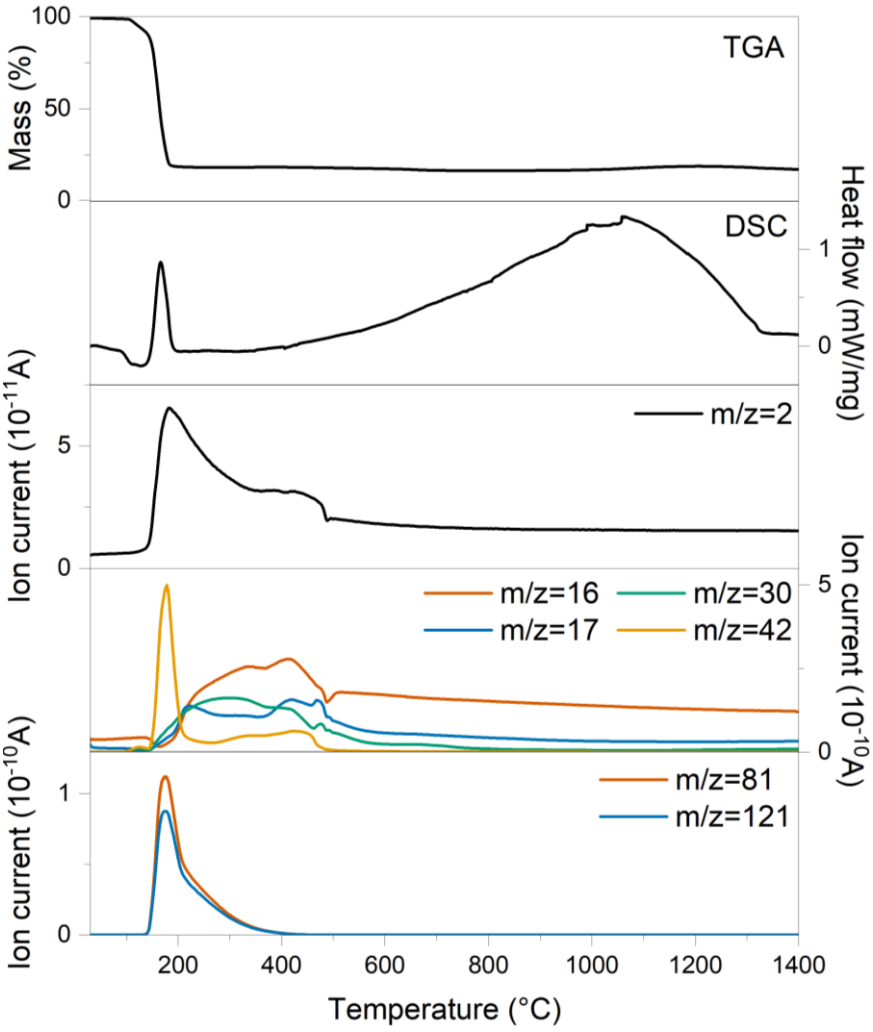

Figure 3.14: The evolution profiles of individual released species recorded from room temperature to 1400 °C.

while H_2 and dehydrogenated MeAB persist until approximately 500 °C. At 250 °C, additional species are also detected, including CH_4 (m/z = 16), NH_3 (m/z = 17), and a range of BNH_x- and NCH_x-type fragments (m/z = 26–31), which are likely products of simultaneous dehydrogenation and dissociation processes. Above 500 °C, only H_2 remains detectable in significant quantities, indicating that PMeAB continues to undergo dehydrogenation at elevated temperatures. This observation is consistent with the DSC curve, which shows a sustained exothermic signal extending into the higher temperature range.

Notably, all PMeAB samples (**PMeAB1** to **PMeAB10**), despite variations in molecular weight (see **Figure 2.5** for sample details), exhibit similar TGA–DSC profiles, as shown in **Figure 3.15**. A minor endothermic dip appears at ~120 °C, just before a major exothermic peak

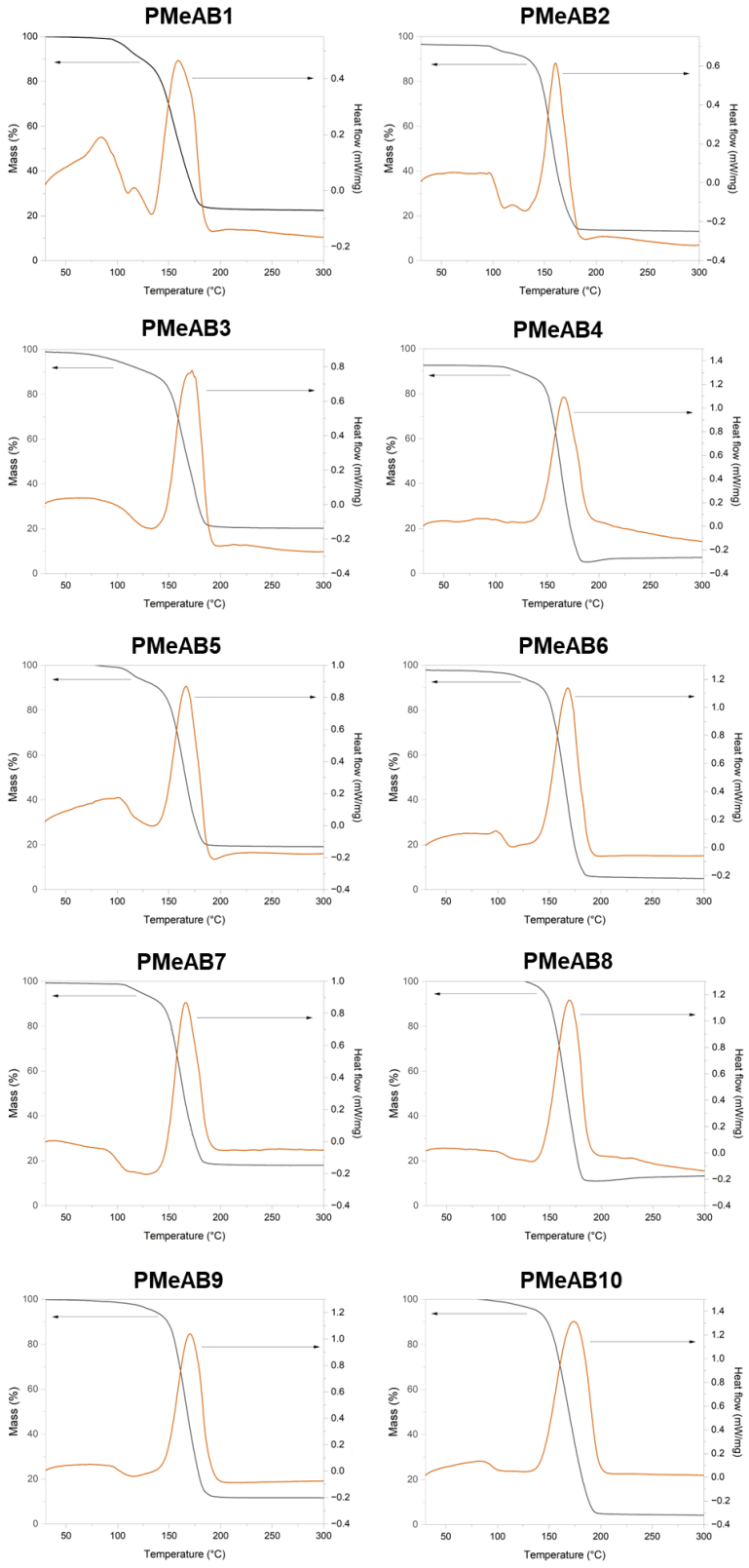

Figure 3.15: TGA–DSC profiles of samples **PMeAB1** to **PMeAB10** were recorded over a temperature range from room temperature to 300 °C.

at ~160 °C. This endothermic feature corresponds to the melting behaviour of PMeAB, which

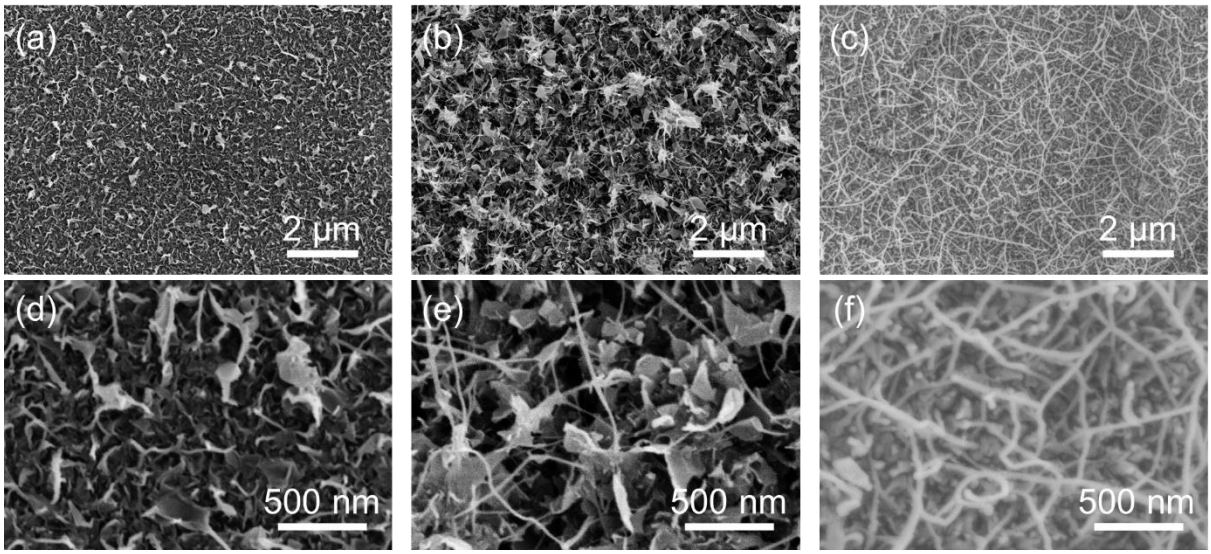

Figure 3.16: SEM images of PMeAB after ammonia thermolysis at (a, d) 1200 °C, (b, e) 1300 °C, and (c, f) 1400 °C.

occurs between 100 °C and 150 °C across all samples. The observed melting point (~120 °C) is significantly higher than that of the monomer MeAB reported in the literature (55 °C)[100] and is comparable to that of AB (114 °C)[219]. These results indicate that the thermal decomposition behaviour of PMeAB is largely independent of molecular weight and follows a similar profile to MeAB and AB with only slight variations in melting and decomposition temperatures—a minor endothermic transition followed by a major exothermic event. Thus, it is reasonable to hypothesize that the B–N–H-containing species detected by MS are similar to those reported in studies of MeAB or AB, and these prior investigations can be used as reliable references.[100,218,219]

To investigate the formation of 1D BNNT and BNNF on the BNNS surface, SEM images were obtained to observe surface morphology changes at different temperatures ranging from 1200 °C to the final target of 1400 °C under ammonia atmosphere thermolysis, as shown in **Figure 3.16**. At 1200 °C (**Figure 3.16a, d**), only BN nanoflake-like structures are present, with relatively small lateral dimensions (below 200 nm) and a flat orientation on the surface. This result is in partial agreement with theoretical studies by Han *et al.*,[224] who employed SCC-

DFTB simulations to examine BN nanostructure formation using NH_3-based precursors in arc plasma environments. In their model, BN nanoflakes formed on small boron clusters under an NH_3-rich environment, resulting in flat structures. This scenario closely resembles my experimental system. As supported by the XPS data presented in **Figure 2.18 and Figure 2.20**, thermolysis of PMeAB leads to the progressive release of carbon and nitrogen, leaving behind a boron-rich matrix. With the continuous supply of NH_3, my system can effectively be regarded as consisting of a boron-rich target exposed to NH_3 feedstock, analogous to the conditions modelled by Han *et al.* In their study, the bombardment of NH_3 supplies nitrogen to form a stoichiometric h-BN sheet with a 1:1 B:N atomic ratio, while hydrogen atoms preferentially bind at the sheet edges. This configuration results in a flat atomic layer that does not roll into a tubular structure, due to edge passivation by hydrogen atoms, a condition that is very likely applicable to the system presented here.

This observation is also analogous to carbon-based systems derived from hydrocarbon precursors, where excess hydrogen released from hydrocarbon decomposition promotes the growth of small carbon nanoflakes during the early stages prior to CNT growth. Khalilov *et al.*[225] simulated CNT nucleation from CH_4 precursors and identified three distinct growth stages. They observed that small, free-standing graphene patches and other early carbon structures can be etched away if the flux of hydrogen atoms is sufficiently high, as is the case in CH_4-based growth environments. This behaviour agrees with experimental study by Rao *et al.*,[226] in which CH_4 precursors at temperatures above 800 °C lead to similar etching and restructuring phenomena during the initial stages of CNT formation.

Upon increasing the temperature to 1300 °C (**Figure 3.16b, e**), 1D BNNT/BNNF begin to emerge, seemingly originating from the BN nanoflakes, as their bases appear connected to the flake surfaces. These hybrid BN nanoflakes/BNNT/BNNF also exhibit a more vertical orientation, protruding from the surface, and the BN nanoflakes themselves grow larger

compared to those at 1200 °C (up to 500 nm). This suggests that BN nanoflake formation initiates at lower temperatures, followed by the growth of BNNT/BNNF as temperature increases.

A similar trend has been reported in carbon systems, where the formation of small, cap-like carbon structures marks the initial stage of CNT and CNF nucleation. Zeng *et al.*[227] demonstrated the metal-catalyst-free growth of CNT/CNF on carbon black (CB) particles, and their TEM analysis revealed that the newly formed CNT/CNF likely extrude from individual CB particles. This mechanism closely resembles my observation of 1D BN nanostructures emerging from BN nanoflakes. In their study, carbon species derived from ethylene (C_2H_4) and acetylene (C_2H_2) precursors deposit onto CB particles, forming multilayer graphene-like structures that eventually lift off to become multi-walled CNT (MWCNT). Analogously, in the system proposed here, BN nanoflakes resemble these multilayer graphene-like structures, while the resulting BNNT/BNNF are analogous to MWCNT. The boron-rich intermediate matrix derived from PMeAB thermolysis plays a role similar to the carbon-rich CB substrate in the carbon system. Importantly, their study provides direct evidence of CNT growth on a non-metal substrate. Unlike CNT grown on metal nanoparticles, where chemical composition significantly influences nucleation, CNT growth on CB follows a vapor–liquid–solid (VLS) mechanism, driven by the structural properties of the carbon substrate itself. Similarly, in my case, no catalyst is used, and the growth of BN nanostructures is driven entirely by the presence of a boron-rich target and an NH_3 atmosphere.

At 1400 °C (**Figure 3.16c, f**), only 1D nanostructures are observed, indicating that the BN nanoflakes have fully transformed into BNNT and BNNF. This strongly supports the hypothesis that BN nanoflakes act as seeds for the subsequent growth of 1D BN nanostructures. The diameters of the BNNT/BNNF increase relative to those formed at 1300 °C, growing from approximately 22 nm to 47 nm.

This observation aligns well with the simulation work by McLean *et al.*,[228] who employed ReaxFF molecular dynamics to model BNNT nucleation via network fusion on nickel and boron catalysts using AB as the precursor. Their study demonstrated that, following catalytic formation and polymerisation of B–N chains and rings, BNNT cap structures form "perpendicular" to the catalyst surface through the direct fusion of adjacent BN networks. This closely resembles the experimental observation of vertically oriented BN nanoflakes in this work. Experimentally, it is also well established that at elevated temperatures, BN nanoflakes tend to disappear as they convert into the more energetically favourable BNNT.[229] This transformation is driven by the thermal instability of hydrogen-passivated flake edges, leading to structural rearrangement that minimizes dangling bonds and edge energy.

These observations provide preliminary insight into the temperature-dependent morphological evolution of the system. However, a more detailed understanding of the growth mechanisms requires theoretical support, which will be addressed in **Chapter 4** through computational modelling. These results also highlight that controlling the thermal profile during ammonia thermolysis enables tuning of BNNS surface morphology in p-BN, allowing for the tailored design of materials for specific applications.

Overall, the dominant thermal decomposition pathways—dehydrogenation, dissociation, and cyclisation—will be discussed in detail in **Chapter 4**, supported by DFT and ReaxFF that further validate and interpret the experimental findings.

3.3.3 From BN to Boron Carbonitride (BCN)

Introducing carbon into h-BN to form B–C–N nanomaterials presents a promising strategy for developing semiconducting materials, offering tunable electronic properties and broad functional applicability.[230] The potentially adjustable bandgap of the B–C–N system enables versatility across applications such as luminescence, electronics, gas sorption, and molecular separation.[231] This tunability comes from the incorporation of carbon into the BN lattice, which alters its electronic structure. Carbon reduces the strong ionic character of BN and introduces regions of π-conjugation, effectively narrowing the bandgap from that of pure BN toward semiconducting or even conductive behaviour. This section demonstrates that the PMeAB-derived route can also be employed to synthesize porous boron carbonitride (p-BCN). By making only minor modifications to the thermolysis conditions, reducing the NH_3-to-Ar ratio to below 1:4, p-BCN can be obtained using the same experimental setup. These findings confirm the feasibility of PMeAB-based synthetic route and highlight its potential for the rational design of B–C–N nanomaterials with tunable compositions tailored for specific applications.

The as-synthesized p-BCN was characterized by FT-IR and XPS to confirm the presence of carbon and to quantify the level of carbon doping. As shown in **Figure 3.17,** the FT-IR spectrum of p-BCN displays two prominent peaks at ∼1338 cm^{-1} and ∼721 cm^{-1}, corresponding to the in-plane stretching vibration of B–N and the out-of-plane bending vibration of B–N–B, respectively.[232] These features are similar to those observed in p-BN (B–N: 1323 cm-1; B–N–B: 763 cm^{-1}, as shown in **Figure 3.11a**), only with slight shifts. The reduced intensity and broadening of these peaks in p-BCN, relative to pure p-BN, suggest an increased degree of structural disorder,[233,234] introduced by carbon binding. The CO_2 peak remains unchanged in intensity across both spectra, which can be a reliable reference. Several

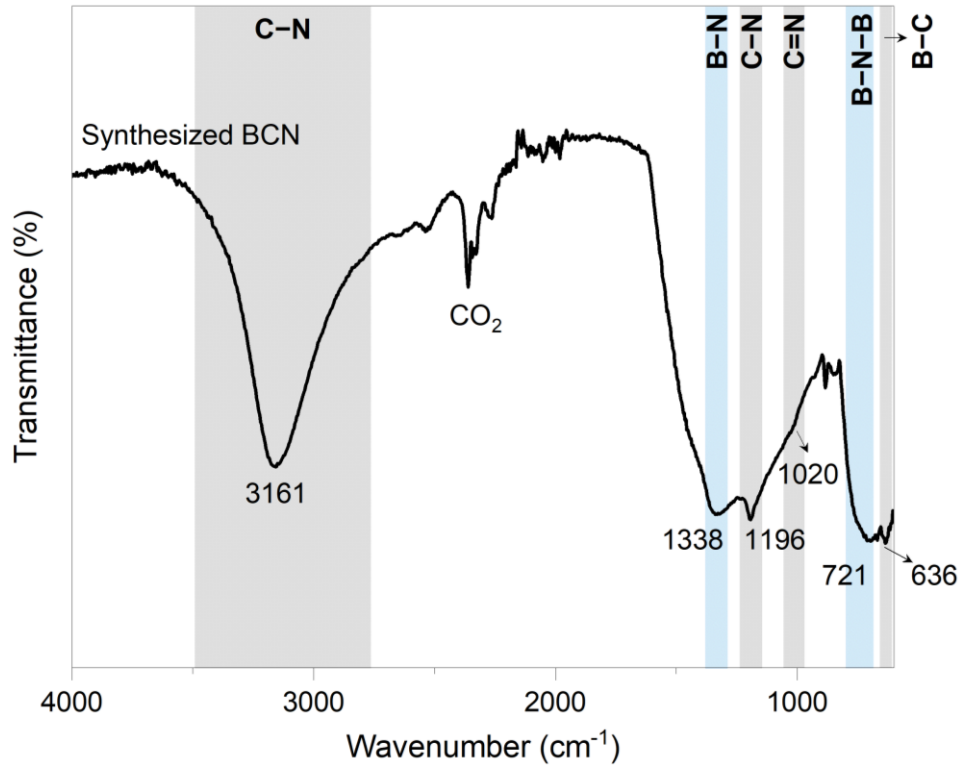

Figure 3.17: FT-IR spectrum of synthesized p-BCN.

carbon-related peaks are observed in the p-BCN spectrum that are absent in p-BN, including peaks at 636, 1020, and 1196 cm^{-1}, corresponding to B–C,[235,236] C=N,[237] and C–N bonds,[235,238] respectively. The peak at 1020 cm^{-1}, attributed to sp^2-hybridized C=N bonds, indicates that carbon and nitrogen atoms are coplanar.[237] In the out-of-plane direction, if graphene- and h-BN-like layers are covalently bonded, a broad band between 2900 and 3200 cm^{-1} can appear, suggesting amide bond formation between the layers.[239] Such a feature is also observed in the p-BCN spectrum. These results suggest that carbon not only dopes into the same plane as h-BN, introducing in-plane disorder, but also contributes to the formation of graphene-like carbon regions that stack and interact with h-BN layers.

XPS analysis was conducted to investigate the chemical states and elemental compositions of the synthesized p-BN and p-BCN, as shown in **Figure 3.18**. The elemental composition results (**Figure 3.18a, e**) indicate that p-BN is highly pure, with boron and nitrogen contents exceeding 96% and a carbon content of approximately 1%, comparable to the high purity

observed in BNF discussed in **Chapter 2**. When the NH_3 concentration was reduced during synthesis, the resulting p-BCN showed a significantly increased carbon content of 11.69%, while boron and nitrogen remained the dominant elements, accounting for a combined 87%. This composition suggests successful carbon doping within the h-BN matrix. Notably, the oxygen content remains below 2%, which is critical as it confirms that carbon incorporation does not compromise the material by introducing significant oxygen contamination. This enables precise compositional control over p-BCN from PMeAB.

The deconvoluted high-resolution spectra of the B 1s, C 1s, and N 1s regions are presented in **Figure 3.18b–d** for p-BN and **Figure 3.18f–h** for p-BCN. Both materials exhibit similar peak positions, indicating comparable bonding environments for B and N atoms. The primary B 1s peak appears at 190.5 eV for p-BN and 190.31 eV for p-BCN, corresponding to B atoms surrounded by N. Likewise, the N 1s peak is located at 398.1 eV for p-BN and 397.94 eV for p-BCN, indicative of N atoms coordinated with B.[230] In the C 1s spectrum of p-BCN, the main peak at 284.49 eV is consistent with sp^2-hybridized carbon, similar to graphite.[240] A sub-peak at 285.02 eV is attributed to C–N bonding, and a minor peak at 282.3 eV corresponds to C–B bonds.[241,242] The corresponding signals of N-C or B-C bonds are also observed as sub-peaks in the N 1s and B 1s spectra located at 389.63/400.53 eV and 188.75 eV, respectively.[241,242] While the B 1s and N 1s peaks are nearly identical in position for both p-BN and p-BCN, the C 1s signal in p-BCN is significantly more intense due to the increased carbon content. The dominant forms of carbon in p-BCN appear to be C=C, indicative of graphene-like regions, and C–N, suggesting in-plane doping of carbon into the h-BN lattice. These findings are consistent with the FT-IR results discussed earlier, supporting a structural model where carbon exists both within and alongside the h-BN layers.

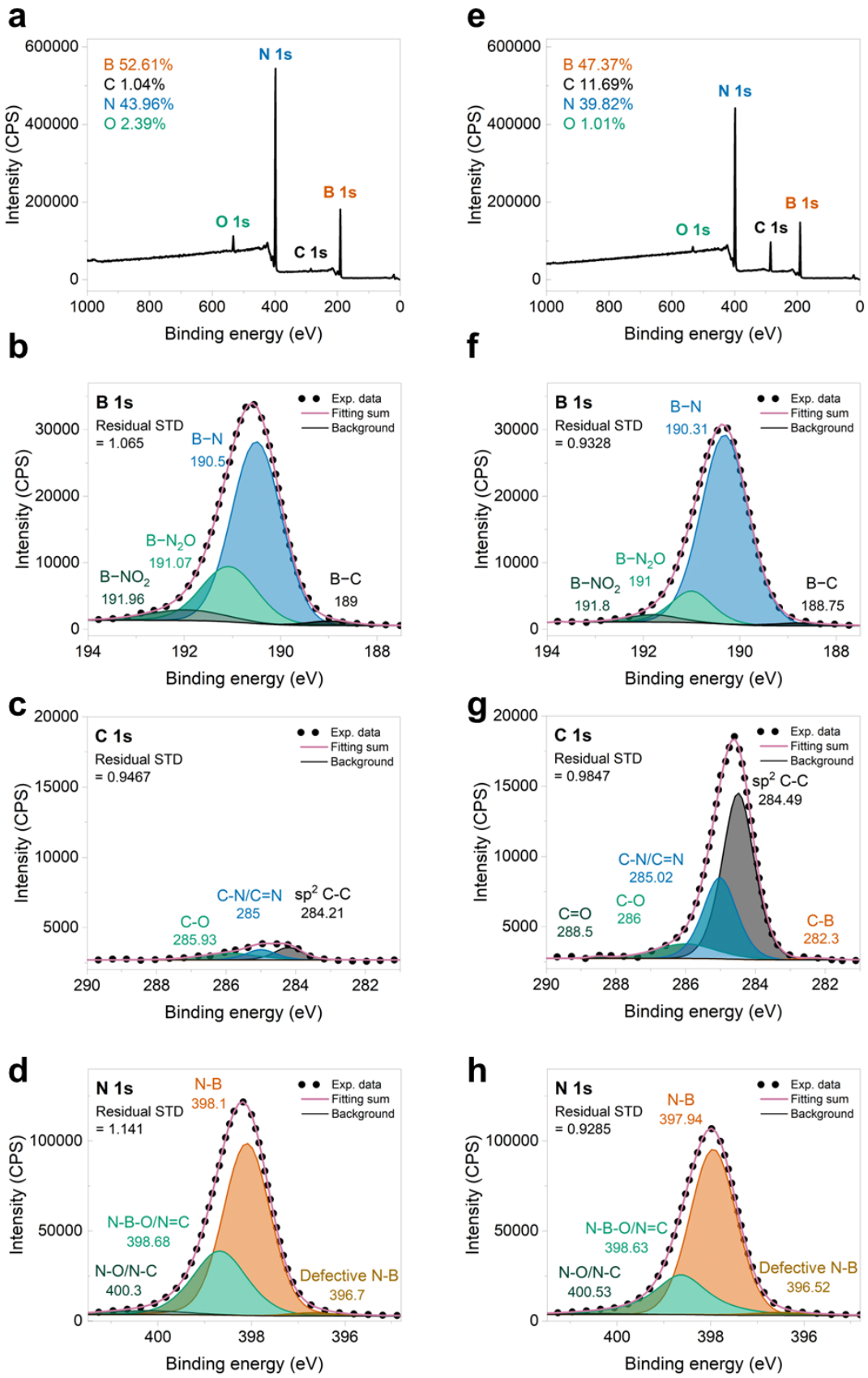

Figure 3.18: Survey spectra of (a) p-BN and (b) p-BCN, inset shows elemental contents of B, C and N calculated from XPS result. Deconvolutions of B1s, C1s and N1s peaks of (b-d) p-BN and (f-h) p-BCN.

3.3.4 PMeAB-Derived Porous BN Thin Films

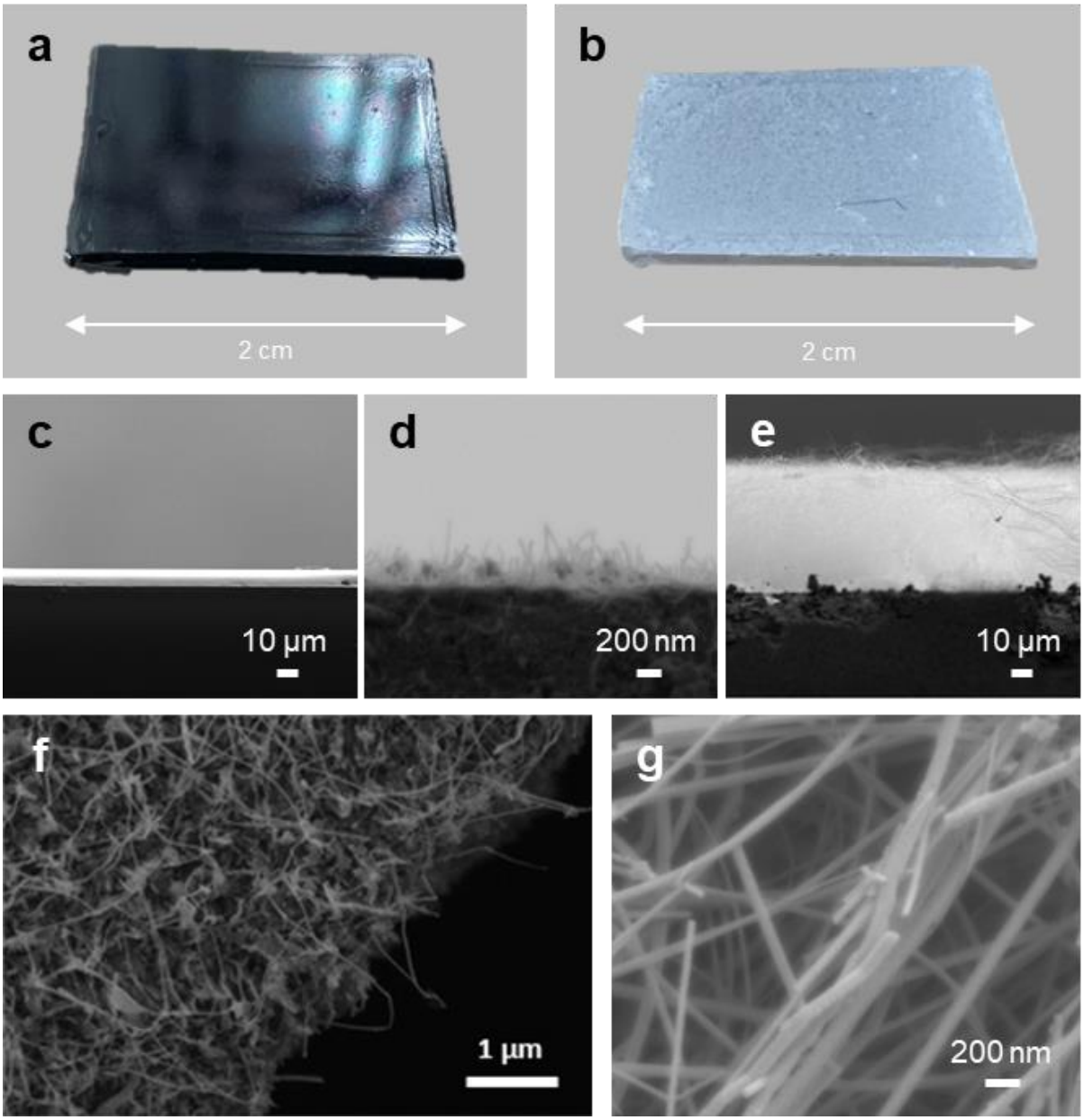

Figure 3.19: The preparation and characterisation of the BN thin film formed from spin coating PMeAB solutions. The actual photo of the Si substrate (a) before and (b) after growth. Cross-sectional SEM images of the thin film on Si substrate (c) before and after growth at (d) 1250 °C and (e) 1400 °C. SEM image of the edge of Si substrate after growth. (g) High-magnification SEM image of the as-grown BNNT/BNNF.

It is important to note that PMeAB, the precursor used in this work, is soluble in common solvents. The solution form of PMeAB enables not only drop-casting into 3D bulk forms, as

demonstrated earlier in this chapter, but also other polymer solution-based processing such as spin-coating onto silicon substrates, which will be presented in this section.

PMeAB can be dissolved in solvents such as THF, DMF, and DMSO at concentrations between 10–20 wt%, forming true solutions rather than particle suspensions, suitable for spin-coating. Outside this concentration window, the solutions are either too dilute or too viscous, resulting in non-uniform or incomplete film coverage on Si substrates. As shown in **Figure 3.19a**, a homogeneous and transparent PMeAB thin film was successfully spin-coated onto a Si substrate. The corresponding cross-sectional SEM image (**Figure 3.19c**) reveals a uniform film thickness of approximately 10 µm. To grow a BNNT-based thin film, the spin-coated Si substrate was subjected to thermolysis at 1400 °C in a horizontal furnace under an NH_3 atmosphere, using the same conditions as in p-BN synthesis. A partially covered combustion boat was employed to trap and accumulate vapor-phase intermediates, promoting BNNT nucleation, similar to mechanisms proposed in thermal CVD processes for BNNT growth.[243] As shown in **Figure 3.19b**, the resulting BNNT/BNNF nanostructures grew directly from the Si substrate surface, forming a non-aligned but adherent BN thin film. The cross-sectional SEM image (**Figure 3.19e**) shows vertically oriented, though non-aligned, nanostructures exceeding 50 µm in length. Additional SEM analysis following thermolysis at 1250 °C (**Figure 3.19d**) reveals early-stage vertical growth of ~300 nm-long 1D BN structures emerging from the Si substrate, supporting the hypothesis that the PMeAB layer acts as a seed layer. **Figure 3.19f** shows the edge of the Si substrate, where BNNT/BNNF growth ceases sharply, again confirming that the film is localised to the PMeAB-coated area. Higher-magnification SEM (**Figure 3.19g**) clearly displays the 1D morphology of the nanostructures, resembling the hybrid BNNT/BNNF forms previously discussed in the case of p-BN (**Figure 3.10**).

The crystallinity of the as-grown BNNT/BNNF film was assessed via Raman spectroscopy and FT-IR (**Figure 3.20**). In Raman, sharp and intense E_{2g} vibrational modes indicate a well-

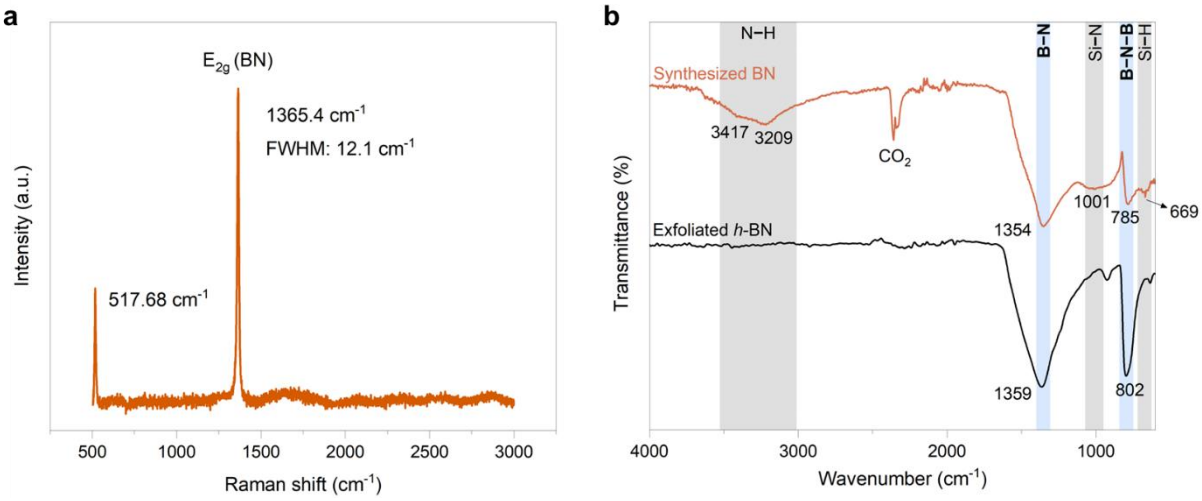

Figure 3.20: (a) Raman spectrum and (b) FT-IR spectrum of as-grown BN thin film on Si substrate.

ordered lattice, whereas peak broadening suggests disorder. Similarly, FT-IR reveals crystallinity through the sharpness and symmetry of B–N stretching bands, with broader features signifying reduced structural order. Raman analysis shows a characteristic h-BN E_{2g} peak at 1365.4 cm^{-1} with a FWHM of 12.1 cm^{-1} (**Figure 3.20a**), closely matching the signal from exfoliated BNNS (**Figure 3.11c**). A prominent peak at 517.68 cm^{-1} is also observed, corresponding to the Si substrate. For reference, the first-order Raman mode of crystalline Si appears at approximately 520.2 ± 0.5 cm^{-1},[244] which is commonly used as a reference and calibration standard in Raman spectroscopy. FT-IR spectra further confirm the presence of BN bonding, showing the in-plane B–N stretching vibration at ~1354 cm^{-1} and the out-of-plane B–N–B bending vibration at ~785 cm^{-1} (**Figure 3.20b**). All additional peaks observed in the FT-IR spectrum of the BN thin film, when compared to exfoliated h-BN, can be attributed to silicon-related bonding. This is consistent with the findings of Dillon *et al.*[245] in their study on ammonia decomposition on silicon surfaces. The peak at 669 cm^{-1} can be assigned to Si–H deformation modes (reported at ~620 cm^{-1} in the reference). The broad feature around 1001 cm^{-1} may result from overlapping contributions of Si_3N stretching vibrations (symmetric at 1088 cm^{-1} and asymmetric at 930 cm^{-1}), SiH_2 scissoring (~910 cm^{-1}), Si–NH_2 stretching (~827 cm^{-1}), and Si_2N–H deformation (~1102 cm^{-1}). The peaks at 3209 cm^{-1} and 3417 cm^{-1} can

be assigned to symmetric and asymmetric stretching modes of Si–NH_2, which have been reported at 3388 and 3465 cm^{-1}, respectively. These observations suggest that the high-temperature NH_3 treatment not only converts the PMeAB thin film into a BN thin film but also significantly nitridises the underlying silicon substrate.

These results are comparable to those obtained using the "B-ink" method for BNNT film fabrication, as reported by Li *et al.*[246] In that approach, a mixture of ball-milled boron powder and metal nitrate catalysts in ethanol is painted onto a Si substrate and annealed in a NH_3 atmosphere at 950–1300 °C to form BNNT films. The resulting films exhibit strong substrate adhesion, with a reported shear failure stress of approximately 4.67 kPa, as measured by DMA adhesion testing, and their high surface roughness leads to super-hydrophobicity (contact angle >170°), making them attractive for applications such as self-cleaning optical coatings.[53] The PMeAB-derived BNNT/BNNF thin films exhibit comparable morphology and hydrophobic functionality (**Figure 3.21**), following similar growth mechanisms. During thermolysis, PMeAB converts into a B-rich intermediate similar to the B-rich matrix in B-ink systems. Both methods rely on NH_3 as a nitrogen source and produce vertically oriented 1D BN nanostructures directly from the substrate. However, unlike the B-ink method, which requires pre-processing such as ball milling and catalyst addition, the PMeAB-route is more straightforward.

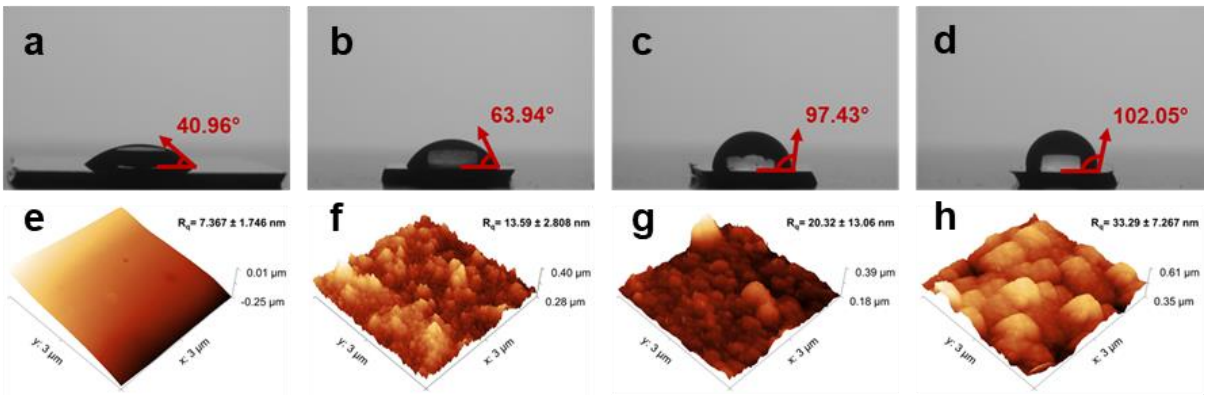

Figure 3.21: Photographs showing the water contact angle on BN thin films synthesised at (a) 1100 °C, (b) 1200 °C, (c) 1300 °C, and (d) 1400 °C. AFM topography images of BN thin films synthesised at (e) 1100 °C, (f) 1200 °C, (g) 1300 °C, and (h) 1400 °C.

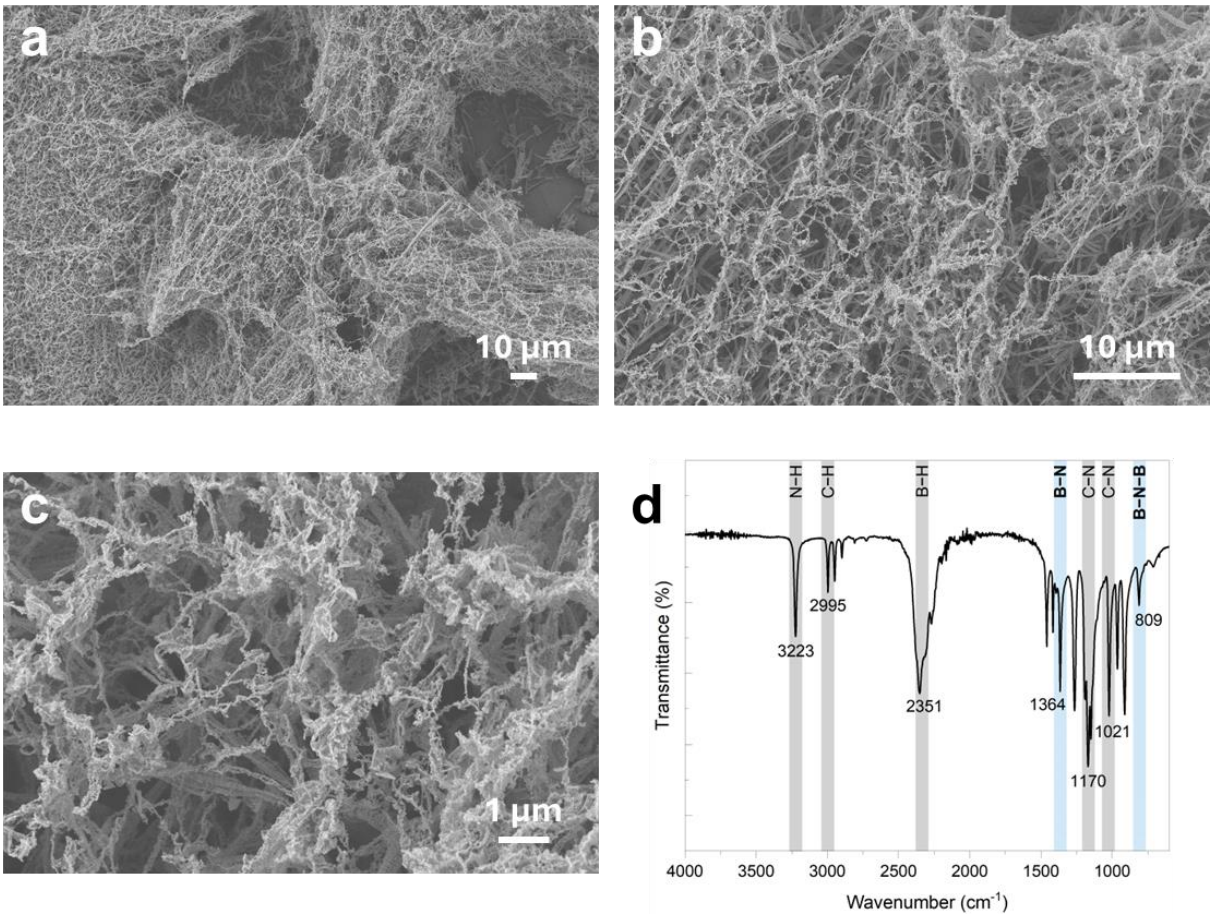

Figure 3.22: Structural and compositional characterisations of as-received MeCTB precursor. (a-c) SEM images. (d) FT-IR spectrum.

3.3.5 N,N,N-Trimethylcyclotriborazane-Derived BN Nanostructures

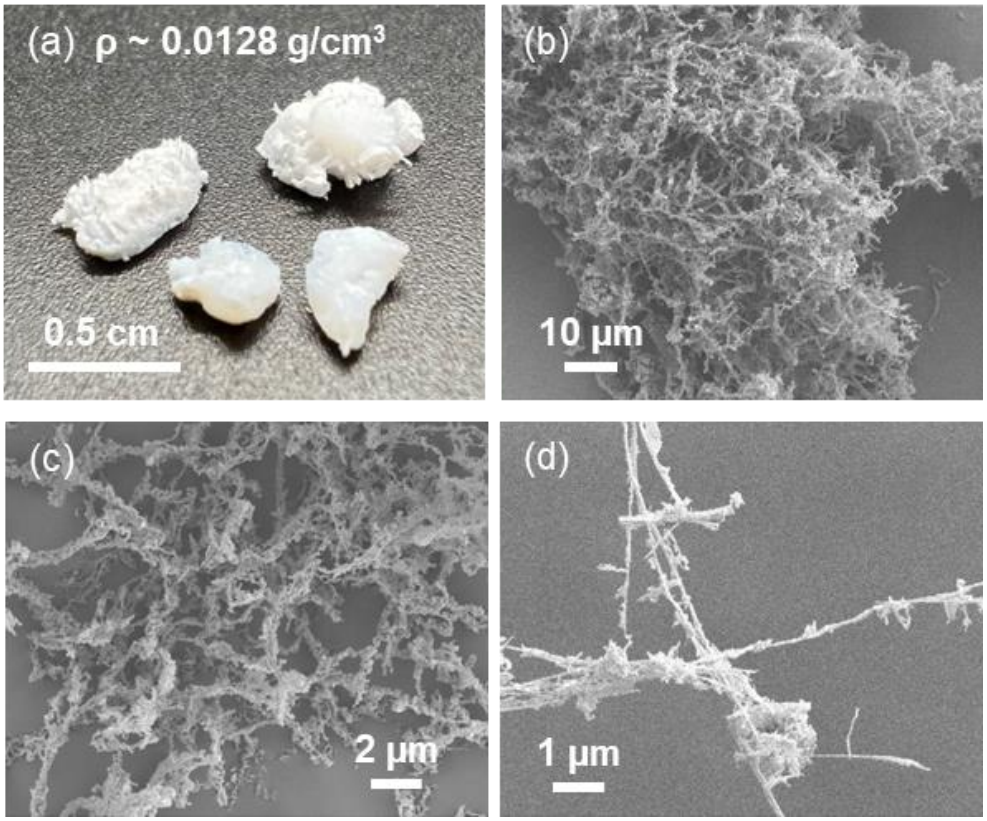

Figure 3.23: (a) Actual photo of MeCTB-derived p-BN. (b-d) SEM images of MeCTB-derived p-BN.

The chemical recycling of carbon-based polymer, particularly their depolymerisation into valuable molecules, is a key strategy in advancing closed-loop circular polymer economies.[247] Similarly, developing efficient approaches to repurpose B–N-containing polymers, such as PMeAB, presents a promising and underexplored opportunity. Recently, Weller's group reported that PMeAB can be selectively depolymerized to yield a single isomer of the cyclic compound *N,N,N*-trimethylcyclotriborazane, $[(H_2BNMeH])_3$, denoted as MeCTB].[207] Following sublimation, MeCTB forms a foam-like porous structure, as shown in Figure **3.22a–c**. The FT-IR spectrum of MeCTB (**Figure 3.22d**) shows distinct characteristic peaks corresponding to the vibrational modes of B–N–B (809 cm^{-1}), C–N (1120, 1171 cm^{-1}), B–N (1364 cm^{-1}), B–H (2351 cm^{-1}), C–H (2995 cm^{-1}), and N–H (3223 cm^{-1}).[230,248,249] Notably, there

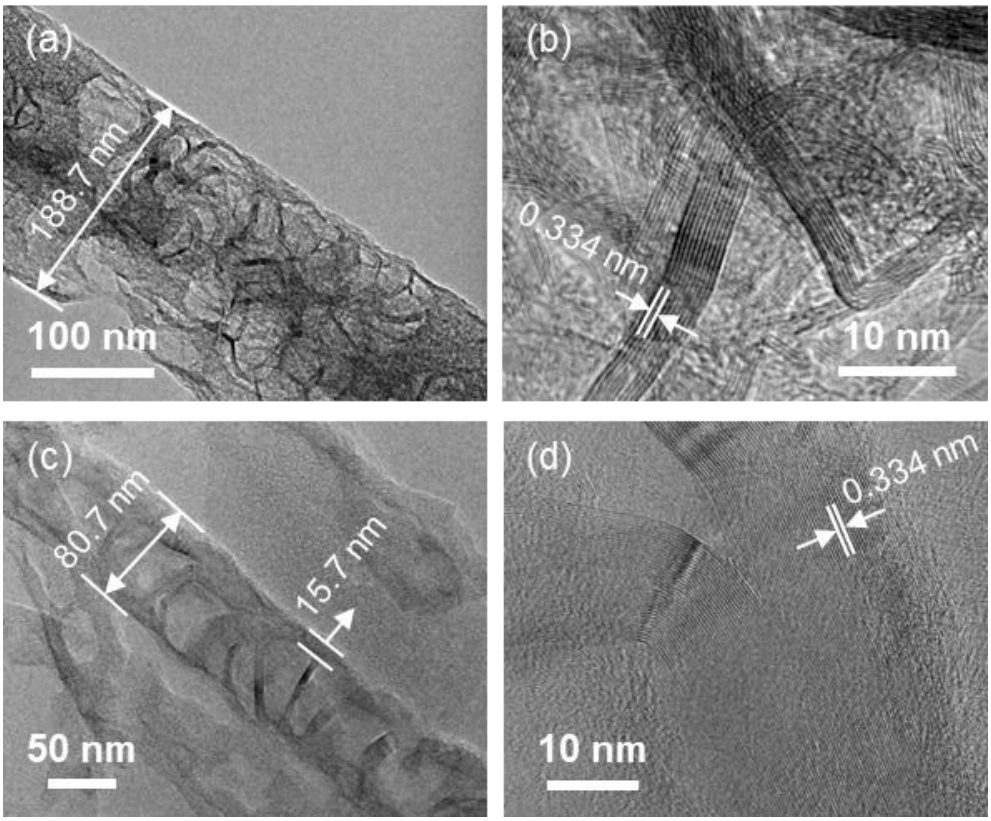

Figure 3.24: TEM images of (a, b) a porous BNNF and (c, d) a bamboo-like BNNT.

are no signals corresponding to B–C bonds (typically observed around 661 or 1080 cm^{-1}) or C–C bonds (around 1580 cm^{-1}), supporting the molecular structural consistency and purity of the MeCTB product.[230]

While the formation mechanism of the porous MeCTB morphology after sublimation remains unclear, the focus of this section is to explore its potential as a precursor for p-BN materials. Owing to its intrinsic B–N ring structure and high B–N–H content, MeCTB offers a promising route for the synthesis of p-BN.[69] For the first time, 3D monolith p-BN has been successfully synthesised from MeCTB via thermolysis under an NH_3 atmosphere (**Figure 3.23**). As shown in **Figure 3.23a**, the resulting material appears as a lightweight, white, 3D bulk solid with a density ρ~0.0128 $g{\cdot}cm^{-3}$, approaching that of air. This combined features is characteristic of what is commonly referred to as a "BN aerogel".[250] **Figures 3.23b–d** show representative SEM images of the internal structure of MeCTB-derived BN aerogel, revealing

a network of densely packed, randomly entangled 1D nanostructures. TEM images further confirm that these 1D nanostructures are either porous BNNF (p-BNNF) (**Figure 3.24a, b**) or bamboo-like BNNT (b-BNNT) (**Figure 3.24c, d**). Both exhibit porous structures that contribute additional nanoscale porosity to the already p-BN aerogel framework. These 1D structures serve as structural skeletons, interweaving to form an open-cell, isotropic network.

The first type, p-BNNF, exhibits relatively disordered structures compared to b-BNNT, and diameters in the range of 150–200 nm, smaller than those typically reported for p-BNF based BN aerogels synthesized via freeze-drying of melamine diborate, which range from ~500 nm to 1 μm.[185,191] The p-BNNF extends several hundred micrometres in length, resulting in ultrahigh aspect ratios (**Figure 3.23**). A representative TEM image (**Figure 3.24a**) shows an individual p-BNNF with a uniform diameter ~188.7 nm. Numerous bubble-like holes are

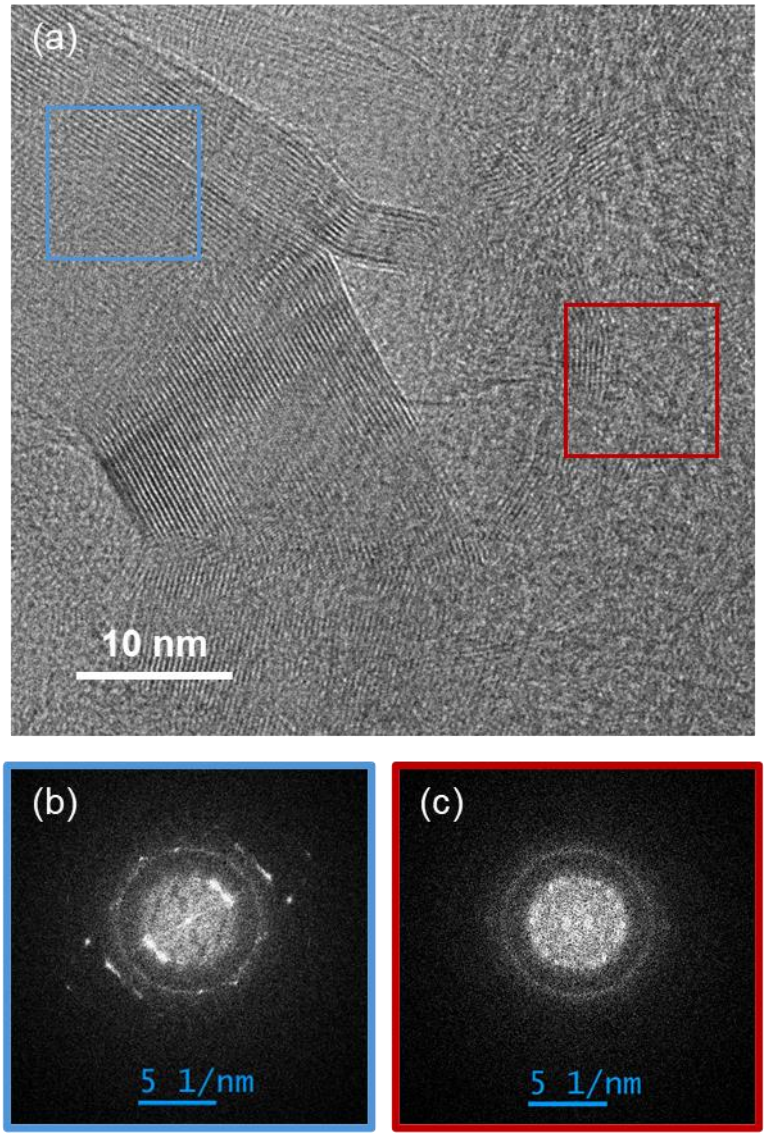

Figure 3.25: TEM characterisation of b-BNNT in synthesized BN aerogel. (a) High-resolution TEM images, showing the intersection of a kink and a wall. (b) Corresponding FFT pattern of the internal kink. (c) Corresponding FFT pattern of the outer wall.

distributed along the fibre body. High-resolution TEM (**Figure 3.24b**) reveals that the walls of these holes are composed of few-layer h-BN with high crystallinity. These few-layered h-BN domains appear randomly distributed and intricately interwoven. The d-spacing of 0.334 nm, corresponding to the (002) planes of h-BN.[251] This porous morphology is attributed to a "chemical blowing" mechanism, as discussed previously in **Section 3.3.2** and illustrated in

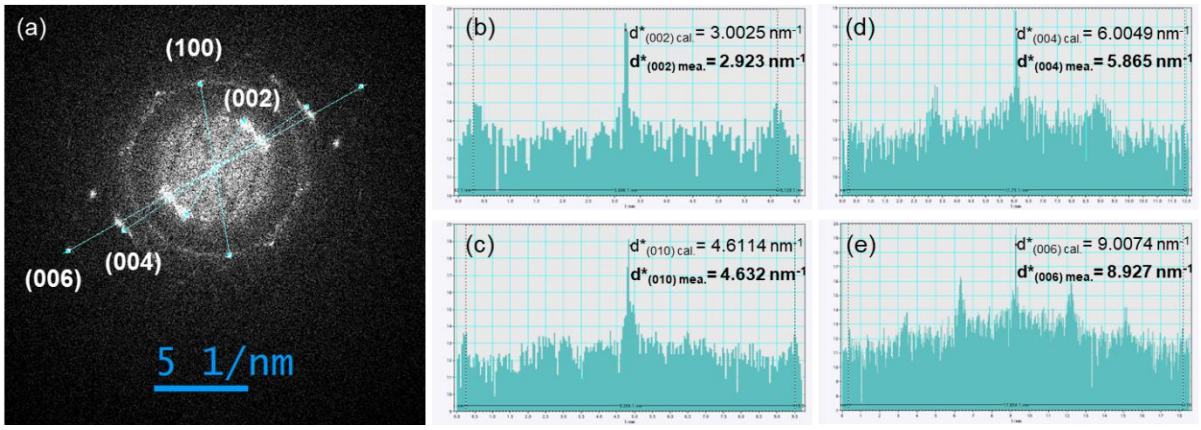

Figure 3.26: (a) FFT pattern of the internal kink. (b-e) Line profiles of FFT, showing d* of 2.923 nm^{-1} for (002) planes, 4.632 nm^{-1} for (100) planes, 5.865 nm^{-1} for (004) planes, and 8.927 nm^{-1} for (006) planes.

Figure 3.12. Notably, the thermolysis of MeCTB under the same conditions as PMeAB also generates sufficient gaseous byproducts to induce a similar foaming effect.

A more crystalline structure, b-BNNT, is also observed in the MeCTB-derived BN aerogel, as shown in **Figures 3.24c, d**. These b-BNNT exhibit diameters below 100 nm and wall thicknesses around 15 nm. The higher degree of structural order in b-BNNT suggests a different growth pathway compared to the less crystalline, chemically blown p-BNNF. Various synthesis methods have been developed to produce b-BNNT, including thermal reactions,[252] ball milling-annealing,[253] and CVD,[254,255] relying on either high-temperature processes or a vapor–liquid–solid (VLS) mechanism. However, the growth mechanism of b-BNNT remains less well understood compared to that of conventional cylindrical BNNT. Previous studies suggest that the growth of b-BNNT is influenced by both catalyst presence and precursor composition.[253,254] For instance, Ma *et al.*[254] synthesized cylindrical BNNT and b-BNNT using ammonia thermolysis of different BN-containing precursors. They found that using $B_4N_3O_2H$ led to the formation of pure cylindrical BNNT, while using commercial BN precursors resulted in the appearance of b-BNNT. They attributed this to the reduced oxygen content in the BN precursor, which limits the supply of boron oxide vapour necessary for continuous tube elongation via nitridation. Such reduction leads to localised growth instability, preventing the

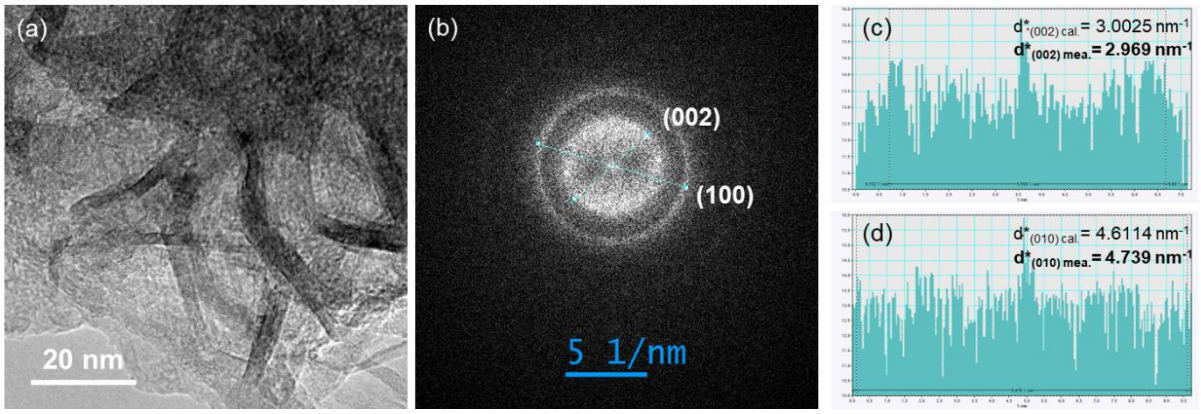

Figure 3.27: (a) High-resolution TEM images, showing few-layer BN randomly distributed across p-BNNF and (b) corresponding FFT pattern. (c-d) Line profiles of FFT, showing d* of 2.969 nm^{-1} for (002) planes and 4.739 nm^{-1} for (100) planes.

formation of long cylindrical tubes and instead favouring the formation of hemispherical caps within the nanotube and sealing the existing tube internally as a way to minimize surface energy. In the present study, MeCTB containing B–C–N was utilised. During thermolysis, the absence of oxygen prevents the formation of boron oxide vapour, inhibiting continuous cylindrical growth and instead promoting localised growth instabilities that eventually lead to bamboo-like segmentation.

Figures 3.25 and **3.26** present detailed TEM and FFT analyses of b-BNNT to assess their crystallinity. As shown in **Figure 3.25a**, the hemispherical caps across the tube, hereafter referred to as 'kinks', exhibit high crystallinity, highlighted in the blue circle. Corresponding FFT patterns (**Figure 3.25b** and **3.26**) display intense diffraction spots, clearly indexed to the h-BN planes (002), (010), (004), and (006).[211] The presence of higher-order reflections such as (004) and (006) further confirms the high degree of crystallinity in the kinks regions. In contrast, the red-circled area in **Figure 3.25**, representing the outer wall of the b-BNNT, shows comparatively lower crystallinity. This is evident from the less intense spots in the FFT (**Figure 3.25c**), indicating a less ordered structure. Both the kinks and wall regions of the b-BNNT demonstrate higher crystallinity than the p-BNNF, as illustrated in **Figure 3.27**. The FFT of

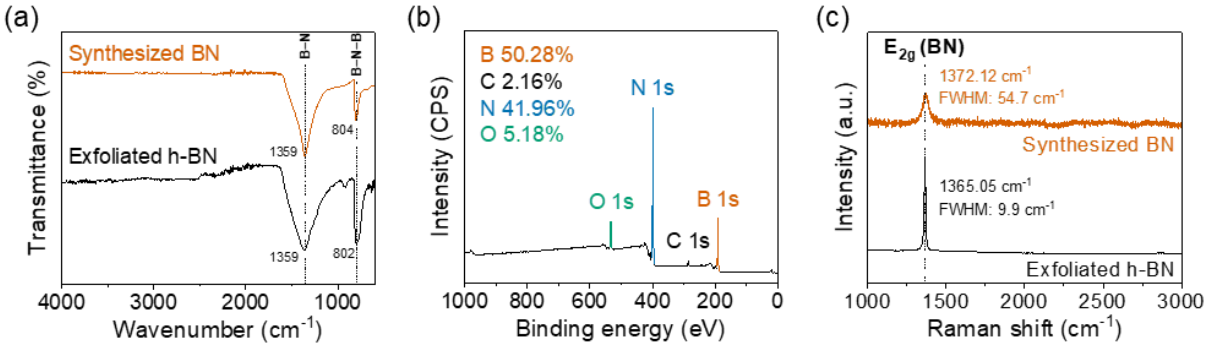

Figure 3.28: (a) FT-IR spectra of synthesized BN aerogel (orange) and exfoliated h-BN (black). (b) XPS survey spectrum of synthesized BN aerogel, inset shows calculated element contents. (c) Raman spectra of synthesized BN aerogel (orange) and exfoliated h-BN (black).

the p-BNNF (**Figure 3.27b**) still shows diffraction spots, but with much lower intensity compared to those in **Figures 3.25b** and **3.25c**, confirming that p-BNNF are less structurally ordered than b-BNNT.

The purity and crystallinity of the MeCTB-derived BN aerogel were further examined using FT-IR, XPS, and Raman spectroscopy. As shown in **Figure 3.28a**, the FT-IR spectrum of the BN aerogel displays characteristic absorption bands at 1359 cm^{-1} and 804 cm^{-1}, corresponding to the B–N stretching and B–N–B bending modes, respectively, closely matching those observed in exfoliated h-BN. Notably, no additional peaks associated with carbon-containing species were detected, suggesting a high level of purity. XPS analysis further confirms the purity of the BN aerogel (**Figure 3.28b**). The carbon content was measured at only 2.16%, indicating that the NH_3 thermolysis process effectively removed the methyl groups from MeCTB while converting it into h-BN. The overall reaction mechanism between MeCTB and NH_3 will be further explored through simulations in **Chapter 4**. Raman spectroscopy corroborates the presence of h-BN, revealing a characteristic E_{2g} peak at 1372.12 cm^{-1}, which is also close to that of exfoliated h-BN (1365.05 cm^{-1}) (**Figure 3.28c**). However, the observed Raman peak is significantly broader, with a FWHM of 54.7 cm^{-1}, indicating reduced crystallinity. This broadening suggests the presence of structural disorder, likely due to a high proportion of p-BNNF. TEM and FFT analyses confirm that b-BNNT also contain

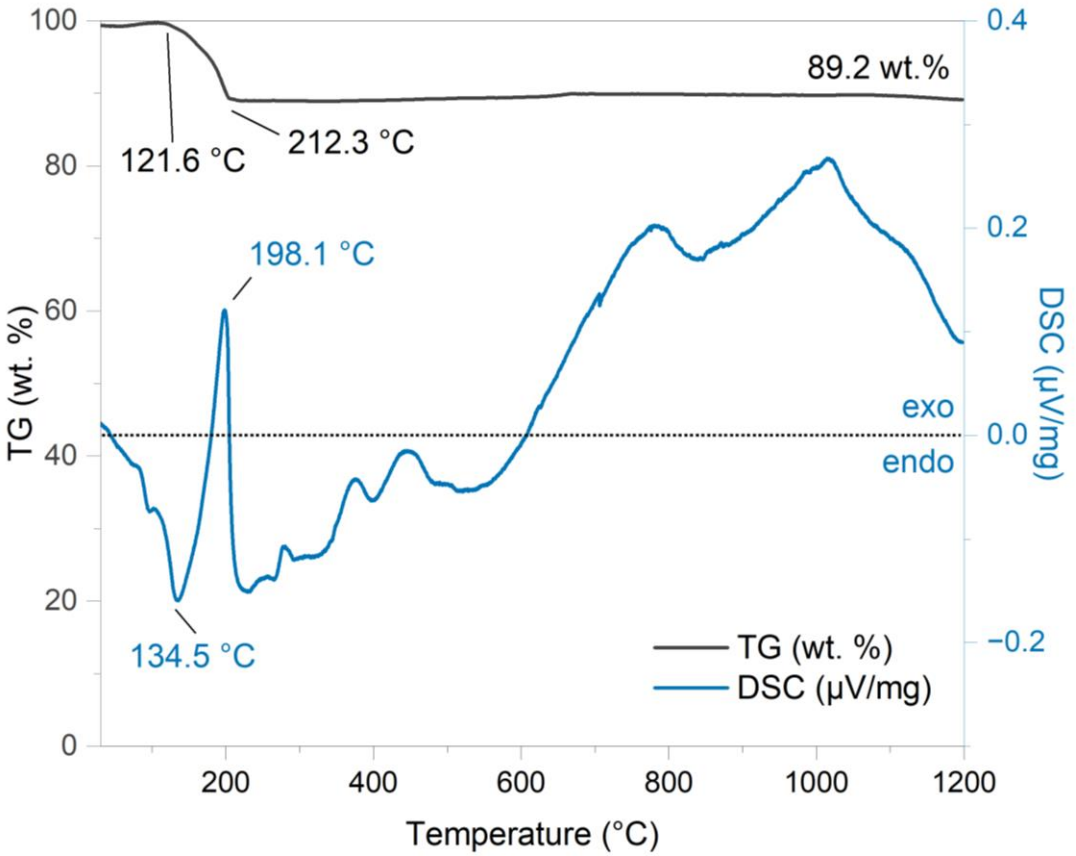

Figure 3.29: TGA (black) and DSC (blue) profiles of MeCTB during heating from room temperature to 1200 °C under an argon atmosphere.

slightly disordered wall regions, and p-BNNF are inherently less ordered. In addition, the porous nature of these nanostructures contribute to the overall reduction in crystallinity.[182] Taken together, the FT-IR, XPS, and Raman results demonstrate that MeCTB, through NH_3 thermolysis, is effectively converted into BN with high purity comparable to that of BN derived from PMeAB, although it exhibits lower crystallinity and a slightly higher oxygen content (5.18% versus 2.39% for PMeAB-derived p-BN).

TGA-DSC was conducted to investigate the formation of the porous structure during thermolysis of MeCTB (**Figure 3.29**). The thermal decomposition of MeCTB begins at approximately 121.6 °C and continues until around 212.3 °C, resulting in a high ceramic yield of 89.2%. The DSC curve reveals an initial endothermic event, attributed to the melting behaviour of MeCTB, followed by a major exothermic peak associated with thermal

decomposition, during which multiple volatile species are simultaneously released. The TGA and DSC profiles exhibit a pattern similar to that observed for PMeAB (**Figure 3.13**). However, a key difference lies in the final ceramic yield after thermolysis at 1200 °C: MeCTB-derived BN retains a significantly higher yield (~89.2%) compared to PMeAB-derived BN (< 20%). This difference is attributed to the intrinsic molecular structure of the precursors. MeCTB contains preformed B–N ring structures, which are more thermally stable and structurally favourable for ceramic conversion,[75] whereas PMeAB is constructed of linear B–N backbone chains. As reported in the literature,[75] BZ and PBZ, B–N ring-structured precursors, can yield up to ~90% BN upon thermolysis, owing to its stable ring configuration that promotes the formation of an h-BN ceramic network. The presence of B–N rings in MeCTB likely facilitates a similar transition, stabilizing the intermediate structure and suppressing excessive reactions and the release of volatile species during thermolysis.

Compared to perfectly ordered cylindrical BNNT, b-BNNT generally possess more structural defects and active surface sites, such as dangling bonds, which make them promising candidates for further functionalisation. Their segmented structure and thinner walls may offer improved hydrogen uptake at elevated pressures,[256] along with enhanced elastic and mechanical properties.[257] These characteristics are relevant for potential applications in electron emission devices and high-performance composite materials. Although the focus of this section is not on applications, the successful synthesis of b-BNNT via the MeCTB route developed in this thesis highlights the potential of MeCTB as a viable precursor for producing b-BNNT based 3D BN aerogel.

3.3.6 Porosity Measurements of Porous BN

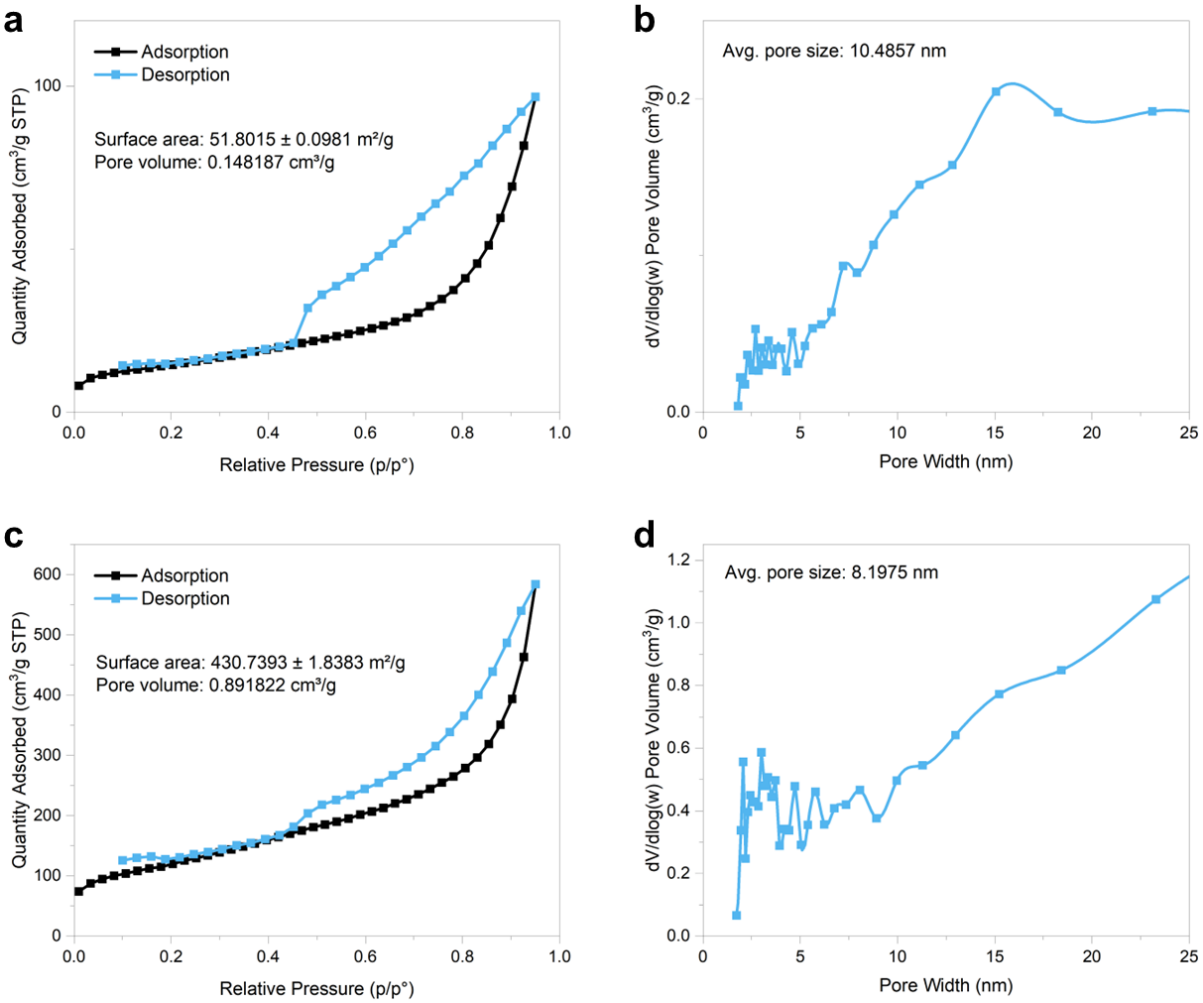

Figure 3.30: N_2 isotherm linear plot of (a) precursor PMeAB and (c) p-BN derived from PMeAB. Pore size distribution of (b) precursor PMeAB and (d) p-BN derived from PMeAB.

The porosity of p-BN synthesized from PMeAB and MeCTB was analysed using Brunauer–Emmett–Teller (BET) N_2 sorption measurements. **Figure 3.30a** shows the N_2 adsorption–desorption isotherms of drop-cast PMeAB, which already exhibit signs of porosity, likely due to the minor release of gases during the drying process of the precursor solution (**Figure 3.12a**). In contrast, **Figure 3.30c** presents the isotherms of p-BN derived from PMeAB, revealing a substantial increase in nitrogen uptake, indicating the successful development of a porous structure upon thermolysis. The calculated specific surface area (SSA) is approximately 431

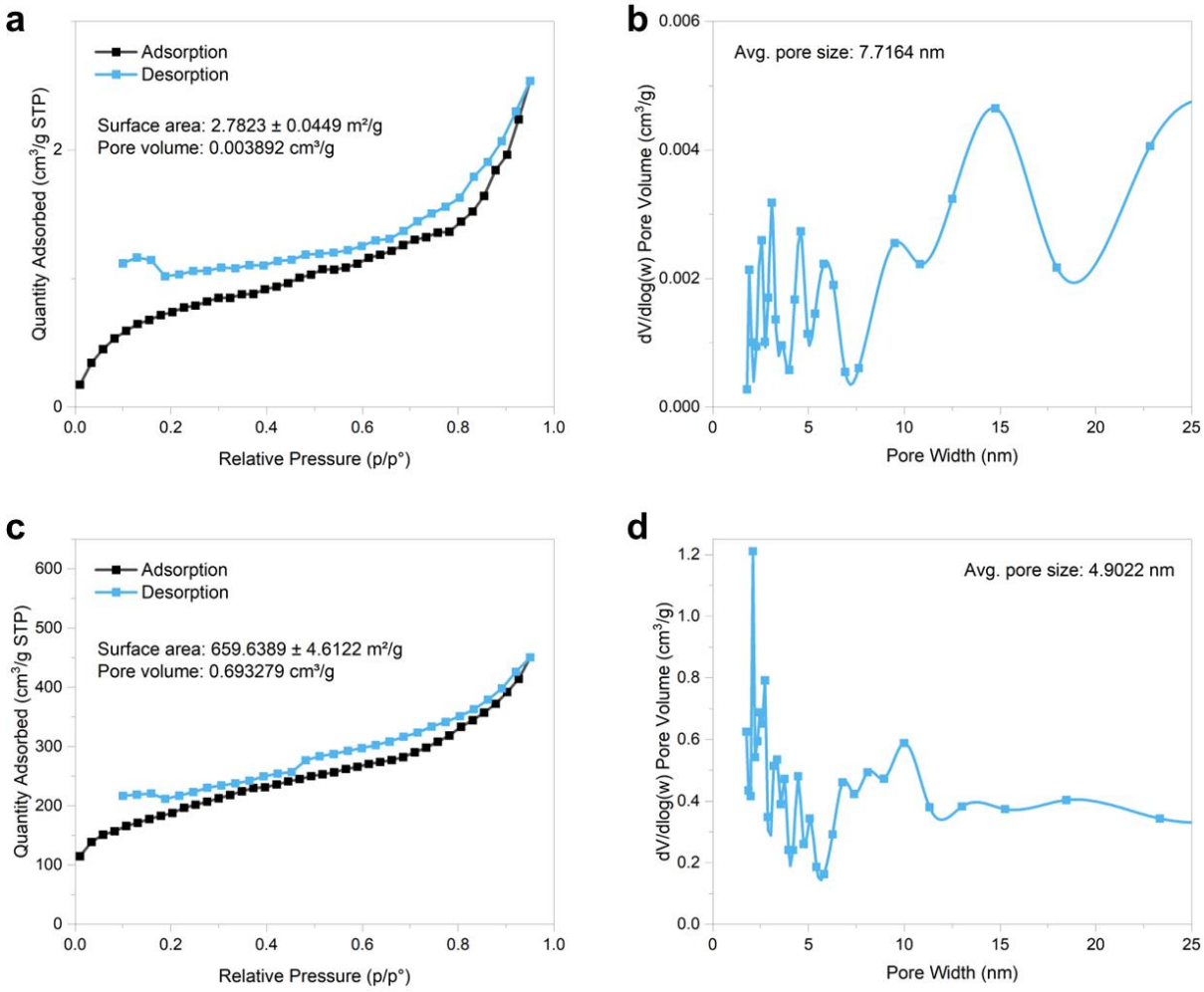

Figure 3.31: N_2 isotherm linear plot of (a) precursor MeCTB and (c) p-BN derived from MeCTB. Pore size distribution of (b) precursor MeCTB and (d) p-BN derived from MeCTB.

$m^2 \cdot g^{-1}$, with a corresponding pore volume (PV) of about 0.892 $cm^3 \cdot g^{-1}$. **Figure 3.31a** shows the isotherms for sublimed MeCTB, which display minimal N_2 adsorption quantity, suggesting a non-porous or very weakly porous structure in the precursor. After thermolysis, the p-BN derived from MeCTB (**Figure 3.31c**) demonstrates a significant enhancement in N_2 adsorption compared to its precursor, confirming the formation of a porous network. The calculated SSA is approximately 660 $m^2 \cdot g^{-1}$, with a corresponding PV of about 0.693 $cm^3 \cdot g^{-1}$.

According to IUPAC classification,[258] the isotherms of both PMeAB- and MeCTB-derived p-BN can be described as a hybrid between Type II and Type IV, accompanied by H3-type hysteresis loops, typical of microporous/mesoporous materials. The similar shape of the

isotherms for both samples indicates that they share comparable pore structures. The non-overlapping adsorption and desorption branches point to capillary condensation and a distribution of pore sizes. At low relative pressures ($P/P_0 < 0.1$), a sharp increase in adsorption indicates the presence of micropores (< 2 nm). A gradual rise at intermediate pressures ($0.1 < P/P_0 < 0.7$) suggests multilayer adsorption within mesopores (2–50 nm), while a steep increase at high pressures ($P/P_0 > 0.8$) reflects capillary condensation within macropores (> 50 nm). The hysteresis loops are characteristic of ink-bottle-shaped pores and confirm mesoporosity.[259] The irreversible and nearly parallel nature of the adsorption and desorption branches over the full pressure range implies the presence of cylindrical pores open at both ends and slit-like pores open on four sides. Notably, the hysteresis loop does not close at low P/P_0, indicating significant residual adsorption capacity and the presence of well-developed micropores that are not easily desorbed. The pore size distribution (**Figure 3.31d**) reveals a dominant pore size around 2 nm for MeCTB-derived p-BN, falling within the micropore range, while **Figure 3.30d** shows a dominant pore size greater than 25 nm for PMeAB-derived p-BN, indicating the presence of larger mesopores. This distinction is consistent with the observed differences in morphology.

The differences in pore size distribution can also be correlated with the TEM images. PMeAB-derived p-BN primarily contains larger pores, which result from a chemical blowing mechanism that forms wide gaps between BNNS (**Figure 3.6b**). In contrast, MeCTB-derived p-BN exhibits smaller, more uniform pores primarily originating from micropores within the p-BNNF and b-BNNT (**Figure 3.24**).

3.4 Summary

In summary, two types of 3D p-BN monoliths, namely BNNS/BNNT/BNNF hierarchical frameworks and BNNT/BNNF hybrid networks, have been successfully synthesized through a thermal treatment process under an NH_3 atmosphere, without the use of any catalysts or ex situ templates. The choice of precursors, PMeAB and MeCTB, plays a crucial role in determining the resulting structures and properties of the p-BN materials. Thermal decomposition of PMeAB yields a BNNS/BNNT/BNNF composite with an SSA~431 $m^2 \cdot g^{-1}$ and PV~ 0.892 $cm^3 \cdot g^{-1}$, while MeCTB leads to a BNNT/BNNF network with an SSA~660 $m^2 \cdot g^{-1}$ and PV~ 0.693 $cm^3 \cdot g^{-1}$. Compared to other reported synthesis routes, the methods presented here involve fewer steps, utilise readily available precursors, and achieve comparable porosity.

A notable feature of the PMeAB route is its ability to control over structure, composition, and surface texture and potentially tunable porosity through a chemical blowing effect upon heating, similar to that proposed for AB. This process, for the first time, results in the formation of BNNF with filament-like morphology. This unique structure is hypothesized to arise from the excessive H_2 generated during thermal dehydrogenation of PMeAB, which stabilises the thermodynamically unfavourable filamentous BNNF structure while suppressing the formation of conventional cylindrical BNNT. In the MeCTB route, a key outcome is the formation of b-BNNT and p-BNNF, which contribute significant microporosity to the resulting p-BN material. The thermal decomposition of MeCTB proceeds more moderately than that of PMeAB, leading to an exceptionally high ceramic yield (~89%), a critical factor for the performance and integrity of the final BN product. Unlike many p-BN materials reported in the literature, which typically consist of amorphous or turbotratic BN phases, the p-BN synthesized in this work exhibit hexagonal BN phase. This crystalline component is essential for applications that

exploit the unique thermal, chemical, and electronic properties of h-BN rather than those of its disordered forms.

These 3D p-BN monoliths, mainly comprising interconnected networks of 1D BN nanostructures, exhibit high purity, phase crystallinity, large SSA, and structural integrity. Their open-cell architecture and lightweight nature may enable extremely low thermal conductivity and contribute to outstanding absorption capacities for a wide range of organic solvents and oils, with high recovery efficiency. Overall, the p-BN developed hold significant promise for a broad range of applications, including space and aerospace components, thermal management composites, wastewater treatment, air purification, catalyst supports, energy storage, and advanced building materials.

Chapter 4

Mechanistic Insights into the Thermal Decomposition Pathways of Polyaminoborane

Contents

4.1 Introduction

When developing a new synthesis methodology, it is critical to understand the reaction mechanisms of the conversion process from precursors to the final product. This is especially true in the case of PDC routes, where the structural and chemical differences between the preceramic polymer and the resulting ceramic material are significant. As such, the conversion process inherently involves a complex network of chemical reactions. The molecular structure and chemical composition of the precursor not only influence the final elemental makeup but also affect the number and distribution of phases, the microstructure, and ultimately, the macroscopic properties of the ceramic material.

The present study focuses on the PDC route from polymer precursor PMeAB and its chemically repurposed cyclic derivative, MeCTB, to ceramic h-BN nanomaterials. Based on the data presented in the previous experimental chapters, I have gained preliminary insights into the key reactions occurring during the thermolysis of PMeAB. TGA-MS (**Figure 3.13 and 3.14**) revealed the release of large amounts of H_2 and small molecular species, indicating the occurrence of dissociation, dehydrogenation, and cyclisation reactions. ^{11}B NMR spectroscopy (**Figure 2.16**) suggested the presence of a stabilised, cross-linked structure, consistent with cyclisation reactions of the linear PMeAB backbone. XPS (**Figure 2.18 and 2.20**) demonstrated a gradual reduction in carbon content, which in this case, the removal of methyl groups from PMeAB during NH_3 thermolysis. However, due to the complexity of the overall conversion process which involves the simultaneous occurrence of above-mentioned reactions with multiple bond-breaking and bond-forming steps, the formation of intermediate species, and phase evolution, experimental techniques alone are insufficient to fully resolve the underlying mechanistic pathways. Limitations in both spatial and temporal resolution hinder the direct observation of critical molecular-scale transformations.

In this respect, computational tools could be very useful in providing direct evidence of chemical reactions occurring at an atomistic scale. Among wide variety of simulation approaches, QM DFT method can offer precise energy and molecule information of the reaction pathway; however, the high computational cost of DFT calculations limits the size of the modelling system (normally limited to <10 picoseconds and <100 atoms).[260] Approximation method based on ReaxFF is, therefore, more useful for simulating large-scale models such as PDC systems, as they enable computationally feasible simulations with reasonable accuracy.

Although experimental and theoretical studies on the thermolysis of MeAB, PMeAB, and MeCTB, as well as their potential for h-BN formation, remain limited in the literature, both DFT and ReaxFF simulations have provided valuable insights into the formation mechanisms of h-BN nanostructures during the thermolysis of their close relative, AB, and derivatives of AB (**Figure 1.3**). Most computational studies based on DFT have focused on elucidating the dehydrogenation mechanisms of AB.[96] Due to its six hydrogen atoms and the low atomic weights of boron and nitrogen, AB possesses a high gravimetric hydrogen content (19.6 wt.% H), making it promising for chemical hydrogen storage materials.[261] However, the thermal decomposition of AB has proven to be more complex than the originally proposed combination of two thermodynamically favoured pathways, namely the AB-to-BZ-to-PBZ-to-BN pathway and the AB-to-PAB-to-PIB-to-BN pathway, through experimental studies.[219] The complexity arises from several reasons: (1) In addition to H_2, several volatile byproducts are formed, including NH_3, DB, IB, BZ. (2) Two possible key intermediates, IB and DADB, initiate decomposition. Both are highly reactive and short-lived, and they can yield linear and cyclic intermediates such as $NH_3BH_2NH_2BH_3$, CDB, CTB, and/or BCDB. (3) Continued H_2 release leads to the formation of linear and branched PAB, PIB, and PBZ. (4) The decomposition of AB within microcrystalline grains is likely to proceed unevenly, resulting in a mixture of

partially decomposed species such as dehydrogenated AB, DADB, and various polymeric products.[96,108]

Given the structural similarity between AB and its methylated analogues, a comparable level of complexity is anticipated in the thermal decomposition of MeAB, PMeAB, and MeCTB. This is supported by the experimental results in **Chapter 2** and **3**, which indicate even greater complexity due to the presence of carbon from methyl groups and the added reaction with reactive NH_3. However, prior DFT studies on AB establish the method's reliability in modelling key reaction steps, including dehydrogenation, dissociation, and cyclisation; thus, transferable to investigating the mechanisms underlying the thermolysis of MeAB, PMeAB, MeCTB and related compounds.

To confirm that the calculated mechanisms are scientifically reliable and feasible, benchmarking against experimental data and established theoretical results is essential. This involves:

- Energy Validation: Comparing calculated activation energies and reaction enthalpies with experimental calorimetric or kinetic data.
- Structural Consistency: Verifying predicted intermediate structures and bond lengths against spectroscopic evidence (e.g., NMR, XPS, IR).
- Cross-Method Comparison: Using multiple computational approaches (DFT vs. ReaxFF) to ensure consistency in predicted trends.
- Sensitivity Analysis: Assessing the influence of simulation parameters (e.g., functional choice in DFT, force-field parameters in ReaxFF) on the results.
- Literature Benchmarking: Aligning predicted pathways with previously reported mechanisms for analogous systems (e.g., AB and its derivatives).

By integrating these validation steps, the computational predictions can be considered robust and scientifically credible, thereby complementing experimental observations and providing a comprehensive understanding of the PDC-to-h-BN conversion process.

DFT calculations using the Becke, 3-parameter, Lee–Yang–Parr (B3LYP)[262,263] functional have been benchmarked and are the most widely applied in theoretical studies of H/B/C/N systems. B3LYP is a hybrid functional that combines Hartree–Fock exchange with density functional exchange-correlation terms, offering a good balance between accuracy and computational cost. It is well-suited for H/B/C/N systems because it reliably predicts geometries, vibrational frequencies, and reaction energetics, making it ideal for modelling both covalent and non-covalent interactions in borane–amine compounds. It has been employed to investigate MeAB and related compounds, including dimethylamine–borane and MeAB octamers. However, existing simulations have primarily focused on the initial release of H_2 ($BH_3-NMeH_2 \rightarrow BH_2-NMeH + H_2$) and do not extend to later stages of decomposition, such as bond dissociation leading to reactive intermediates, cyclisation, or the formation of larger molecular species. In addition, no computational studies have yet explored the polymeric forms of MeAB or larger, more complex molecular structures. While some studies have examined cyclic compounds such as $C_2B_2N_2H_{12}$ and C_4BNH_{12}, these systems incorporate carbon into the ring structure, rather than representing pure B–N ring systems. To better understand pathways relevant to h-BN formation, it is important to investigate B–N-based ring structures such as MeBZ and MeCTB, the methyl-substituted derivatives of BZ and CTB, due to their structural similarity to h-BN and their potential to serve as precursors for h-BN synthesis.

Mapping the potential energy surface (PES) based on DFT provides an efficient approach to identifying reaction pathways by evaluating the energy landscape of molecular structures along predefined collective variables. This method enables the estimation of activation energies, even for barrierless reactions that lack a well-defined transition state (TS), via constrained

minimization techniques. In such cases, once a reaction geometry reaches the dividing surface, the system is minimised under constraints that fix the positions of atoms involved in bond-breaking or bond-forming events. This strategy preserves the reaction coordinate while minimising thermal noise and irrelevant structural fluctuations.[264]

The concept of a reaction pathway has become a key aspect in the investigation of PES associated with chemical reactions. In general, the reaction pathway is defined as the trajectory on the PES that connects the reactant and product regions through the TS. This trajectory is typically determined by following the steepest-descent, or minimum energy path (MEP), from the TS toward both the reactants and the products.[265] Constrained minimisation on the PES provides a first approximation of the reaction barrier height (E_a), which is particularly useful in the preliminary screening of reaction mechanisms,[264] allowing for the prioritisation of pathways before applying more computationally expensive QM methods such as TS theory (TST) or high-level ab initio optimisations. Importantly, this barrier estimation approach is robust and less sensitive to the initial guess structure compared to full TS searches, of which successful location of transition states often depends on good initial guesses and can suffer from convergence failures if the input is poor.[266]

PES scanning has been successfully applied to a wide range of chemical systems. For example, studies on borazine (BZ) formation from ammonia borane (AB),[110] furfural ($C_5H_4O_2$),[267] alkyl formate radicals such as ethyl-2-yl formate (CH_2CH_2OCHO),[264] nitramine explosives like cyclotrimethylenetrinitramine (RDX),[268] and complex ionic liquids such as tributyloctylphosphonium bis(oxalato)borate ($[P_{4,4,4,8}][BOB]$)[269] have demonstrated the effectiveness of PES mapping in prescreening potential reaction pathways. These applications demonstrated the use of PES methods for guiding both subsequent high-level computational investigations and experimental design strategies, particularly in complex or poorly understood systems.

More comprehensive studies on AB-related compounds have been conducted using the ReaxFF approach, beginning with the foundational work of Weismiller *et al.*[123] In their study, the thermal dehydrogenation behaviour of AB was investigated using the $ReaxFF_{HBN}$ parameter set, which they developed and benchmarked specifically for simulating hydrogen–boron–nitrogen systems. This specialised parameterisation was derived by fitting ReaxFF's bond-order-based potential to high-level quantum mechanical data for hydrogen–boron–nitrogen species, ensuring accurate representation of bond dissociation, formation, and charge redistribution during reactive processes. The resulting force field captures the complex interplay of covalent and ionic interactions characteristic of H/B/N systems, making it particularly suitable for simulating AB's thermolysis and combustion pathways under realistic conditions. This parameterisation then served as the basis for a range of studies on related compounds, including ammonium octahydrotriborate ($NH_4B_3H_8$),[270] ammonium aminodiboranate ($NB_2H_8{\cdot}NH_4^+$),[271] and diammoniate diborane ($BN_2H_8^+{\cdot}BH_4^-$).[271] In addition, the $ReaxFF_{HBN}$ framework has been utilised to study AB combustion,[123,272] the formation of BNNT via Ni-catalysed CVD of AB,[228] and the development of the $ReaxFF_{CBN}$ parameter set tailored for simulating liquid CBN-based hydrogen storage materials.[273] It has also been instrumental in exploring growth mechanisms of BNNS on catalytic surfaces[274] and in gas-phase systems involving precursors such as B_2H_6/NH_3.[275]

The original $ReaxFF_{HBN}$ parameters were later extended and refined through additional studies (bond-order parameters, valence angle terms, torsional interactions, and the incorporation of improved charge equilibration schemes to better capture polarisation effects in reactive environments). Notably, Kamat *et al.*[124] applied the method to simulate laser-induced incandescence of soot, while Castro-Marcano *et al.*[121] used it to model the combustion of Illinois No. 6 coal char. These extensions resulted in the development of the $ReaxFF_{HCONSB}$ parameter set, which now enables the simulation of more complex H–B–C–N–O–S systems.

Despite extensive prior experimental and theoretical investigations into AB and its derivatives, certain compounds, particularly MeAB, PMeAB, and MeCTB, remain relatively underexplored. Specifically, the detailed reaction pathways, key intermediates, PES, molecular dynamics (MD), and the kinetics underlying the formation of h-BN nanostructures are still not well understood. To address these knowledge gaps, this study employs a combination of DFT and ReaxFF simulations. In this chapter, I first investigate the pyrolytic decomposition pathways of the three precursors—MeAB, PMeAB, and MeCTB—used in the previous experimental chapters. These pathways are examined using PES mapping, with calculations carried out using the B3LYP functional within DFT. Next, the $ReaxFF_{HCONSB}$ parameter set was validated against the DFT-derived QM data, with particular emphasis on capturing the kinetics of H_2 evolution. Using this validated force field, I conducted both single- and multi-molecule MD simulations of the thermolysis of MeAB, PMeAB, and MeCTB under NVT (constant number of atoms, simulation volume, and temperature) or canonical ensemble conditions. Finally, in order to better reflect the experimental conditions conducted under an NH_3 atmosphere, NH_3 molecules were introduced into the simulation systems for TST explorations. In the case of ReaxFF, due to the inherent timescale limitations of large scale MD simulations, direct reactions between NH_3 and precursor molecules were not readily observed. To address this, a molecular sink model was employed to simulate the removal of CH_x species. The molecular sink concept refers to an artificial mechanism introduced in reactive simulations to mimic an open system where certain species are continuously consumed or transported away. In practice, when CH_x fragments form during decomposition or combustion, they are removed from the simulation domain at predefined intervals or upon detection. This prevents unrealistic accumulation of intermediates that would otherwise occur in a closed simulation box, which could alter reaction kinetics and thermodynamics. By acting as a "sink," the model approximates real physical conditions such as diffusion into surrounding media or catalytic

consumption, enabling more accurate representation of large-scale processes within finite computational systems. These modifications more accurately representing the reactive environment and gas-phase dynamics observed in experimental thermolysis of precursor compounds under NH_3. Overall, the combined DFT/ReaxFF simulations effectively capture the relevant chemistry of the targeted systems associated with (1) dissociation, (2) dehydrogenation, (3) cyclisation, (4) carbon (methyl group) removal, and (5) the formation of ceramic networks.

4.2 Methods

4.2.1 Density Functional Theory (DFT)

All DFT calculations are performed with the Amsterdam Density Functional Package (AMS Version 2024.104).[276] The B3LYP exchange–correlation functional combined with a Double-Zeta (DZ) basis set was employed for all potential energy surface (PES) calculations. Spin-polarisation was included to account for open-shell configurations, and Grimme's DFT-D3 dispersion correction was applied. The system was considered optimized when the residual forces on all atoms were below 5.0×10^{-4} Hartree/Bohr, as determined using the Quasi-Newton optimisation method.

4.2.2 Reactive Force Field (ReaxFF)

All ReaxFF simulations were carried out using the Reactive Force Filed Package (AMS Version 2024.104).[276] To investigate the thermal decomposition pathways of MeAB, PMeAB, and MeCTB, MD simulations were performed using the $ReaxFF_{HCONSB}$ parameter set, an extended version of $ReaxFF_{HBN}$ originally developed by Weismiller *et al.*[123] for studying the thermal decomposition of AB. The key QM data used in the parameterisation of $ReaxFF_{HBN}$

included: (1) bond dissociation energies for B/N/O/H atom combinations, (2) angular distortion potentials in AB-related molecules, and (3) reaction barriers and energies for critical reaction steps, such as H_2 release from AB, dimerisation of IB, and AB oxidation. These properties encompass the majority of the chemical transformations expected during the thermal decomposition of MeAB, PMeAB, and MeCTB, particularly those involving hydrogen, boron, and nitrogen. For the carbon-related interactions (i.e., bond, angle, and torsional parameters) in the ReaxFF force field, the $ReaxFF_{HCONSB}$ parameterisation incorporates QM data from the works of Castro-Marcano *et al.*[121] and Kamat *et al.*[124], thus enabling modelling of systems containing H/B/C/N elements. Given that all the target precursor molecules contain an AB moiety within their main structure and exhibit similar thermal decomposition behaviours as observed experimentally, the $ReaxFF_{HCONSB}$ parameters set is expected to exhibit good transferability and yield reasonably accurate and reliable simulation results for these systems.

To evaluate the effectiveness of the ReaxFF force field, two complementary simulation approaches were employed. In the first approach, a single molecule of PMeAB3-nocap, MeIB, or MeCTB was placed in a periodic cubic simulation box with a side length of 0.75 nm. In the second approach, multiple molecules systems were studied, consisting of (1) 10 uncapped PMeAB3 ($BH_2NHCH_3BH_2NHCH_3BH_2NHCH_3$, denoted as PMeAB3-nocap), (2) 30 MeIB, (3) 10 MeCTB, (4) 30 MeAB, and (5) 10 PMeAB trimers ($BH_3NHCH_3BH_2NHCH_3BH_2NH_2CH_3$, denoted as PMeAB3). These systems were simulated within a larger periodic cube of side length 1.5 nm. All simulations were carried out under both canonical NVT and canonical conditions. Temperature control was achieved using a Berendsen thermostat[277] with a damping constant of 0.1 ps. Due to the requirement to accurately capture translational, rotational, torsional, and vibrational motions of the molecules, a small time step of 0.25 fs was employed.[123]

For the single-molecule simulations, different configurations were sampled to enable a statistical assessment of decomposition behaviour. These configurations were generated from snapshots taken at different time steps of a 300 K equilibration simulation. The time required for the initial release of H_2 from PMeAB3-nocap, MeIB, or MeCTB was determined for each configuration across a temperature range of 1000–3500 K.

The larger multi-molecule systems were subjected to a continuous heating protocol, in which the thermostat temperature was ramped from 300 K to 5000 K at a constant rate of 0.01 K/fs, or held constant for 100 ps at temperatures of 1500, 2000, 2500, or 3000 K. From these simulations, several key metrics were determined, including the rate of H_2 evolution per unit molecule, the release of volatile small B–N species, the formation of larger molecular structures, the development of B–N ring networks, and the temperature-dependent reaction kinetics. To mimic decomposition in an NH_3 environment while avoiding system flooding, a molecular sink model was applied to selectively remove CH_x and H_2 species during the simulation. Post-simulation compositional analysis of product and intermediate species was performed using ChemTraYzer2 (CTY2),[278–280] employing a bond order cutoff of 0.3 to identify molecular fragments. While this cutoff has no effect on the simulation dynamics, it influences molecular recognition. A low cutoff value was chosen to accommodate the relatively weak B–N bonds present in the precursor molecules.[123]

Table 4.1 summarises the initial densities, temperature profiles, starting pressures, and final pressures for each of the MD simulations. High temperatures and pressures promote sufficient collision frequencies, enabling reasonable simulation times.[123]

4.3 Results and Discussion

4.3.1 Thermolysis Pathways of PMeAB to h-BN based on Potential Energy Surface Mapping

Reaction pathways can be elucidated by identifying the transition states (TS) and corresponding activation energies (E_a) through potential energy surface (PES) calculations across various molecular configurations. By mapping the PES for possible reaction routes, comprehensive and rational reaction mechanisms can be proposed for the formation of h-BN, starting from the precursors used in the experimental chapters, namely, PMeAB and MeCTB. Note that the energy profiles shown in this section represent electronic energy rather than Gibbs free energy and does not include entropy contributions. Despite this limitation, the results are still scientifically referenceable because electronic energy provides a reliable measure of relative stability and activation barriers for elementary steps, which dominate reaction kinetics at the molecular level. Therefore, mapping PES based on electronic energy remains an accepted approach for elucidating reaction mechanisms in condensed-phase and polymer systems.

Although PMeAB is a high-molecular-weight polymer, performing full DFT calculations on the entire chain is computationally impractical due to system size and timescale limitations. To address this, representative fragments were selected—PMeAB3-nocap (linear backbone), MeIB (monomer unit), and MeCTB (cyclic derivative)—to capture the key chemical environments and reactive sites. While smaller than the full polymer, these fragments preserve the essential bonding motifs governing cyclisation and dehydrogenation, making them chemically relevant. This approach is widely accepted for polymer-derived ceramic systems because it balances computational feasibility with mechanistic insight, and results are cross-validated against my own experimental data (TGA-MS, NMR, XPS) and literature on analogous systems (e.g., AB derivatives). Thus, the calculations provide reliable molecular-level understanding that can be extrapolated to the full PMeAB-to-h-BN conversion process.

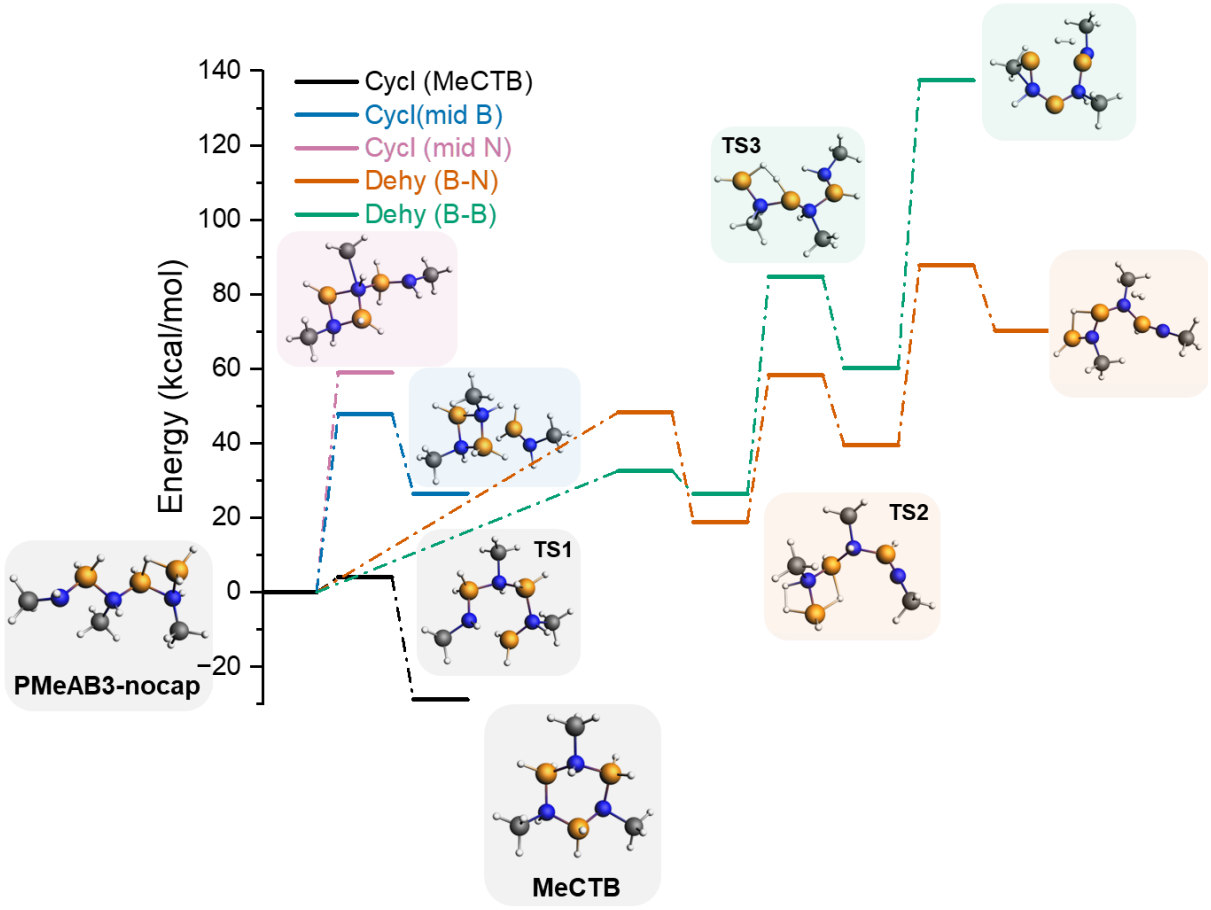

Figure 4.1: Energy diagram for the thermal decomposition of PMeAB3-nocap. Black: cyclisation to form MeCTB; blue: cyclisation to form BCDMeB (middle B atom); purple: cyclisation to form BCDMeB (middle N atom); orange: dehydrogenation across B-N; green: dehydrogenation across B-B. The white, yellow, grey, and blue spheres represent H, B, C, and N atoms, respectively.

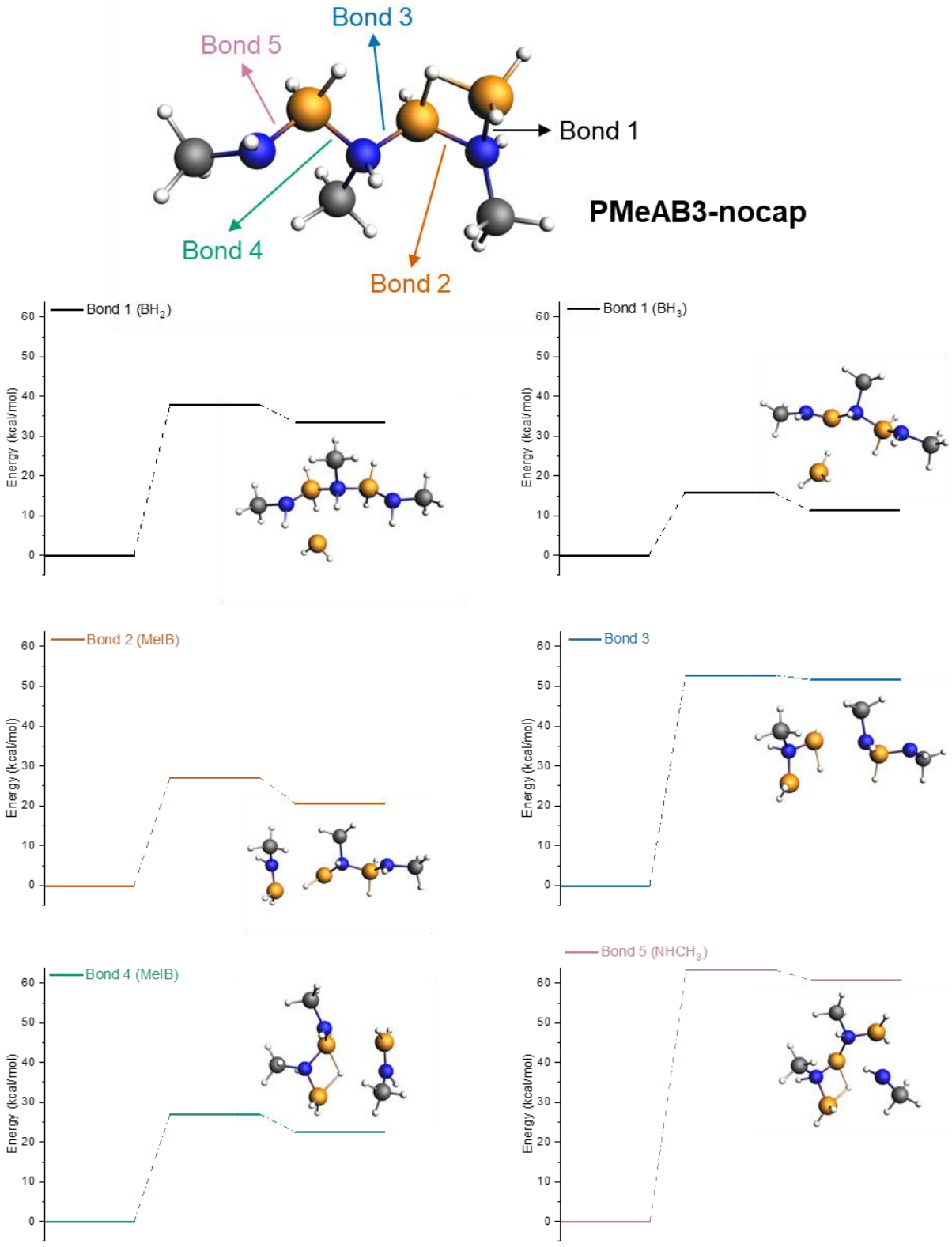

Figure 4.2: Energy diagram for the thermal decomposition of PMeAB3-nocap. Black (left): dissociation of B-N bond 1 to form BH_2; black (right): dissociation of B-N bond 1 to form BH_3; orange: dissociation of B-N bond 2 to form MeIB; blue: dissociation of B-N bond 3; green: dissociation of B-N bond 4 to form MeIB; purple: dissociation of B-N bond 4 to form $NHCH_3$.

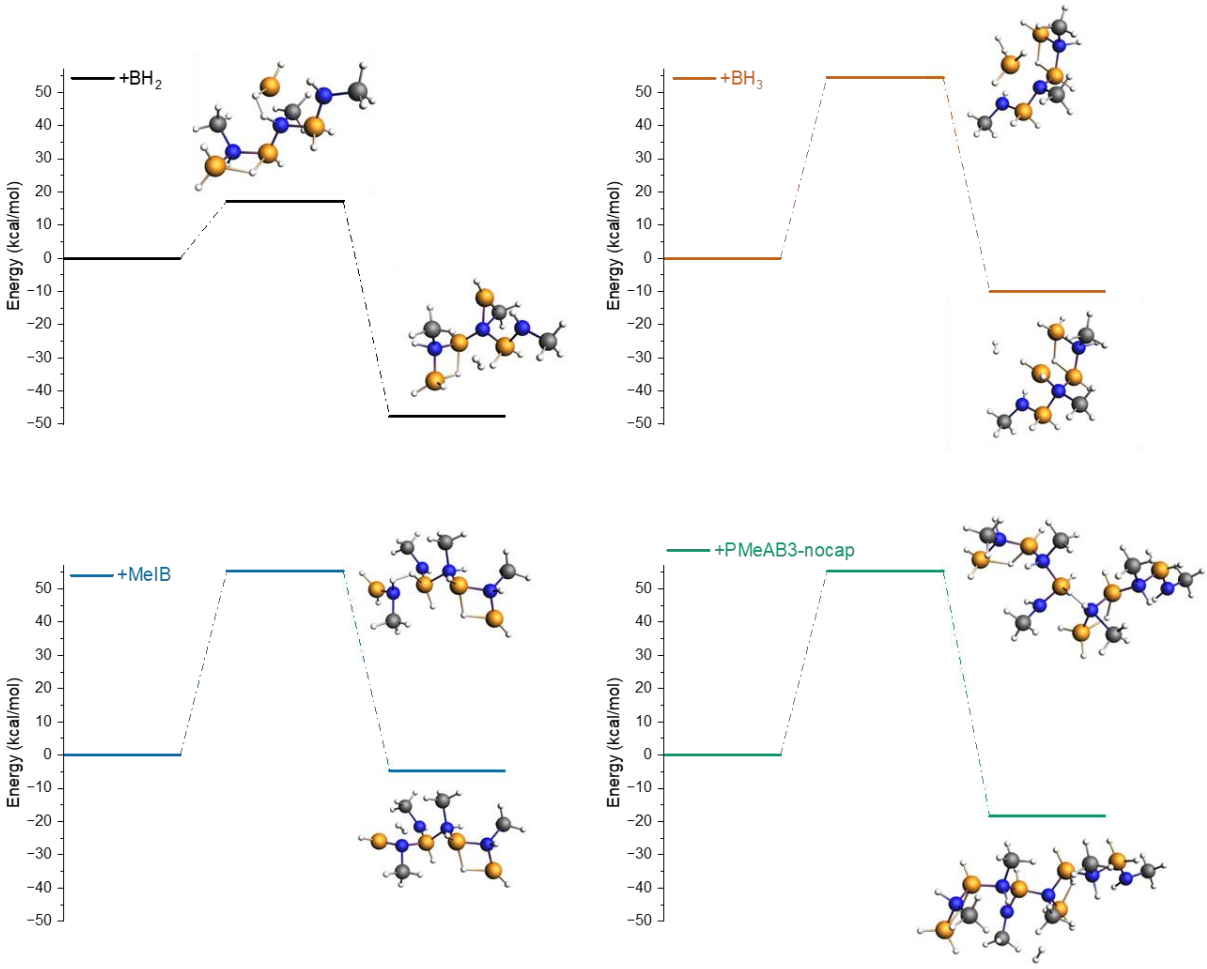

Figure 4.3: Energy diagram for the dehydrogenation of PMeAB3-nocap with additional reaction intermediates. Black: dehydrogenation with BH_2 bonding to the middle N atom; orange: dehydrogenation with BH_3 bonding to the middle N atom; blue: dehydrogenation with the N atom of MeIB bonding to the N end B atom; green: dehydrogenation with the N end B atom of PMeAB3-nocap bonding to the B end N atom.

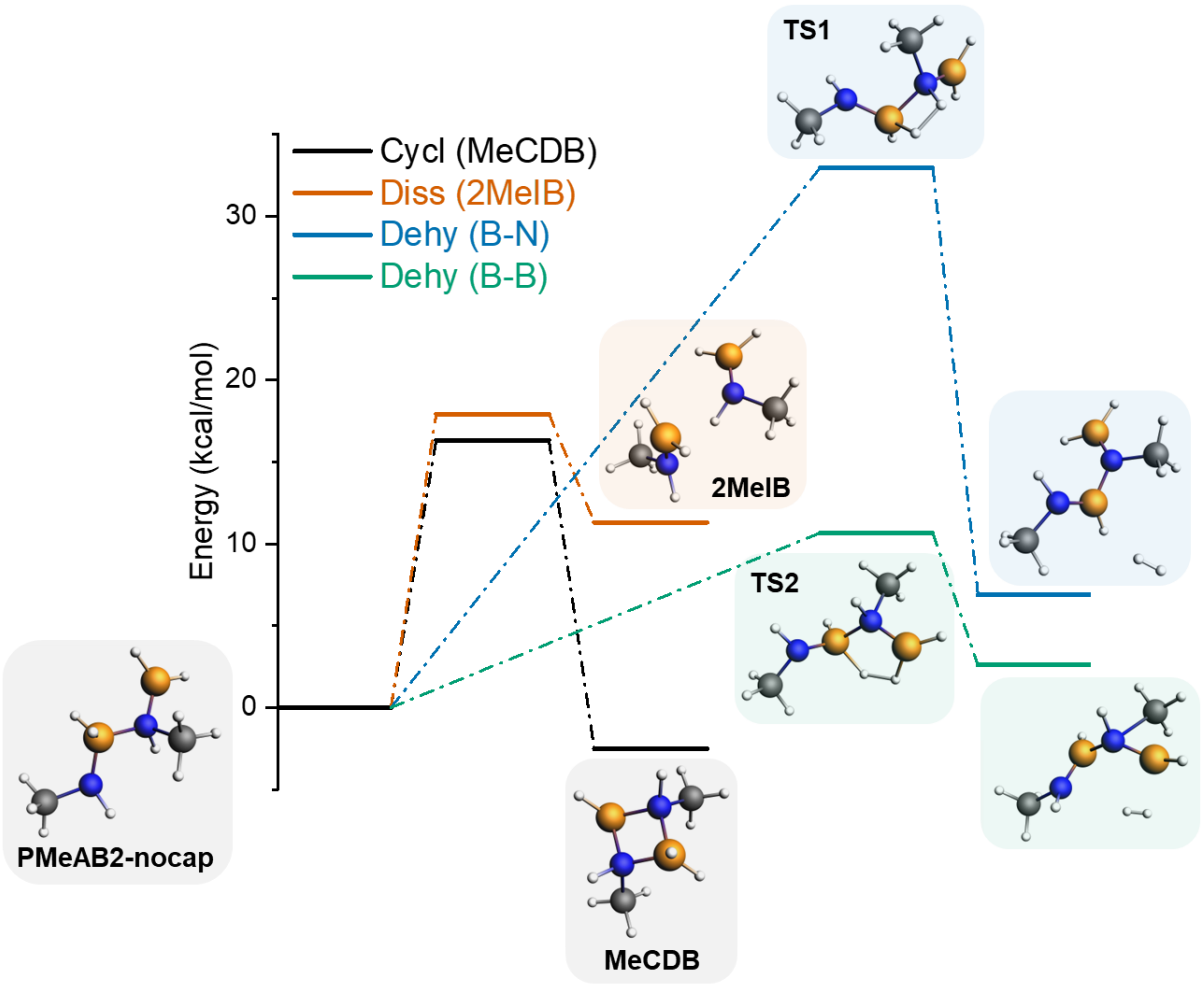

Figure 4.4: Energy diagram for the thermal decomposition of PMeAB2-nocap. Black: cyclisation to form MeCDB; orange: dissociation to form 2 MeIB; blue: dehydrogenation across B-N; green: dehydrogenation across B-B.

The PMeAB3-nocap fragment is designed to represent the linear backbone of the PMeAB polymer while maintaining chemical stability under quantum mechanical optimisation. However, truncation introduces unsaturated terminal atoms, which would otherwise lead to unrealistic dangling bonds and distort the electronic structure. Therefore, the terminal boron atom shares one hydrogen with the adjacent boron, forming a B–H–B bridge bond. This feature is not arbitrary, it reflects boron's electron-deficient nature and its tendency to form three-centre two-electron bonds, as observed in diborane chemistry.

PMeAB3-nocap undergoes three primary thermal decomposition pathways: dehydrogenation, cyclisation, and bond dissociation. Among these, cyclisation to form MeCTB is the most favourable, with a lower activation energy (E_a = 4.1 kcal/mol) compared to dehydrogenation (E_a > 32.56 kcal/mol), dissociation (E_a > 15.16 kcal/mol), or alternative cyclisation pathways such as the formation of BCDMeB (E_a > 47.83 kcal/mol) (**Figure 4.1** and **4.2**). MeCTB emerges as a key intermediate, indicating that the transformation from the linear configuration of PMeAB to the cyclic MeCTB is both thermodynamically favourable and kinetically accessible given low thermal energy. The inherent stability of MeCTB reinforces its importance as a key intermediate likely to present during thermolysis. This can be attributed to several factors: (i) ring closure reduces conformational entropy and creates a rigid, cross-linked structure, lowering steric strain; (ii) the cyclic arrangement enhances orbital overlap between B and N atoms, promoting electron delocalization and reducing electronic energy; and (iii) reactive chain ends present in linear fragments are eliminated, removing high-energy sites. Dehydrogenation is also energetically favourable, particularly across B–N and B–B bonds, with the latter pathway exhibiting a lower barrier (B–N: E_a = 48.33 kcal/mol vs B–B: E_a = 32.56 kcal/mol), in agreement with the single molecules MD simulation results for PMeAB3-nocap presented in **Section 4.3**. However, while the initial release of H_2 across B–B is feasible, subsequent dehydrogenation (second and third H_2 molecules) involve higher barrier (E_a > 50

kcal/mol), suggesting that complete dehydrogenation relying solely on intramolecular reactions is not energetically favourable. Dissociation of various B–N bonds to yield smaller molecular fragments is also observed. Specifically, the dissociation of B–N bonds 1 (E_a = 37.89 kcal/mol to form BH_2 and E_a = 15.66 kcal/mol to form BH_3), 2 (E_a = 27.18 kcal/mol to form MeIB), and 4 (E_a = 26.97 kcal/mol to form MeIB), are among the preferred pathways. These findings suggest that the thermal decomposition of PMeAB through B–N bond cleavage is not random but rather selective. Here, dissociation (bond breakage) is considered because it represents a fundamental step in polymer fragmentation, enabling the formation of smaller, more mobile species that can undergo subsequent cyclisation and dehydrogenation reactions. The resulting intermediates, BH_2, BH_3, and MeIB, are therefore likely to play important roles in later stages of h-BN formation and will be discussed in detail in subsequent figures.

The reactions of these intermediates with PMeAB3-nocap are illustrated in **Figure 4.3**. Among them, BH_2 significantly lowers the activation energy (E_a = 17.27 kcal/mol) for dehydrogenation by forming a bond with the nitrogen atom in PMeAB3-nocap, facilitating the release of one H_2 molecule (one H atom originating from BH_2 and the other H atom from the N atom of PMeAB3-nocap). In contrast, BH_3 (E_a = 54.46 kcal/mol) and MeIB (E_a = 55.44 kcal/mol) do not demonstrate a similar effect. This suggests that dehydrogenation in PMeAB can proceed via both intra- and intermolecular pathways, which likely occur concurrently during thermal decomposition.

Figure 4.4 presents the reaction pathways for the PMeAB2-nocap dimer, a relevant intermediate/product resulting from the dissociation of the PMeAB3-nocap trimer. The dimer exhibits behaviour analogous to the trimer, including cyclisation to form MeCDB (E_a = 16.34 kcal/mol), dehydrogenation across B–B (E_a = 10.67 kcal/mol) and B–N bonds (E_a = 32.95 kcal/mol), and dissociation to yield two MeIB molecules (E_a = 17.92 kcal/mol), all proceeding with relatively low activation energies. Dehydrogenation across B–B is favoured over B–N

because the bridging hydrogens in three-centre two-electron bonds are much weaker bound than N–H bonds. These multi-centre bonds are characteristic of electron-deficient boron species. In contrast, N–H bonds are stronger and more localized due to nitrogen's higher electronegativity and lone-pair stabilisation, requiring significantly higher E_a for cleavage. These findings indicate that the thermal decomposition of PMeAB is largely independent of chain length, and thus, molecular weight. Therefire, the PMeAB3-nocap trimer serves as a suitable and representative model for simulating the thermal behaviour of PMeAB.

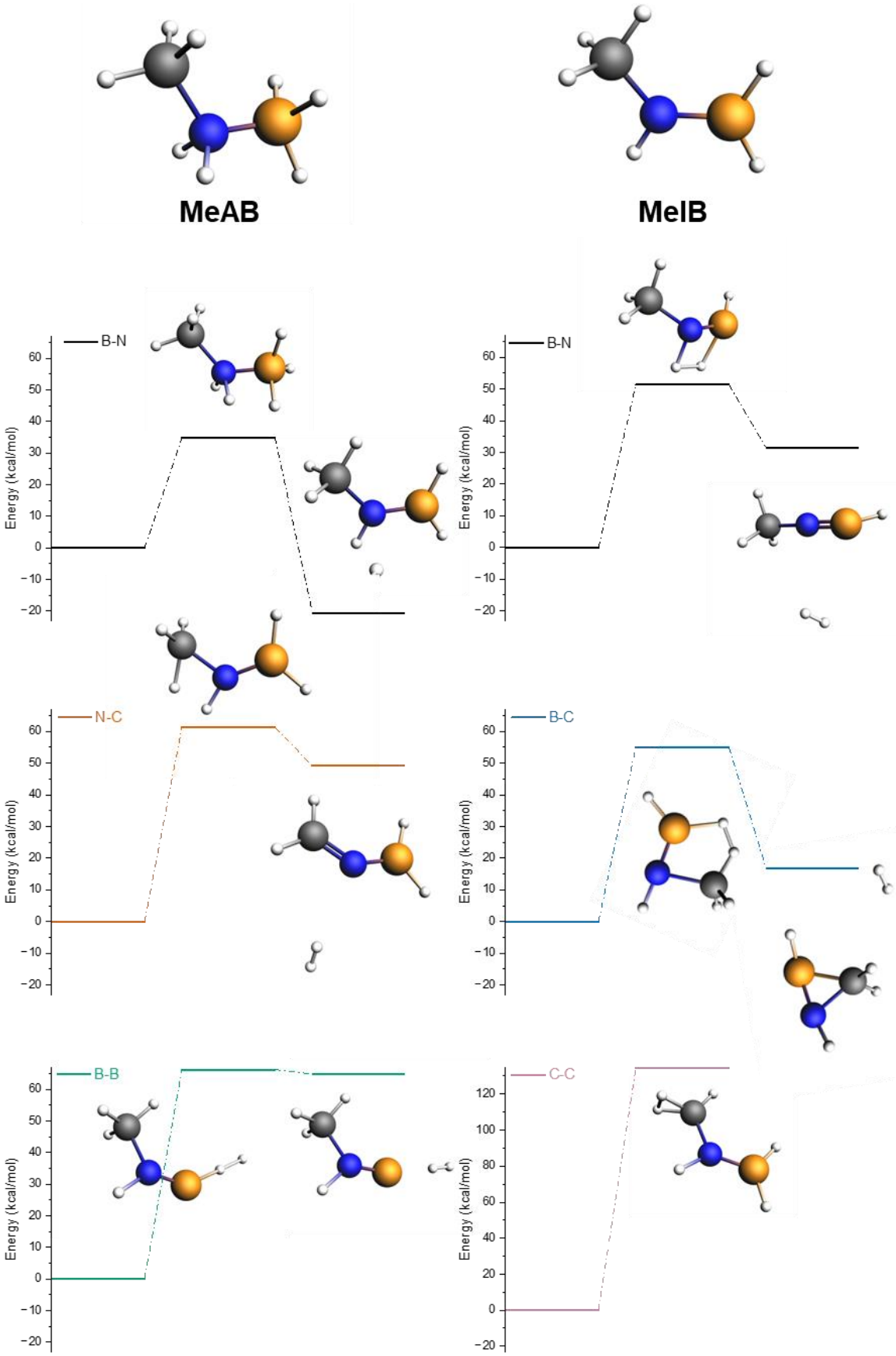

Figure 4.5: Energy diagram for the dehydrogenation of MeAB and MeIB. Black: dehydrogenation across B-N of (top left) MeAB and (top right) MeIB; orange: dehydrogenation across N-C; blue: dehydrogenation across B-C; green: dehydrogenation across B-B; purple: dehydrogenation across C-C.

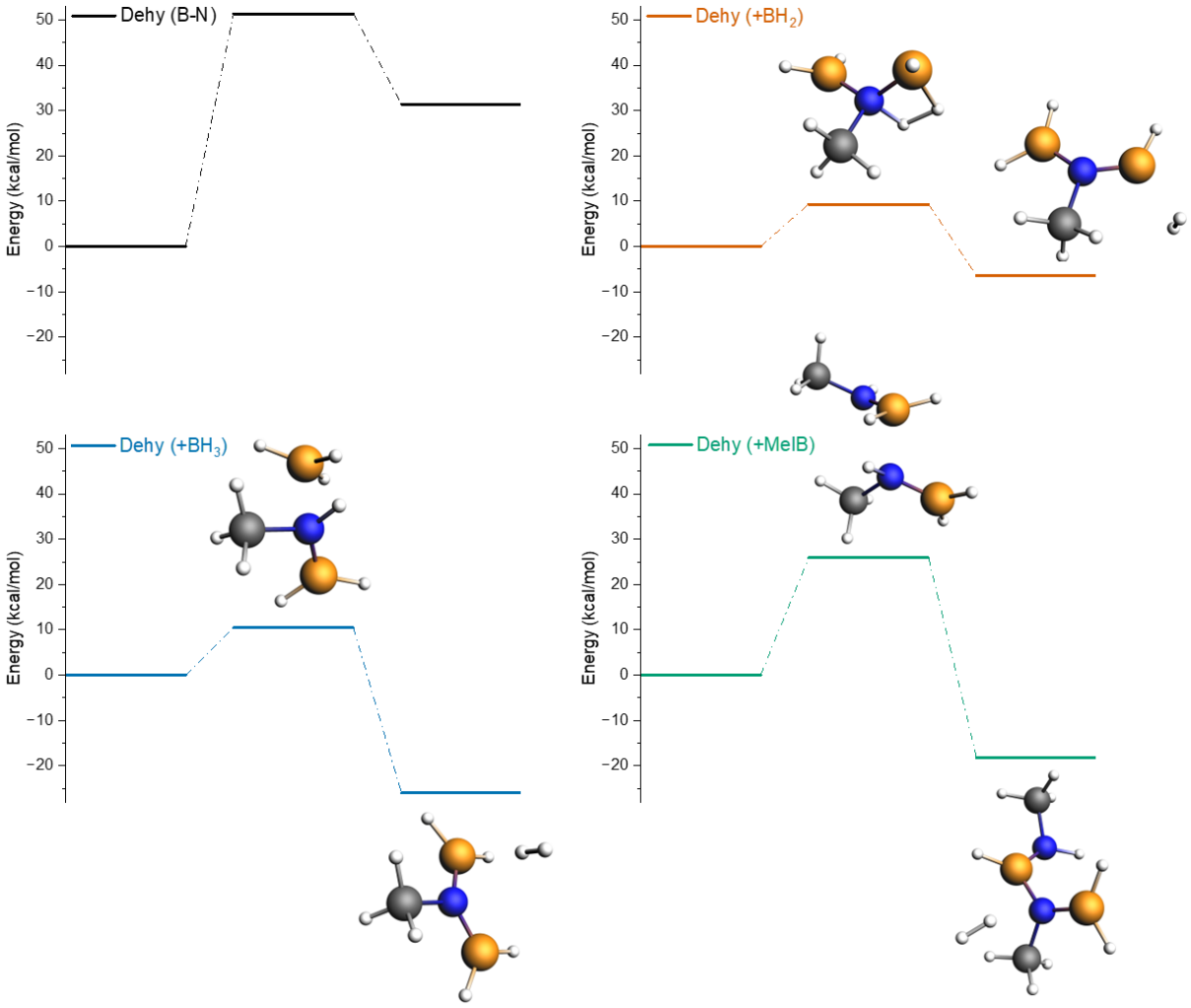

Figure 4.6: Energy diagram for the dehydrogenation of MeIB with additional reaction intermediates. Black: dehydrogenation across B-N; orange: dehydrogenation with BH_2 bonding to the N atom; blue: dehydrogenation with BH_3 bonding to the N atom; green: dehydropolymerisation with MeIB.

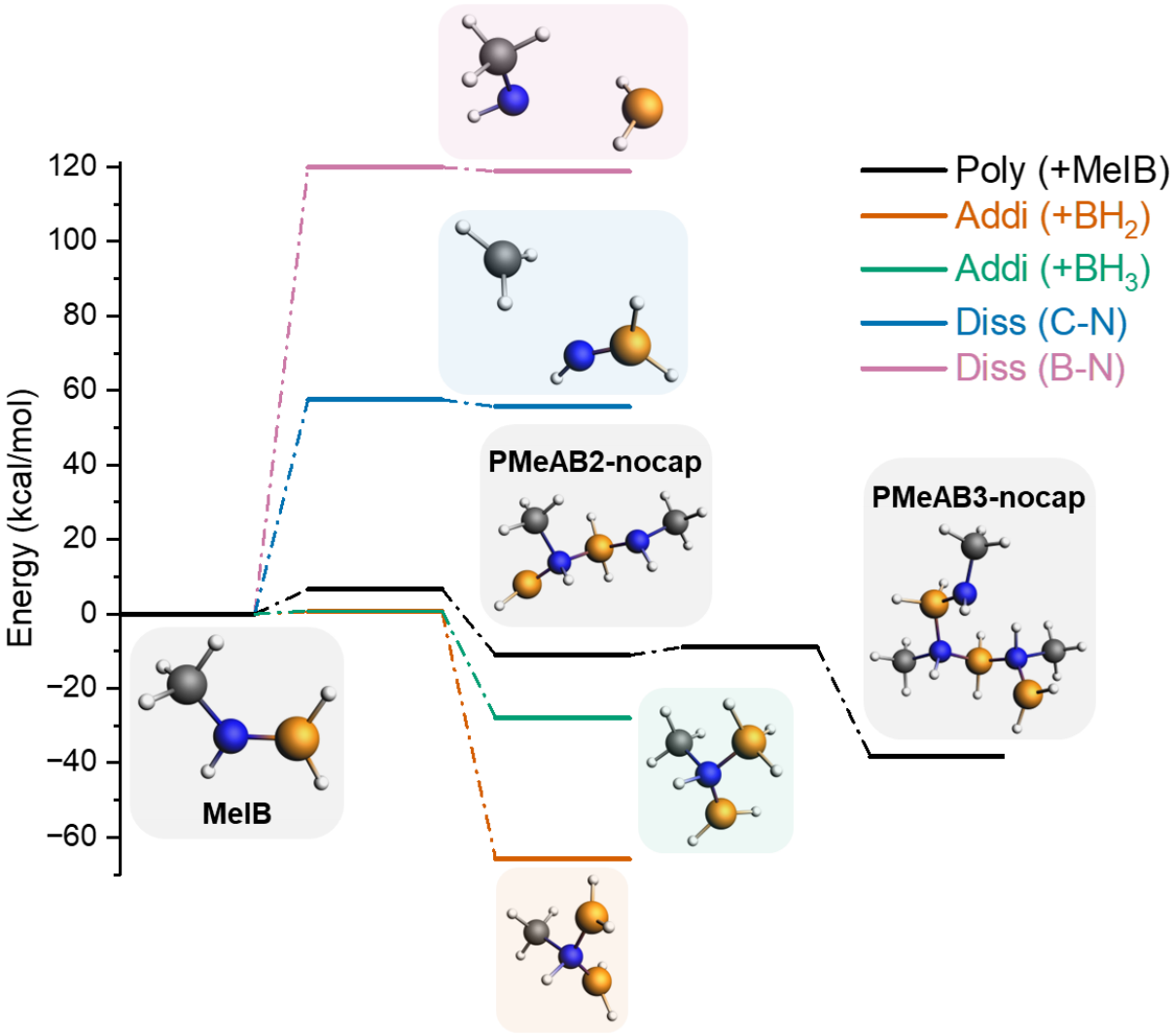

Figure 4.7: Energy diagram for the thermal decomposition and reaction with additional reaction intermediates of MeIB. Black: polymerisation to form PMeAB2-nocap and PMeAB3-nocap; orange: addition of BH_2 bonding to the N atom; green: addition of BH_3 bonding to the N atom; blue: dissociation of C-N bond; purple: dissociation of B-N bond.

Figure 4.5 illustrates the dehydrogenation pathways of the monomers MeAB and MeIB. The dehydrogenation of MeAB across the B–N bond to form MeIB proceeds with a relatively low activation energy (E_a = 34.68 kcal/mol), slightly lower than the values reported in the literature (E_a = 43.3 kcal/mol)[115] and those estimated via the Arrhenius equation based on single-molecule MD simulations (E_a = 38.82 kcal/mol) discussed in **Section 4.3**. In contrast, further dehydrogenation of MeIB exhibits significantly higher activation energies across all examined pathways, B–N (E_a = 51.34 kcal/mol), N–C (E_a = 61.26 kcal/mol), B–C (E_a = 54.93 kcal/mol), B–B (E_a = 66.22 kcal/mol), and C–C (E_a = 134.32 kcal/mol), relative to the initial H_2 release from MeAB. As a result, such subsequent dehydrogenation steps are less likely to occur. However, in practical systems, the presence of various intermediates, reaction products, as well as coexisting monomers MeAB and MeIB or polymers PMeAB may facilitate intermolecular reactions. **Figure 4.6** compares the intramolecular and intermolecular dehydrogenation mechanisms of MeIB. The addition of intermediates such as BH_2 (E_a = 9.34 kcal/mol), BH_3 (E_a = 10.41 kcal/mol), and MeIB (E_a = 25.89 kcal/mol) significantly lowers the activation barriers for MeIB dehydrogenation. These findings suggest that MeIB dehydrogenation predominantly relies on intermolecular interactions rather than intramolecular mechanisms. Notably, the addition of MeIB promotes the so-called “dehydropolymerisation”, leading to the formation of the dimer PMeAB2-nocap.

Figure 4.7 demonstrates that these intermediates can react with MeIB not only via dehydrogenation but also through direct addition reactions that occur with negligible energy barriers (BH_2: E_a = 0.62 kcal/mol; BH_3: E_a = 0.79 kcal/mol; 1st MeIB: E_a = 6.63 kcal/mol; 2nd MeIB: E_a = 2.23 kcal/mol), without the release of H_2. These addition reactions are significantly more favourable than the dissociation pathways of MeIB. This suggests that MeIB is unlikely to undergo further bond cleavage, such as cleavage of B–N (E_a = 119.93 kcal/mol) or N–C (E_a = 57.52 kcal/mol) dissociation. Instead, MeIB is more likely to serve as a stable building block

for the formation of larger molecular structures, such as through polymerisation reactions leading to the dimer PMeAB2-nocap or the trimer PMeAB3-nocap.

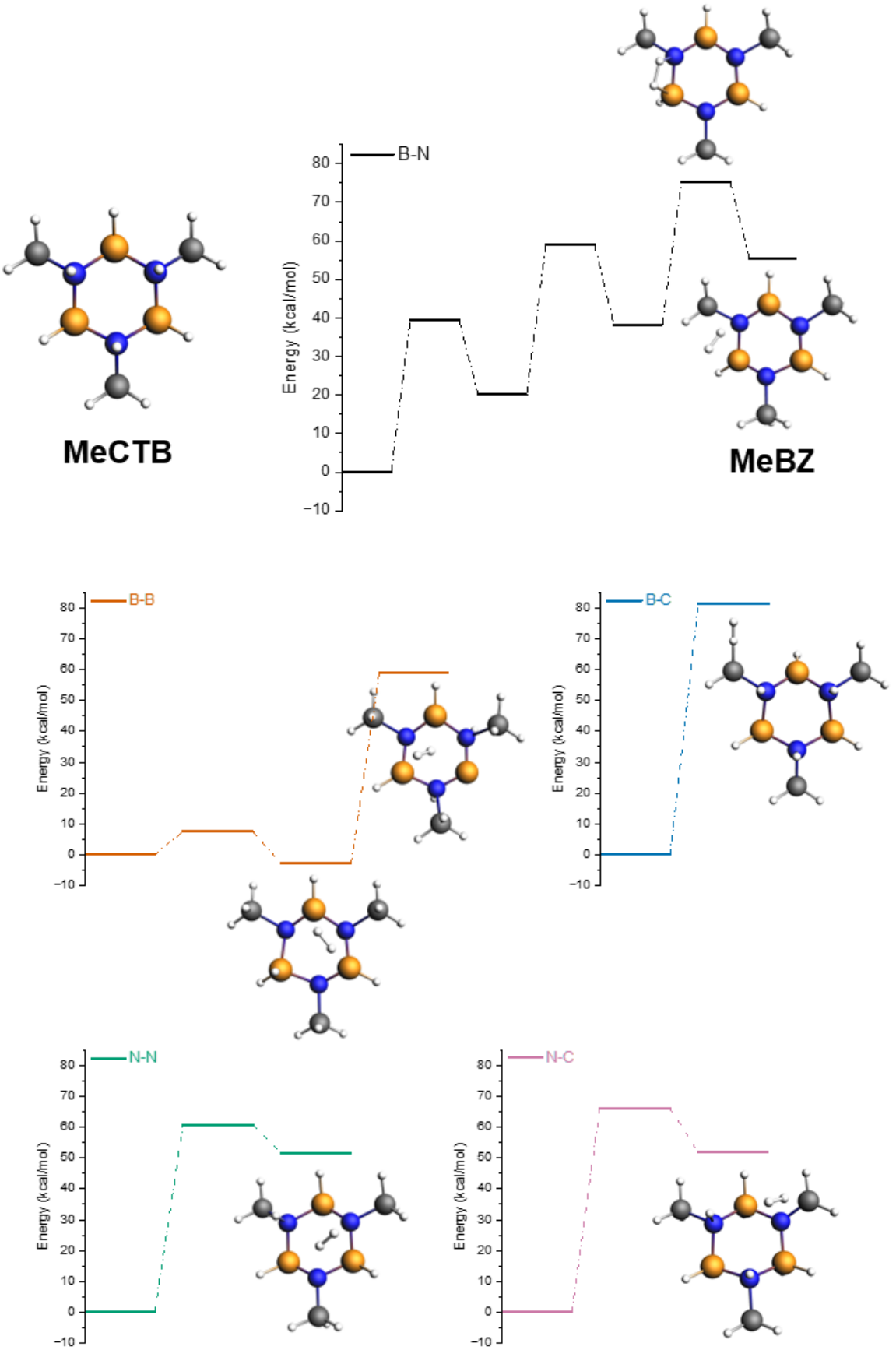

Figure 4.8: Energy diagram for the dehydrogenation of MeCTB. Black: dehydrogenation across B-N; orange: dehydrogenation across B-B; blue: dehydrogenation across B-C; green: dehydrogenation across N-N; purple: dehydrogenation across N-C.

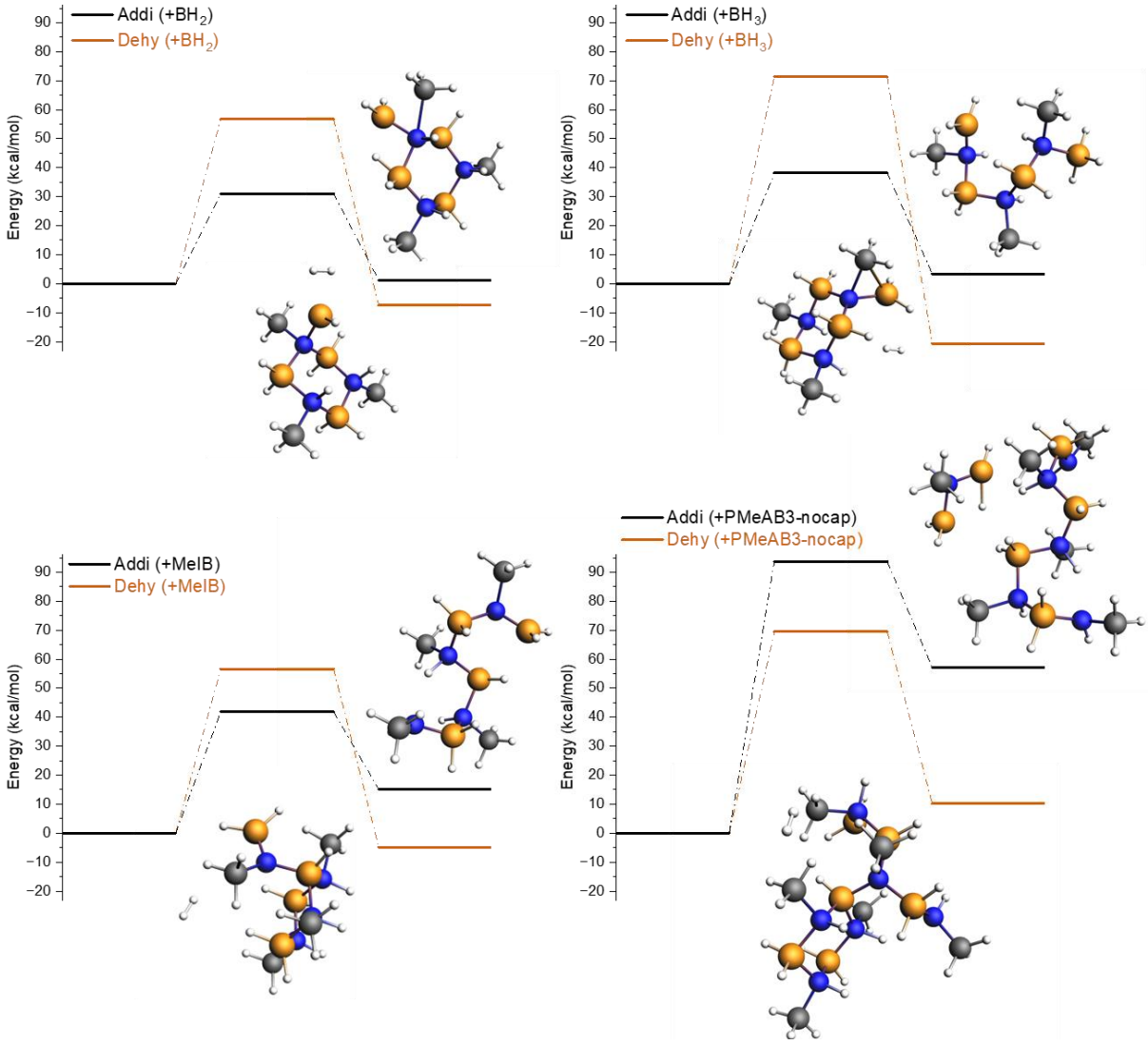

Figure 4.9: Energy diagram for the dehydrogenation and reaction with additional reaction intermediates of MeCTB. Top left: (black) addition of BH_2 bonding to the N atom; (orange) dehydrogenation with BH_2 bonding to the N atom; top right: (black) addition of BH_3 bonding to the N atom; (orange) dehydrogenation with BH_3 bonding to the N atom; bottom left: (black) addition of MeIB bonding to the N atom; (orange) dehydrogenation with MeIB bonding to the N atom; bottom right: (black) addition of PMeAB3-nocap bonding to the N atom; (orange) dehydrogenation with PMeAB3-nocap bonding to the N atom.

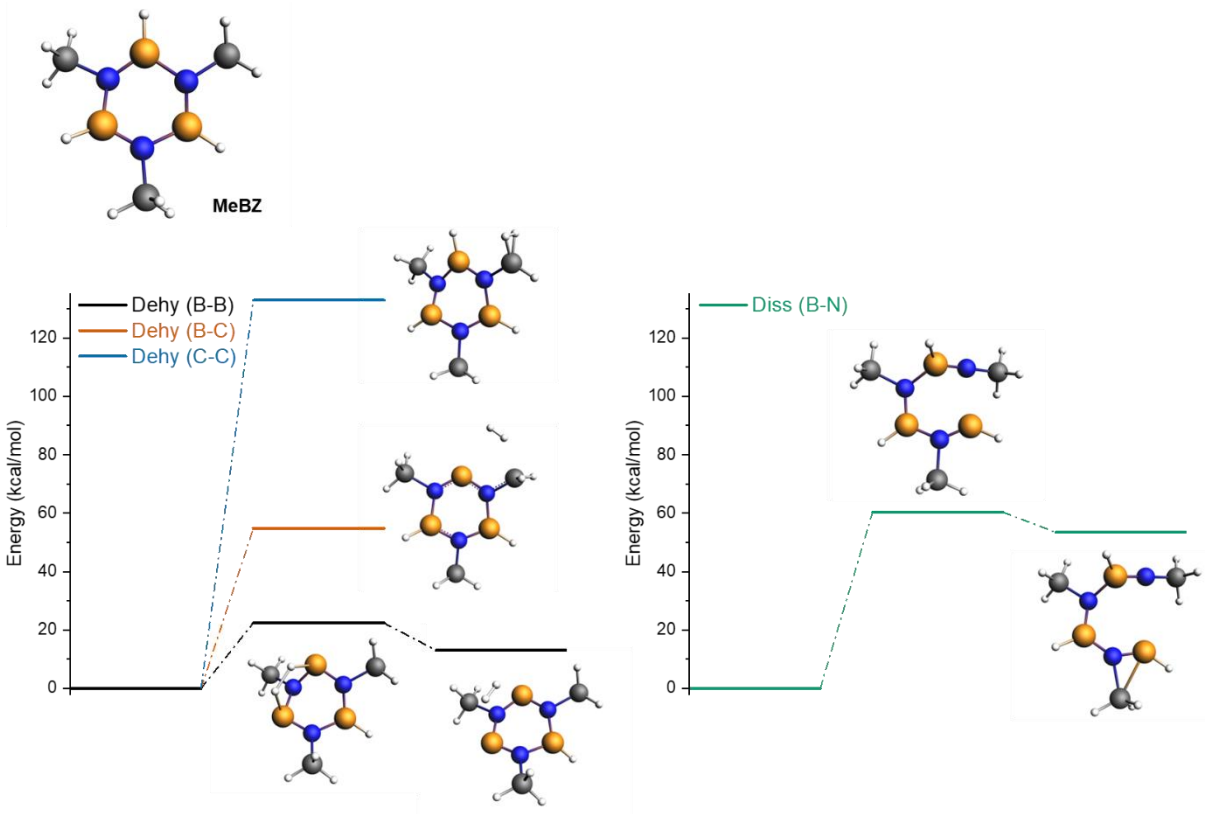

Figure 4.10: Energy diagram for the thermal decomposition of MeBZ. Black: dehydrogenation across B-B; orange: dehydrogenation across B-C; blue: dehydrogenation across C-C; green: dissociation of B-N bond.

Figure 4.8 presents the dehydrogenation behaviour of MeCTB, a thermodynamically stable cyclic derivative of PMeAB. Dehydrogenation is most likely to occur across B–N (E_a = 39.56 kcal/mol) and B–B (E_a = 7.52 kcal/mol) bonds, while pathways across B–C (E_a = 81.5 kcal/mol), N–N (E_a = 60.8 kcal/mol), or N–C (E_a = 66.27 kcal/mol) are less favourable. Specifically, dehydrogenation across B–N bonds can lead to the release of up to three H_2 molecules, ultimately forming another key intermediate, MeBZ. In contrast, dehydrogenation across B–B bonds is not sustainable; the release of the second H_2 molecule requires prohibitively high activation energy (E_a = 61.96 kcal/mol). Notably, the addition of intermediates such as BH_2, BH_3, MeIB, or PMeAB3-nocap does not lower the activation barrier for MeCTB dehydrogenation (**Figure 4.9**), in contrast to their effect on PMeAB3-nocap and MeIB. In fact, these species may destabilise the MeCTB ring structure by bonding with it and inducing ring opening, converting back it into a linear configuration. This suggests that MeCTB is an intrinsically stable compound, thermodynamically more stable than its linear counterpart, PMeAB. **Figure 4.10** illustrates the thermal decomposition of MeBZ, the dehydrogenation product of MeCTB. MeBZ can undergo further dehydrogenation, most favourably across B–B bonds (E_a = 22.39 kcal/mol). This continued dehydrogenation is a critical step, as the final product, h-BN, is a hydrogen-free ring network. Notably, dissociation of MeBZ is not favoured, suggesting that ring-opening reactions leading to linear structure PMeAB are unlikely (E_a = 60.31 kcal/mol). This behaviour is consistent with that observed for MeCTB. Therefore, once cyclisation occurs to form MeCTB and subsequently MeBZ, the system tends to remain in a cyclic configuration, indicating the stability of these ring-based key intermediates during thermolysis. This suggests that such cyclic species play a crucial role in the transformation of the linear PMeAB precursor polymer into the ceramic h-BN ring network.

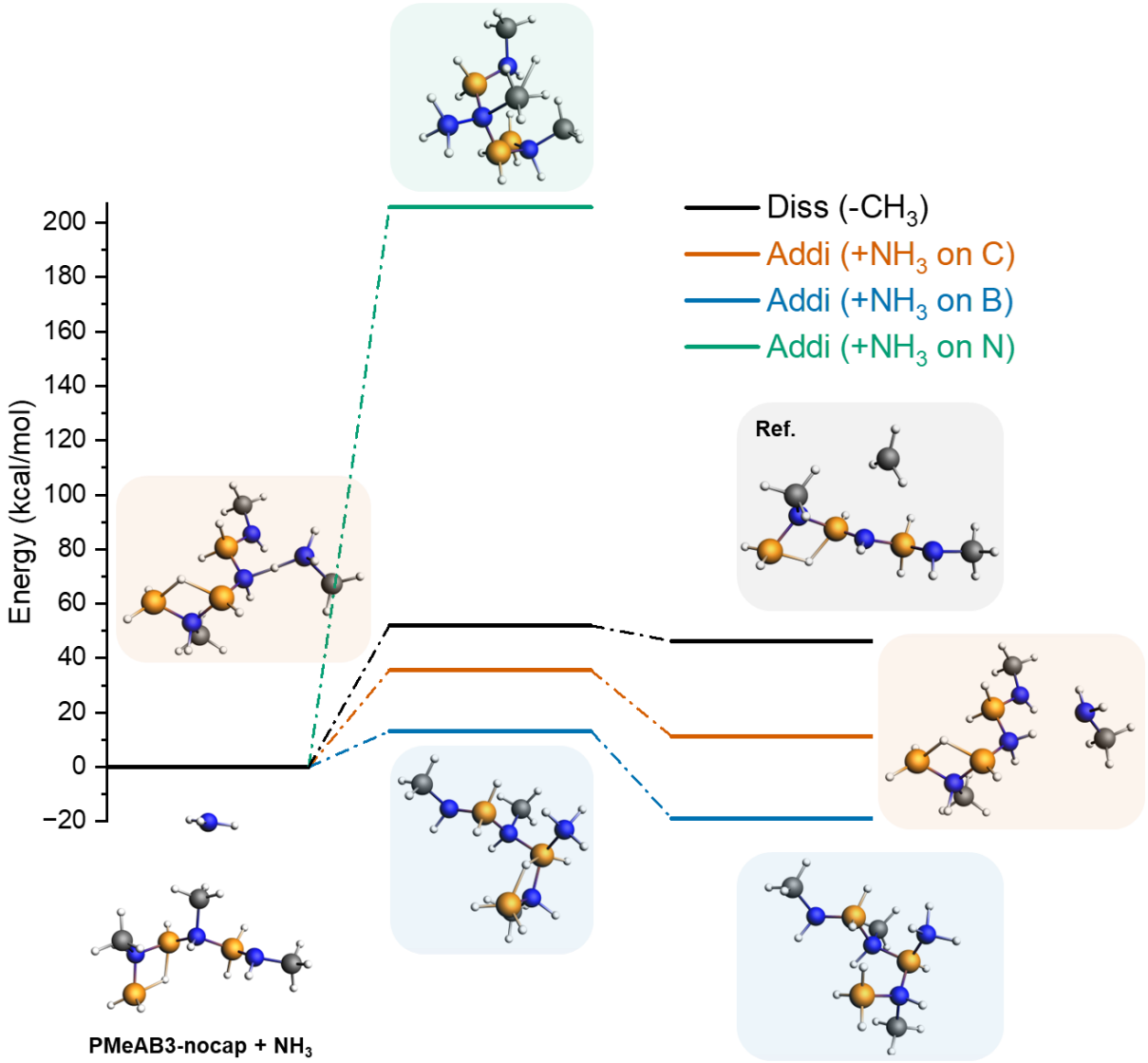

Figure 4.11: Energy diagram for the reaction with additional NH_3 of PMeAB3-nocap. Black: dissociation of the middle N-C bond to form CH_3 (reference); orange: addition of NH_3 bonding to the middle C atom; blue: addition of NH_3 bonding to the middle B atom; green: addition of NH_3 bonding to the middle N atom.

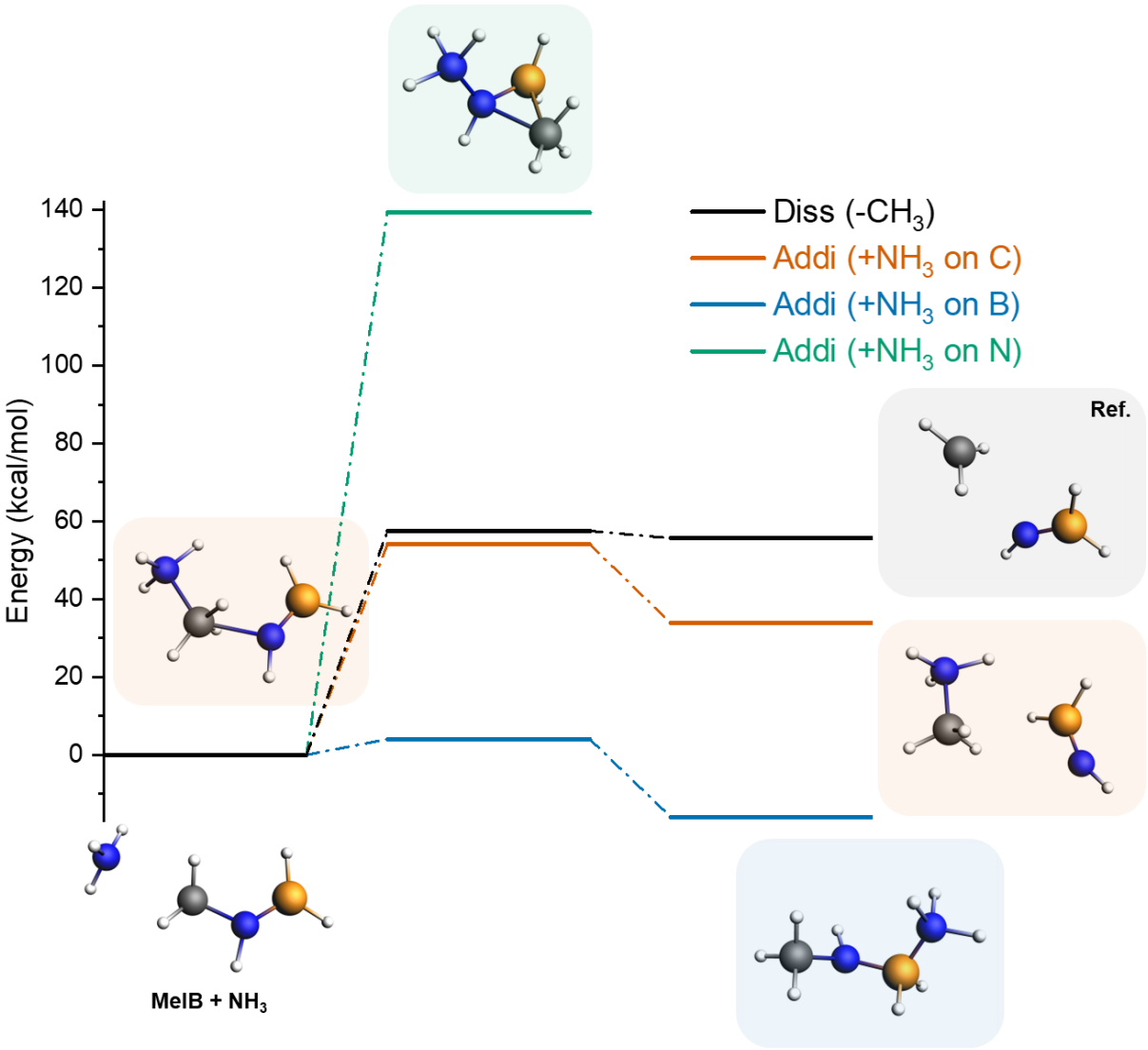

Figure 4.12: Energy diagram for the reaction with additional NH_3 of MeIB. Black: dissociation of the N-C bond to form CH_3 (reference); orange: addition of NH_3 bonding to the C atom; blue: addition of NH_3 bonding to the B atom; green: addition of NH_3 bonding to the N atom.

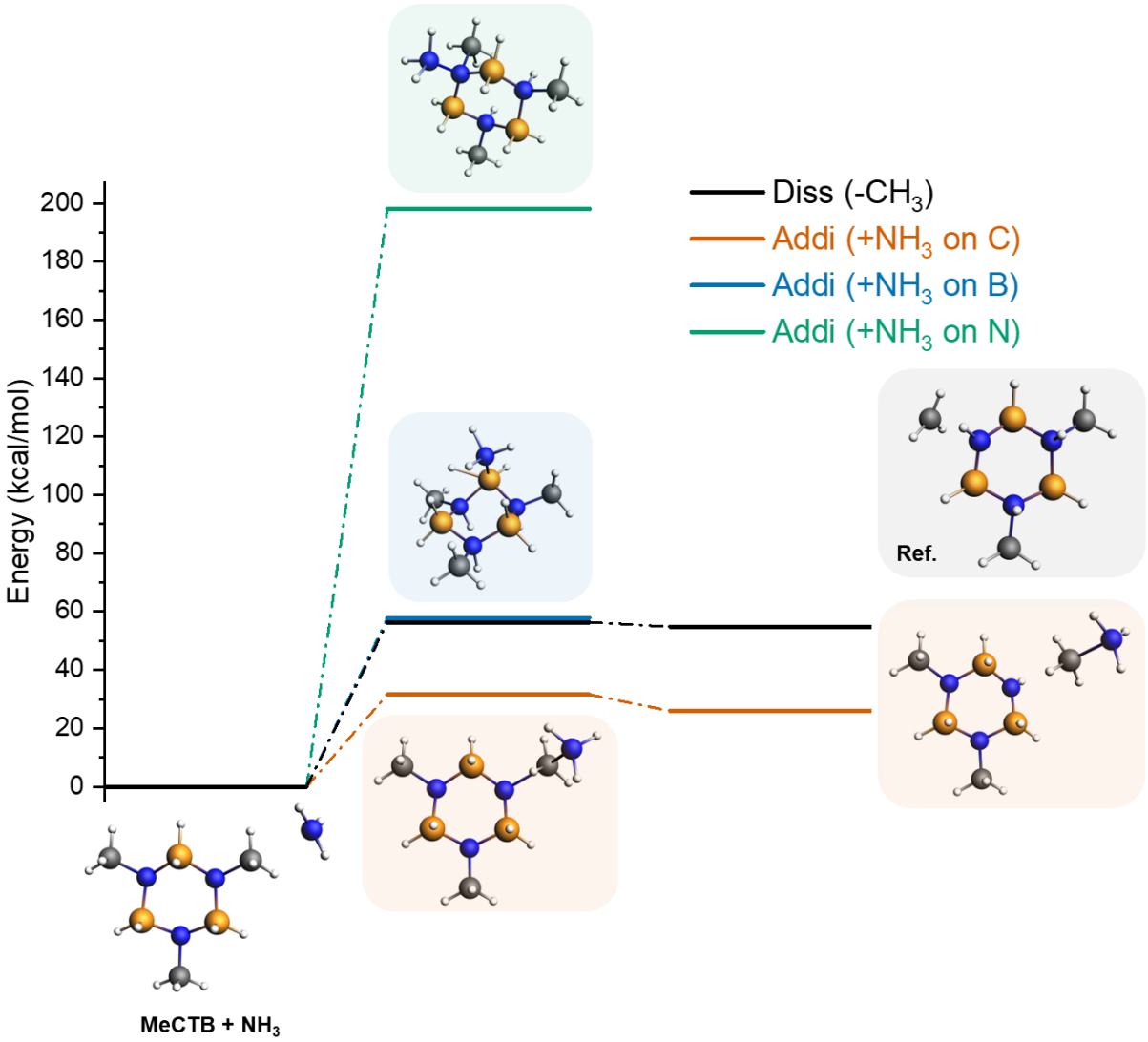

Figure 4.13: Energy diagram for the reaction with additional NH_3 of MeCTB. Black: dissociation of the N-C bond to form CH_3 (reference); orange: addition of NH_3 bonding to the C atom; blue: addition of NH_3 bonding to the B atom; green: addition of NH_3 bonding to the N atom.

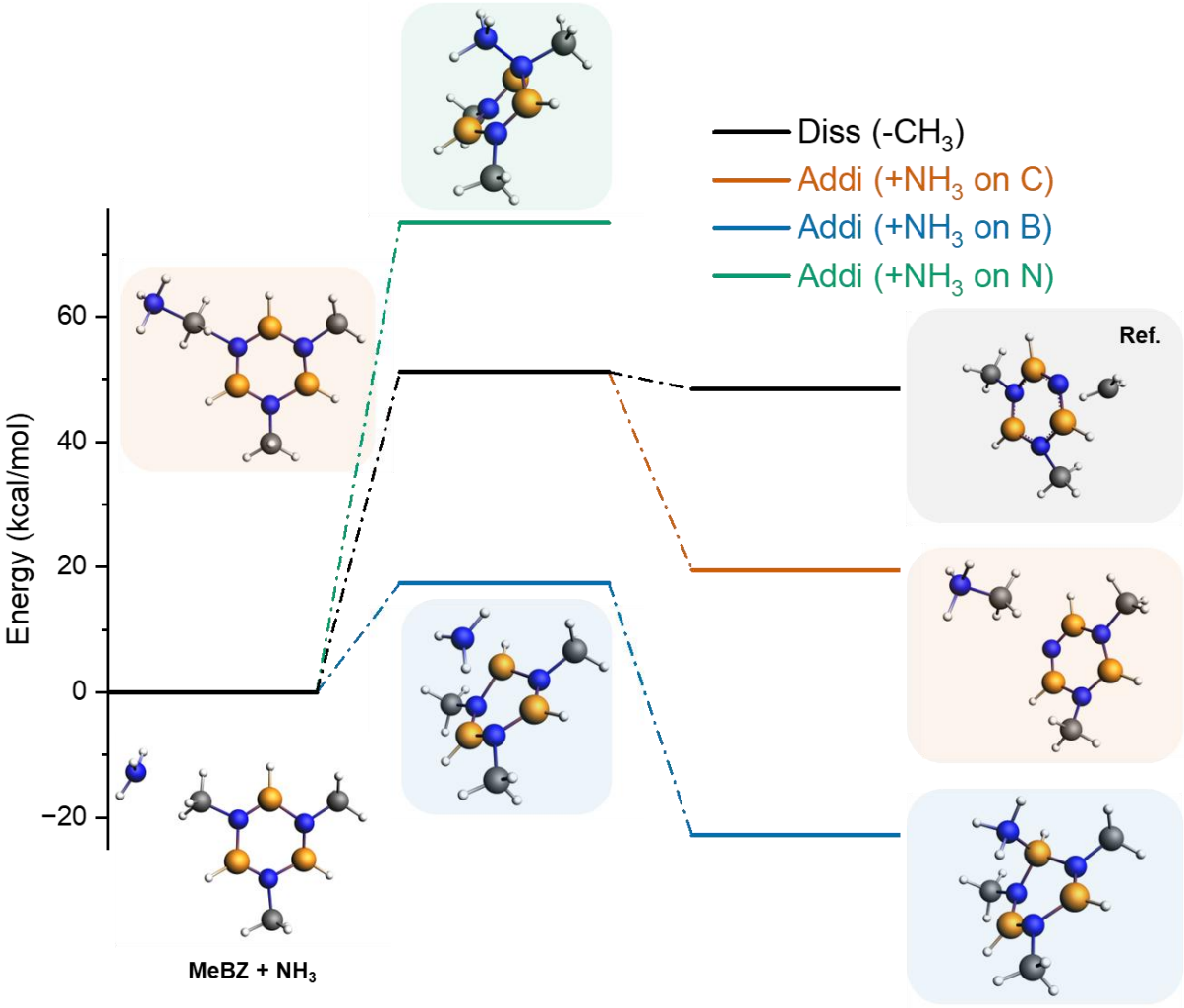

Figure 4.14: Energy diagram for the reaction with additional NH_3 of MeBZ. Black: dissociation of the N-C bond to form CH_3 (reference); orange: addition of NH_3 bonding to the C atom; blue: addition of NH_3 bonding to the B atom; green: addition of NH_3 bonding to the N atom.

To simulate the experimental NH_3 thermolysis process, the interaction of NH_3 with precursor/key intermediate molecules were investigated. Both PMeAB3-nocap and MeIB exhibit similar reactivity toward NH_3, which preferentially bonds to B atom or C atom rather than N atom (**Figure 4.11** and **4.12**). When NH_3 coordinates to a B atom, it tends to remain stably attached, forming a higher coordinated BN_3 environment, effectively incorporating into the molecular structure (PMeAB3-nocap: E_a = 13.16 kcal/mol; MeIB: E_a = 3.99 kcal/mol). In contrast, NH_3 bonding to a C atom results in the abstraction of a CH_3 group from the precursor, facilitating the so-called "demethylation". This demethylation process proceeds with a lower activation energy (PMeAB3-nocap: E_a = 35.47 kcal/mol; MeIB: E_a = 54.1 kcal/mol) compared to the direct dissociation of the CH_3 group from the molecule (PMeAB3-nocap: E_a = 51.91 kcal/mol; MeIB: E_a = 57.52 kcal/mol), indicating that NH_3 can serve as an efficient methyl group scavenger, consistent with literature reports on its role in removing methyl groups from B–N–C polymers.[217]

For MeCTB, NH_3 preferentially bonds to the C atom (E_a = 31.62 kcal/mol), while bonding to the B atom is not favoured (E_a = 57.84 kcal/mol). Similar to the behaviour observed for PMeAB3-nocap and MeIB, NH_3 coordination to the C atom in MeCTB facilitates CH_3 group release, promoting demethylation (direct demethylation E_a = 56.36 kcal/mol). In the case of MeBZ, however, NH_3 preferentially bonds to the B atom (E_a = 17.45 kcal/mol) rather than the C atom (E_a = 51.18 kcal/mol). While NH_3 bonding to the C atom in MeBZ can also lead to CH_3 release, the associated activation energy is not lower than that of direct CH_3 dissociation (E_a = 51.21 kcal/mol). Through its reactions with precursor and key intermediate species, NH_3 not only aids in the removal of carbon from the system but also contributes to the formation of a stabilised, cross-linked BN_3 coordination environment, essential requirements for the synthesis of a carbon-free, pure h-BN network.

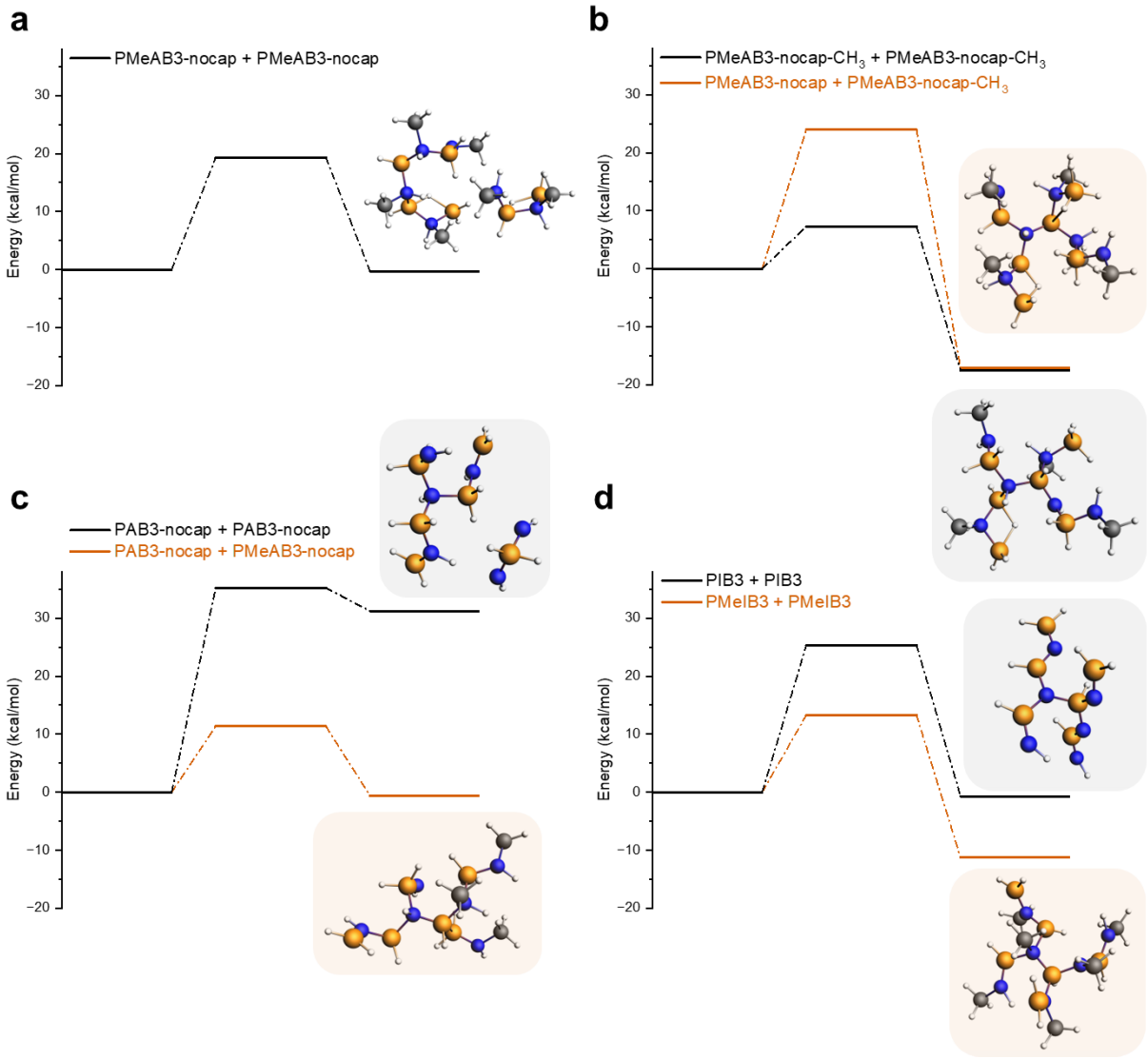

Figure 4.15: Energy diagram for the network formation of PMeAB3-nocap. (a) Reaction of PMeAB3-nocap + PMeAB3-nocap. (b) Black: reaction of PMeAB3-nocap-CH_3 + PMeAB3-nocap-CH_3; orange: reaction of PMeAB3-nocap + PMeAB3-nocap-CH_3. (c) Black: reaction of PAB3-nocap + PAB3-nocap; orange: reaction of PMeAB3-nocap + PAB3-nocap. (d) Black: reaction of PIB3 + PIB3; orange: reaction of PMeIB3 + PMeIB3.

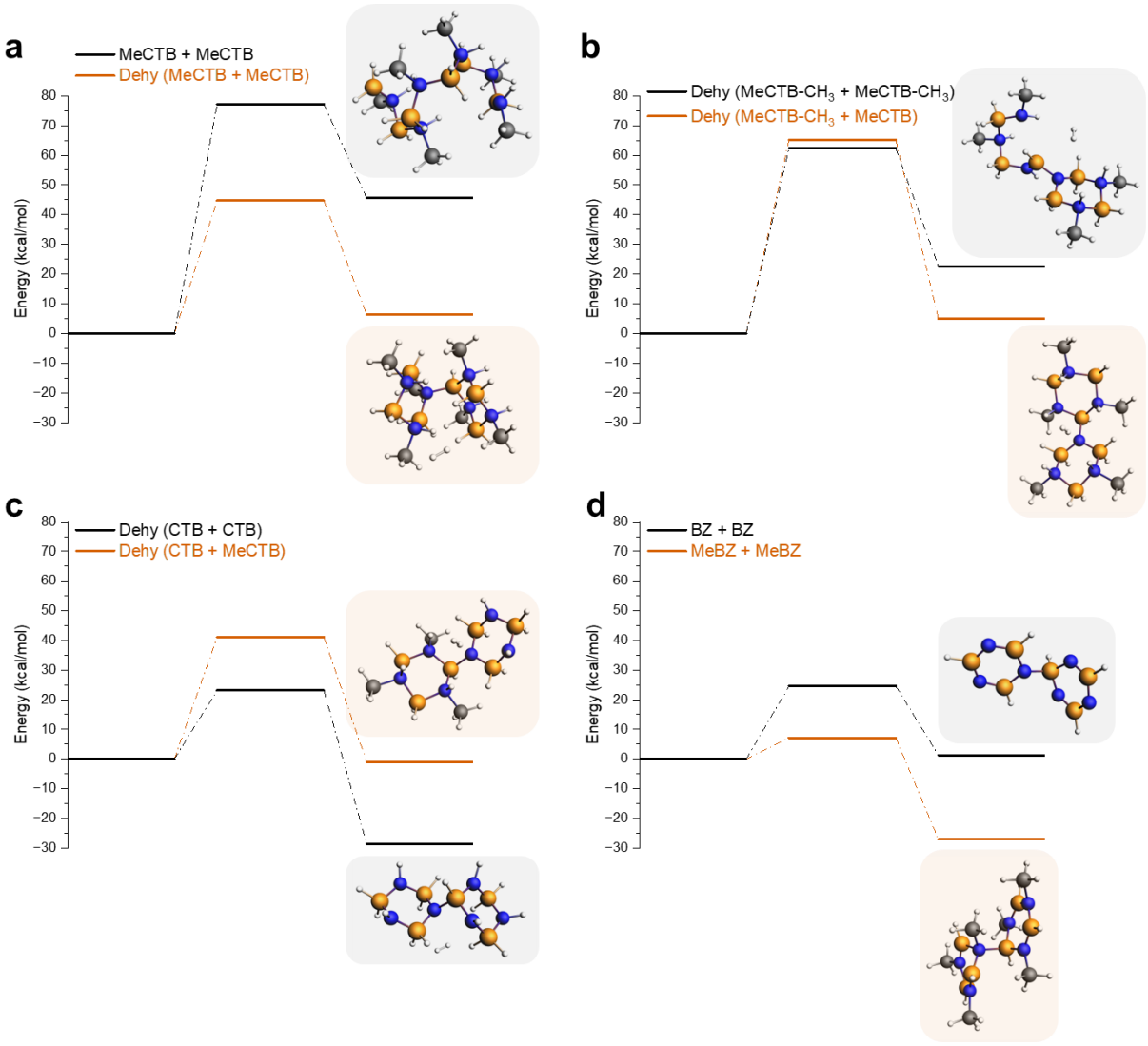

Figure 4.16: Energy diagram for the network formation of MeCTB. (a) Black: reaction of MeCTB + MeCTB; orange: dehydrogenation of MeCTB + MeCTB. (b) Black: dehydrogenation of MeCTB-CH_3 + MeCTB-CH_3; orange: dehydrogenation of MeCTB + MeCTB-CH_3. (c) Black: dehydrogenation of CTB + CTB; orange: dehydrogenation of MeCTB + CTB. (d) Black: dehydrogenation of BZ + BZ; orange: dehydrogenation of MeBZ + MeBZ.

Having established the thermal decomposition pathways of individual precursor molecules, I now examine the interactions between two thermally decomposed species, as these represent the initial steps in the formation of the h-BN network (**Figure 4.15** and **4.16**). **Figure 4.15** illustrates the interaction between two linear B–N species. Two intact PMeAB3-nocap molecules do not favour the formation of a branched network without prior dehydrogenation; in such cases, the polymer chains are prone to eventual fragmentation (**Figure 4.15a**). However, upon prior demethylation to yield PMeAB3-nocap-CH_3, the resulting species tend to form stable branched structures, either with each other (E_a = 7.29 kcal/mol) or with undecomposed PMeAB3-nocap (E_a = 24 kcal/mol) (**Figure 4.15b**). Further demethylation to produce fully demethylated PAB3-nocap enhances this branching behaviour, promoting the formation of cross-linked networks (E_a = 35.24 kcal/mol for bonding between two PAB3-nocap; E_a = 11.35 kcal/mol for bonding between a PAB3-nocap and a PMeAB3-nocap) (**Figure 4.15c**). Additionally, dehydrogenation leading to PMeIB , as well as combined demethylation and dehydrogenation to yield PIB, also favours the formation of stable branched structures (E_a = 13.3 kcal/mol for bonding between two PMeIB; E_a = 25.26 kcal/mol for bonding between two PIB) (**Figure 4.15d**). Both PMeIB and PIB are capable of interacting with each other to form robust, network-like architectures, supporting their role as key intermediates in the early stages of h-BN network formation.

Figure 4.16 illustrates the interaction between two cyclic B–N species. Dehydrogenation facilitates the bonding between two MeCTB molecules (E_a = 44.73 kcal/mol with dehydrogenation; E_a = 77.17 kcal/mol without dehydrogenation) (**Figure 4.16a**), while demethylation to form CTB further promotes the assembly of BN ring networks (E_a = 41.1 kcal/mol for bonding between a MeCTB and a CTB; E_a = 23.16 kcal/mol for bonding between two CTB) (**Figure 4.16c**). Complete dehydrogenation to produce MeBZ, as well as the combined effect of full dehydrogenation and demethylation to produce BZ, also contributes to

network formation (E_a = 7.15 kcal/mol for bonding between two MeBZ; E_a = 24.58 kcal/mol for bonding between two BZ) (**Figure 4.16d**). Overall, this indicates that both dehydrogenation and demethylation are critical in promoting molecular branching and cross-linking, marking the initial transition from linear/cyclic precursors toward the formation of a fully developed, carbon-free h-BN ceramic network.

4.3.2 Verification of the Chosen ReaxFF ($ReaxFF_{HCONSB}$) Parameters Set

To identify the most suitable force field (FF) from the available FF libraries, I conducted a comparative analysis between DFT and ReaxFF-calculated energies for key reactions relevant to PMeAB chemistry. The FF evaluated include $ReaxFF_{HCNOSB}$, $ReaxFF_{CBN}$, and $ReaxFF_{CHONBAlSiCl}$. The selected benchmark reactions are fundamental processes such as B–H, C–H, and N–H bond dissociation (**Figure 4.17**); B–N bond dissociation (**Figure 4.18**); C–C, C–N, and N–N bond dissociation (**Figure 4.19**); angular distortions involving B–N–B, C–N–B, and N–B–N (**Figure 4.20**); and H–H bond formation (**Figure 4.21**). By validating the performance of each FF against DFT reference data for these representative reactions, I can confidently select the most accurate FF for modelling the extended thermal decomposition pathways of precursor PMeAB and related compounds. These benchmark reactions collectively capture the essential chemical transformations underpinning PMeAB thermolysis and are therefore critical for ensuring the reliability of the FF in subsequent simulations.

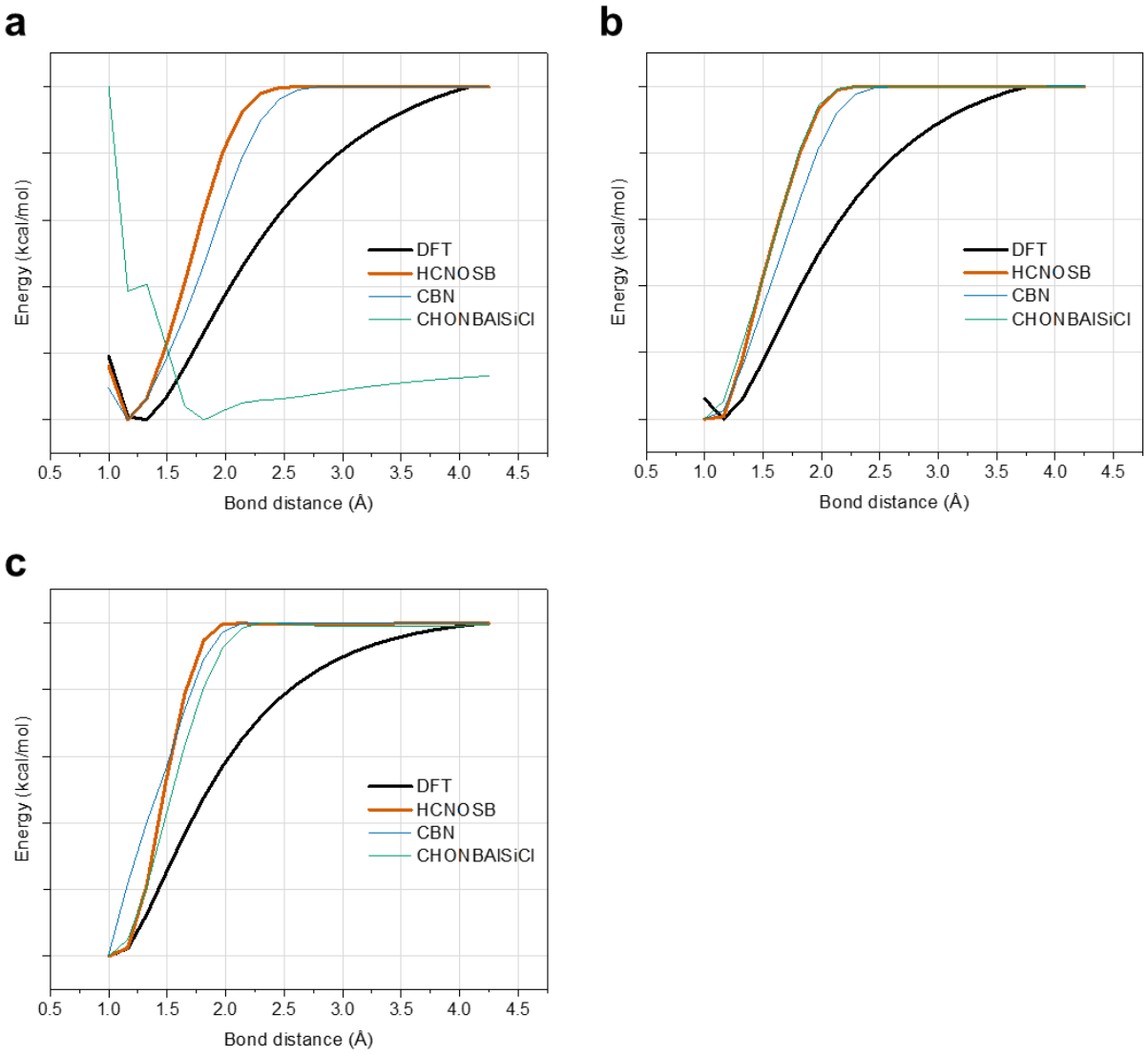

Figure 4.17: Comparison between DFT and ReaxFF for PMeAB related chemistry. The black, orange, blue, and green curve represent result based on DFT, $ReaxFF_{HCNOSB}$, $ReaxFF_{CBN}$, and $ReaxFF_{CHONBAlSiCl}$, respectively. (a) Reaction energy for the B–H bond dissociation of a BH molecule. (b) Reaction energy for the C–H bond dissociation of a CH molecule. (c) Reaction energy for the N–H bond dissociation of a NH molecule.

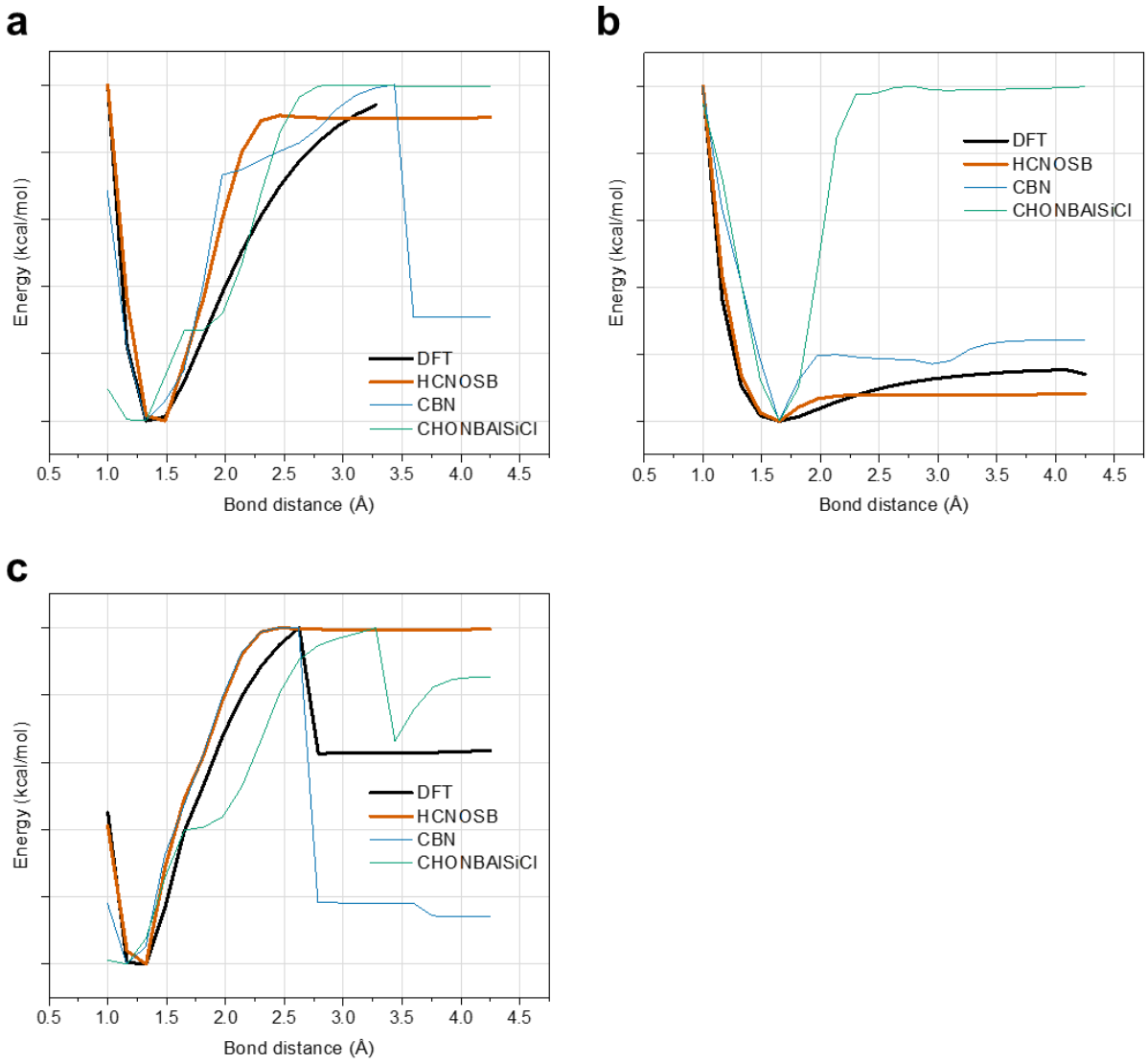

Figure 4.18: Comparison between DFT and ReaxFF for PMeAB related chemistry. The black, orange, blue, and green curve represent result based on DFT, ReaxFF$_{HCNOSB}$, ReaxFF$_{CBN}$, and ReaxFF$_{CHONBAlSiCl}$, respectively. (a) Reaction energy for the B–N bond dissociation of a MeAB molecule. (b) Reaction energy for the B–N bond dissociation of a MeIB molecule. (c) Reaction energy for the B–N bond dissociation of a $BH{=}NCH_3$ molecule.

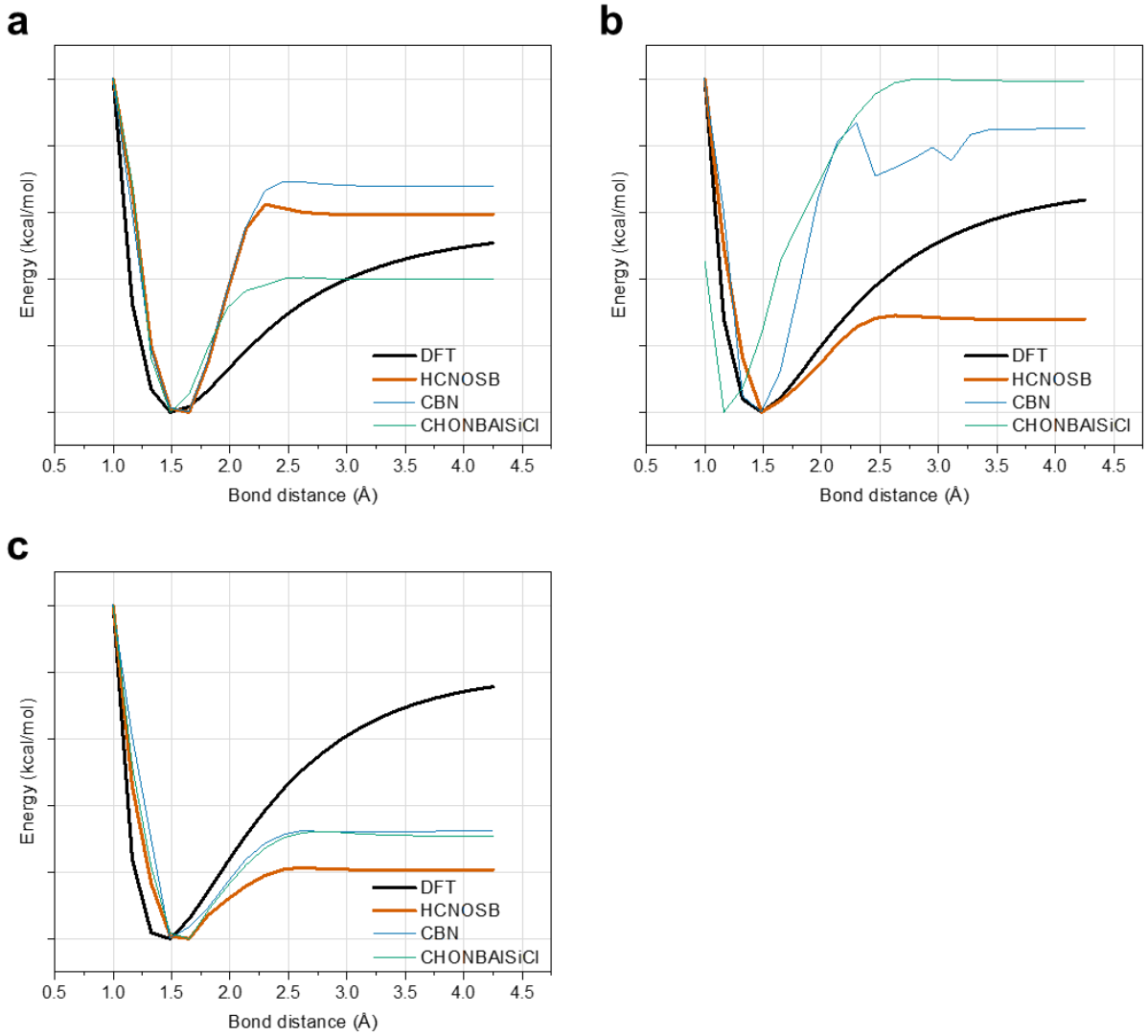

Figure 4.19: Comparison between DFT and ReaxFF for PMeAB related chemistry. The black, orange, blue, and green curve represent result based on DFT, ReaxFF$_{HCNOSB}$, ReaxFF$_{CBN}$, and ReaxFF$_{CHONBAlSiCl}$, respectively. (a) Reaction energy for the C–C bond dissociation of a CH_3–CH_3 molecule. (b) Reaction energy for the C–N bond dissociation of a NH_2–CH_3 molecule. (c) Reaction energy for the N–N bond dissociation of a NH_2–NH_2 molecule.

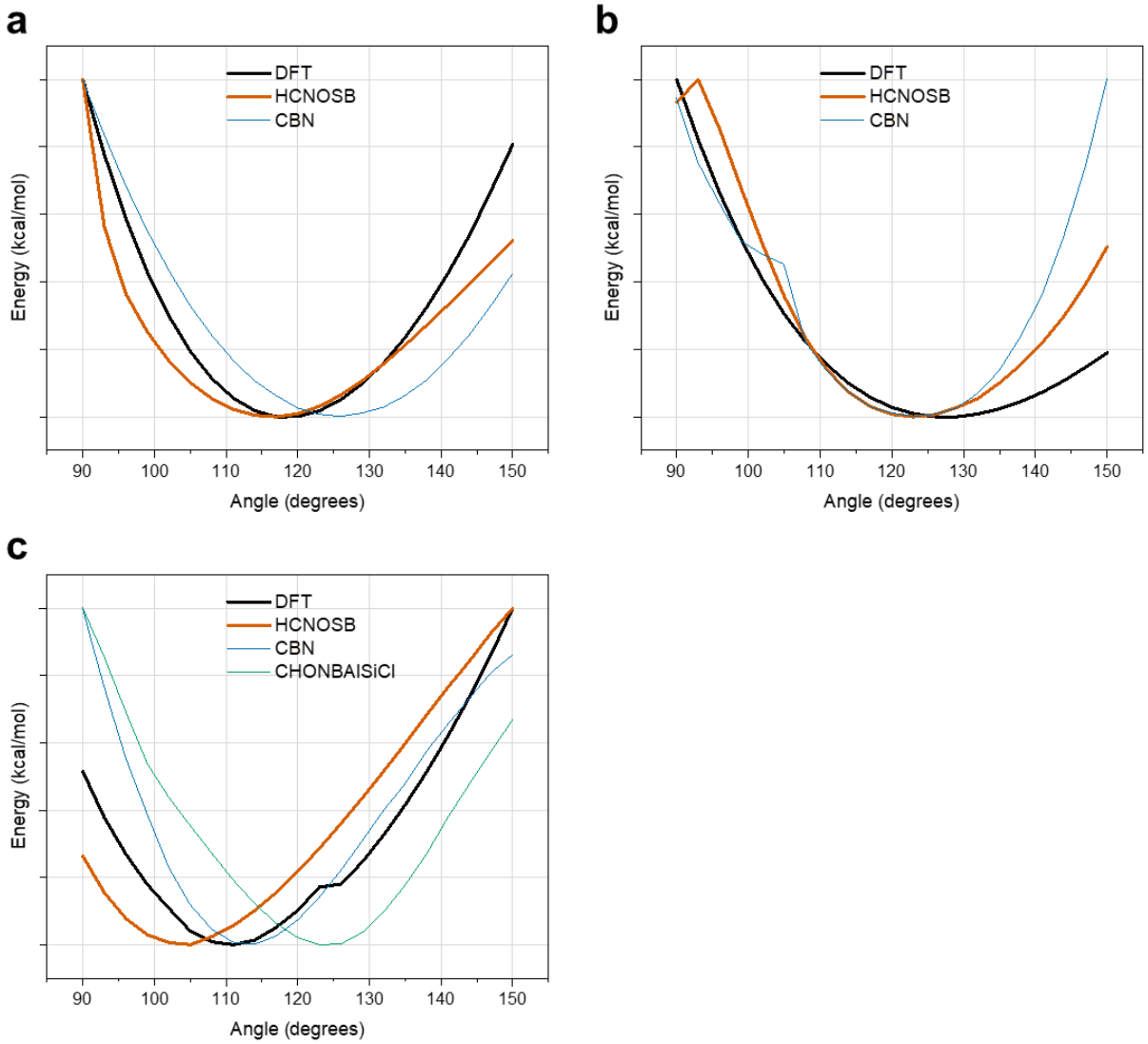

Figure 4.20: Comparison between DFT and ReaxFF for PMeAB related chemistry. The black, orange, blue, and green curve represent result based on DFT, $ReaxFF_{HCNOSB}$, $ReaxFF_{CBN}$, and $ReaxFF_{CHONBAlSiCl}$, respectively. (a) Reaction energy for the B–N–B angle distortion of a $BH_3NHCH_3BH_3$ molecule. (b) Reaction energy for the C–N–B angle distortion of a MeIB molecule. (c) Reaction energy for the N–B–N angle distortion of a $NH_2CH_3BH_2NH_2CH_3$ molecule.

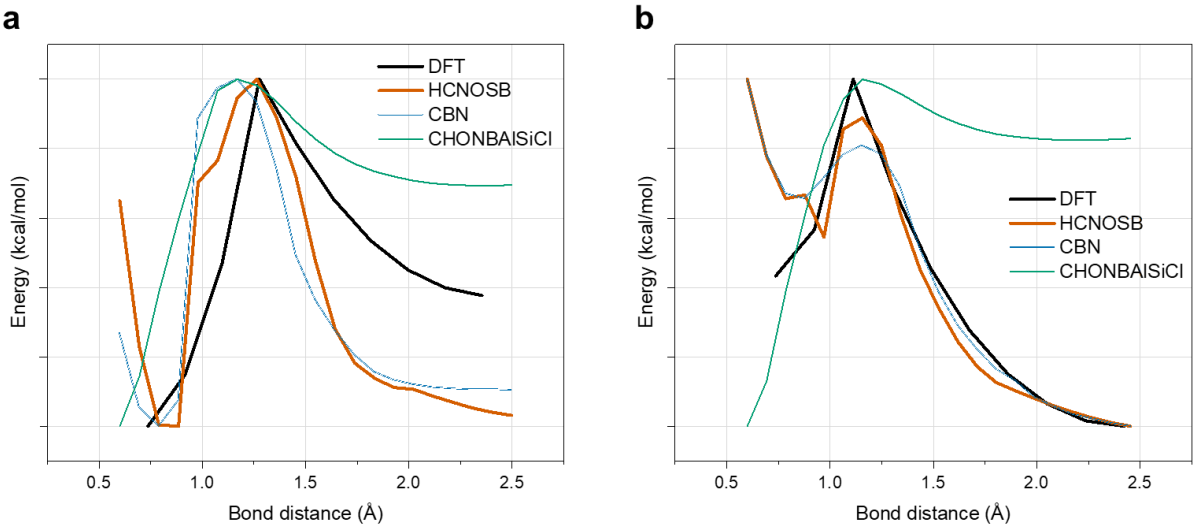

Figure 4.21: Comparison between DFT and ReaxFF for PMeAB related chemistry. (a) Reaction energy for the H–H bond formation of a MeAB molecule across B–N. (b) Reaction energy for the H–H bond formation of a MeIB molecule across B–N.

The ReaxFF$_{CHONBAlSiCl}$ performs poorly in predicting reaction energies for systems containing boron. Specifically, it shows significant deviation from DFT reference data in cases such as B–H bond dissociation (**Figure 4.17a**), B–N bond dissociation (**Figures 4.18b** and **4.18c**), and B–N bond formation in MeAB and MeIB (**Figure 4.21**). Due to its poor agreement with DFT results, this FF was excluded from further consideration. In contrast, the other two FF, ReaxFF$_{HCNOSB}$ and ReaxFF$_{CBN}$, generally show better agreement with DFT data across reactions involving B, C, N, and/or H atoms. However, ReaxFF$_{CBN}$ exhibits abnormal behaviour in certain cases, such as B–N bond dissociation (**Figure 4.18**) and C–N bond dissociation (**Figure 4.19b**), where the energy curves display abrupt drops or discontinuities. These artifacts suggest potential instability or unreliability in MD simulations. On the other hand, ReaxFF$_{HCNOSB}$ consistently produces smooth and continuous energy profiles in all tested cases, indicating more stable and physically meaningful performance. Based on these observations, I expect a decent transferability for the ReaxFF$_{HCNOSB}$ to study the PMeAB-related thermal decomposition chemistry.

4.3.3 Large-Scale Molecular Dynamics Simulations based on ReaxFF$_{HCONSB}$

Single-molecule simulations were performed using multiple unique initial configurations to statistically assess the decomposition behaviour. Atomic coordinates and velocities for these configurations were extracted from different time steps of a prior simulation equilibrated at 300 K. The initiation of H_2 release from PMeAB3, MeAB, and MeCTB is expected to be at least partially unimolecular in nature; thus, single-molecule simulations provide an efficient and appropriate method for investigating this process.

In parallel, multi-molecule simulations were conducted across a range of temperatures by continuously increasing the thermostat from 300 K to 5000 K at a constant heating rate. It is important to note that this temperature ramp represents a computational modelling strategy rather than an experimental condition. The upper limit of 5000 K is intentionally chosen to accelerate reaction kinetics and observe significant chemical transformations within an accessible simulation timeframe, given the constraints of molecular dynamics timescales. These simulations enabled the calculation of the H_2 release rate as a function of temperature, as well as the identification of the temperature at which maximum H_2 evolution occurs. To more accurately represent experimental conditions, a molecular sink model was implemented by selectively removing H_2 and/or CH_x species during the simulation. This approach mimics the effect of NH_3 thermolysis, which removes methyl groups, and prevents excessive H_2 in the system.

A compositional analysis of the reaction products and intermediates was performed using the ChemTraYzer2 model to identify the key molecular species involved in the decomposition

process and to elucidate the overall reaction pathways. The simulation parameters, including temperature range, heating rate, and simulation box dimensions, are summarised in **Table 4.1**.

Table 4.1: Respective configurations for ReaxFF MD simulations.

Simulation	**Temperature [K]**	**Heating Rate [K/fs]**	**Cube Length [nm]**
1 PMeAB3-nocap molec. const. temp.	1200; 1300, 1400; 1500; 1600; 1700; 1800; 1900; 2000	N/A	0.75
1 MeIB molec. const. temp.	2000; 2100; 2200; 2300; 2400; 2500; 2600; 2700; 3000	N/A	0.75
1 MeCTB molec. const. temp.	1000; 1100; 1200; 1300, 1400; 1500; 1600; 1700; 1800; 1900; 2000	N/A	0.75
10 PMeAB3-nocap molec. temp. ramp	300−5000	0.01	1.5
30 MeIB molec. temp. ramp	300−5000	0.01	1.5
10 MeCTB molec. temp. ramp	300−5000	0.01	1.5
10 PMeAB3-nocap molec. const. temp.	1500; 2000; 2500; 3000	N/A	1.5
10 PMeAB3 molec. const. temp.	1500; 2000; 2500; 3000	N/A	1.5
30 MeIB molec. const. temp.	1500; 2000; 2500; 3000	N/A	1.5
30 MeAB molec. const. temp.	1500; 2000; 2500; 3000	N/A	1.5
10 MeCTB molec. const. temp.	1500; 2000; 2500; 3000	N/A	1.5
10 MeBZ molec. const. temp.	1500; 2000; 2500; 3000	N/A	1.5
10 PMeAB3-nocap molec. temp. ramp with molec. sink model (-H_2; -CH_x)	300−5000	0.01	1.5
10 PMeAB3-nocap molec. temp. ramp with molec. sink model (-H_2)	300−5000	0.01	1.5
30 MeIB molec. temp. ramp with molec. sink model (-H_2; -CH_x)	300−5000	0.01	1.5

30 MeIB molec. temp. ramp with molec. sink model (-H_2)	300−5000	0.01	1.5
10 MeCTB molec. temp. ramp with molec. sink model (-H_2; -CH_x)	300−5000	0.01	1.5
10 MeCTB molec. temp. ramp with molec. sink model (-H_2)	300−5000	0.01	1.5

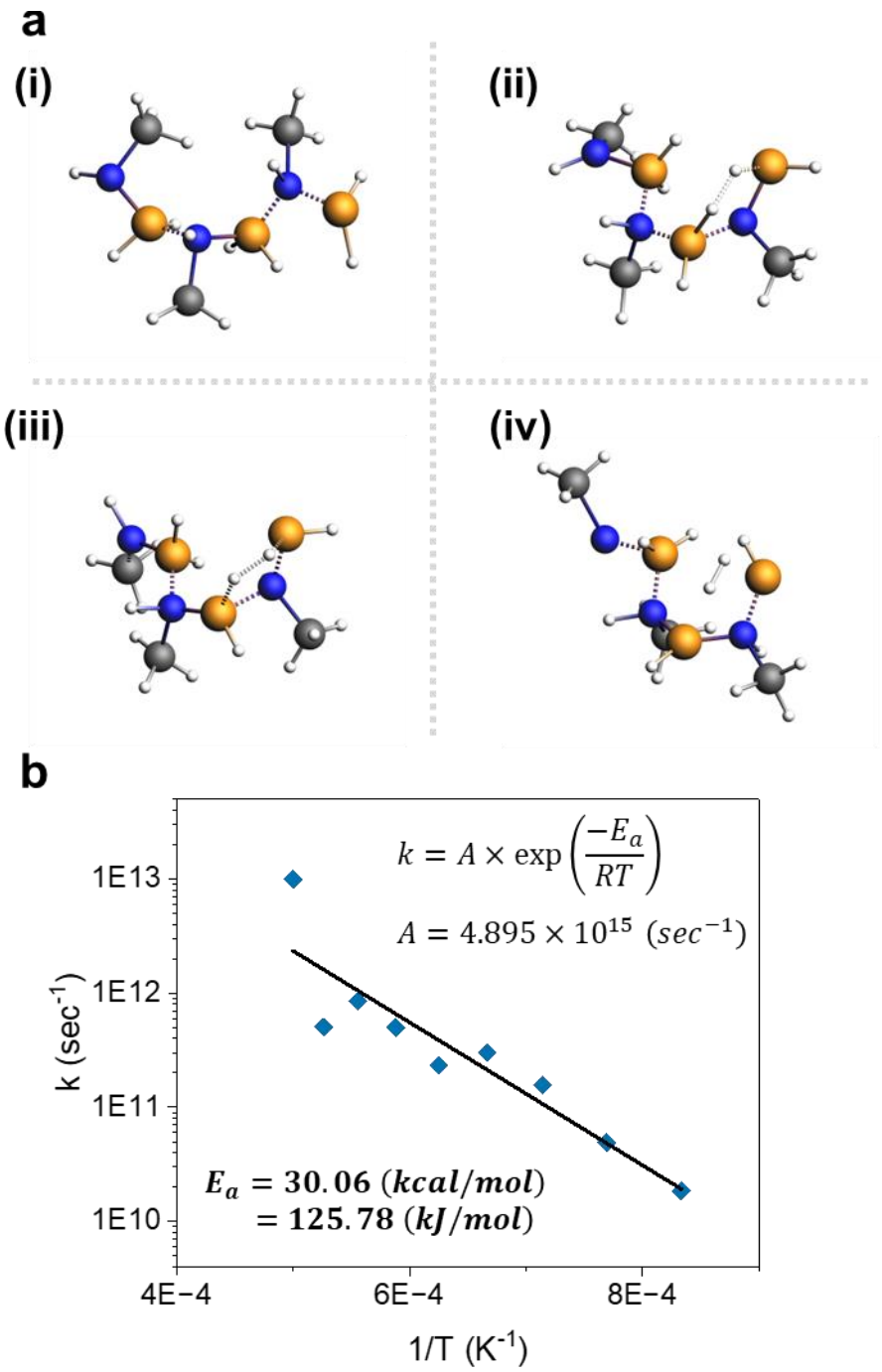

Figure 4.22: A 1 PMeAB3-nocap constant temperature simulations. (a) Sequence of images showing the release of H_2 from PMeAB3-nocap. (b) Reaction rate constant (k) versus inverse temperature, inset shows the calculated activation energy (E_a).

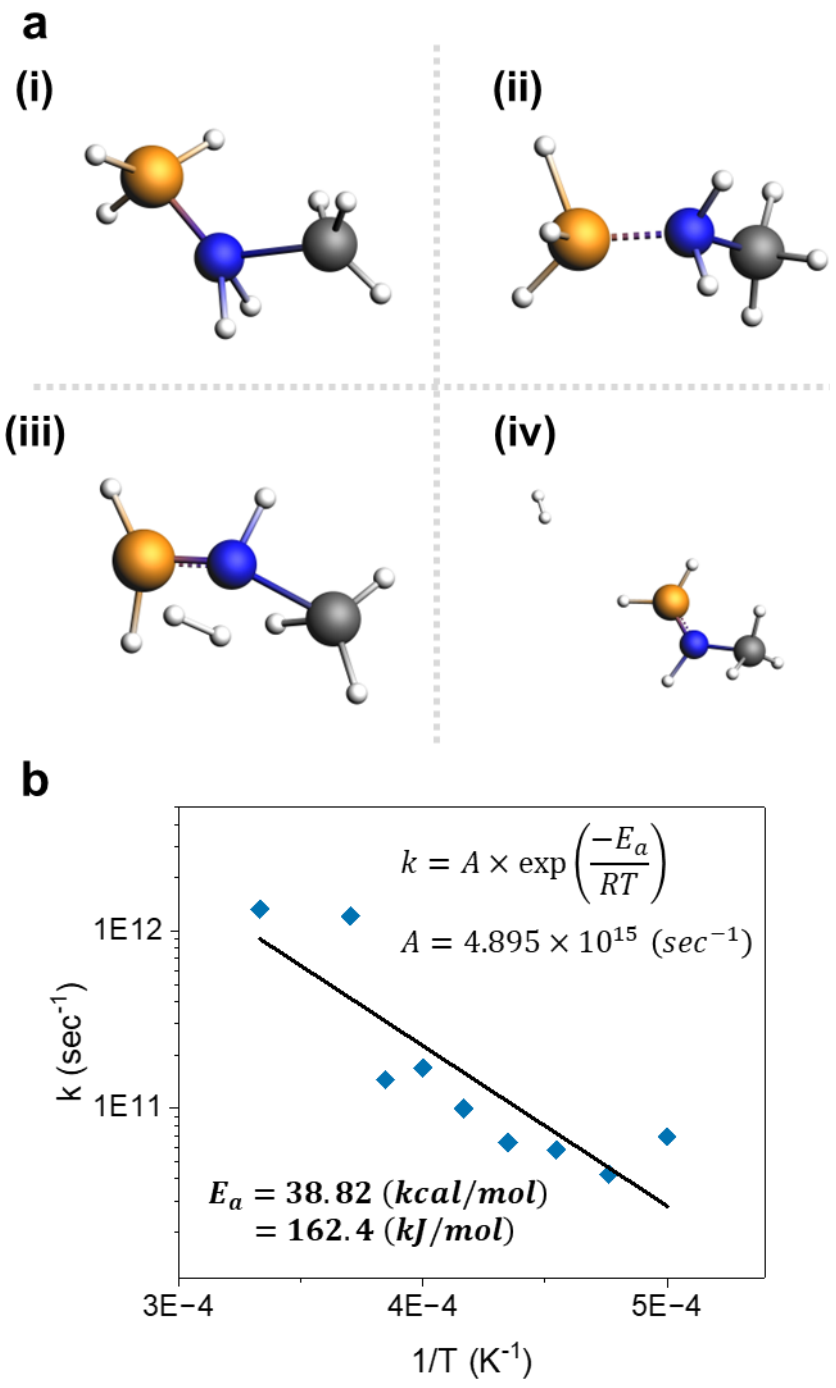

Figure 4.23: A 1 MeAB constant temperature simulations. (a) Sequence of images showing the release of H_2 from MeAB. (b) Reaction rate constant (k) versus inverse temperature, inset shows the calculated activation energy (E_a).

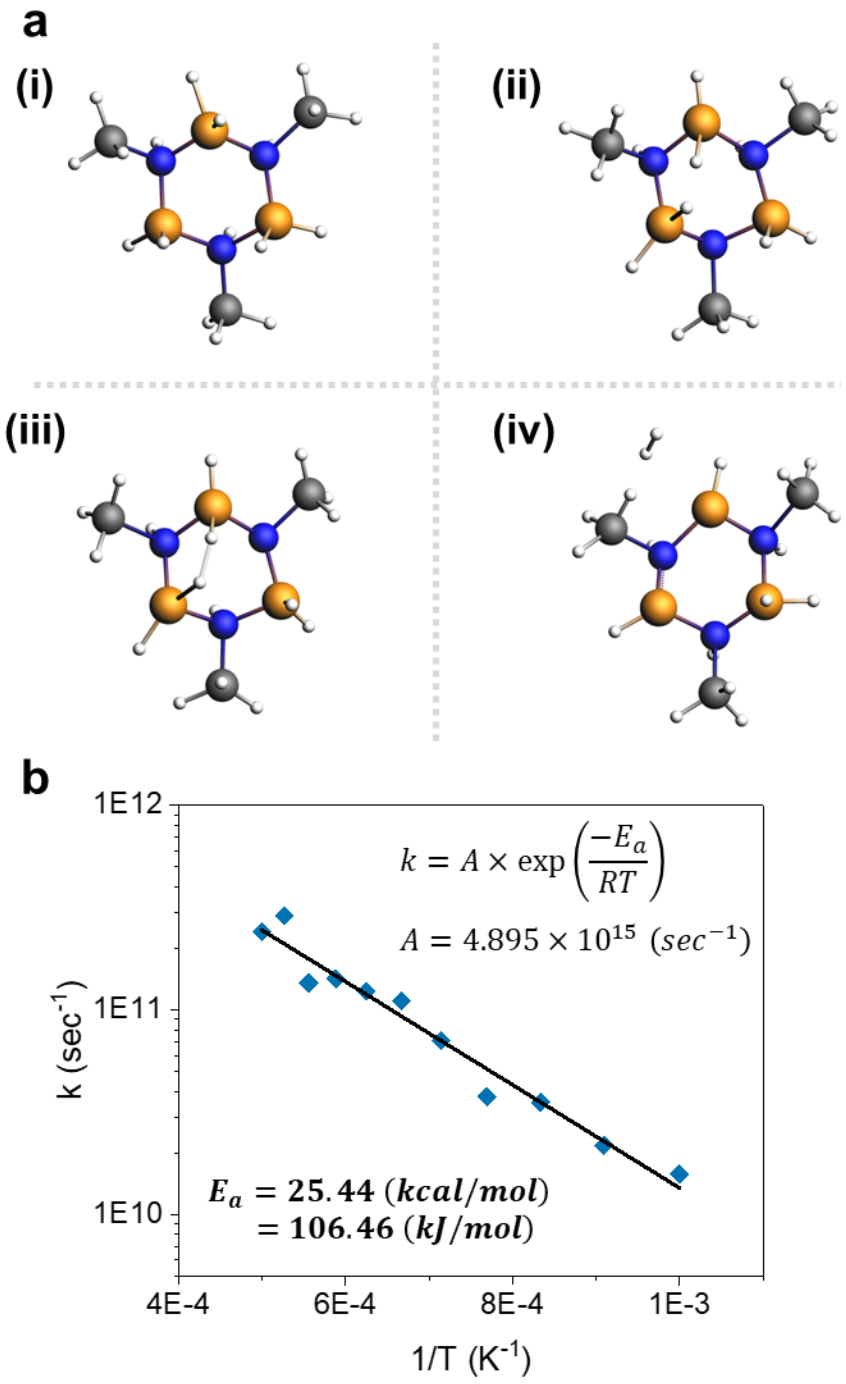

Figure 4.24: A 1 MeCTB constant temperature simulations. (a) Sequence of images showing the release of H_2 from MeCTB. (b) Reaction rate constant (k) versus inverse temperature, inset shows the calculated activation energy (E_a).

Figure 4.22a, **4.23a**, and **4.24a** show the sequence of single molecule simulations for PMeAB3-nocap at 1500 K, MeAB at 3000 K, and MeCTB at 1500 K, respectively, each depicting the release of one H_2 molecule. As the temperature increases, the hydrogen bonds in all three molecules undergo significant stretching. For PMeAB3-nocap and MeCTB, this ultimately results in a H atom bonded to one boron atom forming a bond with a H atom bonded to a neighbouring boron. In the case of MeAB, a H atom bonded to boron forms a bond with a H atom bonded to nitrogen, similar to the mechanism observed in AB ReaxFF simulations by *Weismiller et al*.[123] The newly formed H_2 molecule then dissociates from the parent molecule, leading to a dehydrogenated product. **Figure 4.22b**, **4.23b**, and **4.24b** present plots of the reaction rate constant (k) as a function of the inverse temperature (1/T). The rate constants were determined by conducting single molecule simulations initiated from random configurations after equilibration at 300 K for 100 ps. Simulations were performed across a temperature range of 1000–3000 K, and the time required for H_2 release was recorded. At temperatures above 3000K, molecular backbones frequently dissociate, whereas at temperatures below 1000K, H_2 release occurs over a prolonged timescale, often exceeding hundreds of nanoseconds to microseconds, which is infeasible to capture within the practical duration of typical molecular dynamics simulations (usually limited to 10–100 ps for reactive studies).

An exponential fit to the data was used to extract activation energies based on the Arrhenius equation. The calculated activation energies are as follows: E_a = 30.06 kcal·mol^{-1} (125.78 kJ·mol^{-1}) for PMeAB3-nocap, E_a = 38.82 kcal·mol^{-1} (162.4 kJ·mol^{-1}) for MeAB, and E_a = 25.44 kcal·mol^{-1} (106.46 kJ·mol^{-1}) for MeCTB. E_a of MeAB is in good agreement with the previously reported computational value of 43.3 kcal·mol^{-1}.[115] This value also compares reasonably with the experimental activation energy of 28 kcal·mol^{-1} for the dehydrogenation of AB,[281] and 32.6 kcal·mol^{-1} for the dehydrogenation of C_2H_6.[282] Among the three, MeCTB exhibits the lowest E_a, likely due to its ring structure, which brings two H atoms into close proximity, facilitating

H–H bond formation. It is worth noting that at temperatures approaching 3000 K, some simulation trajectories exhibit dissociation of B–N or N–C bonds, leading to the formation of BH_x + NCH_x or CH_x + BNH_x fragments prior to the target H_2 release. These instances were excluded from my analysis and were not considered in the reported results.

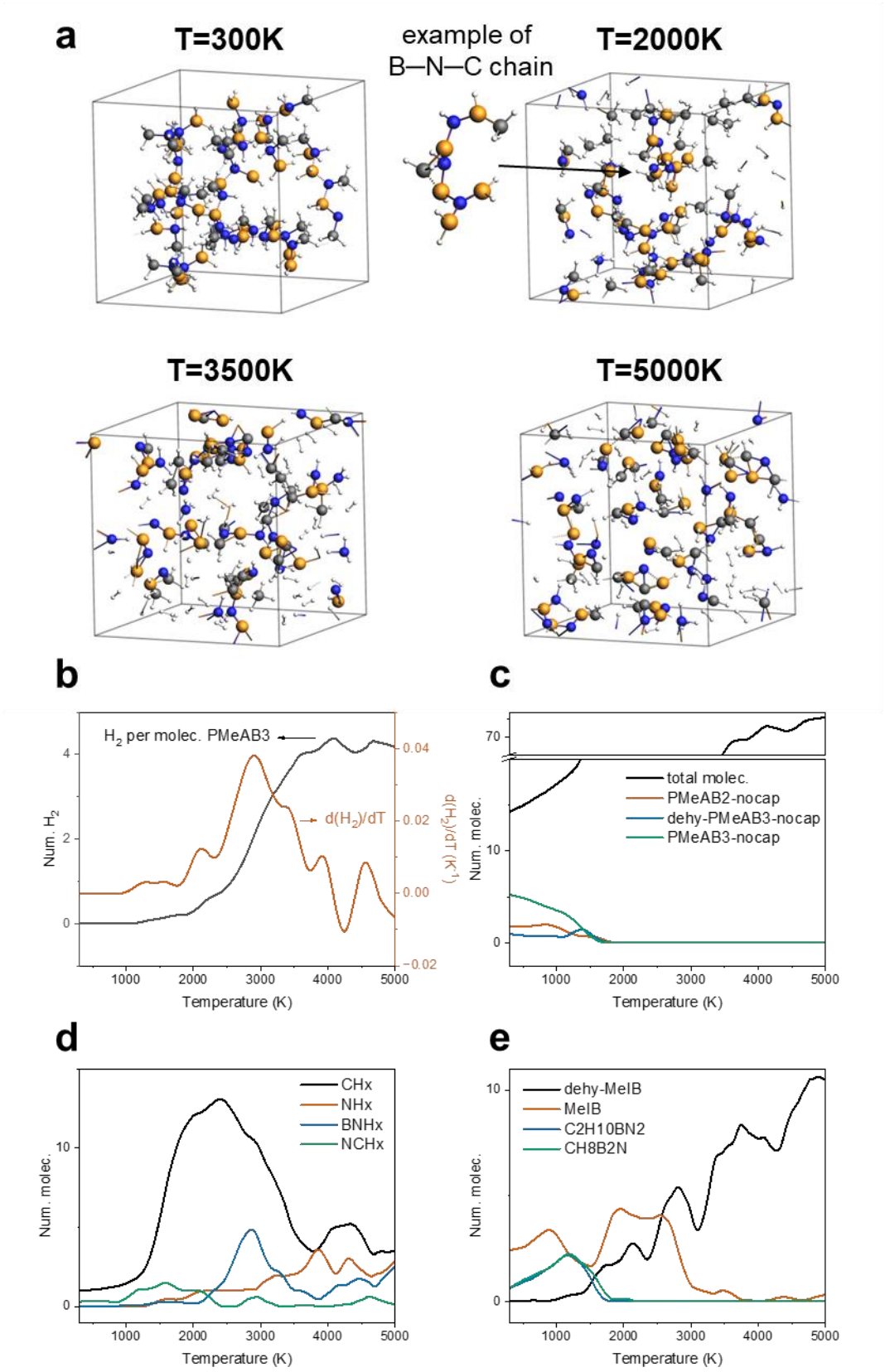

Figure 4.25: A 10 PMeAB3-nocap temperature ramp simulation. (a) Snapshots at 300, 2000, 3500, and 5000 K. (b) Rate of H_2 release per change in temperature. (c-e) Evolution of the reactants, major intermediate products, and radicals observed.

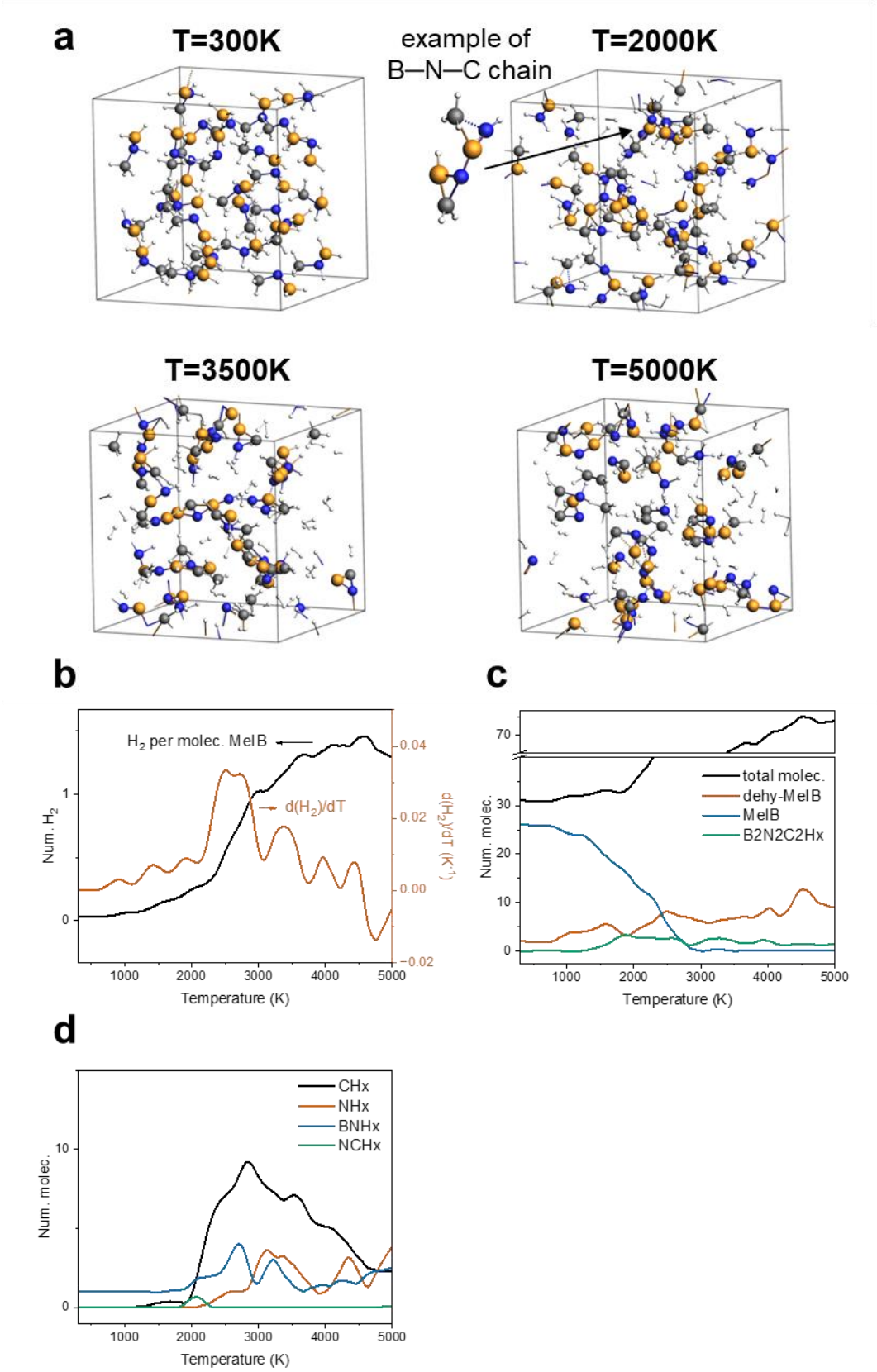

Figure 4.26: A 30 MeIB temperature ramp simulation. (a) Snapshots at 300, 2000, 3500, and 5000 K. (b) Rate of H_2 release per change in temperature. (c-e) Evolution of the reactants, major intermediate products, and radicals observed.

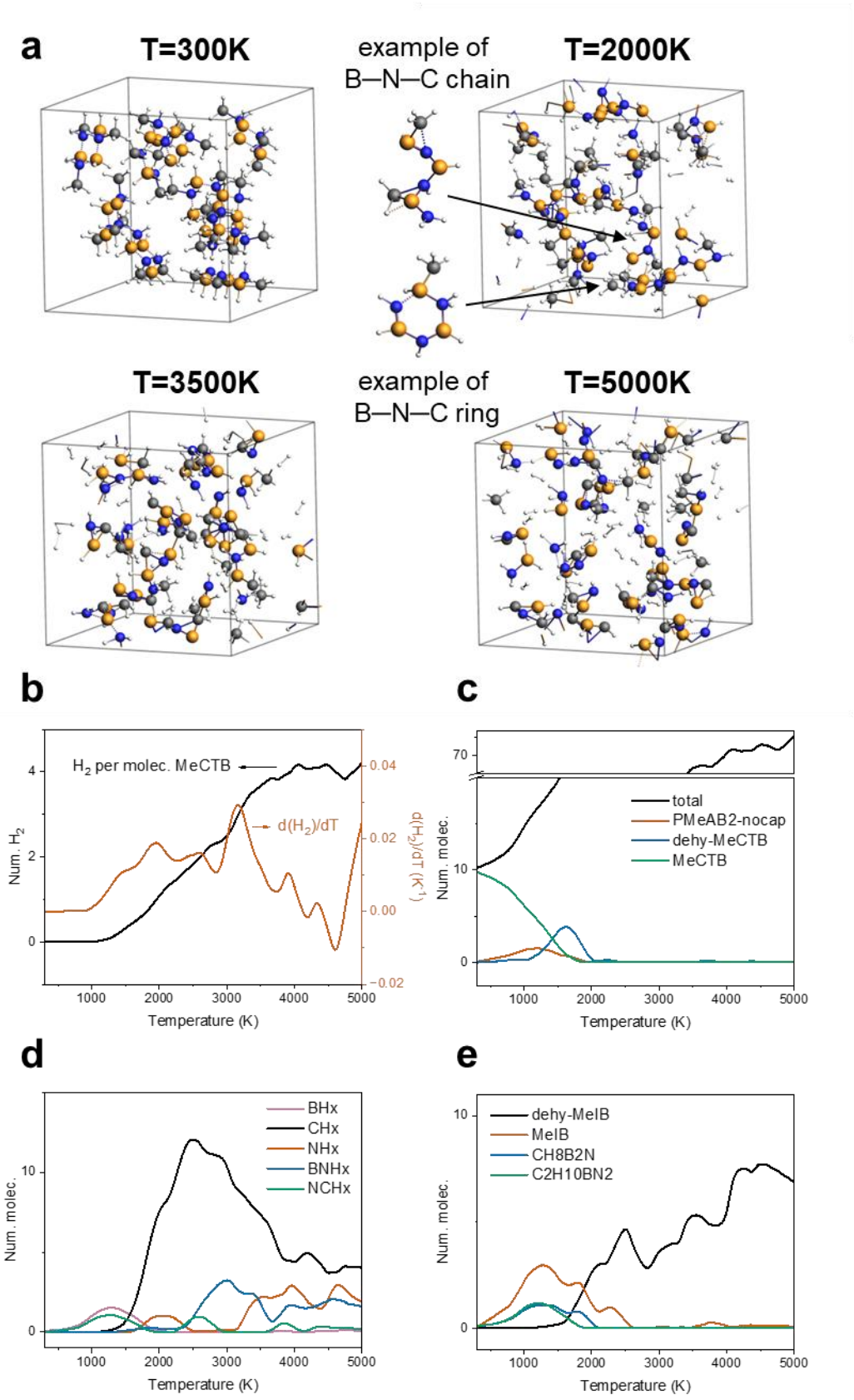

Figure 4.27: A 10 MeCTB temperature ramp simulation. (a) Snapshots at 300, 2000, 3500, and 5000 K. (b) Rate of H_2 release per change in temperature. (c-e) Evolution of the reactants, major intermediate products, and radicals observed.

Figures 4.25b, **4.26b**, and **4.27b** show the rate of H_2 release per molecule from temperature ramp simulations of 10 PMeAB3-nocap molecules, 30 MeIB molecules, and 10 MeCTB molecules, respectively. For PMeAB3-nocap, H_2 release starts at 1800 K, peaks at 2900 K, and remains substantial until 4250 K. In the case of MeIB, H_2 release begins at 2120 K, peaks at 2490 K, and remains until 3760 K. The delayed onset of MeIB dehydrogenation is due to its dependence on dehydropolymerisation, a process that releases H_2 through the formation of polymeric B–N chains, as shown in **Figure 4.26a** at 2000 K. Unlike PMeAB3-nocap, which exhibits a single dominant release peak, MeIB displays three additional minor peaks at 3380 K, 3970 K, and 4440 K, corresponding to ongoing dehydropolymerisation events. For MeCTB, H_2 release starts much earlier at 890 K, peaks at 3160 K, and continues substantially until 3760 K. The early onset of H_2 release in MeCTB is likely due to its ring structure, which spatially favours hydrogen elimination by bringing two hydrogen atoms into close proximity. An additional release peak appears at 1960 K, prior to the main peak, which is attributed to the inherent stability of the B–N ring structure, facilitating early-stage dehydrogenation prior to the volatile dissociation of B–N bonds. As shown in **Figure 4.27a** at 2000 K, intact B–N rings are still observable at this stage. The main dehydrogenation peak at higher temperatures corresponds to H_2 release along B–N chain structures, similar to the behaviour observed in PMeAB3-nocap. At elevated temperatures, most MeCTB rings break apart to form linear B–N chains, leading to dehydrogenation dynamics comparable to those of PMeAB3-nocap.

The release of four equivalents of H_2 per molecule was observed for both PMeAB3-nocap and MeCTB, which explains the earlier onset and of H_2 release and its continuous release over a broader temperature range. In contrast, the MeIB simulations show the release of only approximately one equivalent of H_2 per molecule. Complete dehydrogenation of all three cases require the formation of extended B–N polymeric structures. Although partial polymerisation is observed in the simulations, the time scales required for full polymer growth or ring structure

network formation extend well beyond the duration accessible in these simulations. It is important to note that experimental TGA-MS results in **Chapter 3** show vigorous H_2 release from PMeAB at 92.5 °C (**Figure 3.13**) and MeCTB at 121.6 °C (**Figure 3.29**). MeAB exhibit H_2 release from 55 °C as reported in the literature.[100] To make the simulations computationally feasible, elevated temperatures and rapid heating rates were employed, allowing H_2 release to be captured within the short simulation time frame (~1 ns).[123]

All three molecular precursors produce B–N–C chains, as shown in the insets of **Figure 4.25a**, **4.26a**, and **4.27a**. Carbon atoms are found bonded to boron, nitrogen, or both, which disrupts the formation of stable B–N rings, an essential structural feature for the development of a h-BN ceramics network. To further investigate this effect, I conducted additional simulations incorporating a molecular sink model, which removes H_2 and CH_x species during the simulations. These results serve as a comparison to the standard simulations and will be discussed later. Without removing molecules, only MeCTB yields B–N ring structures, with methyl groups still attached. The preexisting ring structure facilitates ring retention during decomposition. In contrast, PMeAB3-nocap forms only chain-like structures, although these chains are longer than those derived from MeIB due to the molecule's inherently extended structure. MeIB, owing to its small molecular size and greater freedom for bonding, tends to form excessive C–B–N three-member ring structures, interfering with the formation of extended B–N chains, as seen in PMeAB3-nocap.

Figure 4.25c–e, **4.26c–d**, and **4.27c–e** show the evolution of reactants, key intermediate products, and radicals during the simulations. Despite differences in the initial molecular structures, all three systems converge to a similar final count of approximately 70 molecules, indicating a comparable extent of decomposition. The PMeAB3-nocap molecules are fully decomposed by 1630 K, earlier than both MeCTB and MeIB. This can be attributed to the molecular structure of PMeAB3-nocap, which consists of relatively long B–N chains that are

more susceptible to thermal degradation. In contrast, the ring structure in MeCTB provides greater stability, delaying decomposition. Similarly, MeIB's compact results in fewer reactive sites and greater resistance to fragmentation, slowing its decomposition relative to PMeAB3-nocap.

The dissociation pathways of the three molecular precursors: PMeAB3-nocap, MeCTB, and MeIB, are broadly similar, leading to the formation of four common small species: NH_x, CH_x, BNH_x, and NCH_x. Among these, CH_x is the most dominant decomposition product across all three systems. The peak release temperatures for CH_x are 2850 K for MeIB, 2410 K for PMeAB3-nocap, and 2500 K for MeCTB. Larger quantities of CH_x are observed in PMeAB3-nocap and MeCTB compared to MeIB, suggesting that larger molecular frameworks, such as the B–N chains in PMeAB3-nocap and B–N rings in MeCTB, favour CH_x release. This behaviour is likely due to structural stabilisation offered by the B–N motifs, which facilitates selective C–N bond cleavage.[283,284] The formation of BNH_x species follows that of CH_x, though in smaller quantities, indicating partial fragmentation of B–N chains and rings. NH_x formation peaks at higher temperatures than CH_x, as it requires the cleavage of stronger B–N bonds (bond dissociation energy ~90–105 kcal/mol), compared to N–C bonds (~70–85 kcal/mol).[285] These four dominant species are consistent with the TGA-MS results (**Figure 3.13**), where my initial assignments suggest that the signals at m/z = 15–17 likely correspond to CH_x and NH_x fragments, while those at m/z = 26–31 are attributable to BNH_x and NCHv species. Small amounts of NCH_x are observed at lower temperatures (~1500 K), while BH_x species are notably absent as major products. This observation somewhat contradicts the experimental TGA-MS data (**Figure 3.13**), where I detected a signal at m/z = 13, likely corresponding to BH_3, and another at m/z = 26, which can be attributed to B_2H_6. Previous studies on AB pyrolysis also identify BH_3 and B_2H_6 as key intermediates, playing a critical role in the dehydrogenation process and appearing as dominant species during thermal decomposition.[218] The absence of

BCH_x species also reflects the unfavourable nature of B–C bonding in these systems, as both boron and carbon preferentially form bonds with nitrogen.[286] Larger molecular fragments, such as PMeAB2-nocap, MeIB, CH_8B_2N, and $C_2H_{10}BN_2$, are also detected in the MeCTB and PMeAB3-nocap simulations. These fragments result from the dissociation of the B–N backbone, either along the chain or within the ring, reflecting the various dissociation pathways accessible at high temperatures. In the case of MeIB, polymerisation is observed, including the formation of $B_2N_2C_2H_x$-type dimers, which peak around 1840 K (see **Figure 4.26a** for the example dimer). Ultimately, all three precursor types converge toward the formation of MeIB-like units, which continue to dehydrogenate up to 5000 K, following similar thermal behaviour in the latter stages of decomposition.

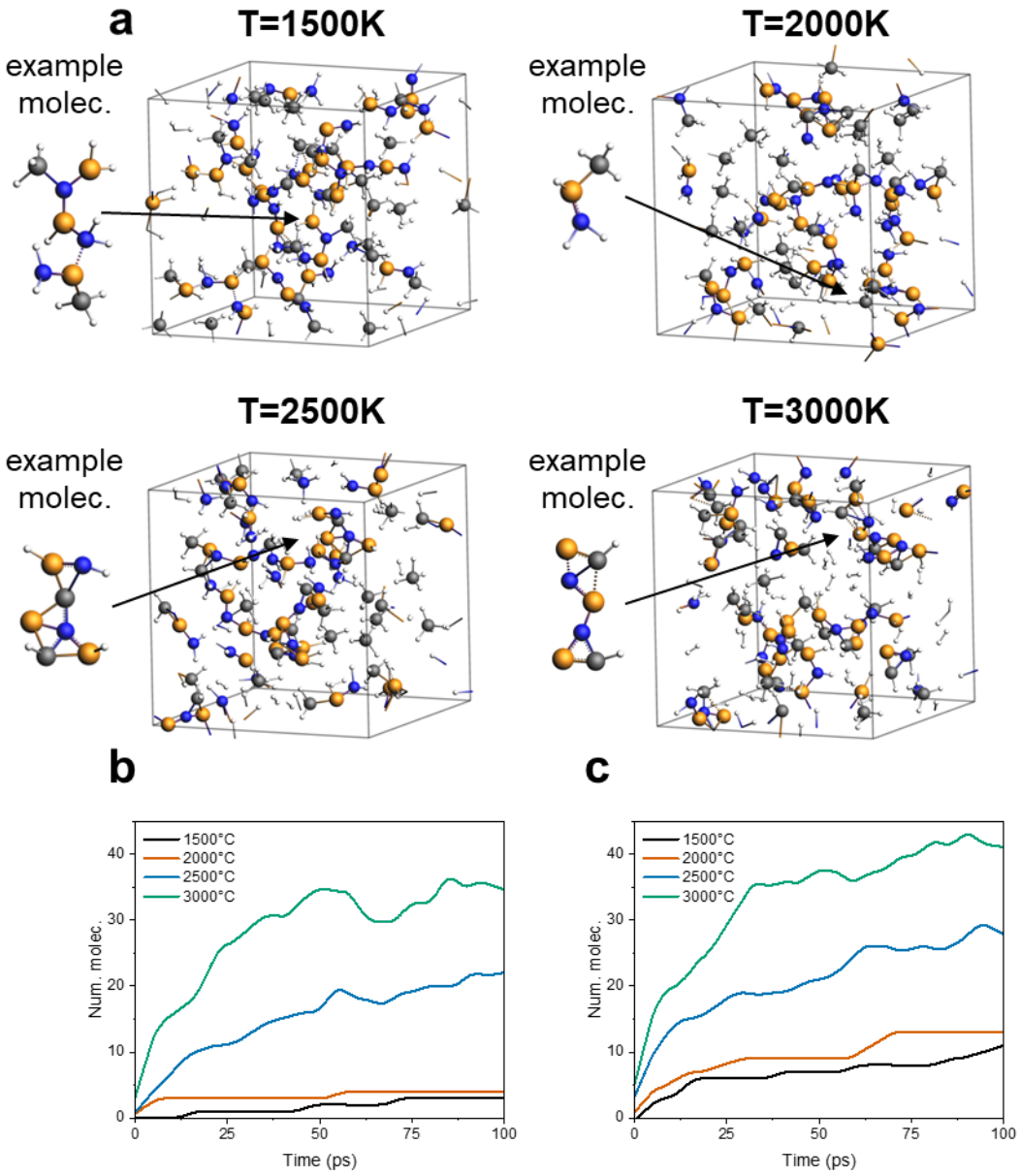

Figure 4.28: 10 PMeAB3-nocap constant temperature simulations at 1500, 2000, 2500, and 3000 K for 100 ps. (a) Snapshots of 1500, 2000, 2500, and 3000 K at 100 ps. (b) Rate of H_2 release versus time at 1500, 2000, 2500, and 3000 K. (c) 10 PMeAB3 constant temperature simulations. Rate of H_2 release versus time at 1500, 2000, 2500, and 3000 K.

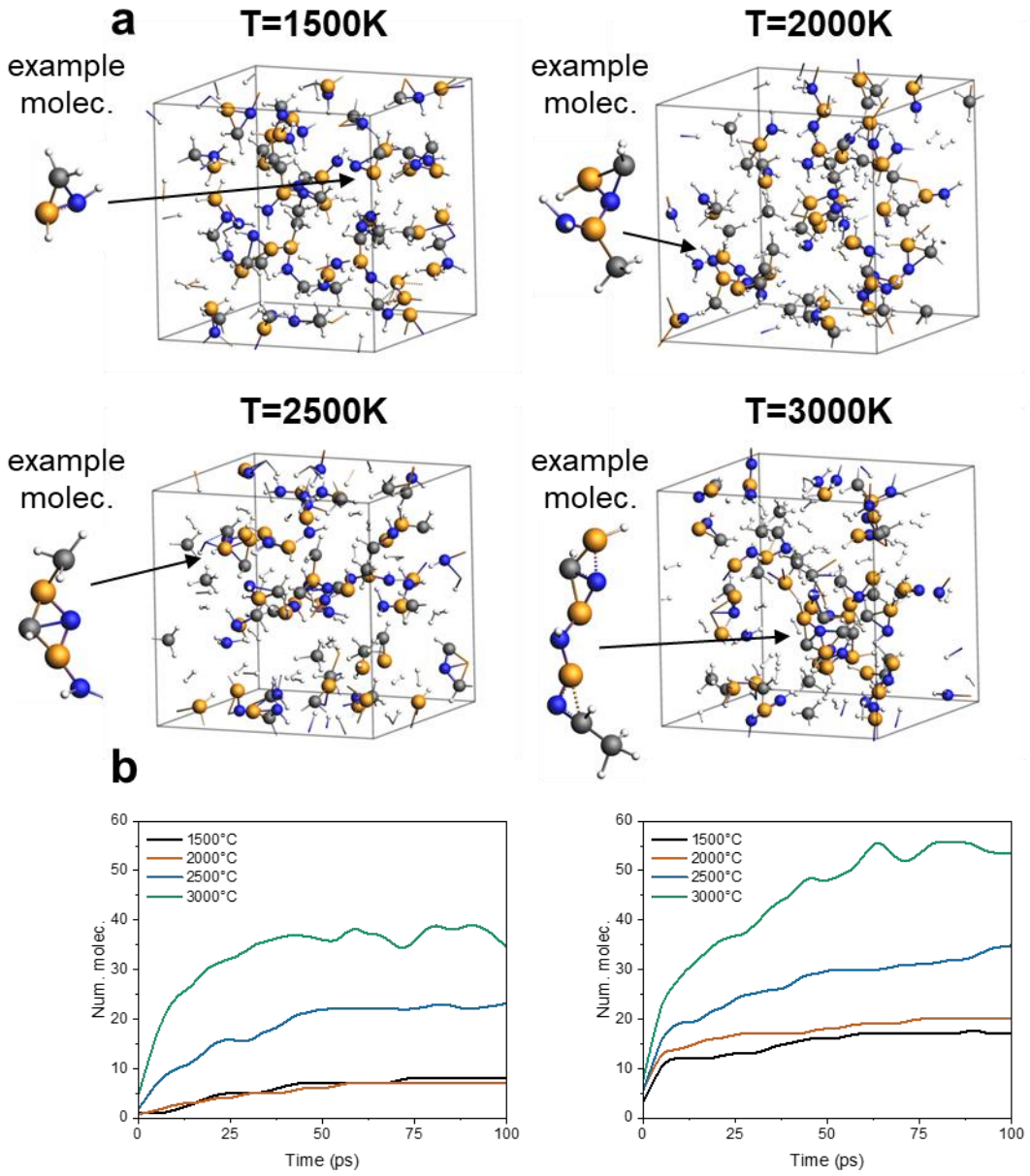

Figure 4.29: 30 MeIB constant temperature simulations at 1500, 2000, 2500, and 3000 K for 100 ps. (a) Snapshots of 1500, 2000, 2500, and 3000 K at 100 ps. (b) Rate of H_2 release versus time at 1500, 2000, 2500, and 3000 K. (c) 30 MeAB constant temperature simulations. Rate of H_2 release versus time at 1500, 2000, 2500, and 3000 K.

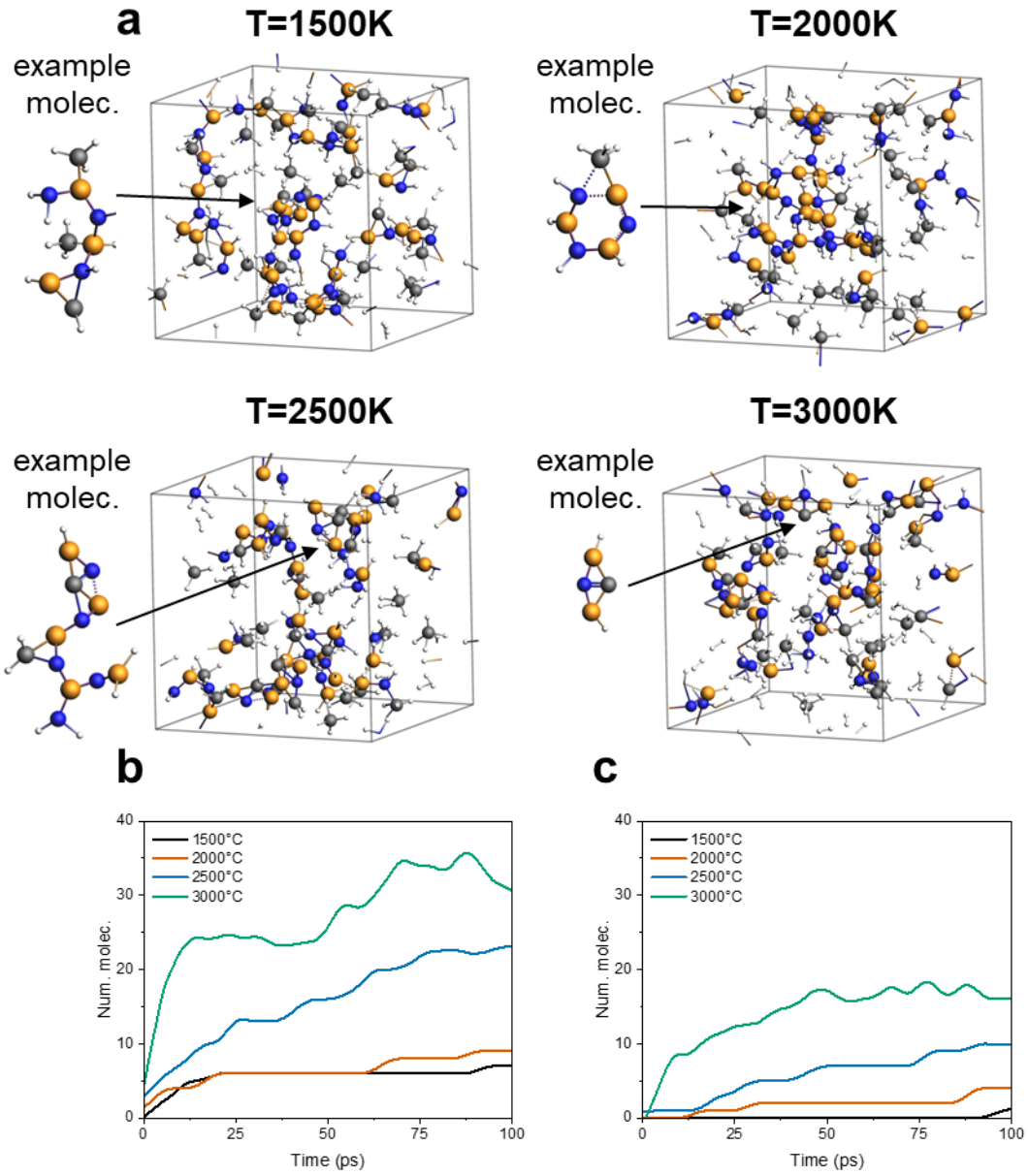

Figure 4.30: 10 MeCTB constant temperature simulations at 1500, 2000, 2500, and 3000 K for 100 ps. (a) Snapshots of 1500, 2000, 2500, and 3000 K at 100 ps. (b) Rate of H_2 release versus time at 1500, 2000, 2500, and 3000 K. (c) 10 MeBZ constant temperature simulations. Rate of H_2 release versus time at 1500, 2000, 2500, and 3000 K.

In addition to the temperature ramping simulations, I also investigated the dehydrogenation process under constant temperature conditions. **Figure 4.28**, **4.29**, and **4.30** show the number of released H_2 molecules as a function of simulation time for PMeAB3-nocap, MeIB, and MeCTB, respectively, at fixed temperatures of 1500, 2000, 2500, and 3000 K. These temperatures were selected based on the observation of significant B–N bond formation and dissociation events in the temperature ramping simulations (**Figure 4.25**, **4.26**, and **4.27**). For all three molecules, the amount of H_2 released increased with temperature and eventually saturated over time (**Figures 4.28b**, **4.29b**, and **4.30b**). At 1500 K and 2000 K, all three systems released a similar amount of H_2 (~5–10 molecules). However, at 2500 K, the amount nearly doubled to around 20 molecules, and at 3000 K, it doubled again to around 40 molecules, indicating a strong temperature dependence of the dehydrogenation process, and suggesting the existence of a threshold temperature above which significant H_2 volatilisation occurs.

At 1500 K, after 100 ps, the B–N chains in PMeAB3-nocap remained largely intact, with only minimal chain breaking observed, resulting in the preservation of B–N trimer chains (see inset for an example molecule). However, methyl groups exhibited mobility, either dissociating from the B–N chain or re-bonding to boron or to both boron and nitrogen atoms. This suggests that the N–C bond is less stable than the B–N bond, which may facilitate conversion to BN-based materials in experiment, suggesting the potential of PMeAB as a precursor for BN materials with minimal carbon impurity. For MeIB, due to its small molecular structure and the relatively low temperature, no significant polymerisation into extended B–N chains was observed within 100 ps. This could potentially change over longer simulation times. In addition, the formation of B–N–C three-membered ring structures was frequently observed, likely due to the uncapped nature of the B and N atoms, which readily form bonds with carbon. These small ring structures appear to hinder the formation of extended B–N chains. In the case of MeCTB, the majority of the ring structures broke apart within 100 ps, transforming into chain-

like structures resembling those of PMeAB3-nocap. Despite the relatively low temperature, sufficient simulation time allowed for ring opening. Once converted into chains, methyl groups exhibited similar behaviour to those in PMeAB3-nocap, either migrating along the chain or dissociating. Notably, MeCTB exhibited the highest number of H_2 molecules released (~10) at 1500 K, compared to PMeAB3-nocap (~5) and MeIB (~7), which aligns with single-molecule simulation results showing that MeCTB has the lowest E_a for dehydrogenation among the three.

At 2000 K, the B–N chains in PMeAB3-nocap tend to break apart, leading to the formation of MeIB-like units, although most H atoms remain attached. This suggests that the temperature has not yet reached the threshold required for extensive H_2 release, limiting the re-polymerisation of MeIB units into extended B–N chain structures. In the case of MeIB, partial polymerisation is observed, with the formation of B–N dimers; however, no trimers are detected. This may be attributed to a higher degree of H_2 release compared to PMeAB3-nocap, despite both systems being primarily composed of MeIB-like units at this temperature. Notably, in MeCTB, a reformation of ring structures is observed at 2000 K, contrasting with the behaviour at 1500 K, where B–N chains were predominant. This phenomenon is likely due to increased H_2 release at higher temperatures, which creates more available bonding sites on boron and nitrogen atoms, thus facilitating ring closure. Additionally, an increased release of methyl groups may reduce the formation of B–N–C three-membered rings, which would otherwise hinder the reformation of larger B–N rings. However, B–N chain structures similar to those seen at 1500 K are still present.

At 2500 K, all three systems exhibit extensive bonding among boron, nitrogen, and carbon atoms, resulting in the formation of large, yet disordered structures. The temperature exceeding the dehydrogenation threshold, leading to significant H_2 release and the consequent creation of numerous active bonding sites on boron, nitrogen, and carbon atoms. Among the three, PMeAB3-nocap yields the least ordered molecular structures after 100 ps, with no obvious B–

N chains observed. In contrast, MeIB exhibits some degree of ordering with the presence of short B–N chains, although the overall structure remains relatively small and less developed. MeCTB shows the highest degree of structural ordering. Long, alternating B–N chains are predominantly observed throughout the system and are likely to grow further into longer chains or networks with extended simulation time. Moreover, coordination environments resembling BN_3 and BN_4 motifs are observed in MeCTB, suggesting the initial formation of cross-linked, stabilised networks. These features are consistent with those detected in experimental ^{11}B NMR data discussed in **Chapter 2** (**Figure 2.16**), further supporting the potential of MeCTB as a promising precursor for BN-based materials.

At 3000 K, both PMeAB3-nocap and MeIB continue to evolve into larger and more ordered structures compared to those observed at 2500 K. In contrast, the ordered structures previously observed in MeCTB at 2500 K are no longer present. Instead, MeCTB primarily forms smaller B–N–C species at 3000K or above, often with double or triple bonds. This behaviour suggests that different precursor molecules have different optimal temperature windows for the formation of B–N ordered structures. Below this window, insufficient thermal energy prevents overcoming E_a, limiting the growth of large, ordered B–N networks. On the other hand, at temperatures above this optimal range, the pre-formed ordered structures tend to decompose into smaller fragments. Therefore, identifying and maintaining an optimal temperature is crucial in experimental settings to achieve high-quality, well-ordered h-BN materials.

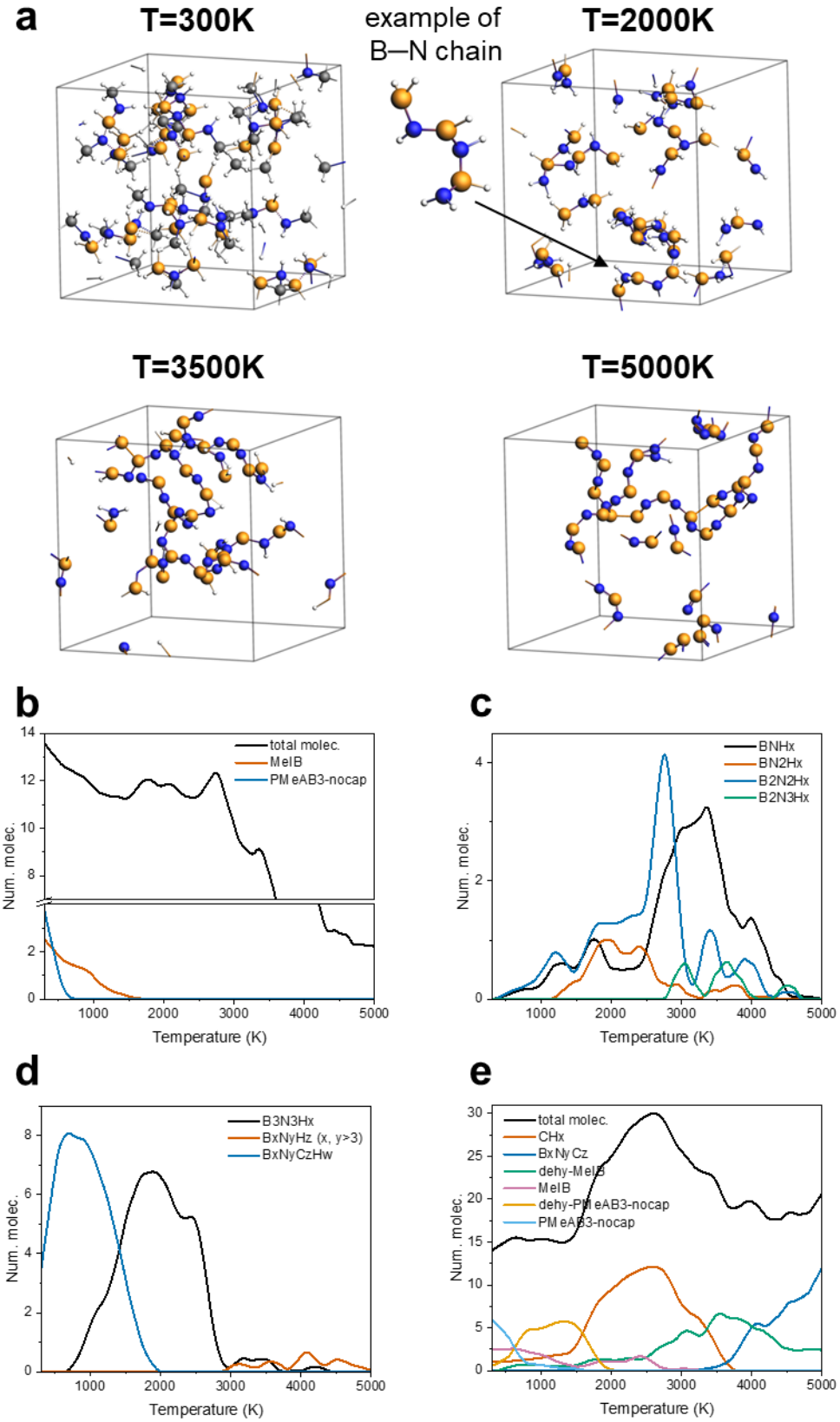

Figure 4.31: A 10 PMeAB3-nocap temperature ramp simulation with a molecule sink model removing H_2, CH, CH_2, CH_3, and CH_4 every 0.25 fs. (a) Snapshots at 300, 2000, 3500, and 5000 K. (b-d) Evolution of the reactants, major intermediate products, and radicals observed. (e) A 10 PMeAB3-nocap temperature ramp simulation with a molecule sink model removing H_2 every 0.25 fs. Evolution of the reactants, major intermediate products, and radicals observed.

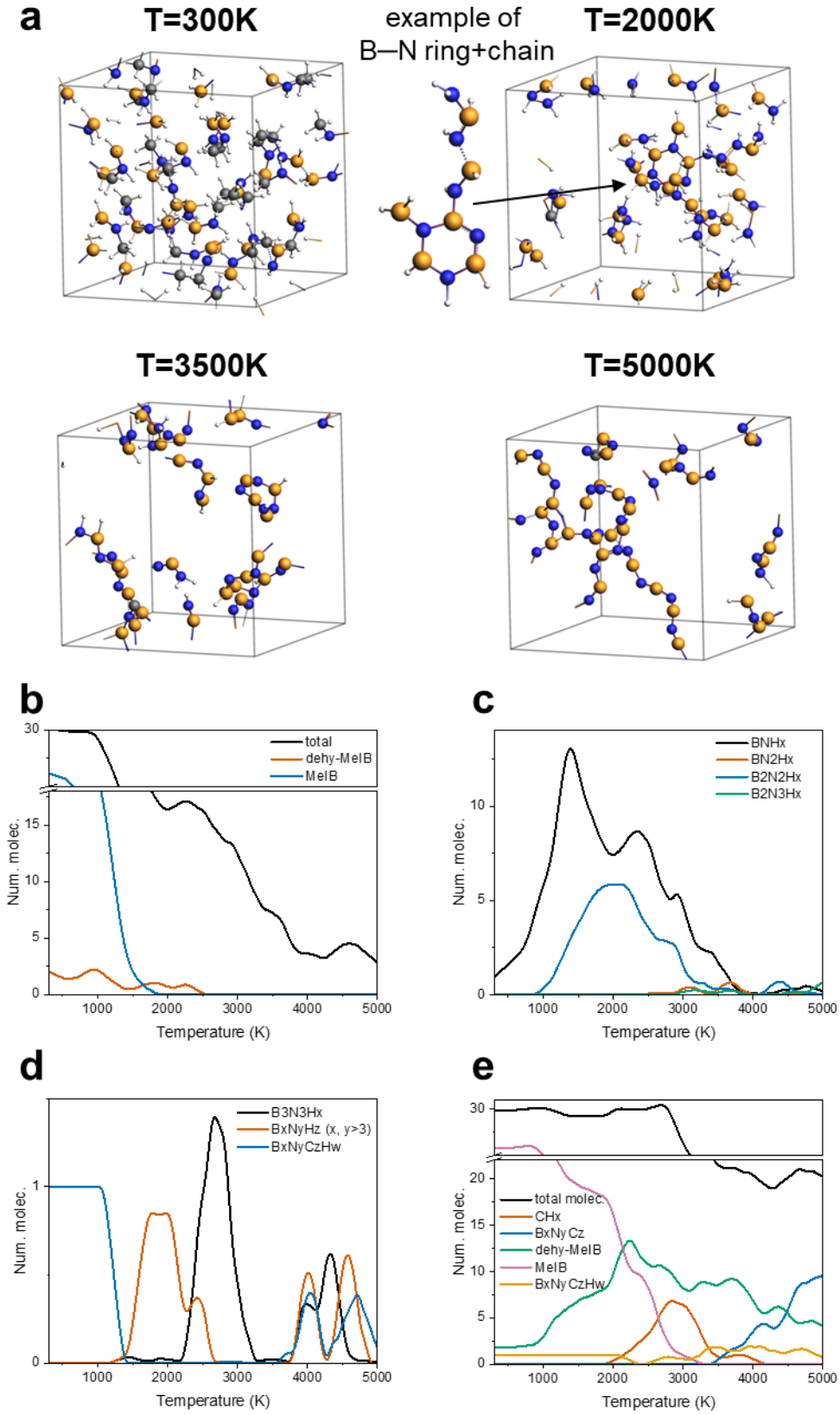

Figure 4.32: A 30 MeIB temperature ramp simulation with a molecule sink model removing H_2, CH, CH_2, CH_3, and CH_4 every 0.25 fs. (a) Snapshots at 300, 2000, 3500, and 5000 K. (b-d) Evolution of the reactants, major intermediate products, and radicals observed. (e) A 30 MeIB temperature ramp simulation with a molecule sink model removing H_2 every 0.25 fs. Evolution of the reactants, major intermediate products, and radicals observed.

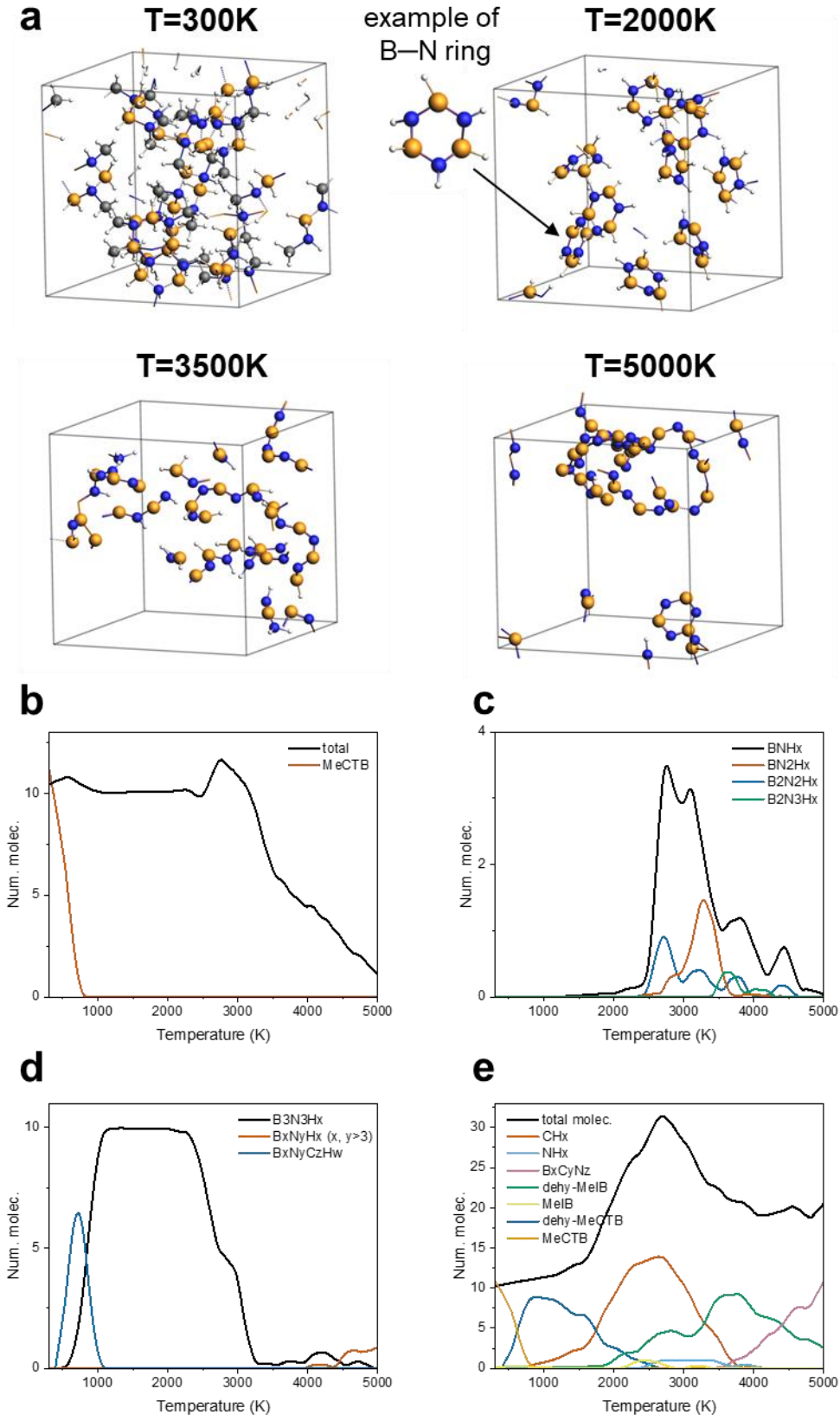

Figure 4.33: A 10 MeCTB temperature ramp simulation with a molecule sink model removing H_2, CH, CH_2, CH_3, and CH_4 every 0.25 fs. (a) Snapshots at 300, 2000, 3500, and 5000 K. (b-d) Evolution of the reactants, major intermediate products, and radicals observed. (e) A 10 MeCTB temperature ramp simulation with a molecule sink model removing H_2 every 0.25 fs. Evolution of the reactants, major intermediate products, and radicals observed.

To mimic the continual removal of carbon during NH_3 thermolysis (**Figure 2.18**), a molecule sink model was applied in which H_2, CH, CH_2, CH_3, and CH_4 species were removed from the system every 25 fs. Across all three precursors, PMeAB3-nocap, MeIB, and MeCTB, at all temperatures (2000K, 3500K, 5000K), only B–N bonds were observed; no B–B or N–N bonds were detected.

At 2000 K, PMeAB3-nocap formed B–N chains without methyl groups. The removal of methyl groups, which otherwise tend to bond with boron or migrate along the B–N backbone (see **Figure 4.25a**), helped stabilise the linear B–N chain structures. However, no B–N ring structures were observed, likely due to PMeAB3-nocap's linear configuration, which prevents the chain ends from interacting within the limited simulation timeframe. For MeIB, the product showed the highest degree of molecular ordering among the three systems, with both B–N chains and rings being prominent. This supports the claim that MeIB, upon releasing CH_x and H_2 yielding IB (BH_2NH_2) and BHNH-like units, serves as an efficient building block for constructing extended B–N chain and ring structures. These findings are consistent with prior experimental and theoretical studies. Thompson *et al.* reported that the major product formed from the reaction of pulsed-laser-ablated boron atoms with NH_3 is BHNH, a highly reactive molecule that trimerizes under ambient conditions to form BZ.[287] The theoretical study from Cheng *et al.* further support this, suggesting that both BHNH and IB species directly contribute to BN flake growth by reacting with the edges of h-BN crystals.[32] Similarly, Anafcheh *et al.* proposed that BHNH plays a crucial role in expanding square-ring motifs within BN cages, facilitating the formation of larger h-BN nanostructures.[288] For MeCTB, only pure B–N rings were observed, with no evidence of B–N chain formation. Among the ring structures, $B_3N_3H_6$, also known as BZ, was predominant, which is a well-known intermediate or product in the thermal decomposition of AB. This selectivity toward BZ is due to the inherent ring structure of MeCTB and the absence of disruptive methyl groups, preventing ring opening.

At 3500 K, all three precursors began to partially decompose into smaller fragments compared to 2000 K, although some large structures remained intact. This suggests that the temperature exceeds the stability threshold for some B–N bonds. At 5000 K, all three systems formed extremely large molecular networks, with most of the system effectively converting into a single, interconnected B–N structure. This occurs because nearly all H_2 and CH_x species have been removed, leaving boron and nitrogen atoms free to bond extensively. Notably, at 5000 K, MeCTB formed pure B–N rings entirely free of hydrogen for the first time, structures that serve as fundamental building units of h-BN. These results strongly suggest that, given sufficient simulation time and the continued application of the molecule sink model, the formation of a more ordered, ceramic-like h-BN network is likely.

Figure 4.31b–d, **4.32b–d**, and **4.33b–d** illustrate the evolution of reaction products and intermediates over time. The total number of molecular species in all three systems exhibits a similar trend: after an initial period of relative stability, the molecule count begins to decline, marking the onset of H_2 and CH_x formation as the temperature increases. For PMeAB3-nocap, this decline begins at 2760 K. In the case of MeIB, molecular decomposition starts earlier at 960 K. MeCTB shows a slight increase in molecular count at 2460 K, followed by a decline at 2760 K. In all three systems, the predominant reaction products are $B_3N_3H_x$, $B_2N_2H_x$, and BNH_x species. These molecules are more abundant than species containing unequal B:N ratios or those incorporating carbon atoms. This indicates that all three precursors preferentially decompose into products with B:N stoichiometry = 1:1, indicating their suitability as precursors for the synthesis of BN-based materials with minimal structural irregularities. A modified molecule sink model, in which only H_2 was removed while CH_x species remained, was also evaluated (**Figures 4.31e**, **4.32e**, and **4.33e**). The results show that, without H_2 accumulation, the evolution of reaction products and intermediates closely mirrors the behaviour observed in simulations without any molecule removal (**Figures 4.25**, **4.26**, and

4.27), both in terms of composition and quantity. This indicates that the presence of excess H_2 in the system does not significantly influence the overall decomposition pathway. Furthermore, no evidence of passivation or re-bonding of H to B–N-containing molecules was observed, confirming that H_2 does not substantially interfere with the formation or breakdown of B–N networks in the simulations.

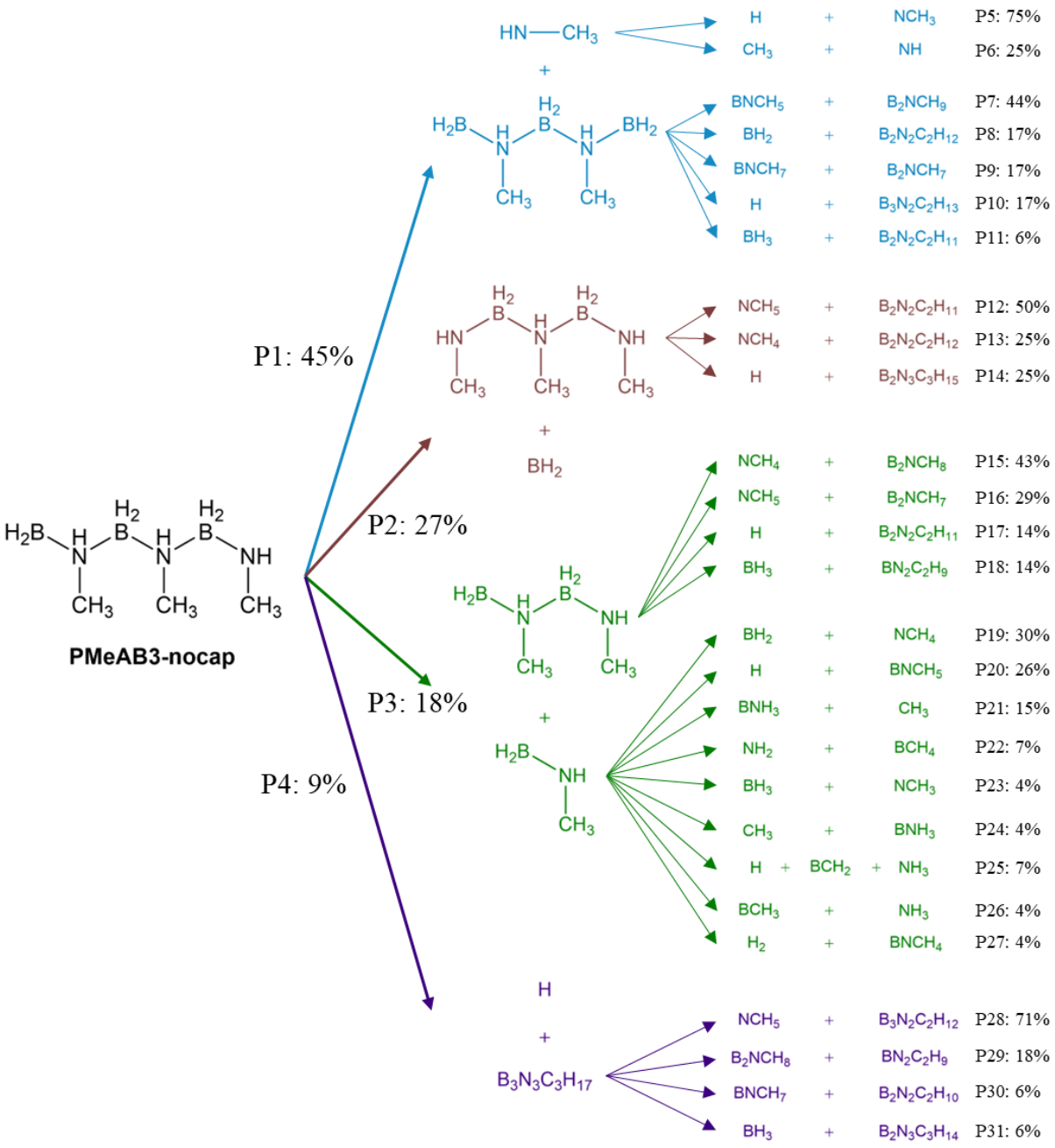

Figure 4.34: Main thermal decomposition pathways of PMeAB3 observed during a 10 PMeAB3 temperature ramp simulation (T= 300–5000K) coupled with ChemTrayzer2. Captions P1–P31 indicate each pathway by percentage of occurrence. The occurrence percentage is calculated statistically by dividing the number of times each reaction pathway occurs throughout the entire simulation by the total number of reaction events detected. This provides a normalized measure of pathway prevalence across the simulation trajectory.

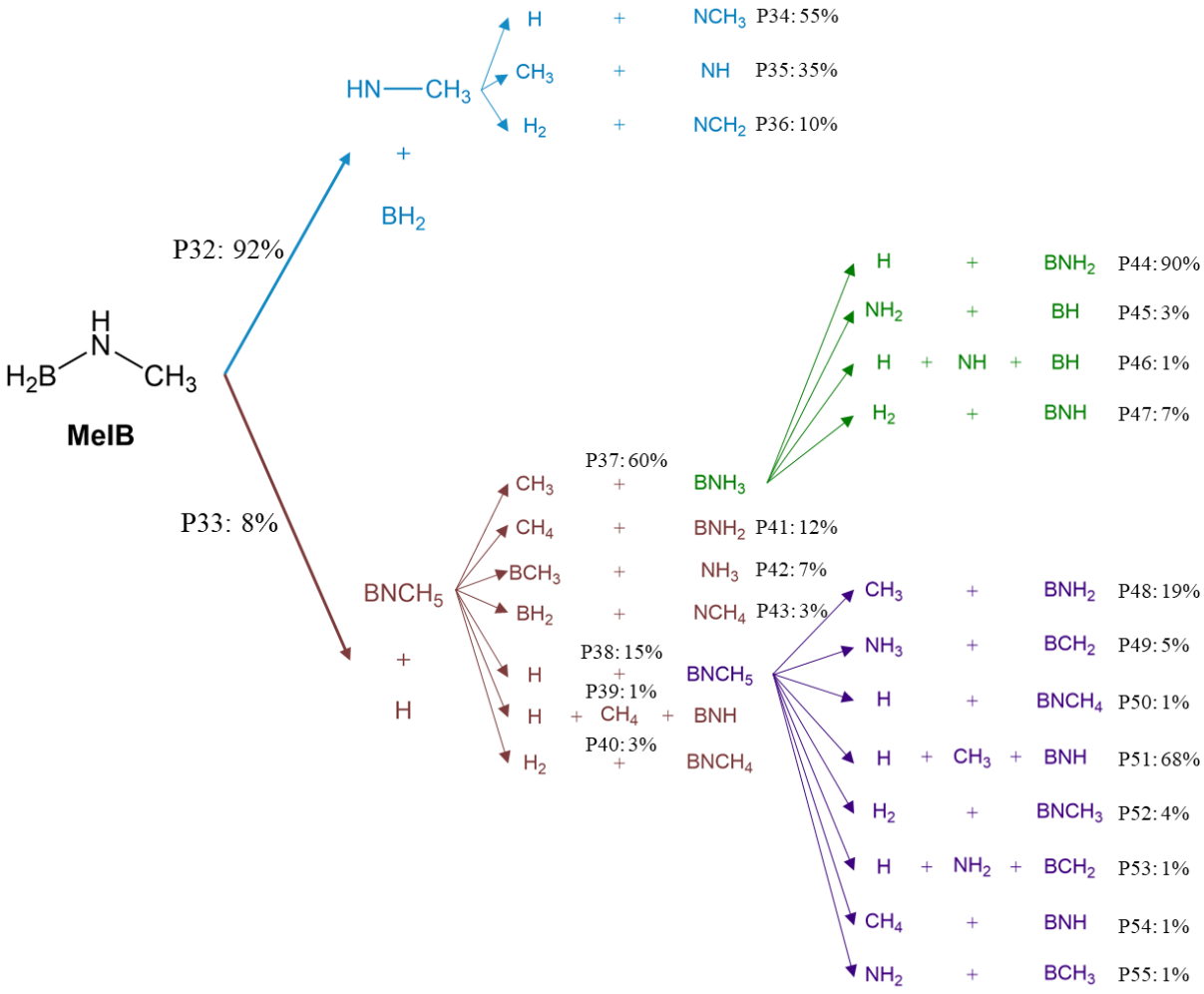

Figure 4.35: Main thermal decomposition pathways of MeIB observed during a 30 MeIB temperature ramp simulation (T= 300–5000K) coupled with ChemTrayzer2. Captions P32–P55 indicate each pathway by percentage of occurrence.

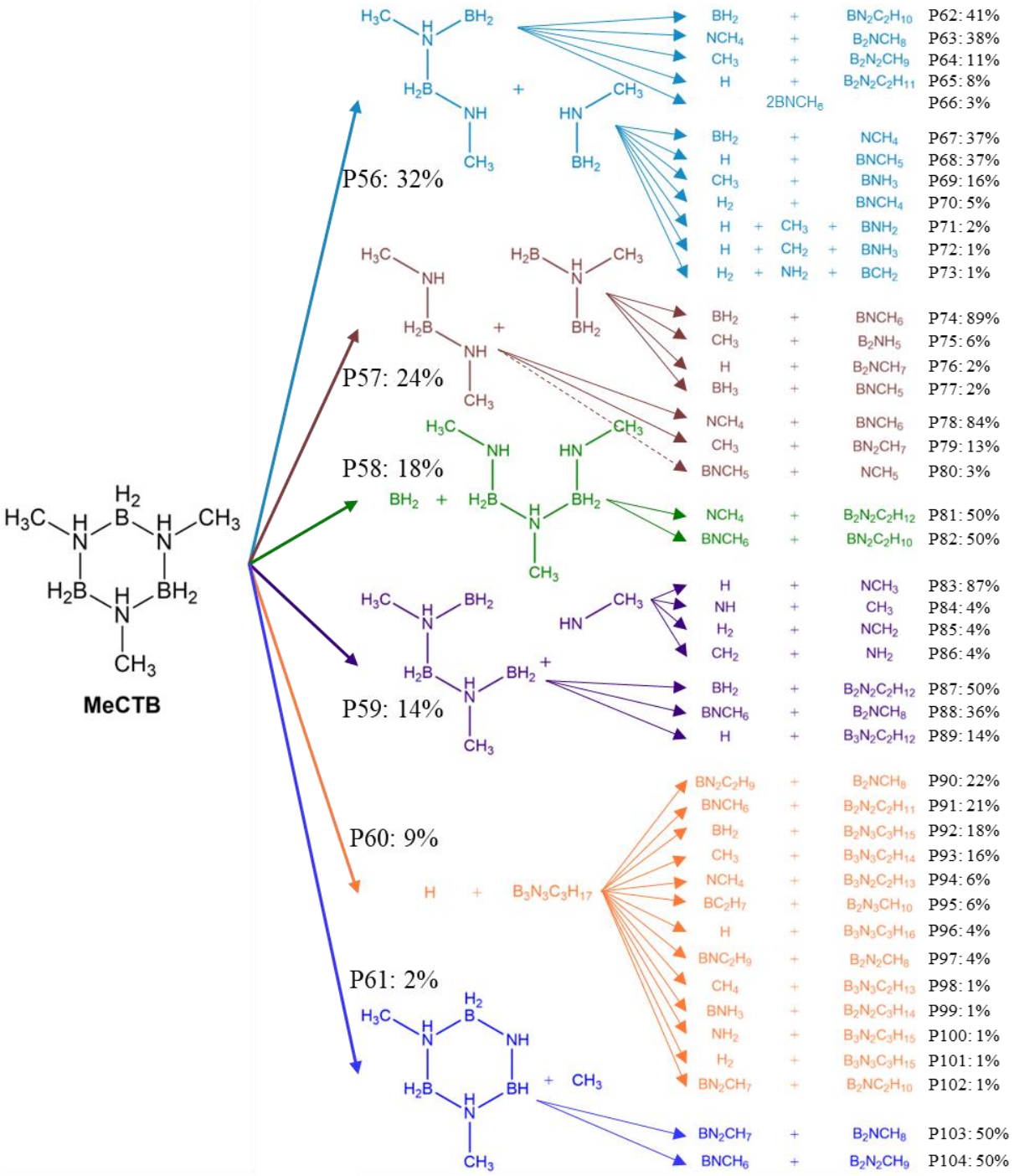

Figure 4.36: Main thermal decomposition pathways of MeCTB observed during a 10 MeCTB temperature ramp simulation (T= 300–5000K) coupled with ChemTrayzer2. Captions P56–P104 indicate each pathway by percentage of occurrence.

To statistically analyse the composition of thermal decomposition products, I employed the CTY2 package to study the evolution of reaction products, intermediates, and radicals in temperature ramping simulations of three systems: 10 PMeAB3-nocap molecules (representing a polymeric precursor), 30 MeIB molecules (representing a monomeric precursor), and 10 MeCTB molecules. Notably, more than 100 unique reactions and distinct chemical species were identified. These large numbers reflect the successful identification of transient reactive intermediates, providing a comprehensive view of the decomposition pathways.

To better understand the thermal decomposition process of these precursors, I analysed the initiation steps and subsequent reactions in detail (**Figure 4.34**, **4.35**, and **4.36**). For PMeAB3-nocap (**Figure 4.24**), the most frequently observed reactions involved dissociation pathways, including the cleavage of various B–N bonds along the B–N chain (P1–P3). These yielded intermediate species such as $NHCH_3$ + $BH_2NHCH_3BH_2NHCH_3BH_2$, BH_2 + $NHCH_3BH_2NHCH_3BH_2NHCH_3$, and BH_2NHCH_3 + $BH_2NHCH_3BH_2NHCH_3$. Dehydrogenation reactions were also observed, producing species such as H + $B_3N_3C_3H_{19}$ (P4). These intermediates underwent secondary reactions (P5–P31), leading to smaller fragments including H, H_2, BH_2, BH_3, NH_2, CH_3, NCH_x, BNH_x, $BNCH_x$, B_2NCH_x, and minor quantities of BCH_x. These computational findings are in good agreement with the TGA-MS results (**Section 3.3.2**, **Figure 3.13**). Specifically:

- m/z =1–2 corresponds to H and H_2,
- m/z =13–17 is attributed to BH_2, BH_3, NH_2, and CH_3,
- m/z =26–31 likely represents both AB-like species (BNH_x) and NCH_x,
- m/z =38–42 is more plausibly attributed to MeAB-like species ($BNCH_x$), rather than earlier assumptions of B_3H_x or B_2NH_x, given the low detection of methyl-free species,
- m/z =51–54 is more consistent with B_2NCH_x than with $B_2N_2H_x$, as the latter's ring structures are rarely observed in the simulations.

Additionally, m/z =78–82 and 120–122 are likely associated with BZ and MeBZ-type species. While such ring structures were not directly observed in the simulation given the limited simulation timescale, I propose that these signals may also correspond to dehydrogenated dimers (PMeAB2) or trimers (PMeAB3) alongside BZ and MeBZ. Here, m/z stands for mass-to-charge ratio, a key parameter in mass spectrometry that represents the ratio of an ion's mass (m) to its charge (z).

For MeIB (**Figure 4.35**), only two primary reaction pathways were detected: B–N bond dissociation (P32) and dehydrogenation (P33). This observation is consistent with previous transition state studies of its close analogue, AB, which undergoes two dominant intramolecular reactions: dissociation into NH_3 and BH_3, and dehydrogenation to form IB.[32] The products resulting from the initial dissociation and dehydrogenation of MeIB undergo secondary (P34–P43) and ternary reactions (P44–P55), which include further dissociation and dehydrogenation steps. The final decomposition products include small species such as H, H_2, BH_2, BH_3, NH_2, CH_3, CH_4, NCH_x, BNH_x, and $BNCH_x$, closely resembling those observed in the decomposition of PMeAB3-nocap. This similarity suggests that the thermal decomposition mechanisms of monomeric and polymeric forms MeIB are fundamentally alike. It also implies that the molecular weight of PMeAB has a limited effect on the overall thermal decomposition behaviour.

For MeCTB (**Figure 4.36**), the primary decomposition pathway involves ring opening through the dissociation of B–N bonds (P56–P59), while dehydrogenation (P60) and demethylation (P61) are observed as minor pathways. The subsequent secondary reactions (P62–P104) appear to be more complex and diverse compared to those in PMeAB3-nocap and MeIB. However, the resulting decomposition products are largely similar to those observed in the other two systems. These include H, H_2, BH_2, BH_3, NH_2, CH_2, CH_3, CH_4, NCH_x, BNH_x, and $BNCH_x$, B_2NCH_x, BN_2CH_x.

Table 4.2: Comparison of the main products from TGA–MS and simulations.

m/z	Products from TGA-MS	Favourable intermediates/products from PES mappings	Example products observed from ReaxFF MD simulations
1–2	H H_2	H_2 	H  H_2 
13–17	BH_3 CH_4 NH_3	BH_2  BH_3 	BH_2  CH_2  CH_4  NH_3  BH_3  CH_3  NH_2  NH_4 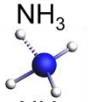
26–31	BNH_X NCH_X	-	BNH_4  NCH_5 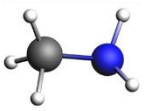
38–42	B_3H_X B_2NH_X $BNCH_X$ (MeAB MeIB)	MeIB 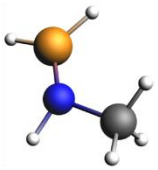	MeIB 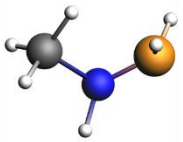
51–54	B_2NCH_X $B_2N_2H_X$ (CDB)	B_2NCH_8 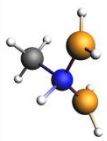 B_2NCH_9 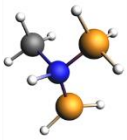	B_2NCH_8 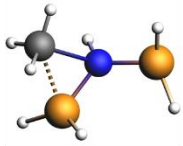
78–82	$B_3N_3H_X$ (CTB BZ) $B_2N_2C_2H_X$ (PMeAB2 MeCDB)	dehy-PMeAB2  MeCDB 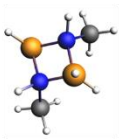	dehy-PMeAB2 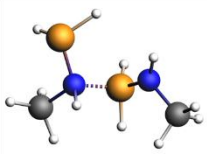
120–122	$B_3N_3C_3H_X$ (PMeAB3 MeCTB MeBZ)	MeCTB 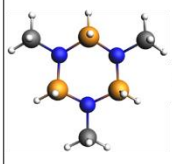 dehy-PMeAB3 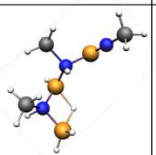	dehy-PMeAB3 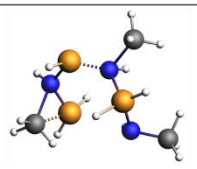

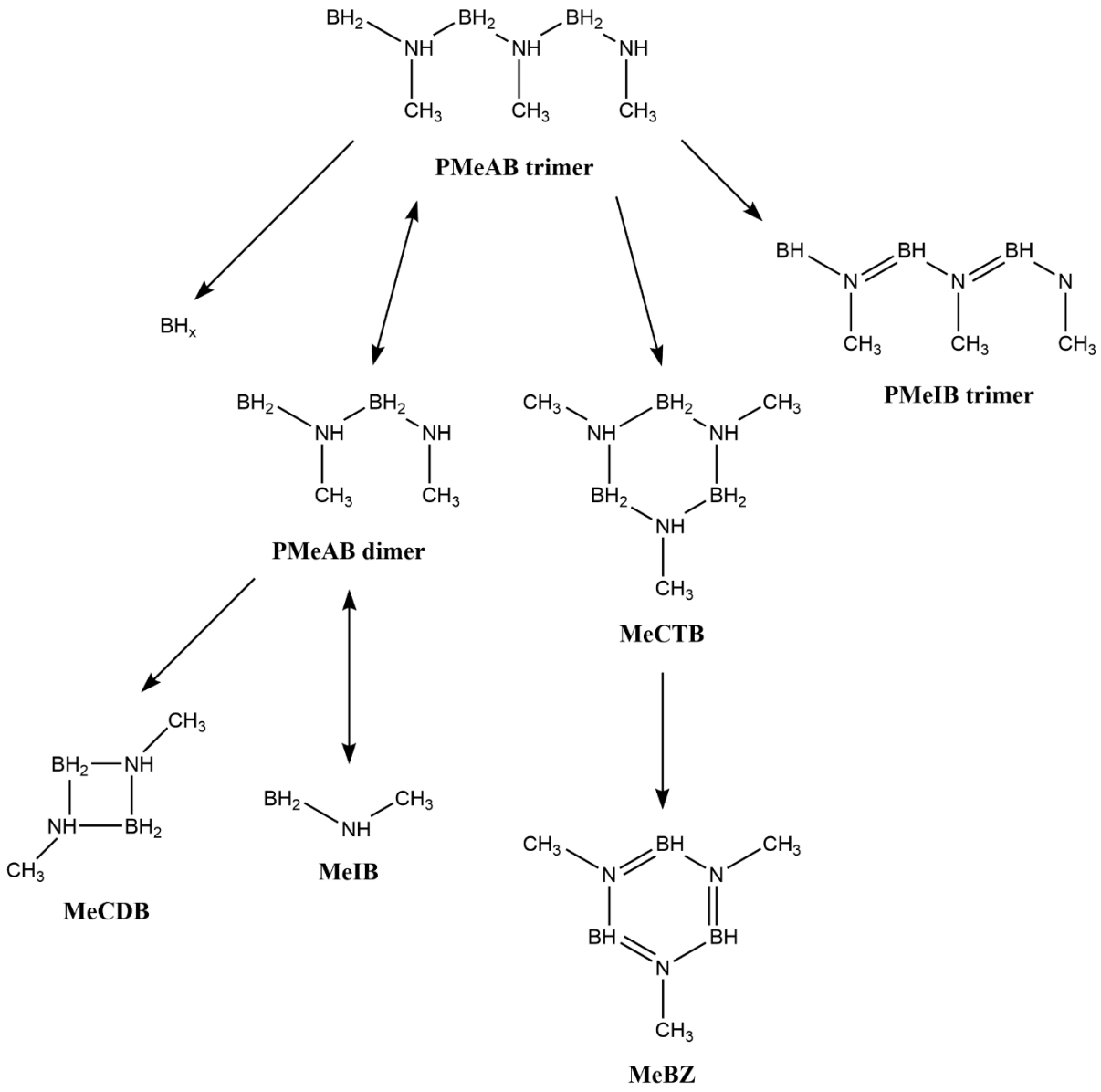

Figure 4.37: Proposed thermal decomposition pathways of PMeAB.

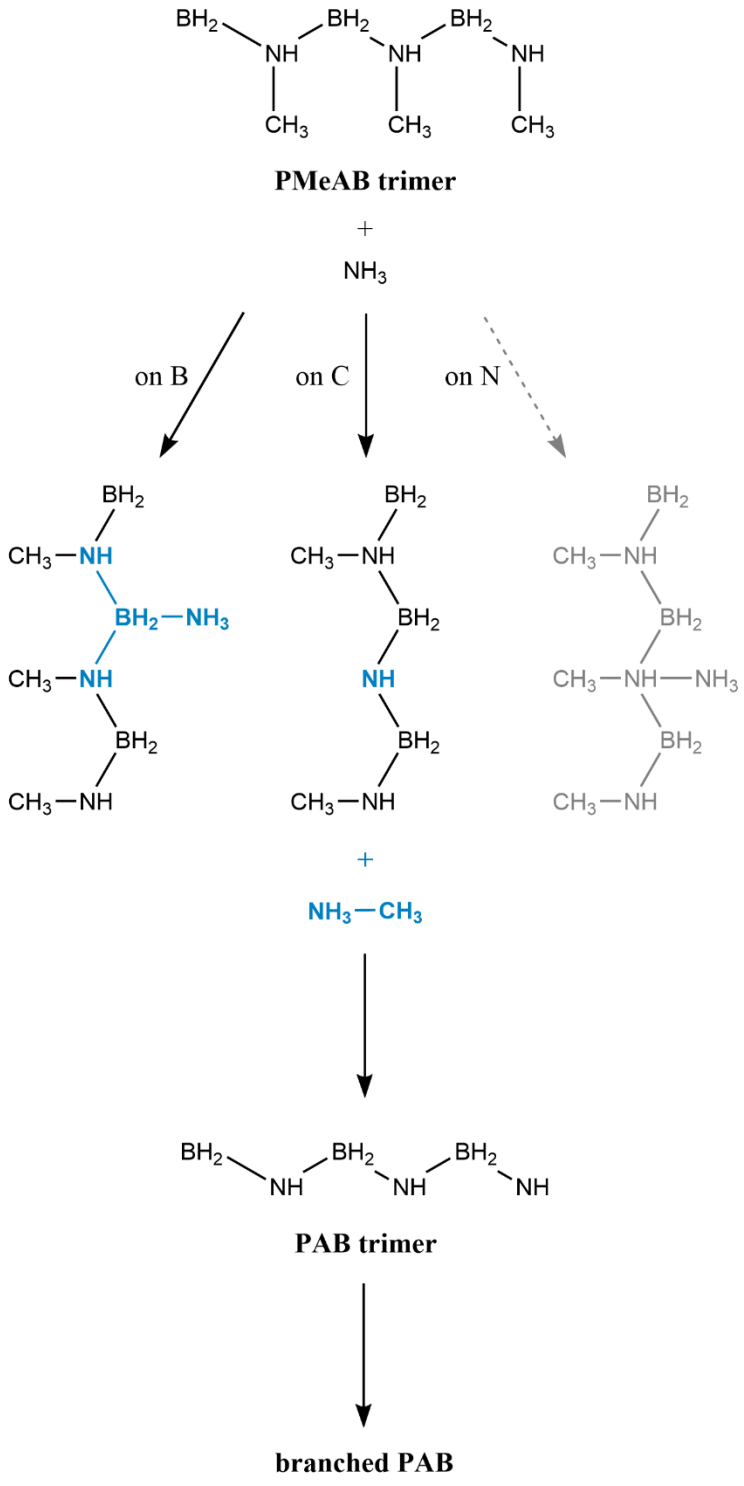

Figure 4.38: Proposed reaction pathways of PMeAB under NH_3 thermolysis.

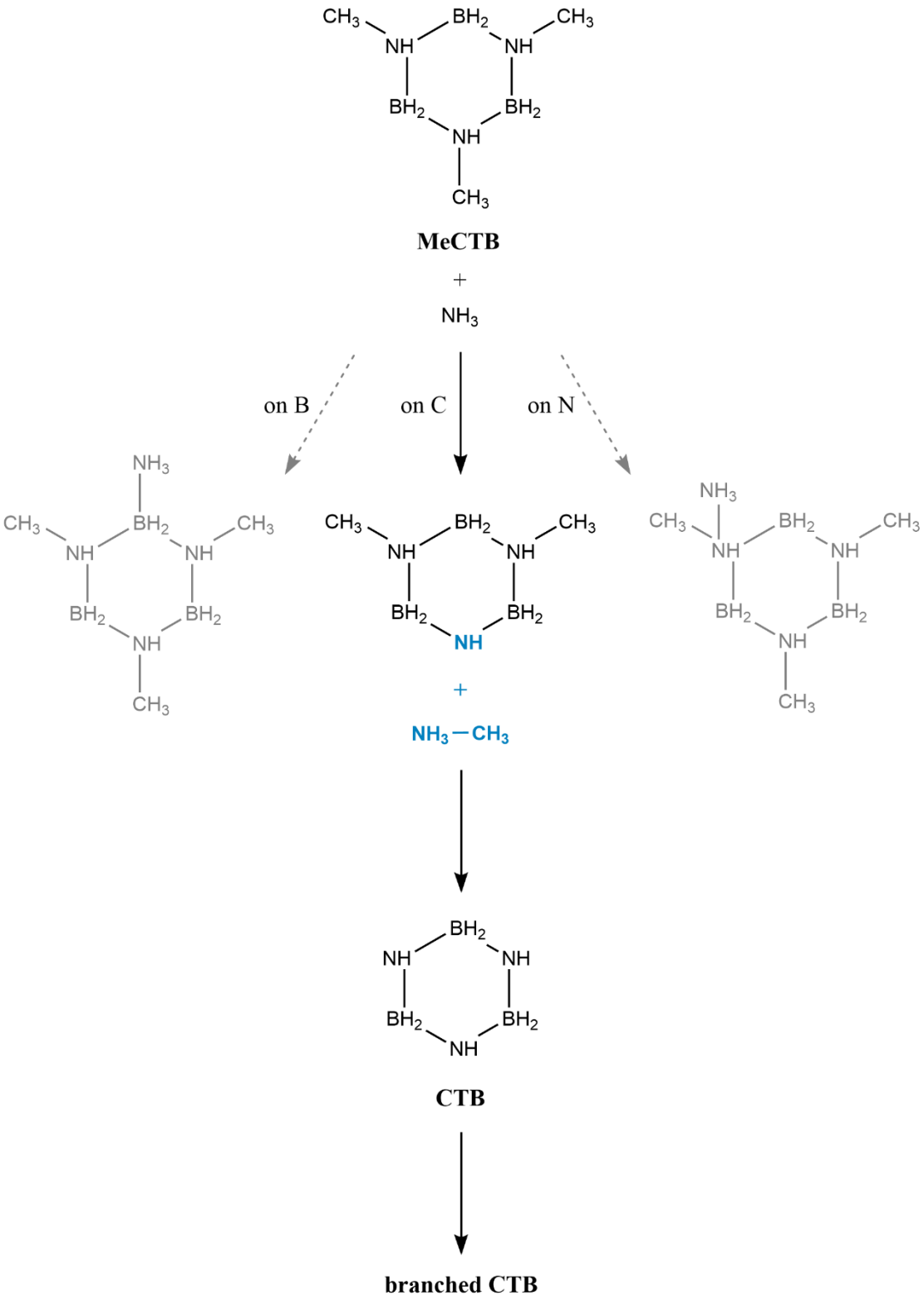

Figure 4.39: Proposed reaction pathways of MeCTB under NH_3 thermolysis.

Table 4.2 compares the thermal decomposition species identified through three different approaches: experimental detection via TGA-MS, predicted molecule structures from PES based on DFT calculations, and large-scale simulations from ReaxFF-based MD. The tentative assignments of molecular species to observed m/z values have become clearer, with additional structural insights supported by both computational methods.

- m/z = 1–2: These species are unambiguously assigned to hydrogen atoms and molecules (H and H_2).
- m/z = 13–17: These species are likely composed of all BH_x, NH_x, and CH_x units, with several plausible structural configurations now supported by PES and MD analyses.
- m/z = 26–31: Both BNH_x and NCH_x structures were confirmed, consistent with the initial hypotheses.
- m/z = 38–42: These species are most likely MeIB or partially dehydrogenated MeAB, as both computational approaches yield similar species.
- m/z = 51–54: Strong evidence from both PES and MD supports the assignment to B_2NCH_x species.
- m/z = 78–82: These are better described as PMeAB dimer or cyclic derivative MeCDB, rather than the previously assumed CTB or BZ structures.
- m/z = 120–122: These species are most likely dehydrogenated PMeAB trimer and their cyclic derivative MeCTB.

This comprehensive comparison provides important insights into the likely reaction intermediates and products, and help construct an overall thermal decomposition pathway from the PMeAB precursor to the final BN structure.

Figure 4.37 illustrates the proposed thermal decomposition pathways of PMeAB. Three primary mechanisms—dissociation, cyclisation, and dehydrogenation—are all thermodynamically favourable. These pathways lead to the formation of borane, cyclic species

MeCTB and MeCDB, monomeric building units MeIB, and dehydrogenated products such as PMeIB. In addition to pyrolytic decomposition, the reactivity of PMeAB in an NH_3 atmosphere is shown in **Figure 4.38**, and interactions between MeCTB and NH_3 shown in **Figure 4.39**. NH_3 preferentially bonds with boron and carbon atoms rather than nitrogen, promoting the removal of methyl group and enhancing the boron coordination environment. The subsequent elimination of methyl groups enables molecular branching, an essential early step in the formation of extended BN networks. Collectively, these results shed light on the mechanistic transformation of PMeAB toward h-BN.

4.4 Summary

In this chapter, I presented a comprehensive investigation of the thermal decomposition pathways of PMeAB and related compounds by integrating PES mapping using DFT and MD simulations using ReaxFF. DFT-based PES calculations enabled the identification of essential reaction steps, including transition states and key intermediates, during the evolution of the precursor. Among the various pathways explored, cyclisation of linear PMeAB to form the thermodynamically stable cyclic intermediate MeCTB was identified as the most favourable, occurring with nearly barrierless energy compared to dehydrogenation or bond dissociation. Intramolecular dehydrogenation across B–N and B–B bonds was found to be energetically preferred over other combinations for both linear and cyclic precursors, though the E_a increases significantly for the second and third H_2 releases. Selective B–N bond dissociation in PMeAB yields small molecular fragments such as BH_2, BH_3, and the monomer MeIB, species that further facilitate dehydrogenation reactions. These findings demonstrate that both intra- and intermolecular dehydrogenation mechanisms contribute to the overall decomposition process. MeIB, a key thermal decomposition intermediate/product, is shown to be a likely fundamental building unit in the formation of extended BN structures due to its strong tendency to undergo addition and polymerisation, rather than further dissociation or dehydrogenation. Moreover, NH_3 is found to act as an efficient methyl scavenger, preferentially bonding to the methyl groups of precursor molecules. By bonding with carbon atoms, NH_3 effectively abstracts methyl groups with a lower E_a than direct methyl dissociation. In addition, NH_3 bonding to boron atoms forms higher-coordination BN_3 environments, promoting cross-linking and structural stabilisation, both critical for the formation of a pure, carbon-free h-BN network. This behaviour was further supported by modelling the interactions between pairs of precursor molecules. The formation of branched structures is promoted by both dehydrogenation and

demethylation, representing early stage of h-BN network formation. These pathways are critical in transitioning from molecular precursors to an extended h-BN network.

To enable large-scale simulations, I evaluated several ReaxFF for their accuracy in modelling PMeAB-related thermal chemistry. Among the available parameter sets, $ReaxFF_{HCNOSB}$, adapted from the $ReaxFF_{HBN}$ developed for AB (a monomeric structural analogue of PMeAB), showed the best agreement with DFT benchmarks for dehydrogenation and bond dissociation energies; thus, it was selected for further MD simulations. Single-molecule MD simulations combined with CTY2 statistical analysis revealed that H_2 release occurs via both intra- and intermolecular mechanisms. However, full dehydrogenation requires long simulation times. Multi-molecule simulations indicated that dissociation into BH_x, CH_x, NH_x, NCH_x, BNH_x, $BNCH_x$ (MeIB), and B_2NCH_x are dominant pathways, occurring alongside dehydrogenation. To mimic experimental NH_3 thermolysis, I incorporated a molecular sink model to remove CH_x species, which are known to hinder B–N network formation by forming excessive and disruptive bonds with boron and nitrogen atoms within B–N chains and rings. Among the studied species, MeIB, despite being the smallest precursor, forms the most extensive B–N networks, including both B–N chains and rings. PMeAB predominantly forms linear B–N chain structures, while MeCTB favours the formation of B–N ring structures with six hydrogen atoms, the so-called BZ species, which have also been observed both experimentally[219] and in simulations[110] during the pyrolysis of AB.

Overall, the integration of DFT-based PES mapping and ReaxFF-based MD simulations provides a powerful computational framework for investigating thermal decomposition pathways under both pyrolytic and NH_3 reactive conditions. The mechanistic insights gained here into precursor evolution and key intermediate formation offer valuable guidance for the experimental synthesis of h-BN and related BN nanostructures. More broadly, the identification of critical intermediates and fundamental building units represents a foundational

step toward predicting reaction kinetics, growth dynamics, and resulting material morphologies across a range of synthesis environments and material systems.

Chapter 5

Outlook

Contents

5.1 Conclusions

The primary objective of this thesis was to develop straightforward and versatile synthesis pathways for the fabrication of low-dimensional h-BN nanostructures, while advancing the fundamental understanding of the underlying formation mechanisms. This concluding chapter summarises the major findings of the study and outlines potential directions for future research aimed at fully utilising the exceptional properties of h-BN nanomaterials for real-world applications.

This work has demonstrated the feasibility of novel synthesis strategies for producing a diverse range of h-BN nanostructures, including:

- Solid micro- and nano-fibres

- Cylindrical and bamboo-like nanotubes
- Filamentous and porous nanofibres
- Few-layer nanosheets
- Vertical nanoflakes

, and their macroscopic assemblies into nonwoven mats, 3D interconnected monoliths, and thin films. These pathways represent a significant step toward straightforward, and potentially scalable h-BN nanomaterial production.

The synthesis approaches are primarily based on the morphological processing of the PMeAB precursor using techniques including electrospinning, drop casting, and spin coating, followed by NH_3 thermolysis. For the MeCTB precursor, sublimation is required prior to NH_3 treatment. Electrospun BNF exhibit smooth, non-porous morphologies with tunable diameters ranging from the microscale down to the nanoscale. Few-layer BNNS were synthesised via a chemical blowing effect, reported here for the first time using PMeAB, showing behaviour analogous to that of AB. The formation of cylindrical BNNT, filamentous BNNF, and BN nanoflakes proceeds via a catalyst-free surface growth mechanism, relying on the reaction of reactive, boron-rich PMeAB intermediates with NH_3. This enables precise control over surface morphology and porosity. Bamboo-like BNNT and porous BNNF were produced from MeCTB through moderate thermal decomposition and NH_3 treatment, also under catalyst-free conditions, leading to enhanced microporosity.

Comprehensive characterisation of the synthesised h-BN nanostructures revealed notable advantages over existing methods, including high phase and chemical purity, minimal carbon and oxygen contamination, and a high degree of crystallinity in the hexagonal BN phase. These properties are critical for applications that require well-defined h-BN structures rather than disordered or amorphous forms.

Complementary computational modelling supported the experimental findings and provided deeper insight into the mechanisms governing the PMeAB-to-h-BN evolution. The simulation study concludes that the cyclic intermediate MeCTB plays a pivotal role in the transition from linear PMeAB precursors to ring-based h-BN networks. MeIB, formed through precursor dissociation, serves as a fundamental building block in B–N network growth. H_2 release in PMeAB and its derivatives proceeds via a combination of intra- and intermolecular mechanisms. NH_3 functions as an effective methyl scavenger, and the resulting demethylation, combined with dehydrogenation, promote the h-BN network formation. The proposed theories offer a valuable framework for future researchers, serving as a guideline for the rational design and synthesis of a broader array of h-BN nanostructures from B–N molecular precursors.

It is intended that information gained from the experiments and simulations presented in this thesis are used to guide future experimental design for enhanced-production or control of PMeAB and MeCTB-derive h-BN nanomaterials synthesis.

5.2 Future Work

The results of this thesis highlight several recommended paths for future research following on.

5.2.1 Downsizing to Electrospun BN Nanofibres

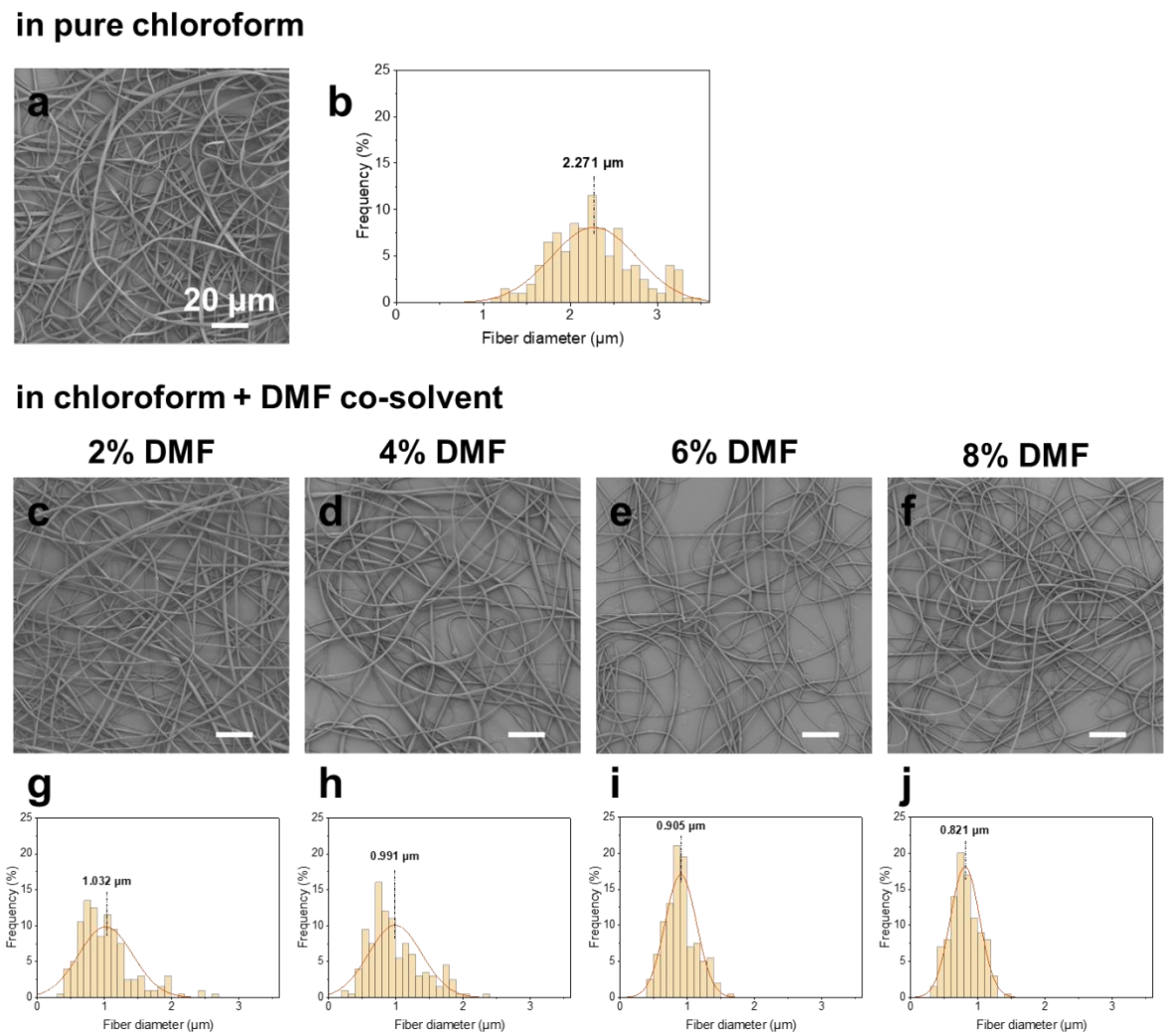

Figure 5.1: SEM image and fibre diameter distribution of PMeABF spun from (a, b) a pure chloroform solution, (c, g) a 2% DMF/98% chloroform solution, (d, h) a 4% DMF/96% chloroform solution, (e, i) a 6% DMF/94% chloroform solution, (f, j) a 8% DMF/92% chloroform solution.

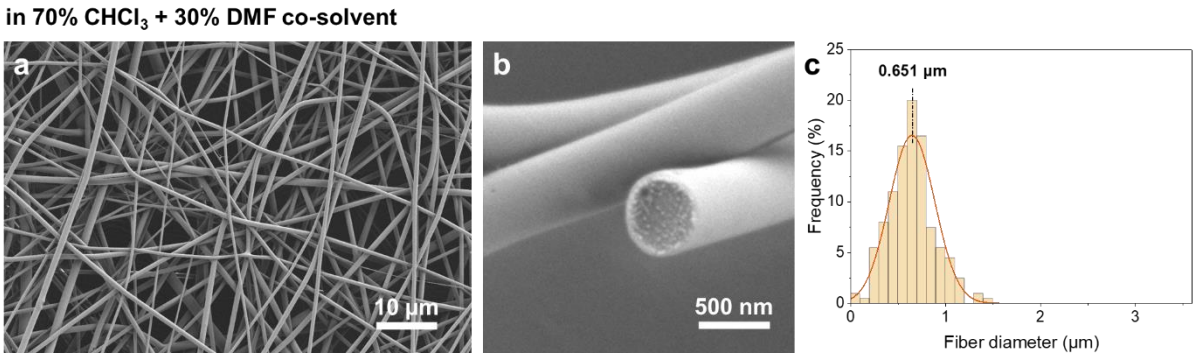

Figure 5.2: (a) SEM image, (b) cross-sectional HRSEM image, and (c) fibre diameter distribution of PMeABF spun from a 30% DMF/70% chloroform solution.

To achieve more control over the diameter of electrospun PMeABF, and consequently the diameter of the resulting BNF, which is directly influenced by the precursor fibre, I investigated several co-solvent systems for electrospinning PMeAB solutions. The originally used pure chloroform was replaced with mixtures of DMF and chloroform. As shown in **Figure 5.1**, the addition of just 2 vol.% DMF significantly reduced the average diameter of electrospun PMeAB) from above 2 µm to ~1 µm. With further increases in DMF content up to 8 vol.%, the fibre diameter dropped below 1 µm. At 30 vol.% DMF content (**Figure 5.2**), the average fibre diameter approached 600 nm. The observed diameter reduction is attributed to enhanced jet splaying induced by DMF, which increases the solution's conductivity and reduces fibre coalescence. Similar trends have been reported for poly(ε-caprolactone) (PCL), where adding 10 vol.% DMF to chloroform enabled the production of fibres with diameters around 150 nm, compared to an average diameter of 450 nm when using pure chloroform alone.[289] Furthermore, the addition of DMF yielded a narrow, unimodal PCL fibre diameter distribution, in contrast to the bimodal distribution typically associated with electrospinning from highly volatile solvents, such as pure chloroform. This trend was also observed in the PMeAB system: electrospinning PMeAB from pure chloroform produced a bimodal distribution with peaks at 2.35 µm and 3.15 µm. In addition to size reduction, a distinct morphological transformation was noted, the fibre cross-section changed from ribbon-like (**Figure 2.6**) to cylindrical. This shift is consistent with the known effect of solvent volatility on fibre morphology.[290,291] The

high volatility of chloroform (boiling point ≈ 61 °C) can lead to rapid solvent evaporation and collapse of the fibre surface, resulting in ribbon-like structures. By contrast, the addition of DMF (boiling point ≈ 153 °C) moderates the evaporation rate, reduces skin collapse, and promotes the formation of cylindrical fibres.[292]

These findings suggest that further reduction of PMeABF diameters to the sub-micrometer or even nanoscale range, and consequently, the fabrication of nanoscale BNF, is achievable through solvent system modification alone. While additional optimisation is required, particularly since the inclusion of DMF has been observed to reduce overall fibre yield compared to pure chloroform, the ability to decrease fibre diameter without altering the experimental setup demonstrates a straightforward and effective strategy for fine-tuning PMeABF/BNF morphology. A systematic investigation of various solvent systems is recommended to better understand the relationship between solvent composition and fibre morphology, as well as to optimise fibre yield.

5.2.2 Up-Scaling BN Fibres Assemblies

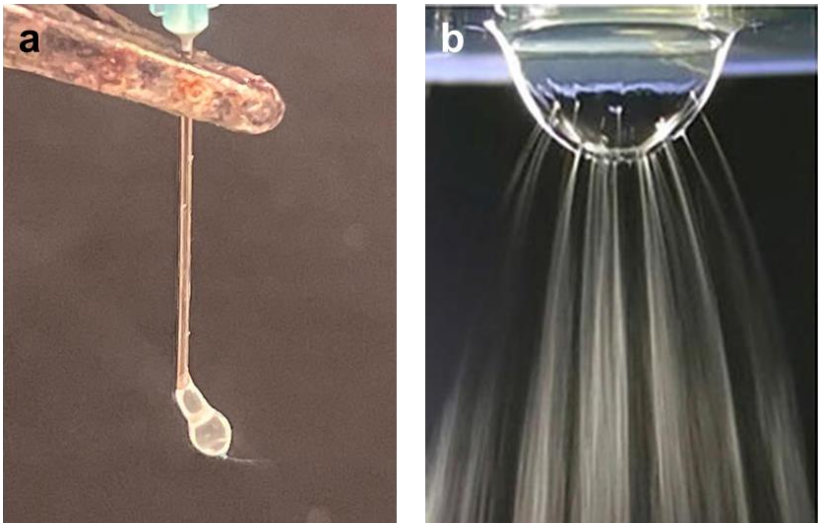

Figure 5.3: Actual photo of electrospinning setups: (a) needle-based electrospinning of PMeAB solution, as employed in **Chapter 2** of this thesis; (b) needle-free electrospinning of a PVA solution.[320]

The traditional single-needle electrospinning setup, typically employing a metallic hollow capillary as the spinneret, is inherently limited in production capacity, yielding only 0.01–0.1 g/h, as it only generates a single jet during operation. To overcome this constraint and enhance fibre production, needleless electrospinning has emerged as a promising alternative.[18] This technique fundamentally changes the formation of Taylor cones: due to electrohydrodynamic instabilities, the polymer solution spontaneously organizes into an array of capillary waves on the free liquid surface, each acting as a Taylor cone. This self-organized jet formation not only eliminates issues associated with nozzle clogging but also significantly increases the number of jets, enabling more scalable fibre production.[293]

As shown in **Figure 5.3a**, electrospinning of PMeAB solution using the single-needle setup produces only one visible jet throughout the process. To upscale the production of PMeABF and the subsequent BNF, the adoption of needleless electrospinning with multiple jets is recommended for future investigation (**Figure 5.3b**). However, successful implementation will require systematic investigation of several key parameters, including solution properties, applied voltage, working distance, and the potential integration of a rotating collector and controlled solution feeding system.

5.2.3 Fabrication and Applications of BN Fibres-Filled Polymer Composites

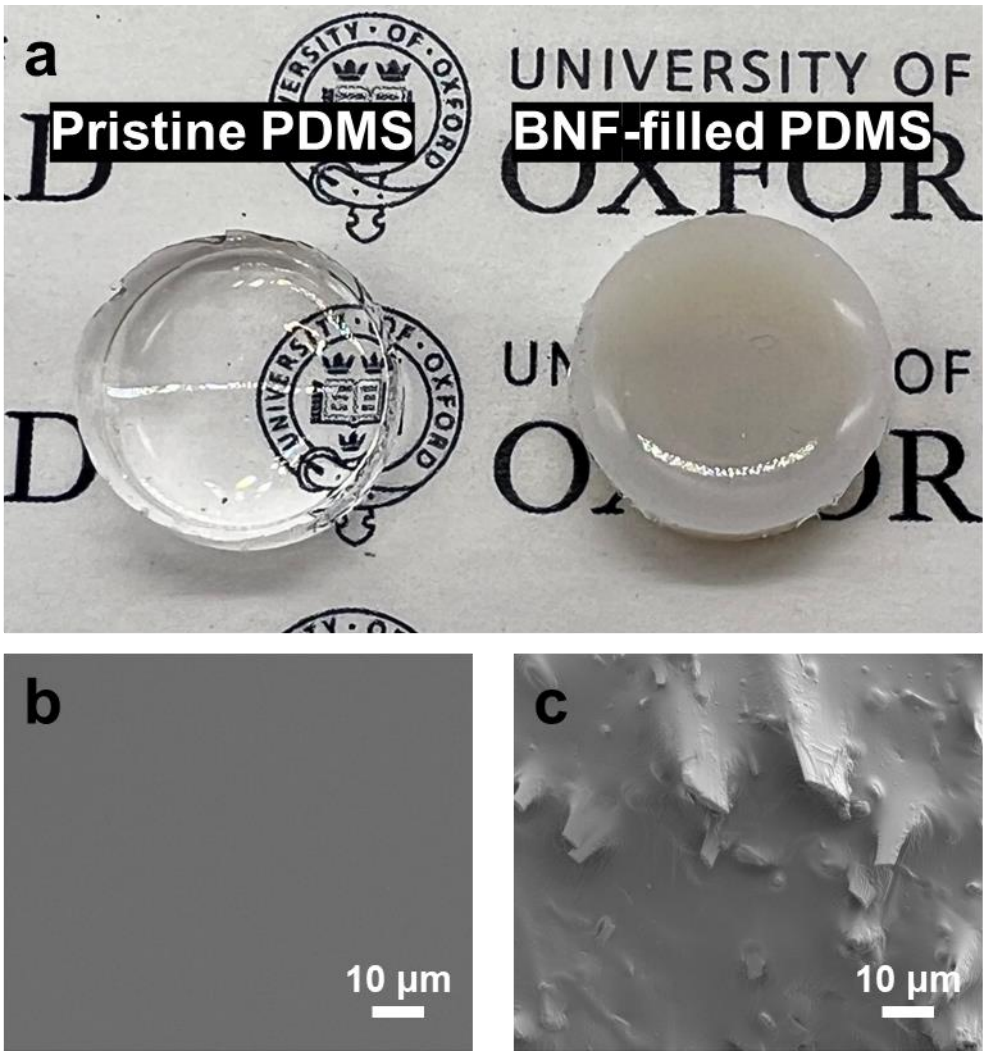

Figure 5.4: BNF/PDMS composites. (a) Actual photo of a pristine PDMS and a BNF-filled PDMS composite. SEM image for (b) a pristine PDMS and (c) a BNF-filled PDMS composite.

By incorporating the synthesised BNF into a polydimethylsiloxane (PDMS) matrix, good dispersibility (**Figure 5.4**) is achieved using a co-solvent approach adapted from the work of Snapp *et al.*[294] on BNNT/PDMS composites. Direct mixing of BNF into PDMS proved unfeasible, as even at a loading of 1 wt.%, the resulting mixture became too viscous for effective stirring, the stirrer failed to rotate. This is due to the 1D morphology of the BNF,

which promotes extensive entanglement, a behaviour also reported for BNNT.[294] To address this challenge, I implemented a co-solvent strategy by introducing THF into the system at a PDMS:THF ratio of up to 1:1 by volume. This significantly reduced the viscosity of the PDMS, as PDMS is soluble in THF, resulting in a homogeneous and diluted solution. Under these conditions, BNF could be added at concentrations up to 10 wt.% while maintaining adequate stirrability, thus enabling uniform dispersion within the polymer matrix. During stirring, the container is left open to allow gradual evaporation of THF overnight. Once the solvent has fully evaporated, a homogeneous dispersion of BNF in pure PDMS remains, with no detectable residual THF. The results demonstrate that the BNF synthesised in this work can be effectively incorporated into a polymer matrix and processed into composites, confirming the potential of this approach for the development of BNF-based composite materials.

Future work should focus on increasing the BNF loading beyond the current maximum of 10 wt.% by exploring alternative solvent systems that are compatible with PDMS. Achieving higher BNF loadings is essential to realise more significant enhancements in the mechanical, thermal, or functional properties of PDMS-based composites.

5.2.4 PMeAB: Potential Precursor for 2D h-BN & BCN

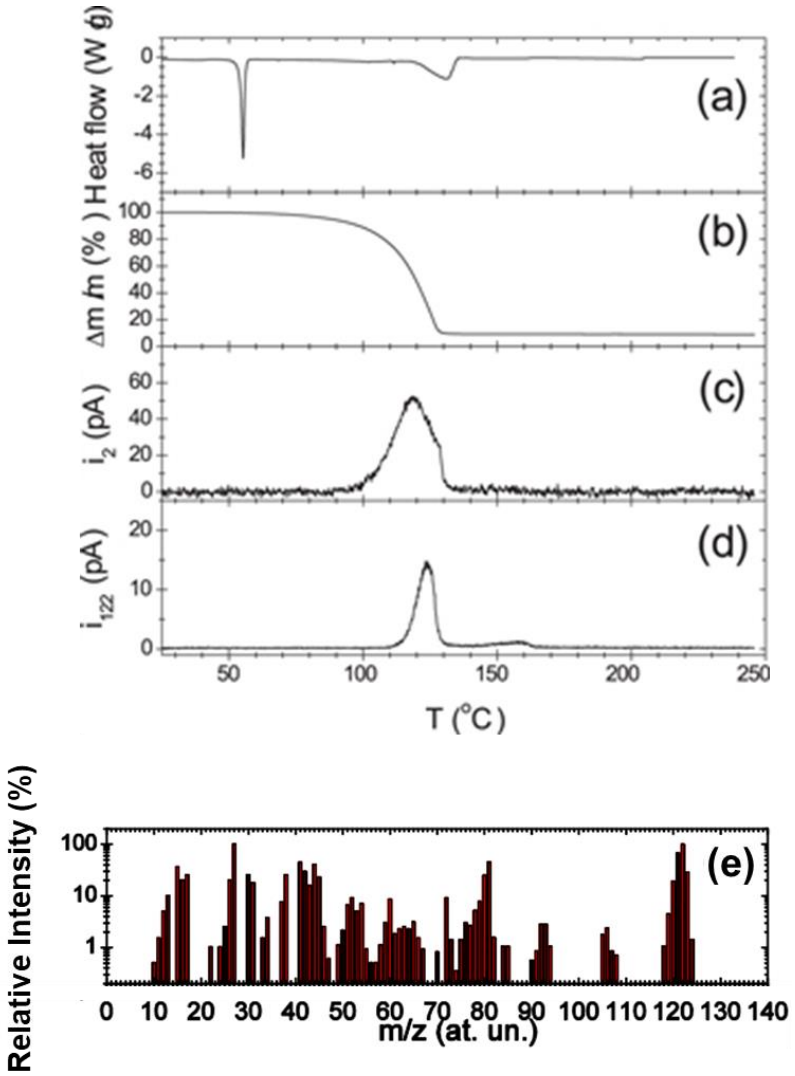

Figure 5.5: TGA–DSC–MS measurements of MeAB under Ar flow. (a) DSC result. (b) TGA result. MS result at (c) m/z = 2 corresponding to H_2 and (d) m/z = 122 corresponding to MeBZ. (e) MS result of the gas released during MeAB thermolysis at 125ºC in the m/z range 1–140 a.m.u. (excluding the H_2 peak at m/z=2).[295]

The use of MeAB as a single-source precursor for the CVD growth of 2D BCN layers has been previously demonstrated by Leardini *et al*.[295] The gaseous species released during the thermolysis of MeAB under CVD conditions have been identified via TGA-MS (**Figure 5.5**), revealing the evolution of gaseous MeAB (m/z = 43) and cyclic MeBZ (m/z = 122), which serve as the actual precursors for 2D BCN formation on copper substrates. This synthesis pathway leads to the formation of graphene-like and h-BN nanodomains within the resulting

BCN films. MeAB, being the monomeric unit of PMeAB, exhibits thermal decomposition behaviour that closely resembles that of PMeAB, as evidenced by TGA-MS analyses (**Figure 3.13–3.15**). Both compounds release the same major gaseous products: H_2 (m/z = 2), MeAB fragments (m/z ~ 42), and cyclic MeBZ (m/z ~ 121). TGA–DSC further confirms their similarity: MeAB displays an endothermic peak at 55 °C (corresponding to its melting point), followed by decomposition onset at ~100 °C, peaking at 125 °C and ending around 135 °C. In comparison, PMeAB shows an endothermic peak at 125 °C (melting), with decomposition starting at 100 °C, peaking at 160 °C, and ending near 200 °C. These findings confirm the analogous thermal behaviour of MeAB and PMeAB, suggesting that PMeAB can potentially serve as a viable single-source precursor for 2D BCN synthesis via CVD.

The CVD synthesis of 2D BCN and h-BN layers has also been successfully achieved using a chemically similar H–B–C–N compound, trimethylamine borane [$(CH_3)_3N{\cdot}BH_3$], as a single-source precursor.[284] By carefully controlling the sublimation temperature, Tay *et al.* were able to incorporate carbon doping into the h-BN lattice, effectively tuning the composition of the resulting BCN films. These findings suggest the potential of single-source molecular precursors for precise compositional control in 2D h-BN and BCN synthesis. Building on this, future work should investigate the use of PMeAB in CVD processes, with controlled adjustment of key parameters, such as sublimation temperature, growth atmosphere, and substrate type, to enable the tailored growth of both 2D BCN and phase-pure h-BN films.

5.2.5 Molecule Separation of Synthesized BN Assemblies

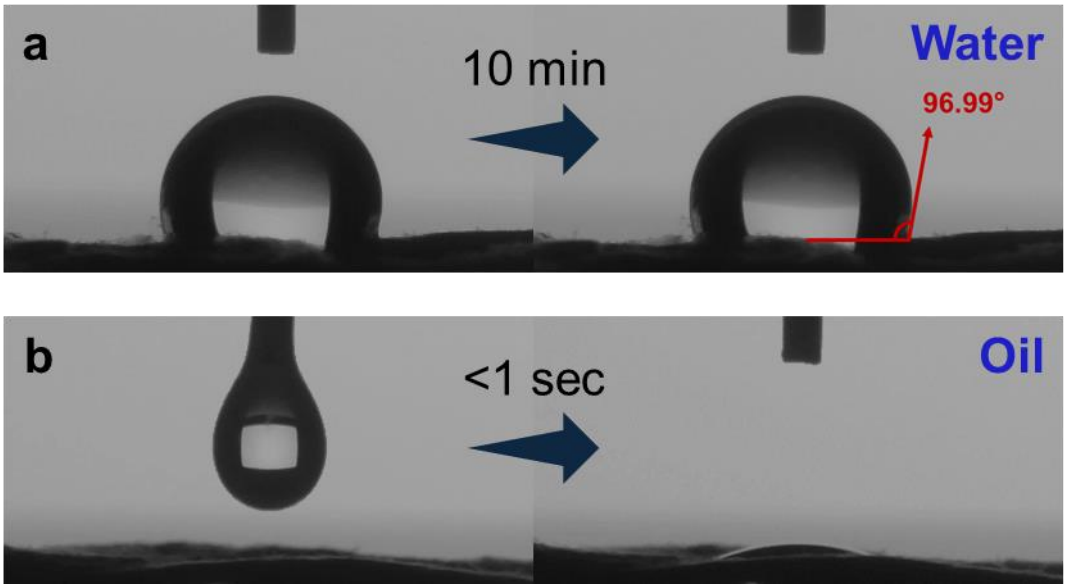

Figure 5.6: Contact angle profile of (a) water and (b) silicone oil on an electrospun PMeABF derived BNF mat.

The separation of oil and water remains a significant global challenge, driven by the growing volume of oily industrial wastewater, increasingly polluted oceanic waters, and the rising frequency of oil spill incidents.[296] BN nanomaterials have been investigated as potential candidates for this application,[297] primarily in the form of nanosheet films,[298,299] fibre aerogels,[300] and nanotube mats.[301] Among advanced fibrous materials, electrospun fibres stand out due to their tunable surface wettability, large specific surface area, high porosity, interconnected structure, flexibility, and scalable production.[302] These attributes make them highly promising for environmental applications such as oil–water separation. To date, however, BNF produced via electrospinning have not been evaluated for oil–water separation performance. In this study, preliminary findings based on contact angle measurements of water and silicone oil on electrospun BNF mats were investigated (**Figure 5.6**). Water exhibited a contact angle of approximately 97°, maintaining the droplet over an extended period without absorption. In contrast, silicone oil was immediately absorbed into the BNF mat in under one second. These results suggest that the synthesised BNF exhibits a combination of

hydrophobicity and lipophilicity, the key characteristics for effective oil–water separation membranes.[303] Future work should focus on evaluating the actual separation efficiency of the BNF mats with various types of oily wastewater, aiming to further establish their potential for practical environmental remediation applications.

5.2.6 ReaxFF Simulations for Extended BN Nanostructures

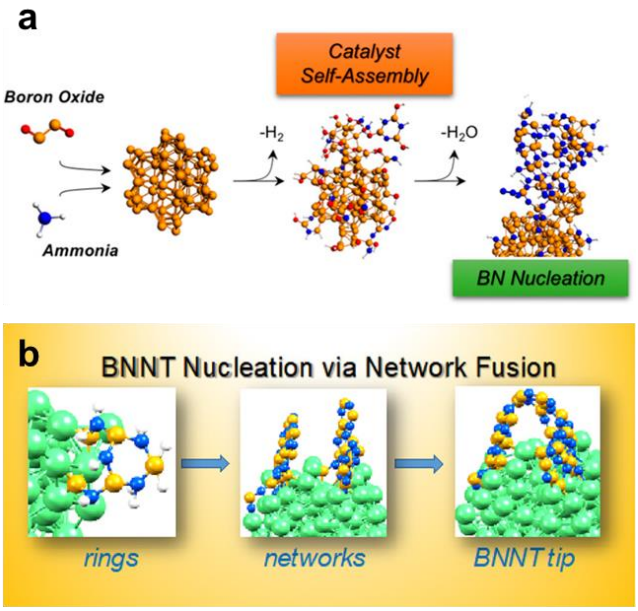

Figure 5.7: MD simulations demonstrating (a) h-BN nucleate during boron oxide CVD using B_2O_3 and NH_3 as precursors[305] and (b) BNNT cap structures form during Ni-catalysed CVD of ammonia borane.[228]

In this thesis, the computational results provide an initial insight into the molecular evolution of PMeAB toward the formation of h-BN. However, due to limitations in computational resources and simulation time (less than 1 ns), only the formation of isolated h-BN rings was observed in my simulations. To gain a more comprehensive understanding of the nucleation and growth mechanisms leading to extended h-BN networks, future studies should employ larger-scale simulations, ideally utilizing high-performance computing facilities. Moreover,

experimentally observed h-BN nanostructures, such as filamentous nanofibres and vertically oriented nanoflakes, may also be explored computationally to better understand their formation mechanisms. Simulating the growth pathways of these complex morphologies could provide valuable insight into how processing conditions influence structural outcomes.

The MD simulation in **Chapter 4** is based on an existing ReaxFF parameter set, $ReaxFF_{HCONSB}$, which, although validated, could be further optimised. The development of a customized ReaxFF parameter set, possibly using the ParAMS module within the Amsterdam Modelling Suite, could improve the accuracy of the simulation results.

Previous studies have demonstrated the use of MD simulations in elucidating the CVD nucleation processes of BN (**Figure 5.7**).[228,304,305] Building on this, I propose that the key reaction intermediates and decomposition products identified in this work could serve as starting units or building blocks in future simulations. This approach could help reveal which molecular species are most effective in driving the formation of the experimentally observed BN nanostructures, ultimately advancing the understanding of h-BN growth mechanisms from molecular precursors.

Appendices

Contents

Appendix A. PMeAB Synthesis

A.1 Detailed Reaction Conditions

Table A.1: Reaction conditions for the synthesis of PMeAB.

Entry	Code	Cat.	Cat. loading (mol%)	Scale MeAB (g)	[MeAB] (M)	Temp (°C)	Additional Comments	Selectivity [d] (%)	Yield (%)	M_n (g mol^{-1})	M_w (g mol^{-1})	Đ
1	PMeAB1	**2**	0.01	10	5	60[c]	Dropwise[f]	-	-	27,900	46,700	1.68
2	PMeAB2	**2**	0.01	10	5	40[c]	Dropwise[f]	-	-	47,900	71,800	1.5
3	PMeAB3	**2**	0.01	10	5	20[a]	-	99	-	74,200	110,500	1.49
4	PMeAB4	**1**	0.1	1.12	2	20[b]	-	99	64	76,600	112,800	1.47
4a	PMeAB4a	**1**	0.1	0.1	2	20[b]	5 eq. NH_2Me[e]	99	55	103,600	181,300	1.75
5	PMeAB5	**2**	0.01	50	5	20	Dropwise[f]	99	-	101,200	148,600	1.47
6	PMeAB6	**2**	0.01	10	5	5[a]	Dropwise[f, g]	99	87	115,400	172,000	1.48
7	PMeAB7	**2**	0.01	10	5	0[a]	Dropwise[f, g]	99	82	131,800	205,200	1.56
8	PMeAB8	**3**	0.033	5	1	20[b]	10 eq. NH_2Me[e]	99	78	162,300	250,500	1.54
9	PMeAB9	**1**	0.1	5.6	2	−15[b]	5 eq. NH_2Me[e]	99	92	186,300	290,500	1.56
10	PMeAB10	**1**	0.1	1.12	2	−15[b]	5 eq. NH_2Me[e] Dropwise	99	74	196,100	318,300	1.62
11	PMeAB11	**4**	0.1	0.1	2	20[c]	-	99	66	146,000	218,600	1.49

Temperature: (a) Reaction temperature of the vessel was maintained by water/ice bath, (b) Temperatures maintained by circulating cooler, (c) Temperature maintained by an oil bath. (d) As measured by ^{11}B NMR spectroscopy of aliquot taken upon catalysis completion. **Amine (NH_2Me):** (e) For reactions with **1** where methyl amine was indicated as a reagent, 5 equivalents relative to the catalyst were used. For reactions with **3** where methyl amine was indicated as a reagent, 10 equivalents relative to the catalyst were used. In each case the amine was added in tandem with the catalyst addition as a 2 M solution in THF. Entries 4 and 4a exemplify the increase in molecular weight when NH_2Me (5 equiv., 2M in THF solution) is added. **Dropwise addition:** (f) With precatalyst **1**, the catalyst was dissolved in THF, NH_2Me was added and then MeAB was added by slow addition of an MeAB/THF solution via syringe pump (0.1 mL/min) to the reaction vessel throughout the duration of the reaction. With pre-catalyst **2**, 10% of the MeAB was initially added to **2** to initiate catalysis. Once active catalysis commenced (bubbling), 90% of the MeAB was added by slow addition of an MeAB/THF solution via syringe

pump (0.33 mL/min) to the reaction vessel throughout the duration of the reaction. **Conditions:** (g) Reaction initially set up in air.

A.2 NMR Spectra

^{11}B NMR spectra of PMeAB samples: solution state

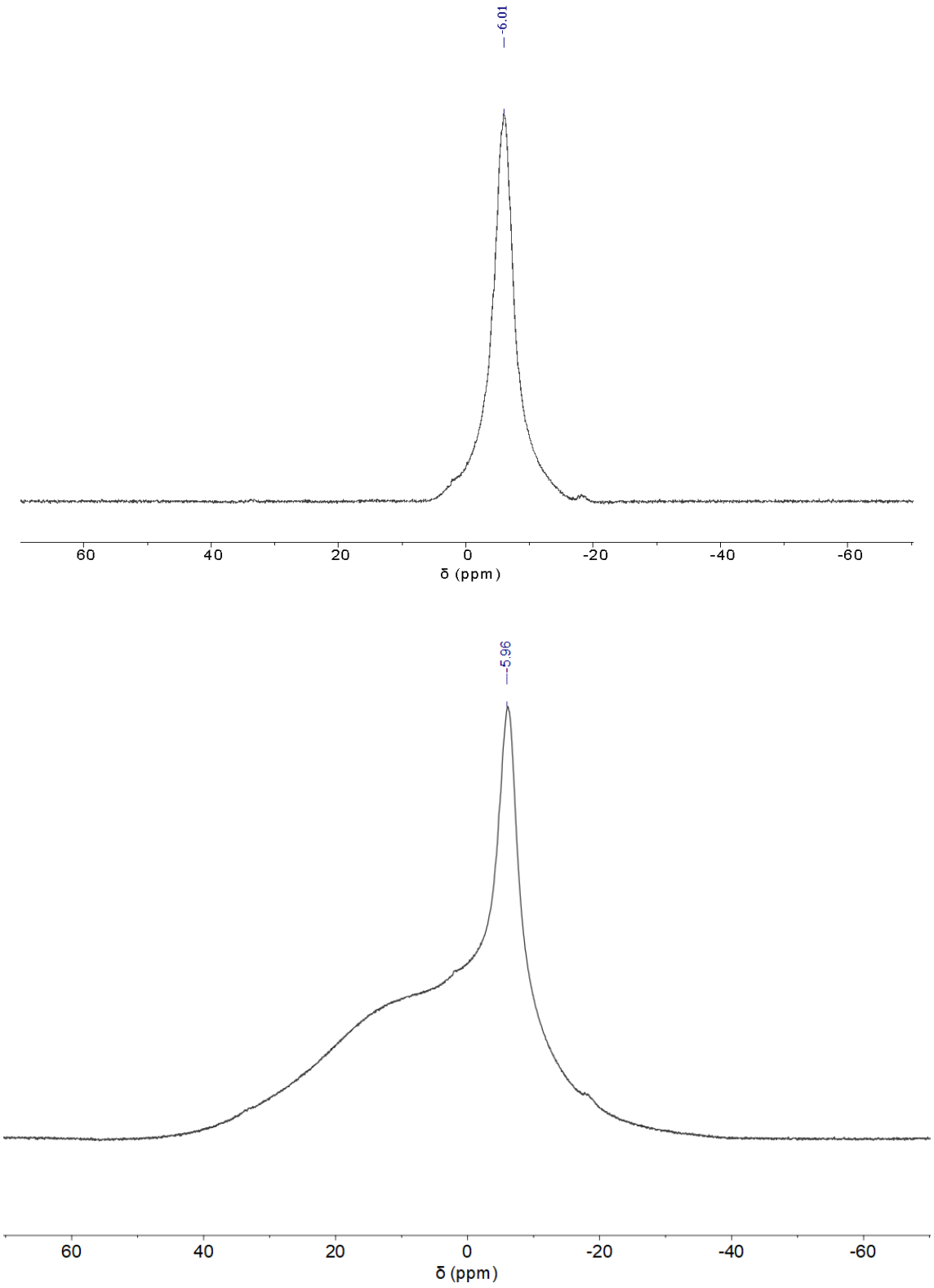

Figure A.1: ^{11}B NMR spectra of Entry 3 (PMeAB3). Baseline corrected and uncorrected, top and bottom respectively: $CDCl_3$, 193 MHz, 298 K.

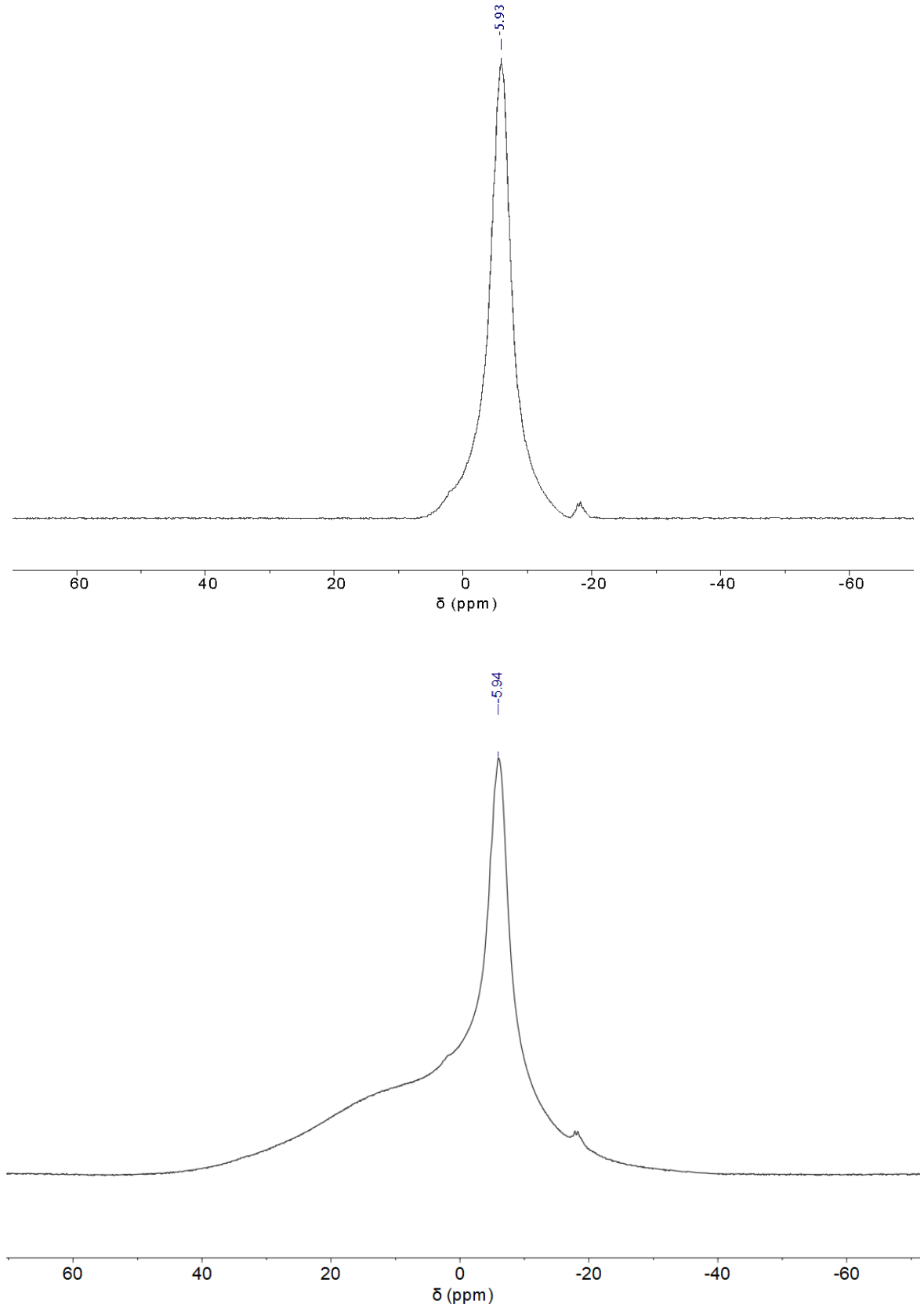

Figure A.2: ^{11}B NMR spectra of Entry 5 (PMeAB5). Baseline corrected and uncorrected, top and bottom respectively: $CDCl_3$, 193 MHz, 298 K.

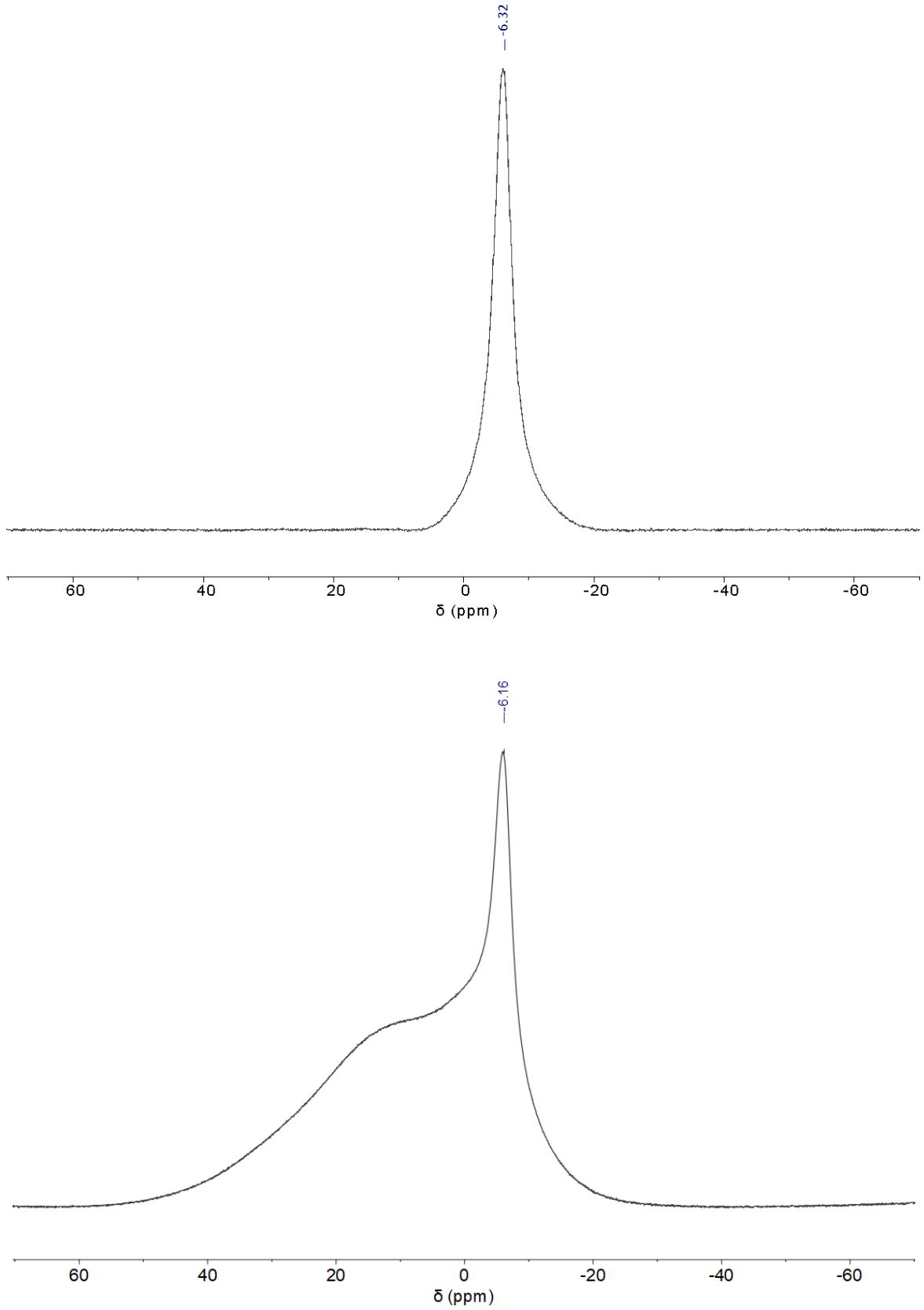

Figure A.3: ^{11}B NMR spectra of Entry 6 (PMeAB6). Baseline corrected and uncorrected, top and bottom respectively: $CDCl_3$, 193 MHz, 298 K.

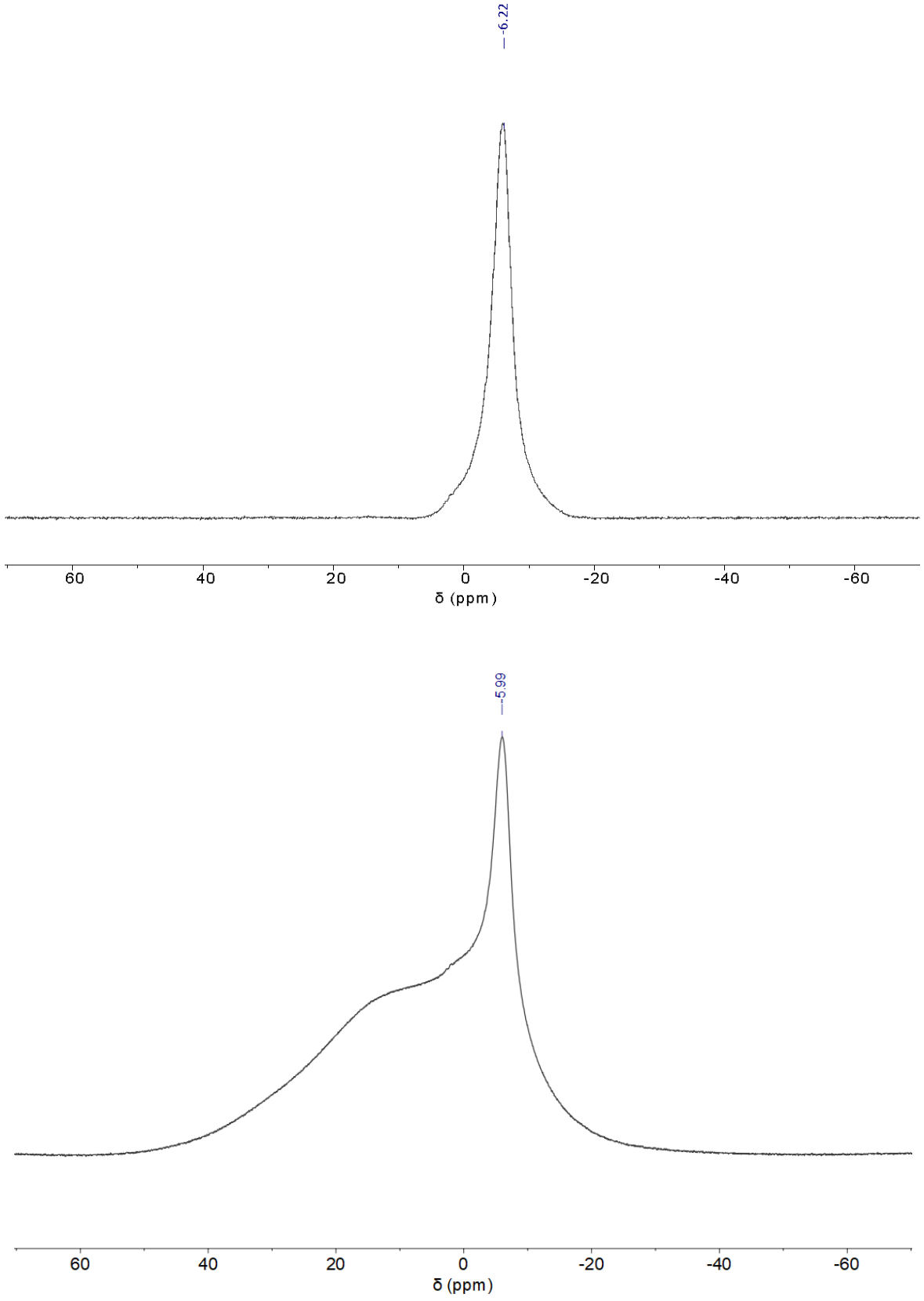

Figure A.4: ^{11}B NMR spectra of Entry 7 (PMeAB7) Baseline corrected and uncorrected, top and bottom respectively: $CDCl_3$, 193 MHz, 298 K.

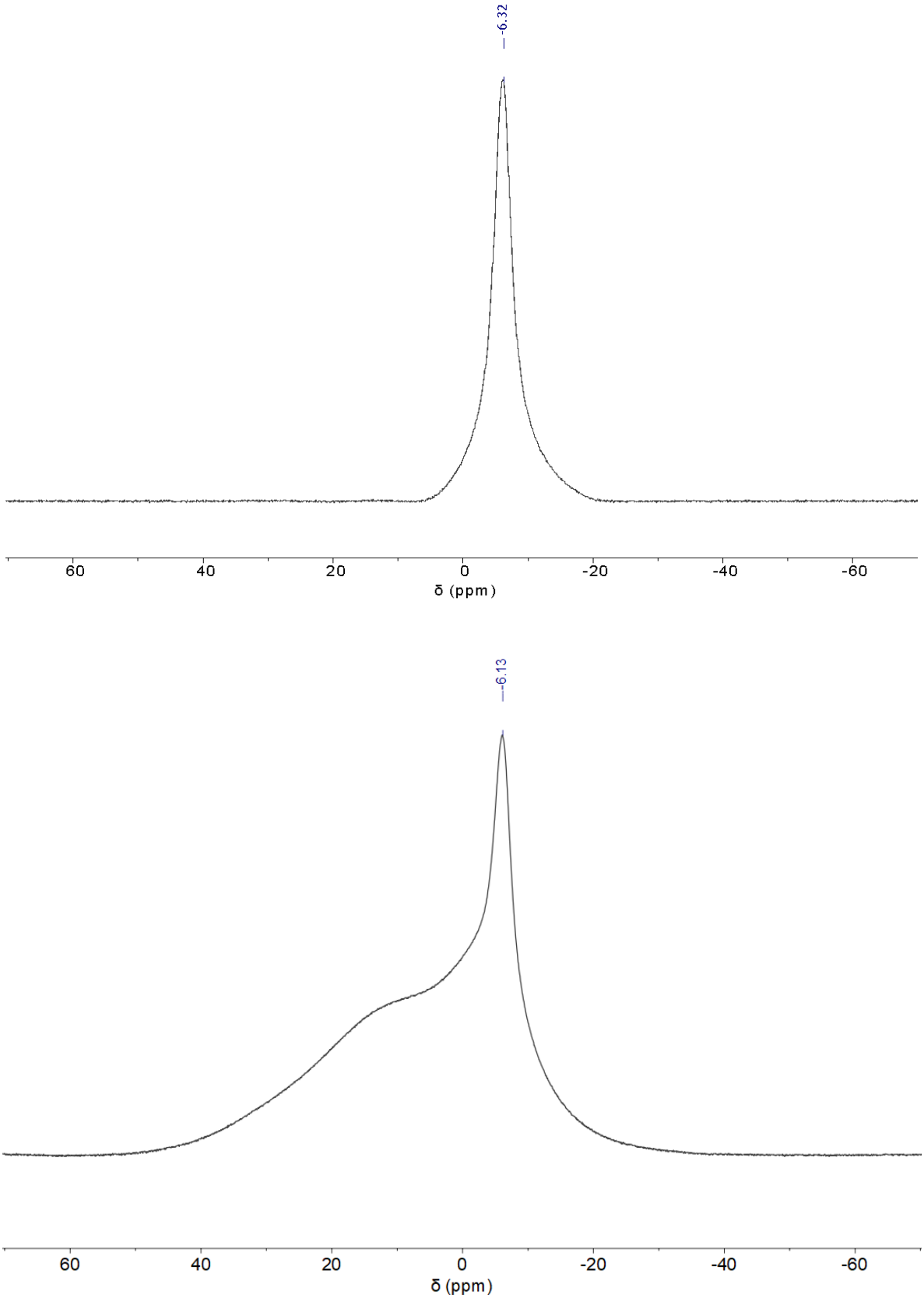

Figure A.5: ^{11}B NMR spectra of Entry 8 (PMeAB8) Baseline corrected and uncorrected, top and bottom respectively: $CDCl_3$, 193 MHz, 298 K.

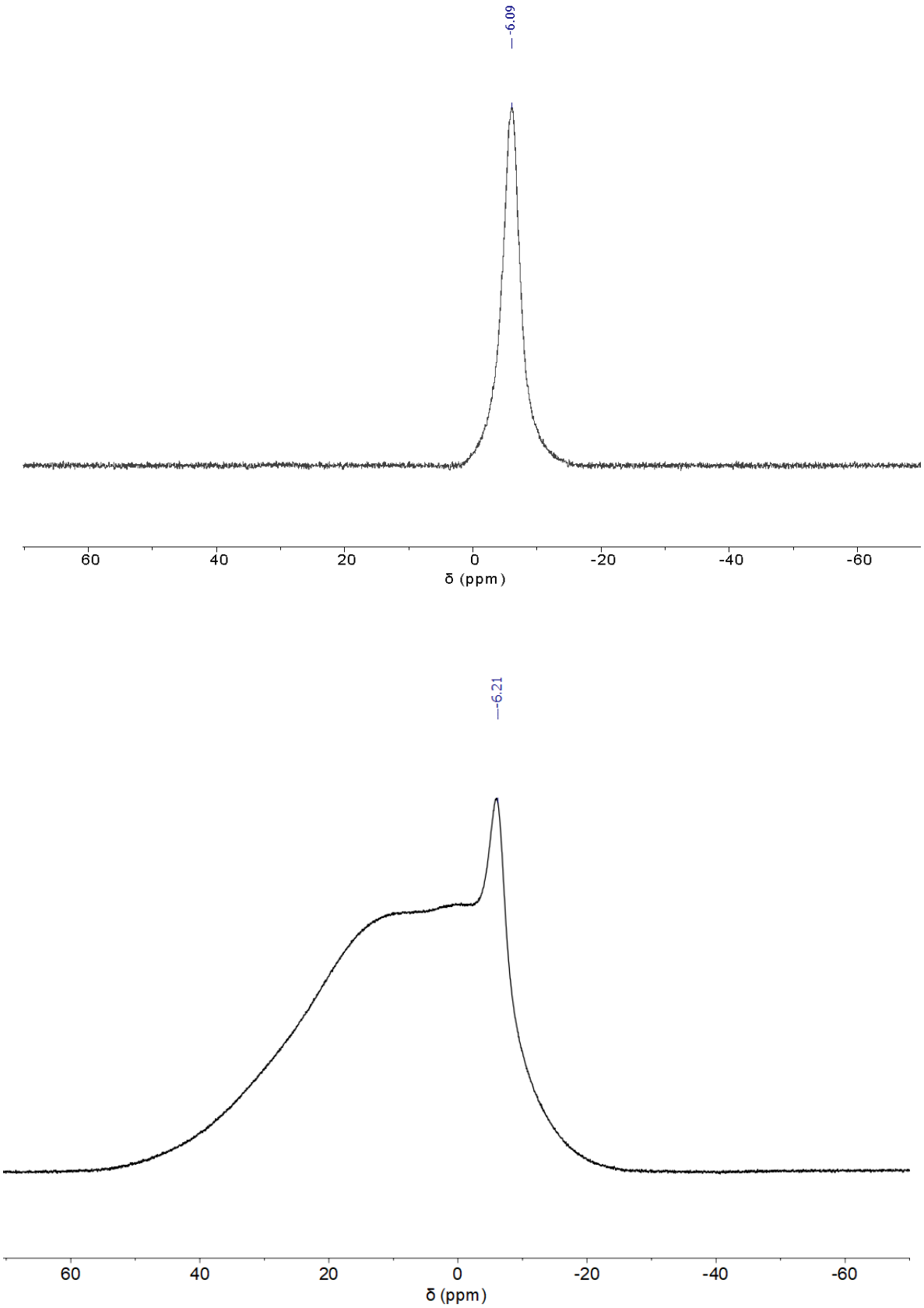

Figure A.6: ^{11}B NMR spectra of Entry 9 (PMeAB9) Baseline corrected and uncorrected, top and bottom respectively: $CDCl_3$, 193 MHz, 298 K.

^{1}H and ^{11}B NMR spectra of PMeAB samples, electrospun fibres, and cured fibres

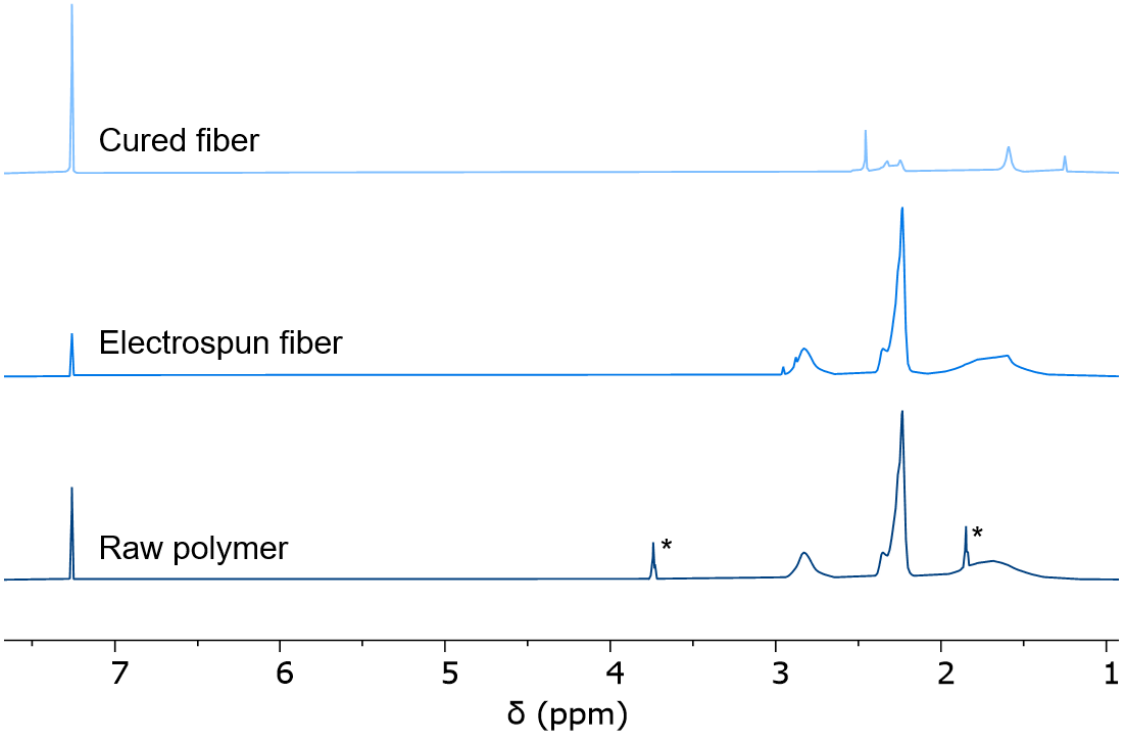

Figure A.7: ^{1}H NMR spectra of Entry 7 (PMeAB7), 600 MHz, $CDCl_3$, 298 K. Raw powder (bottom), Electrospun fibre (middle) and cured fibre (top). Note: the cured fibre was very insoluble in chloroform compared to the electrospun fibre [* indicates residual solvent (THF)].

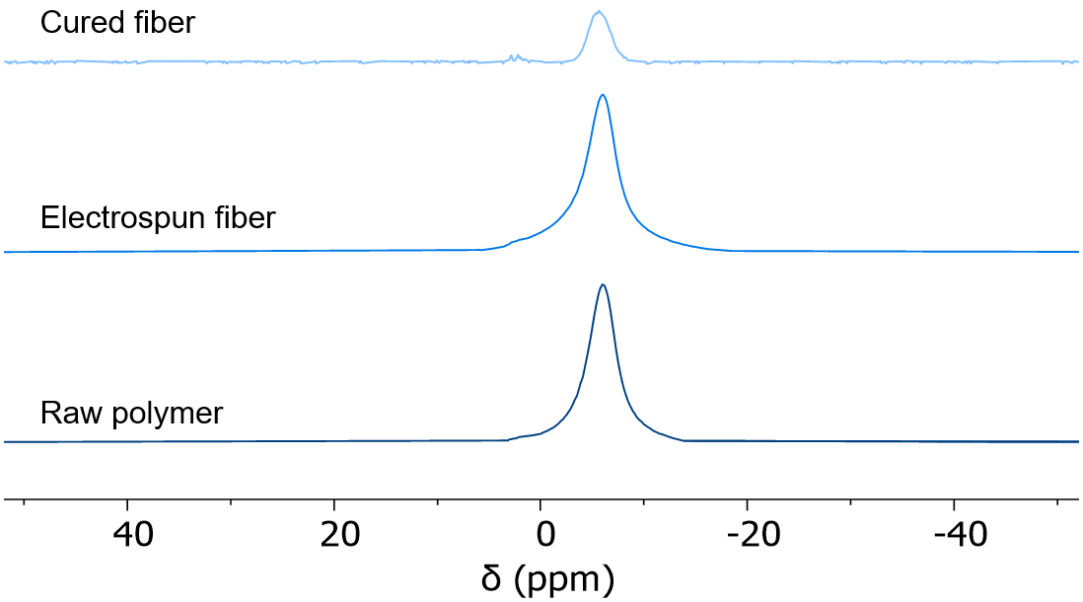

Figure A.8: ^{11}B NMR spectra of Entry 7 (PMeAB7), 600 MHz, $CDCl_3$, 298 K. Raw powder (bottom), Electrospun fibre (middle) and cured fibre (top). Note: the cured fibre was very insoluble in chloroform compared to the electrospun fibre.

^{11}B NMR spectra of PMeAB samples: solid state

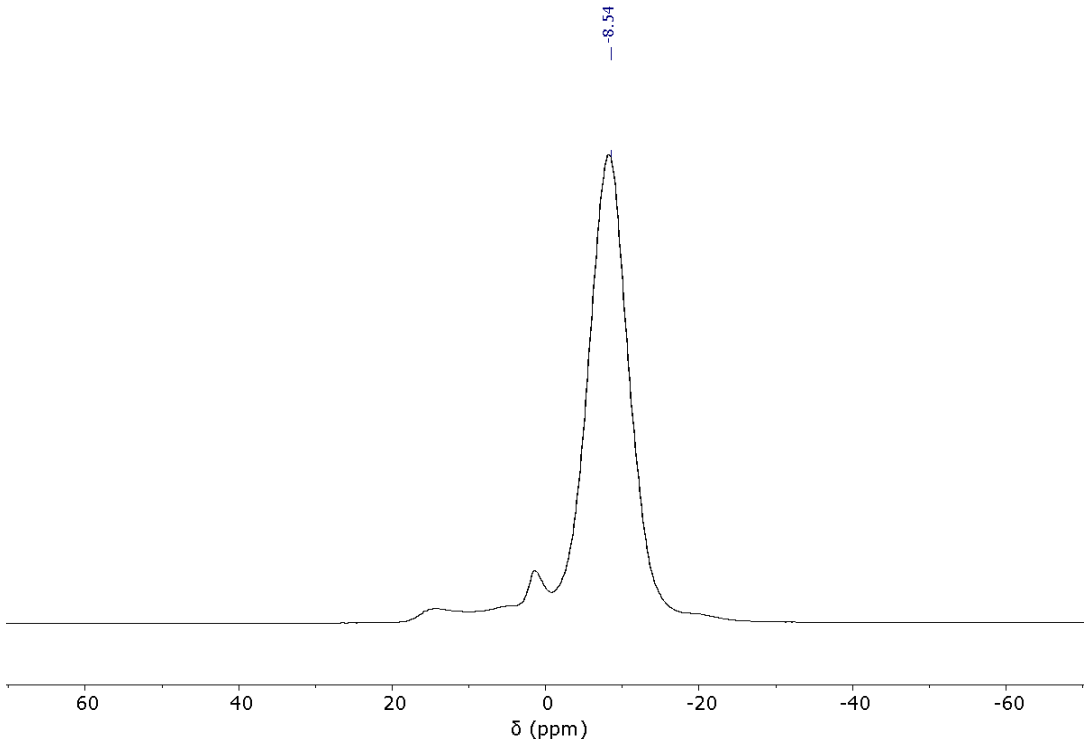

Figure A.9: ^{11}B Solid state NMR of Entry 6 (PMeAB5) – raw polymer (128 MHz, 12 kHz spin rate, 303 K).

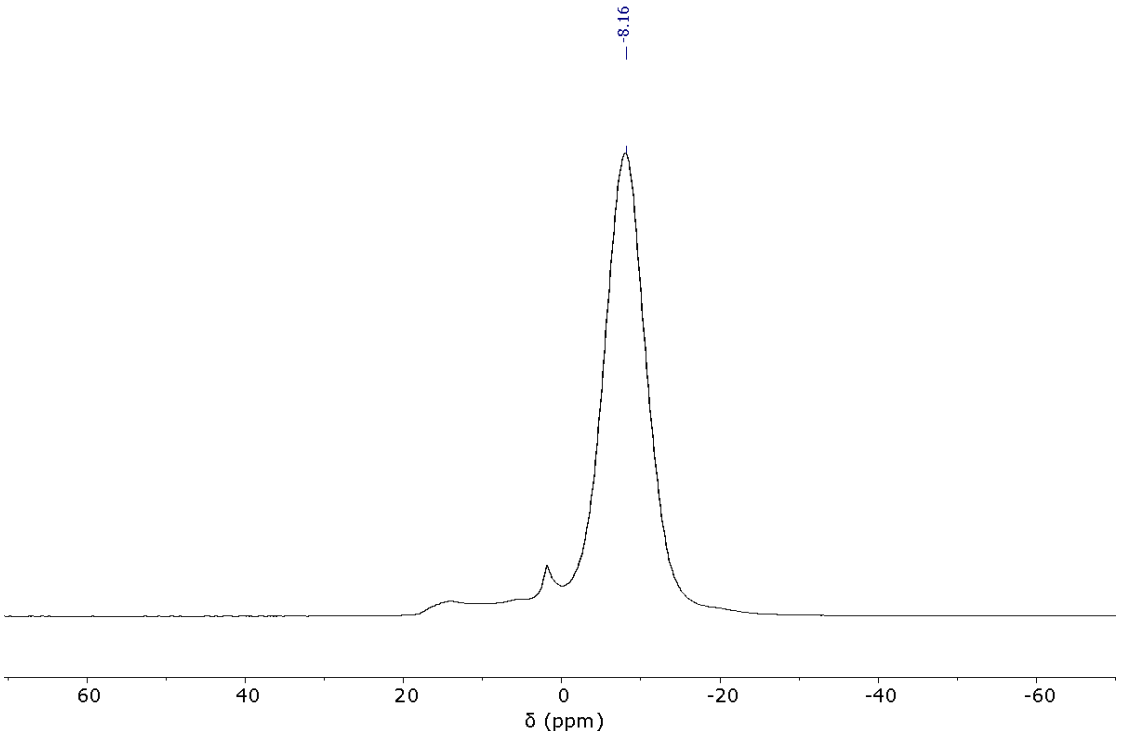

Figure A.10: ^{11}B Solid state NMR of Entry 5 (PMeAB5) – as-spun fibers (128 MHz, 12 kHz spin rate, 303 K).

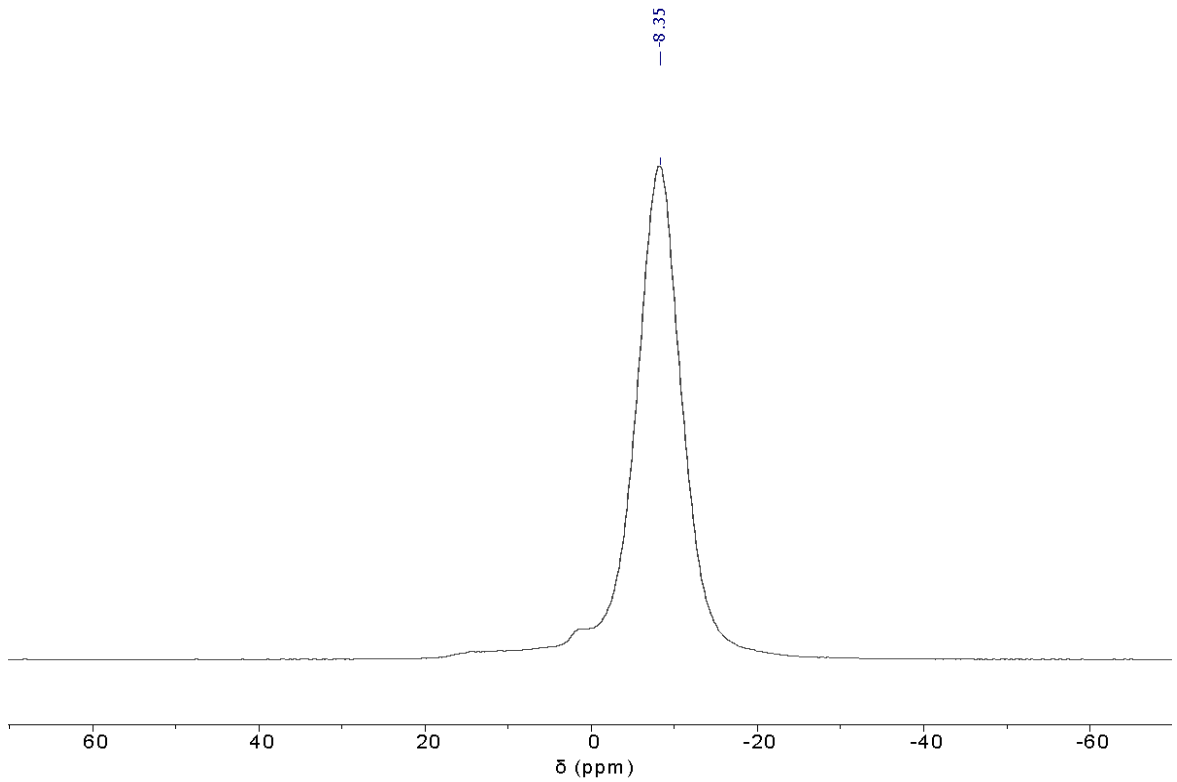

Figure A.11: ^{11}B Solid state NMR of Entry 7 (PMeAB7) – raw powder (128 MHz, 12 kHz spin rate, 303 K).

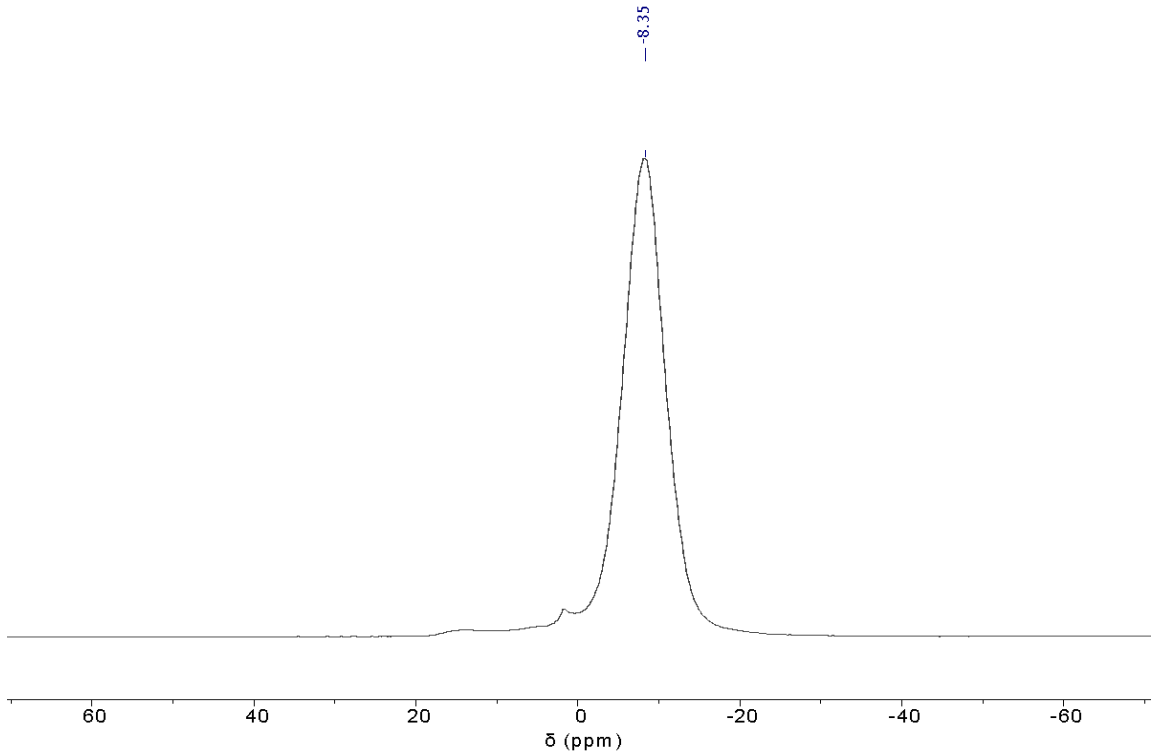

Figure A.12: ^{11}B Solid state NMR of Entry 7 (PMeAB7) – as-spun fibers (128 MHz, 12 kHz spin rate, 303 K).

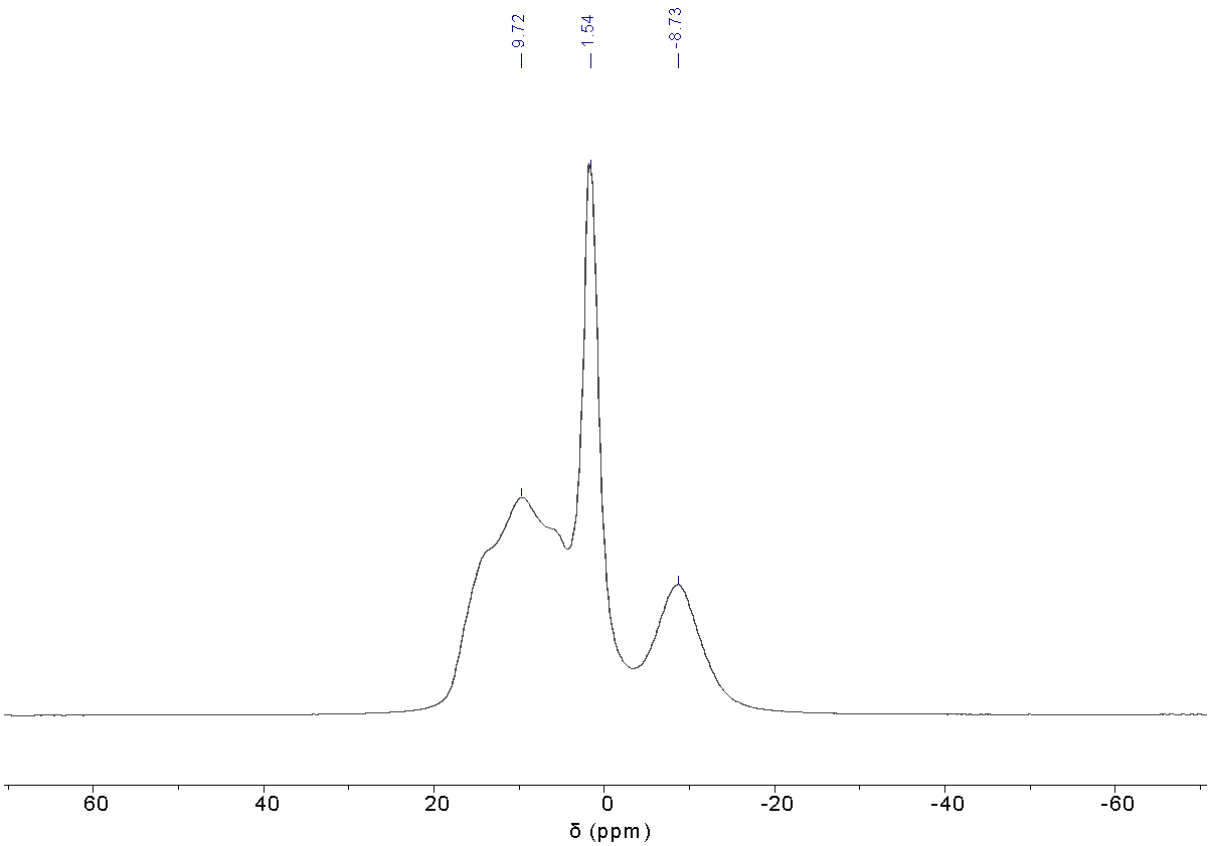

Figure A.13: ^{11}B Solid state NMR of Entry 7 (PMeAB7) – as cured fibers (128 MHz, 12 kHz spin rate, 303K).

MQMAS

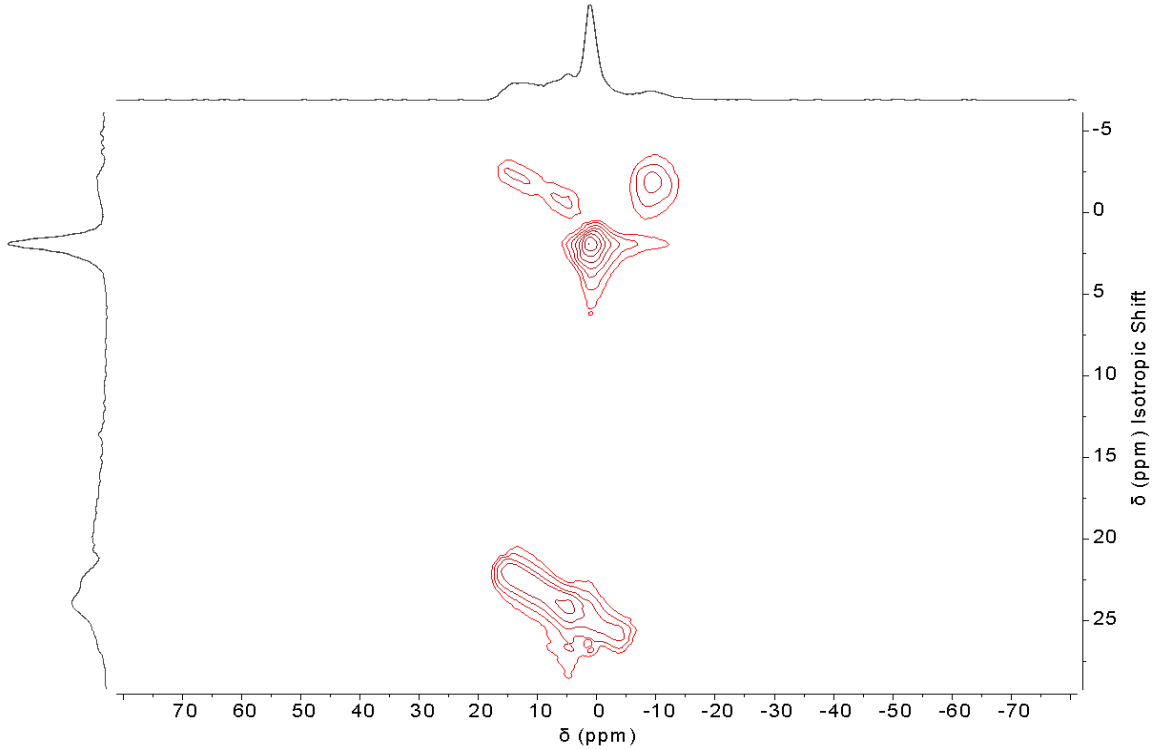

Figure A.14: ^{11}B MQMAS of Entry 7 (PMeAB7) – as cured fibers (Performed on aBruker Avance III HD spectrometer, 128 MHz, 12 kHz spin rate, 300K).

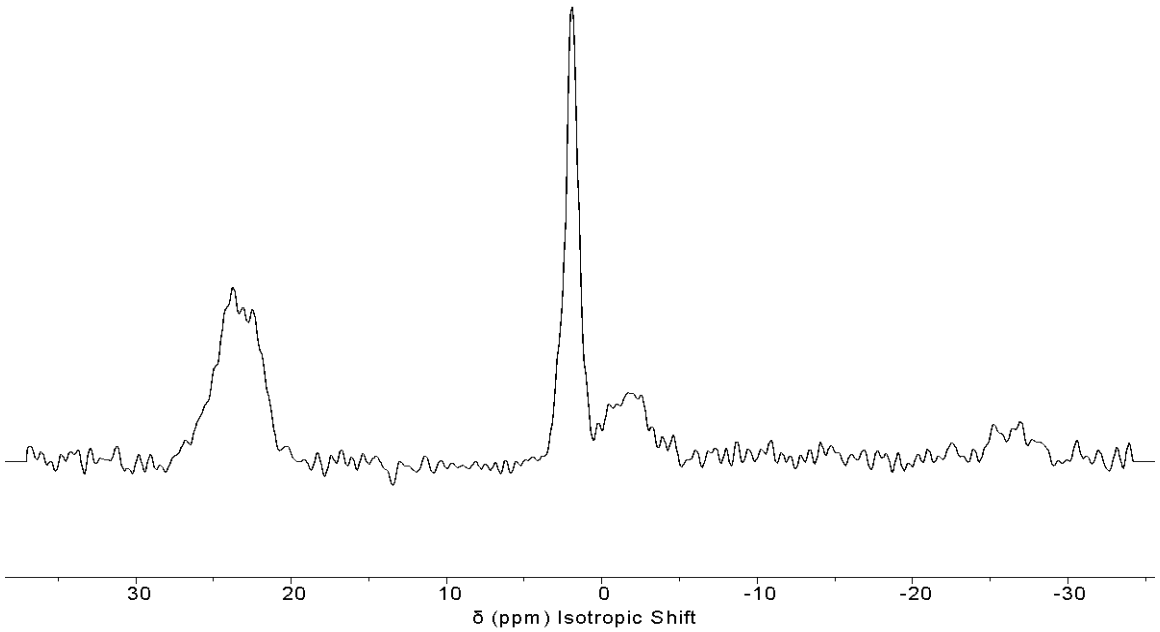

Figure A.15: ^{11}B MQMAS isotropic trace of Entry 7 (PMeAB7) – as cured fibers (12 kHz spin rate, 300 K).

ICP-OES

Table A.2: ICP-OES analysis of polymer samples.

Sample	Element	Concentration (ppm w/w)
PMeAB7 Raw powder	Rh	183
PMeAB7 Electrospun fibers	Rh	191
PMeAB7 Cured fibers	Rh	241

Appendix B. Computational NMR Studies

B.1 Validation of the KT2 Functional with the Experimental Data[276,306,307]

The Marcel's group have made a data set of boron containing compounds with experimentally known chemical shifts. They found a linear correlation between the experimental data and their computed results. Based on the linear fit, they can rationalise the possibility of various nitrogen and carbon containing boron intermediates in the nanomaterials that may be present in the reaction mixture.

Results for the data set

The geometry of each of the compounds of the data set was optimized with S12g/TZ2P (COSMO, ZORA), after which the NMR shielding constants were computed with KT2/ET-pVQZ (COSMO, ZORA). These were used to compute the chemical shifts δ_{calc} (as shown in the Tables below). Plotting the computed shifts against the experimental values, an almost perfect linear correlation was observed, with an offset of 7.2 ppm. This systematic difference between experiment and theory is most likely due to vibrational, dynamical or spin-orbit effects, and influence of the choice of density functional used in the optimisations and NMR nuclear shielding calculations. Because of its systematic nature and the almost perfect correlation, they can use it to predict the experimental chemical shift, by adding the 7.2 ppm offset to the computed chemical shift.

Implicit solvation: CH_2Cl_2

Compound	^{11}B $\delta_{calc.}$ (ppm)	^{11}B $\delta_{exp.}$ (ppm)	^{11}B $\delta_{prediction}$ (ppm)
$B(NHMe)_3$	17.4	24.5[308]	24.7
$B(NMe_2)_3$	20.6	27.3[308]	27.9
$(Me_2N)_2BNCO$	13.0	21.1[309]	20.3
$(Me_2N)_2BNCS$	10.6	19.5[309]	17.9

Implicit solvation: $CHCl_3$

Compound	^{11}B $\delta_{calc.}$ (ppm)	^{11}B $\delta_{exp.}$ (ppm)	^{11}B $\delta_{prediction}$ (ppm)
$B(OMe)_3$	13.3	19.0[310]	20.6
$B(OPh)_3$	9.4	16.4[310]	16.7
BH_3NEt_3	-23.0	-14.0[311]	-15.8
Ph_2BOH	37.9	45.7[312]	45.2
BEt_3	81.1	86.5[313]	88.6
tBu-B≡N-tBu	-2.3	2.4[308]	4.9
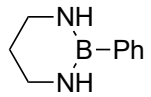	20.0	28.4[312]	27.3
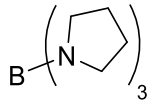	15.5	24.0[310]	22.7

Implicit solvation: Benzene

Compound	^{11}B $\delta_{calc.}$ (ppm)	^{11}B $\delta_{exp.}$ (ppm)	^{11}B $\delta_{prediction}$ (ppm)
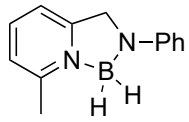	-9.0	-2.6[314]	-1.9
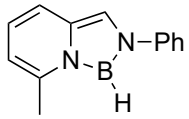	9.9	19.7[314]	17.1
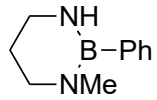	20.7	28.9[312]	28.0
iPr_2N-B≡N-tBu	-0.09	5.8[308]	7.1
Trimethyl Borazine	24.7	33.2[315]	32.0
Borazine	21.7	30.2[316]	29.0

Implicit solvation: THF

Compound	^{11}B δ_{calc} (ppm)	^{11}B $\delta_{exp.}$ (ppm)	^{11}B $\delta_{prediction}$ (ppm)
BH_3NH_3	-29.1	-22.0[317]	-22.0
$[B(NHMe)_4]^-$	-3.2	0.2[318]	4.0

BMe_3	78.7	86.0[313]	86.2

B.2 Correlation of Experiment and Theory

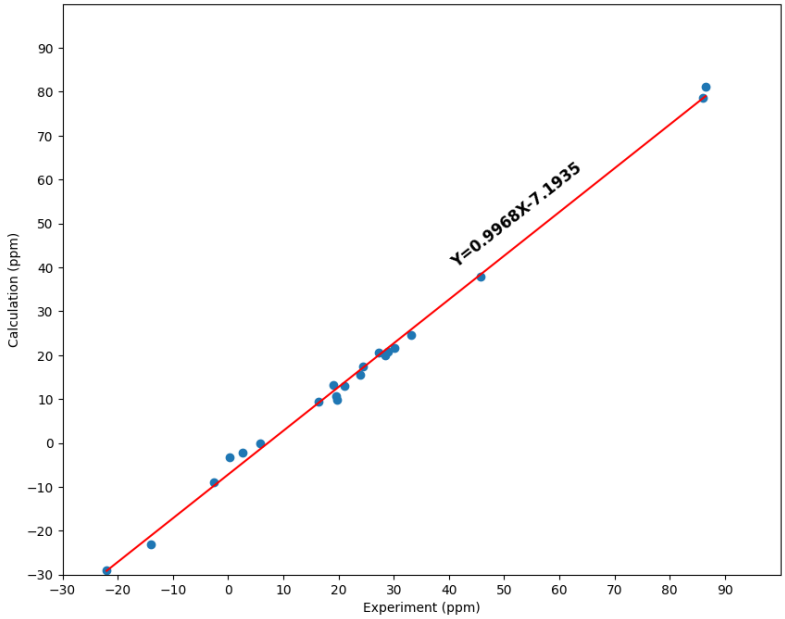

RMSE=1.5306ppm $R^2 = 0.9965$

Their results with KT2 shows good correlation with the experimental results.[5] They then moved on to the nanomaterials, where they explored a wide range of different geometries of small compounds, within different conformations. Shown in the Tables below are the results for the PMeAB)-related compounds that are consistent with the experimentally observed peaks.

PMeAB-related compounds (calculated chemical shift value in red beside the target boron nucleus)

(i) Precursor PMeAB

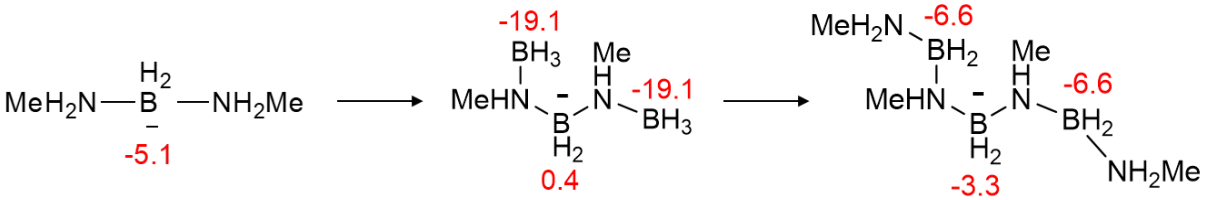

(ii) Cured PMeAB

- Central boron bonded to three nitrogen atoms

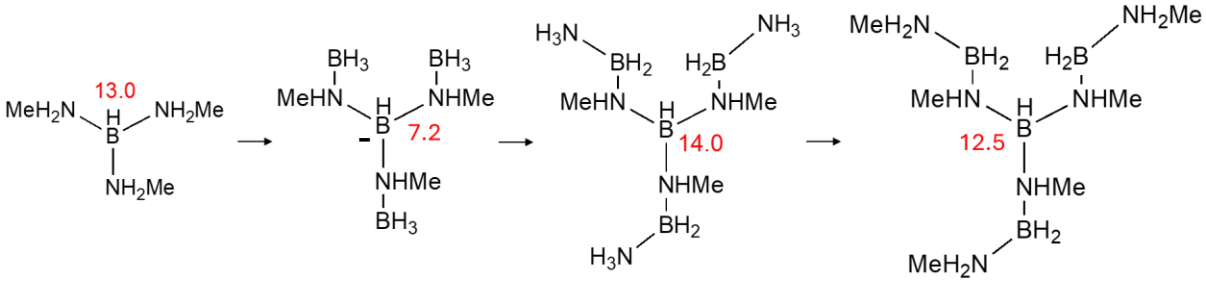

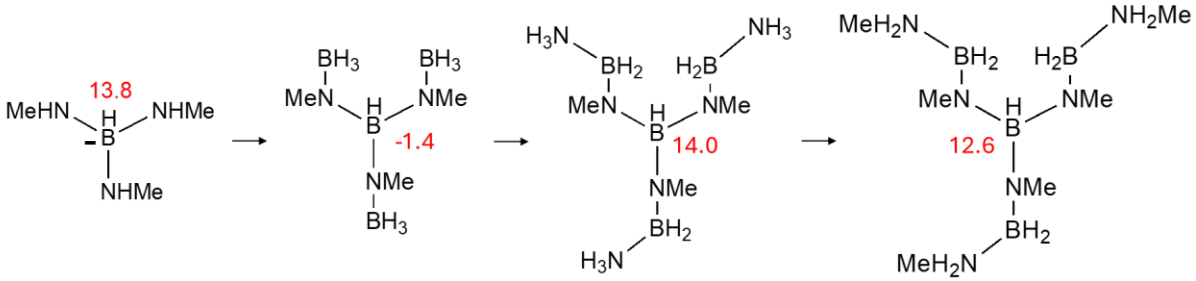

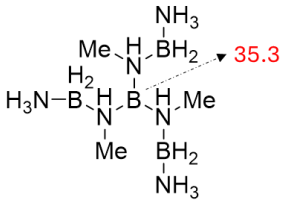

- Central boron bonded to four nitrogen atoms

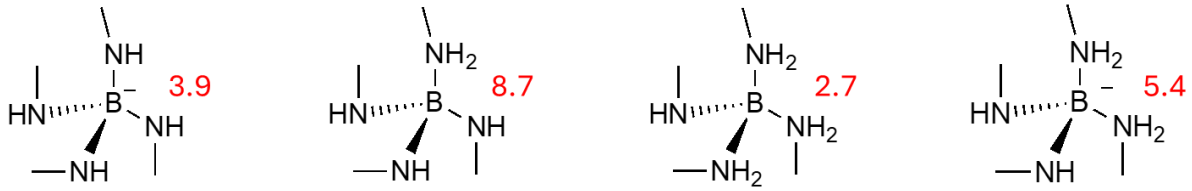

Compound	^{11}B $\delta_{calc.}$ (ppm)	^{11}B $\delta_{prediction}$ (ppm)	^{11}B $\delta_{solution}$ (ppm)	^{11}B δ_{solid} (ppm)
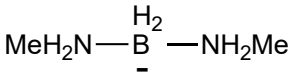	-12.3	-5.1	-6.2	-8.7
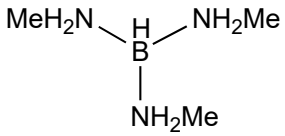	5.8	13.0	-	9.7
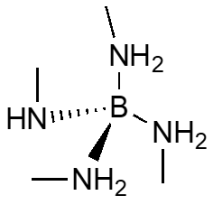	-4.5	2.7	-	1.5

Appendix C. Configurations and Energy Profiles of PES Mapping

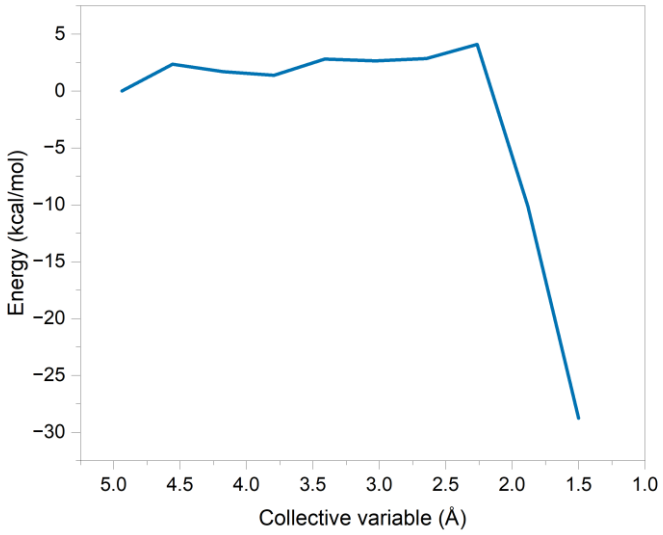

Figure C.1: PES energy profile of the cyclisation reaction of PMeAB3-nocap to form MeCTB.

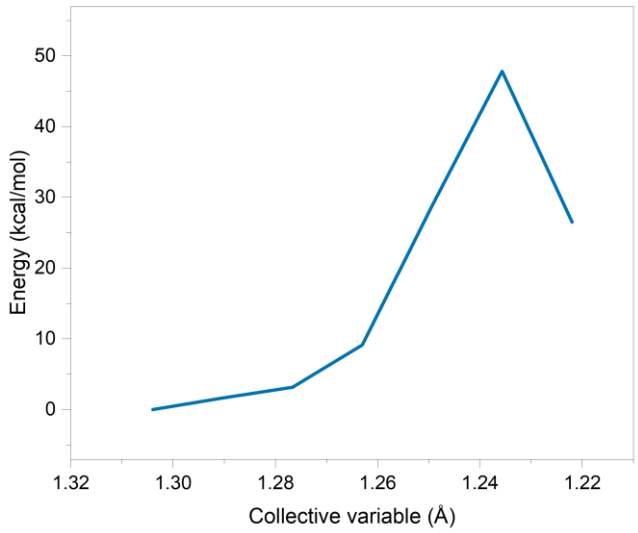

Figure C.2: PES energy profile of the cyclisation reaction of PMeAB3-nocap to form BCDMeB (middle-boron bonding).

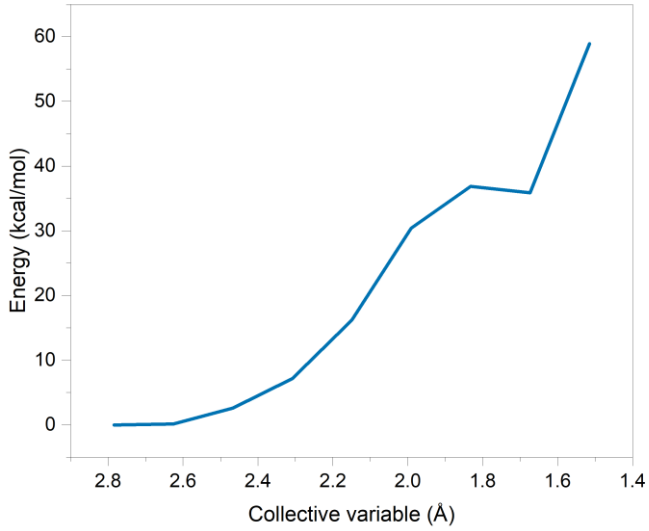

Figure C.3: PES energy profile of the cyclisation reaction of PMeAB3-nocap to form BCDMeB (middle-nitrogen bonding).

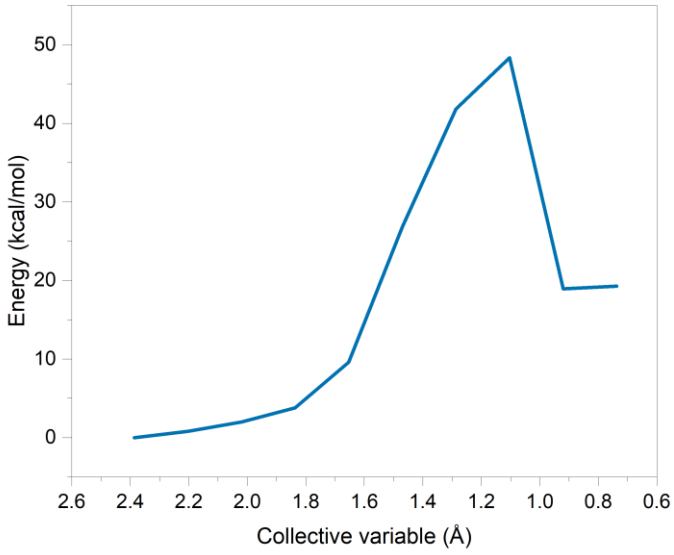

Figure C.4: PES energy profile of the dehydrogenation reaction of PMeAB3-nocap across (B─N) (1st H_2 release).

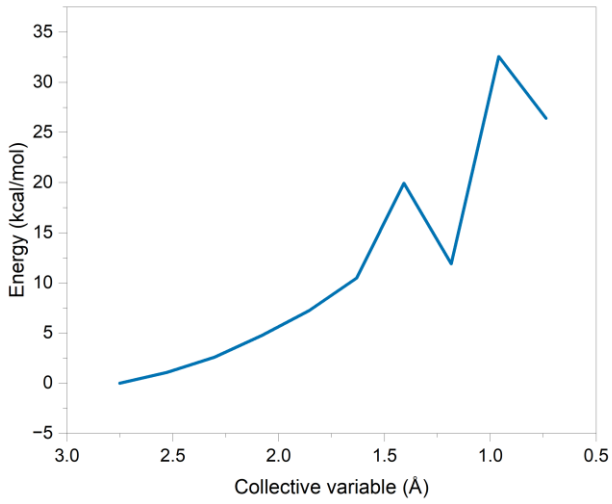

Figure C.5: PES energy profile of the dehydrogenation reaction of PMeAB3-nocap across (B─B).

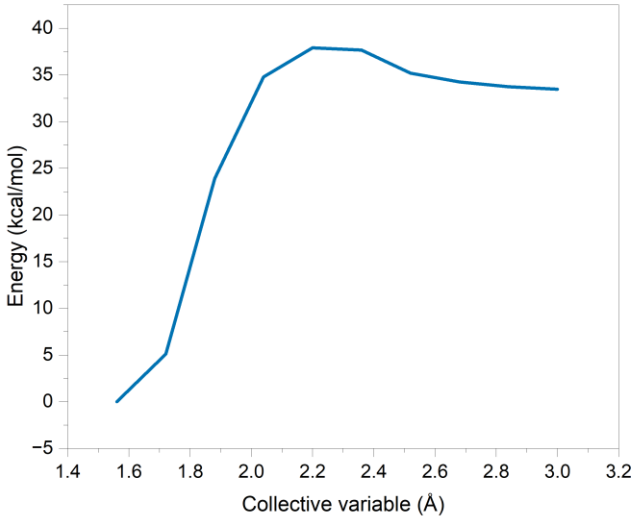

Figure C.6: PES energy profile of the dissociation reaction of PMeAB3-nocap (1st B─N) to produce BH_2.

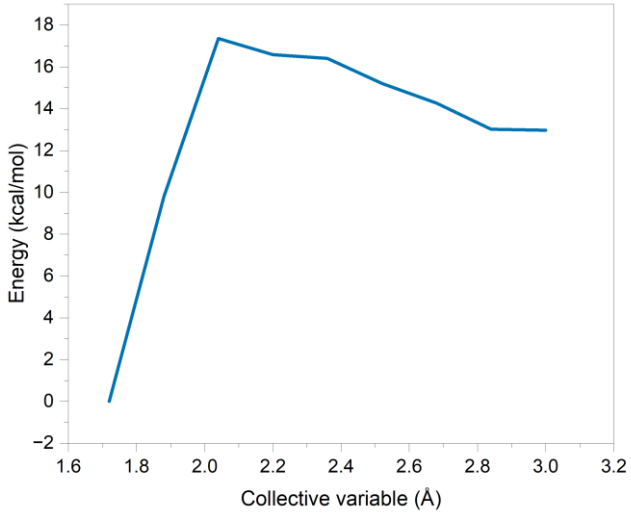

Figure C.7: PES energy profile of the dissociation reaction of PMeAB3-nocap (1st B─N) to produce BH_3.

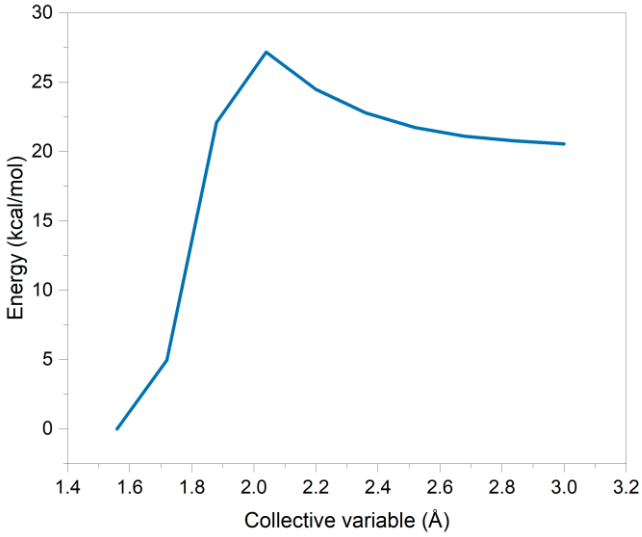

Figure C.8: PES energy profile of the dissociation reaction of PMeAB3-nocap (2nd B─N) to produce MeIB.

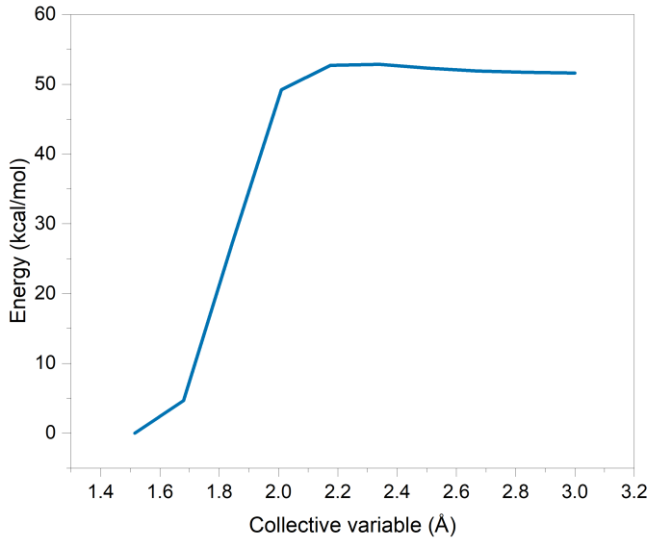

Figure C.9: PES energy profile of the dissociation reaction of PMeAB3-nocap (3rd B─N).

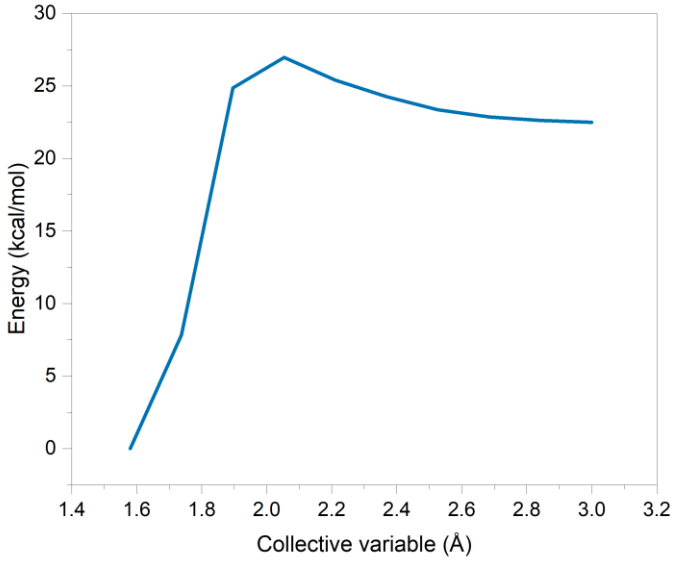

Figure C.10: PES energy profile of the dissociation reaction of PMeAB3-nocap (4th B─N) to produce MeIB.

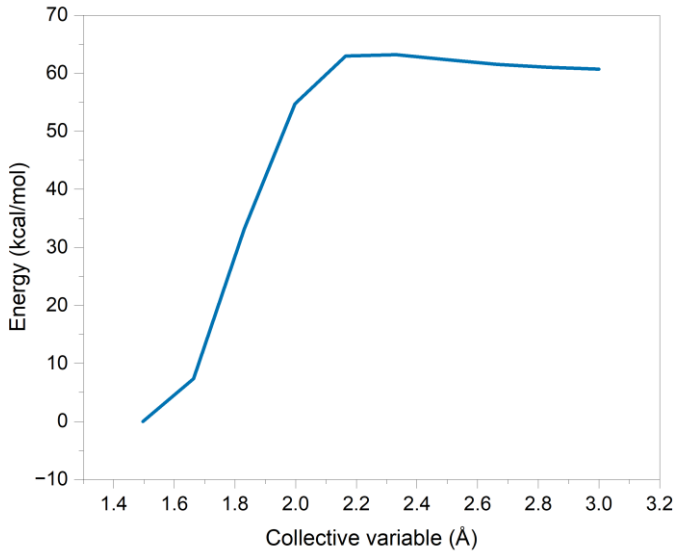

Figure C.11: PES energy profile of the dissociation reaction of PMeAB3-nocap (5th B─N).

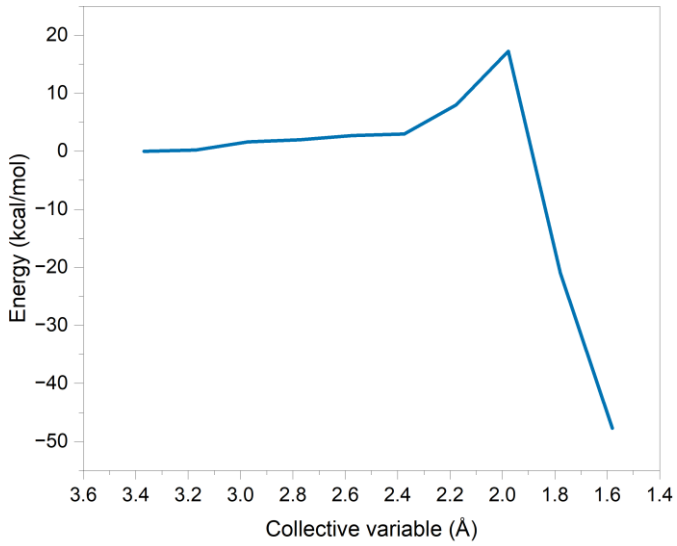

Figure C.12: PES energy profile of the addition/dehydrogenation reaction of PMeAB3-nocap with BH_2.

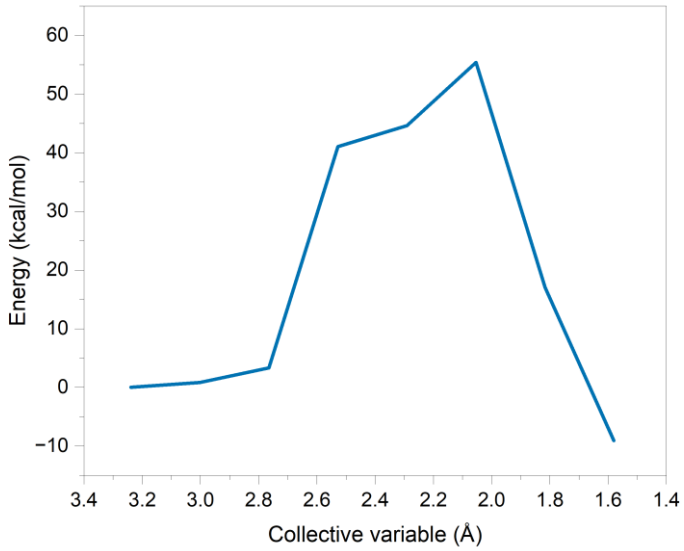

Figure C.13: PES energy profile of the addition/dehydrogenation reaction of PMeAB3-nocap with BH_3.

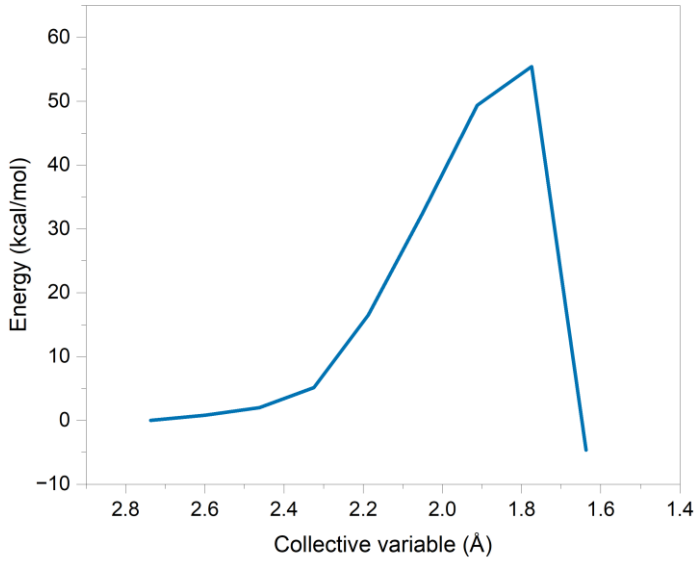

Figure C.14: PES energy profile of the addition/dehydrogenation reaction of PMeAB3-nocap with MeIB.

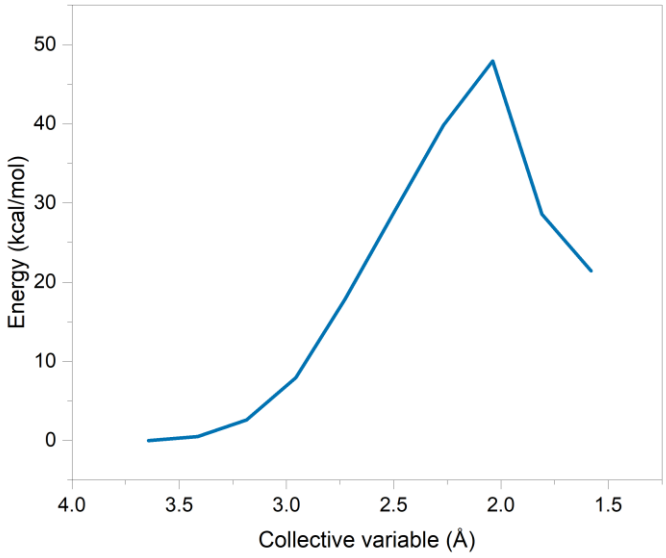

Figure C.15: PES energy profile of the addition/dehydrogenation reaction of PMeAB3-nocap with PMeAB3-nocap.

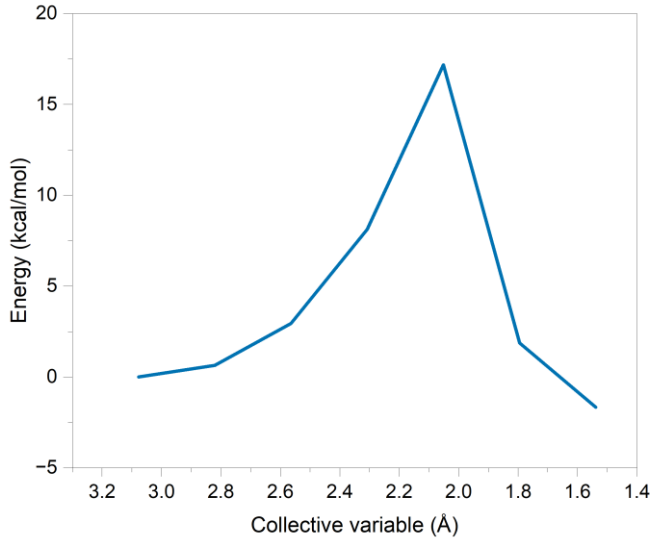

Figure C.16: PES energy profile of the cyclisation reaction of PMeAB2-nocap to form MeCDB.

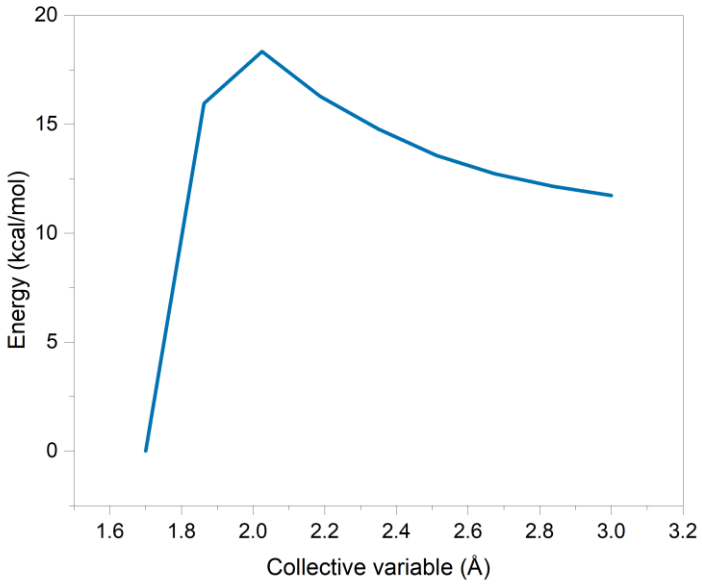

Figure C.17: PES energy profile of the dissociation reaction of PMeAB2-nocap to form MeIB.

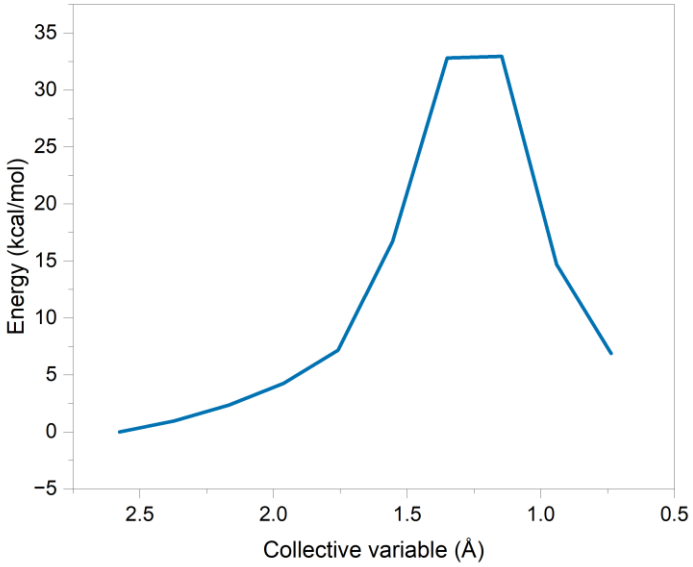

Figure C.18: PES energy profile of the dehydrogenation reaction of PMeAB2-nocap across (B─N).

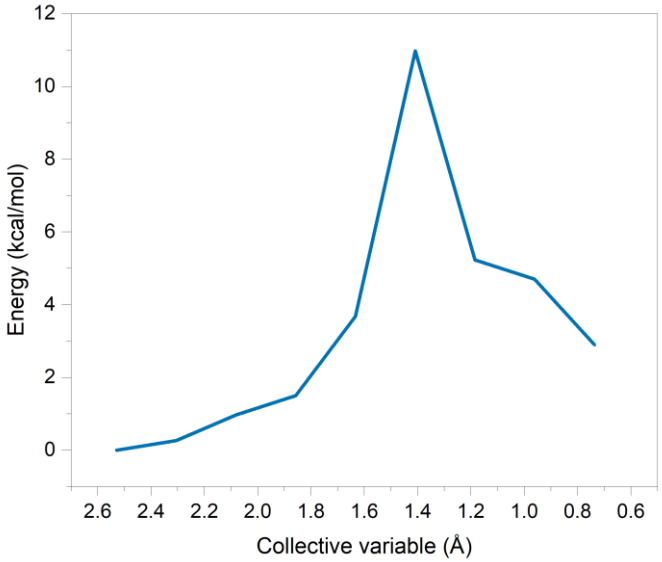

Figure C.19: PES energy profile of the dehydrogenation reaction of PMeAB2-nocap across (B─B).

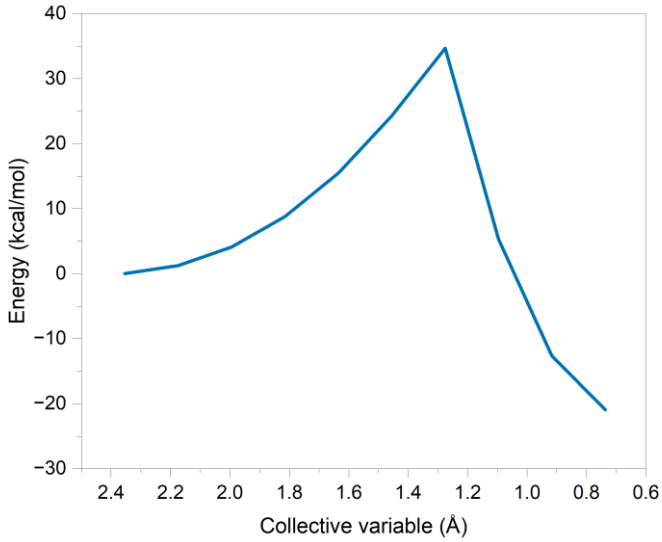

Figure C.20: PES energy profile of the dehydrogenation reaction of MeAB across (B─N).

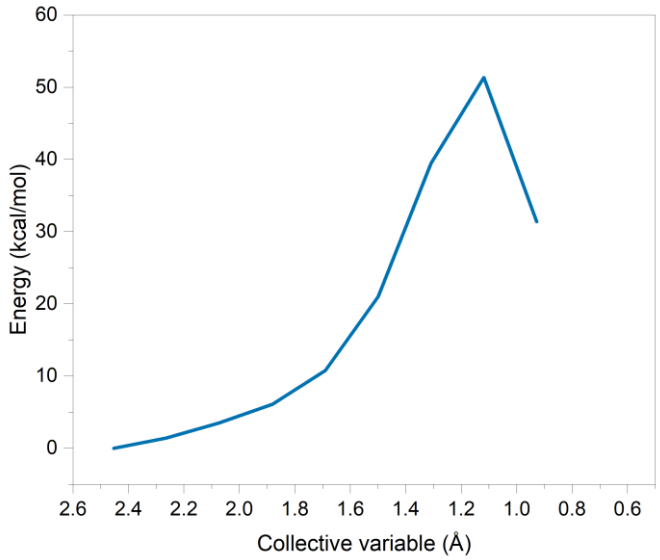

Figure C.21: PES energy profile of the dehydrogenation reaction of MeIB across (B─N).

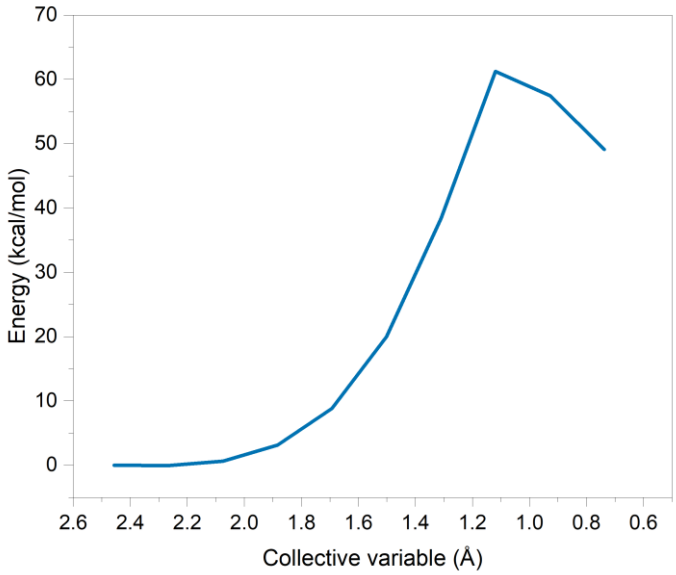

Figure C.22: PES energy profile of the dehydrogenation reaction of MeIB across (N─C).

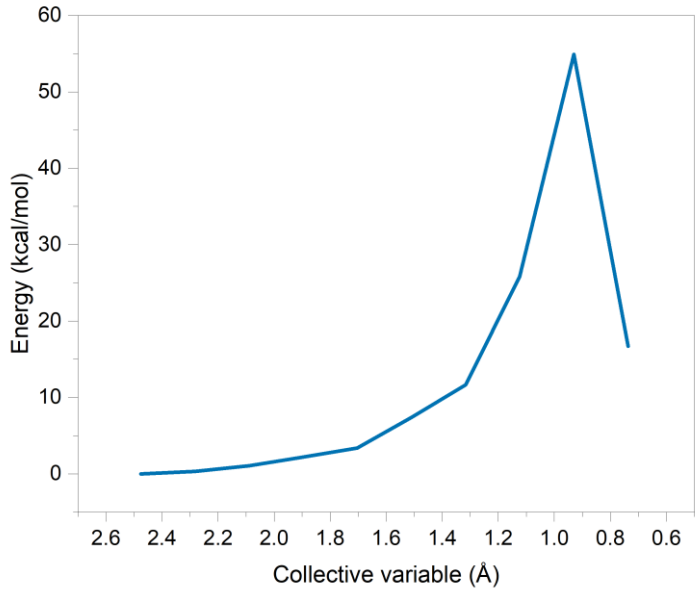

Figure C.23: PES energy profile of the dehydrogenation reaction of MeIB across (B─C).

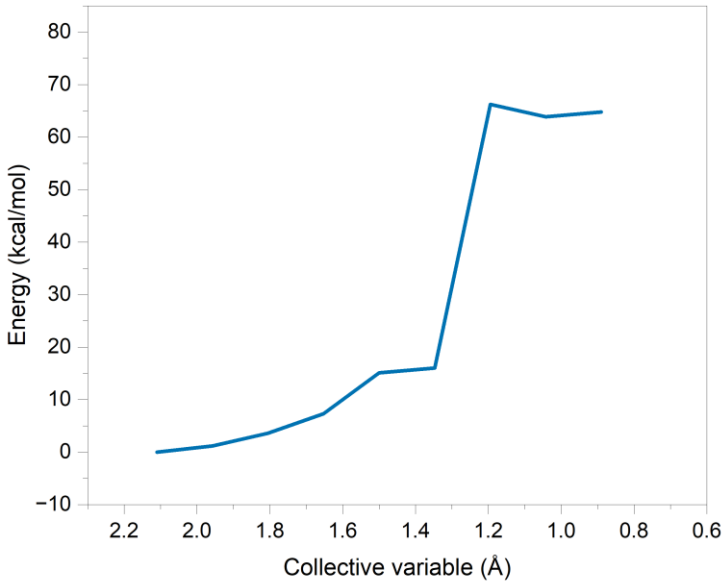

Figure C.24: PES energy profile of the dehydrogenation reaction of MeIB across (B─B).

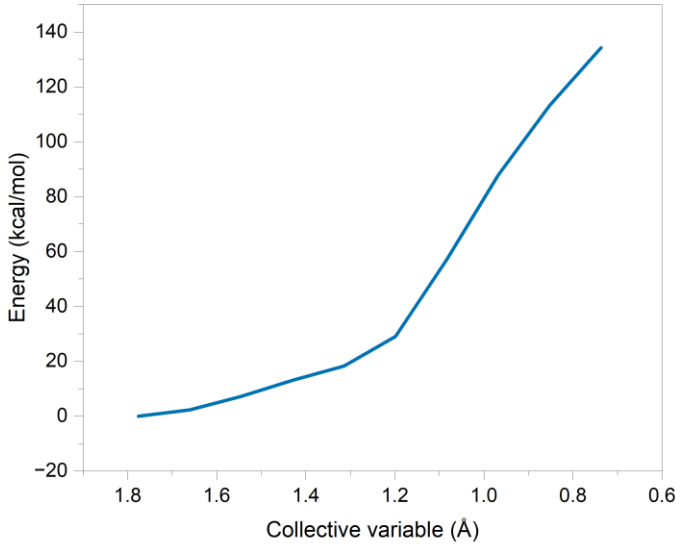

Figure C.25: PES energy profile of the dehydrogenation reaction of MeIB across (C─C).

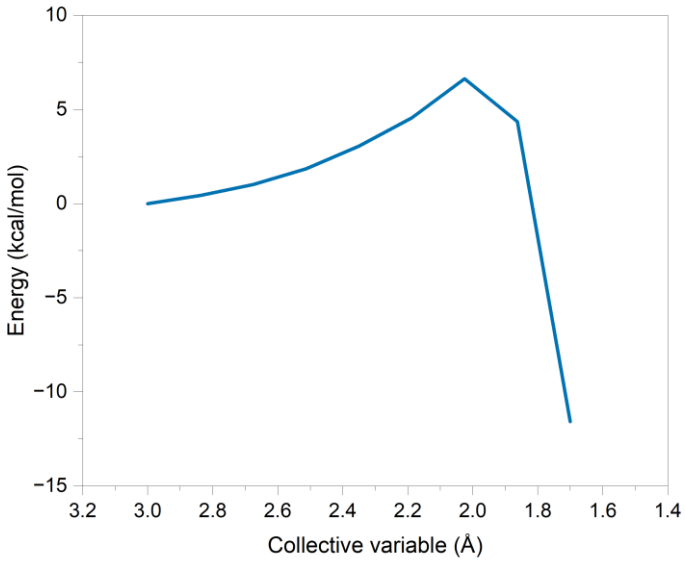

Figure C.26: PES energy profile of the polymerisation reaction of MeIB to form dimer.

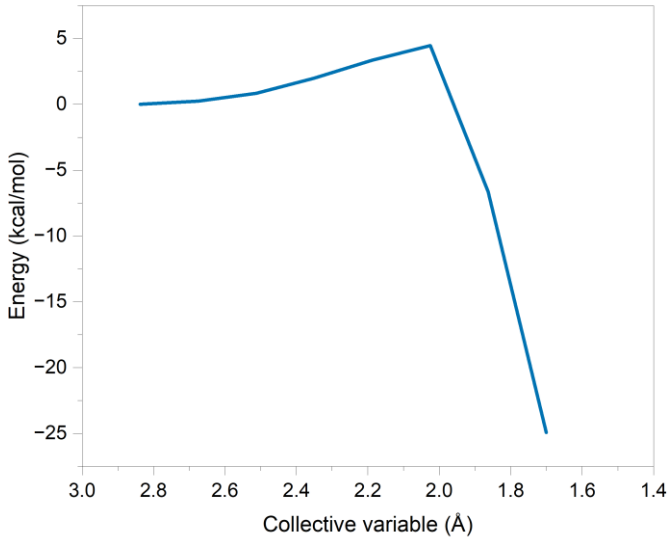

Figure C.27: PES energy profile of the polymerisation reaction of MeIB to form trimer.

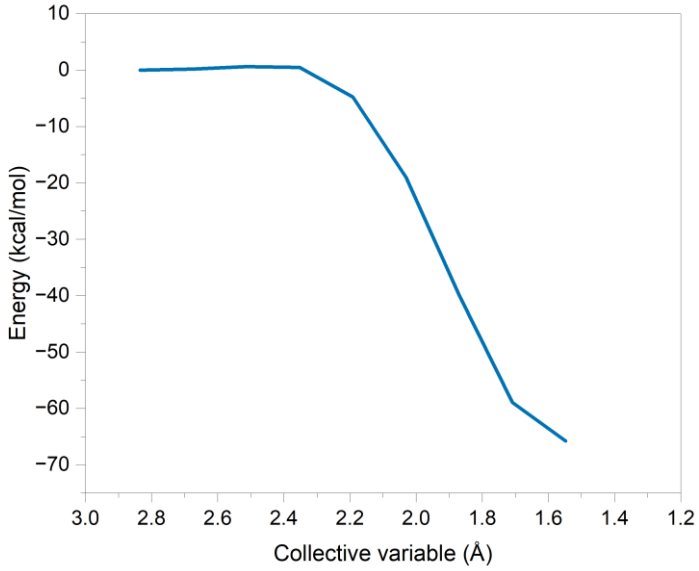

Figure C.28: PES energy profile of the addition reaction of MeIB with BH_2.

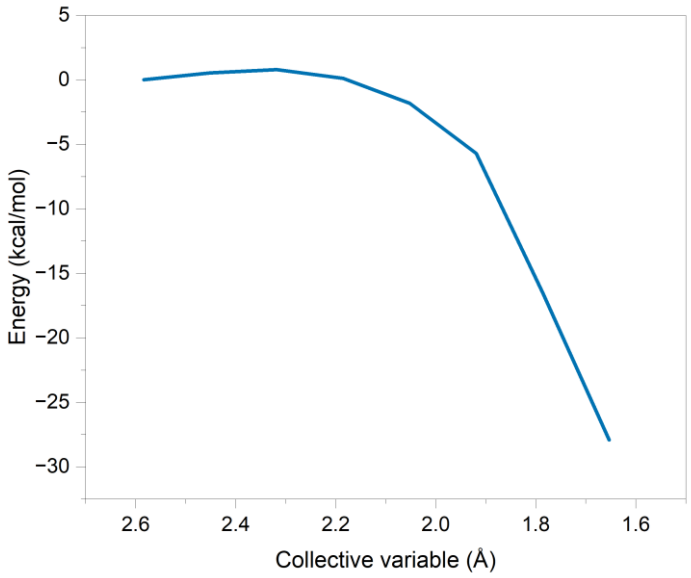

Figure C.29: PES energy profile of the addition reaction of MeIB with BH_3.

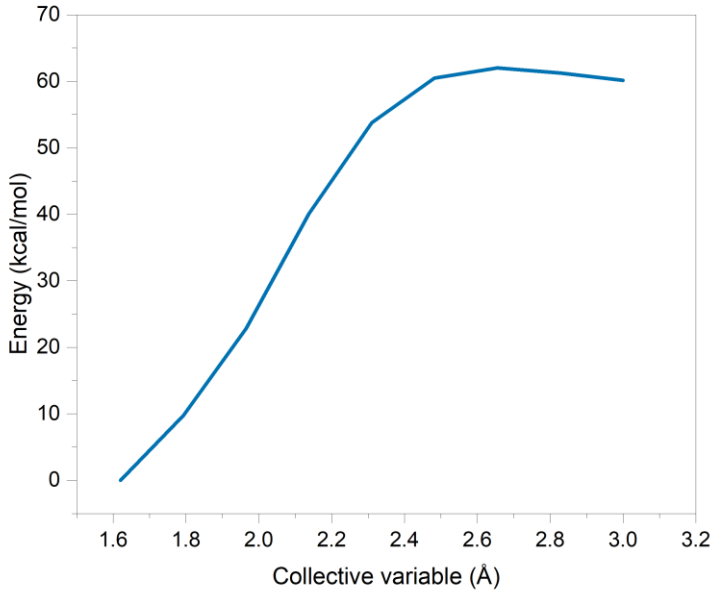

Figure C.30: PES energy profile of the dissociation reaction of MeIB (C─N).

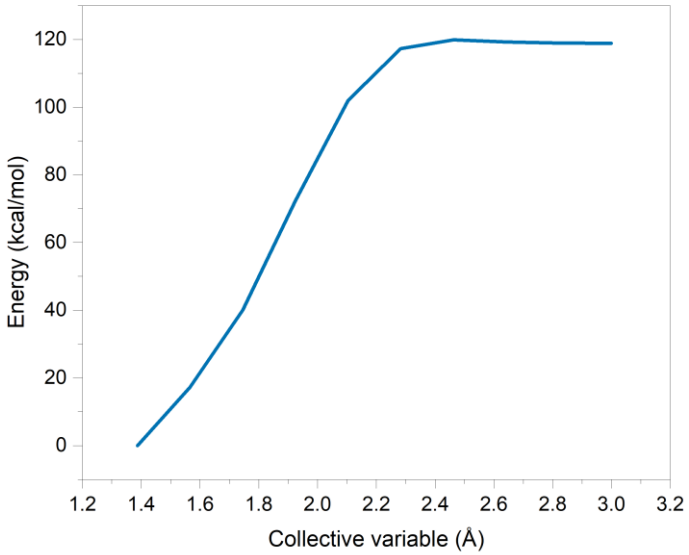

Figure C.31: PES energy profile of the dissociation reaction of MeIB (B─N).

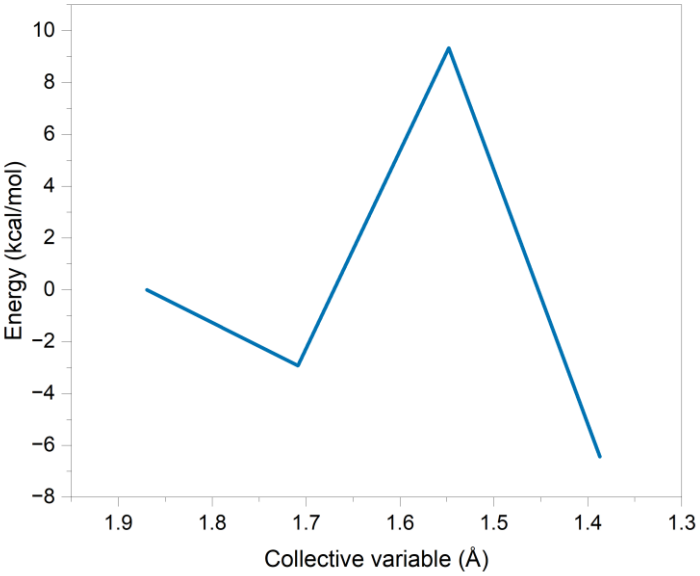

Figure C.32: PES energy profile of the addition/dehydrogenation reaction of MeIB with BH_2.

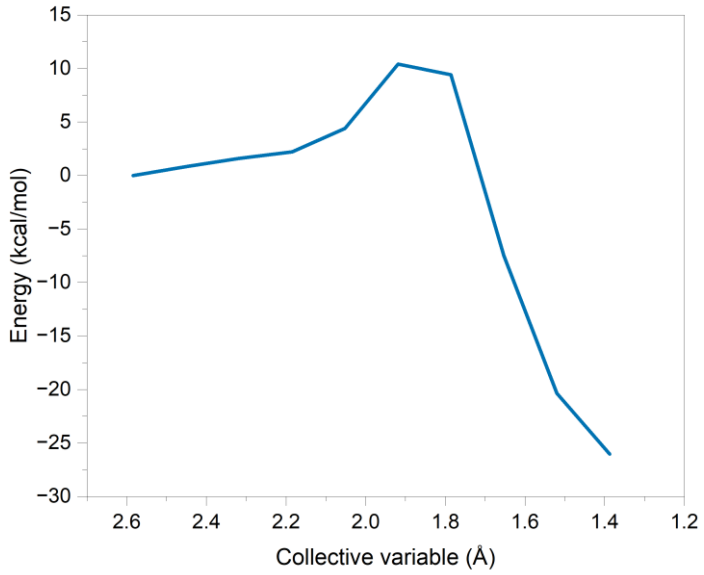

Figure C.33: PES energy profile of the addition/dehydrogenation reaction of MeIB with BH_3.

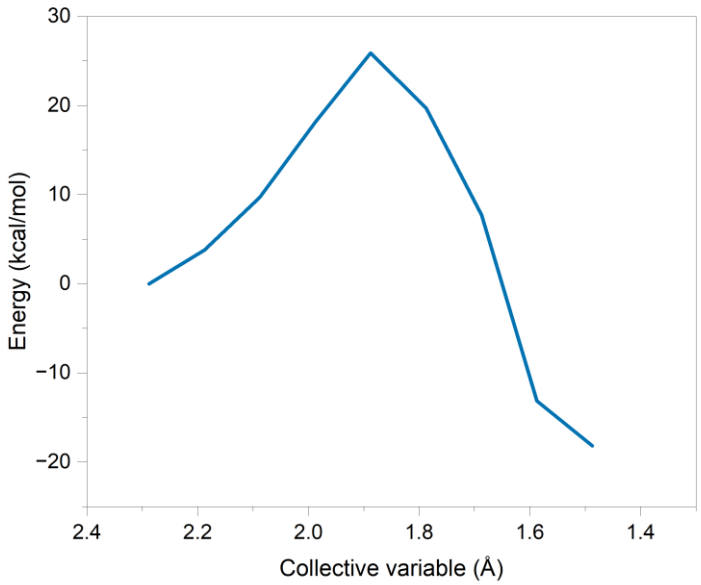

Figure C.34: PES energy profile of the addition/dehydrogenation reaction of MeIB with MeIB.

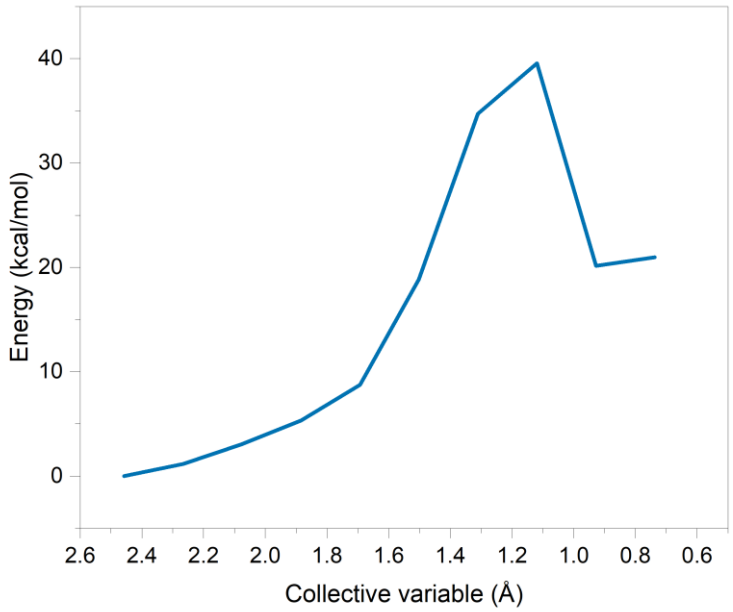

Figure C.35: PES energy profile of the dehydrogenation reaction of MeCTB across (B─N) (1st H_2 release).

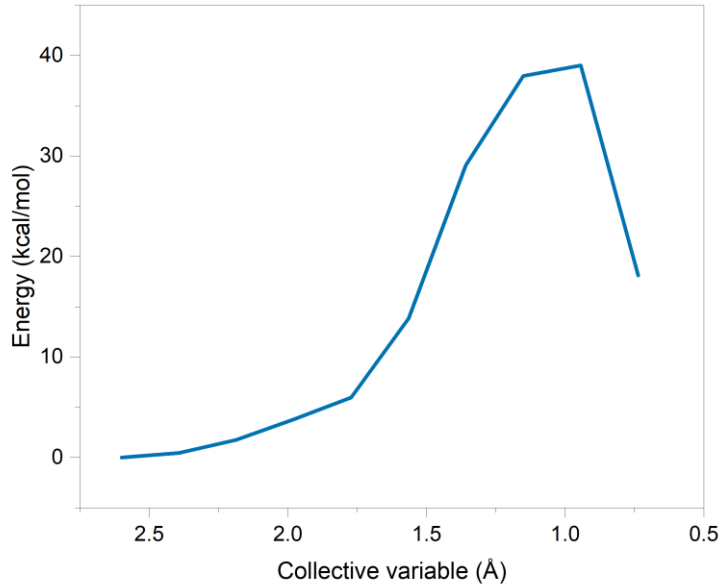

Figure C.36: PES energy profile of the dehydrogenation reaction of MeCTB across (B─N) (2nd H_2 release).

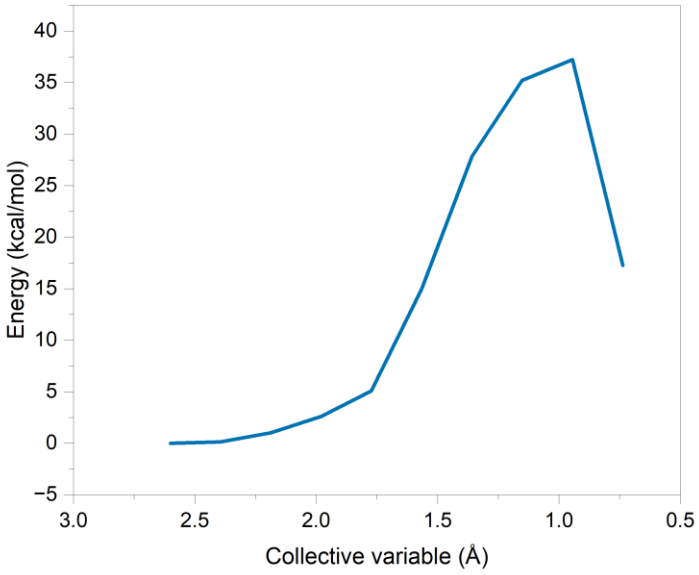

Figure C.37: PES energy profile of the dehydrogenation reaction of MeCTB across (B─N) (3rd H_2 release).

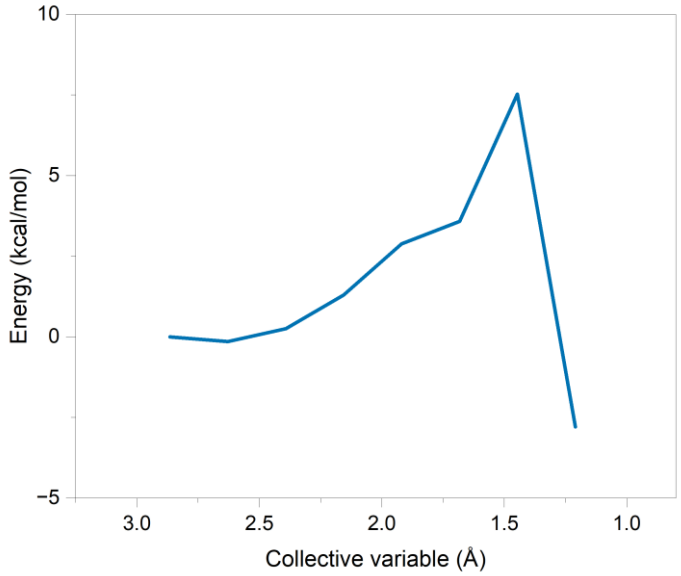

Figure C.38: PES energy profile of the dehydrogenation reaction of MeCTB across (B─B) (1st H_2 release).

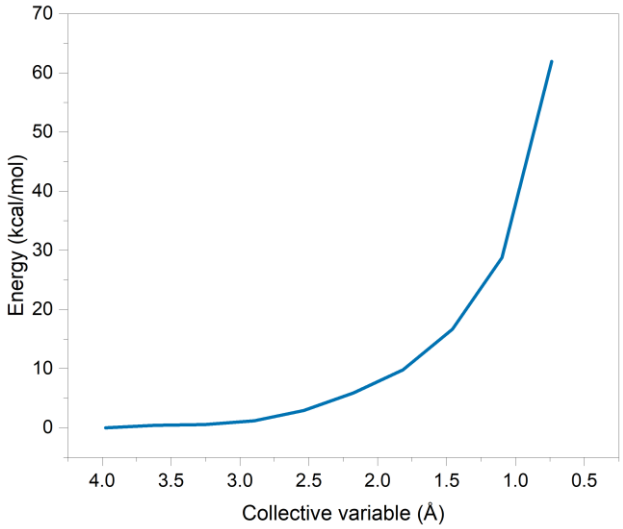

Figure C.39: PES energy profile of the dehydrogenation reaction of MeCTB across (B─B) (2nd H_2 release).

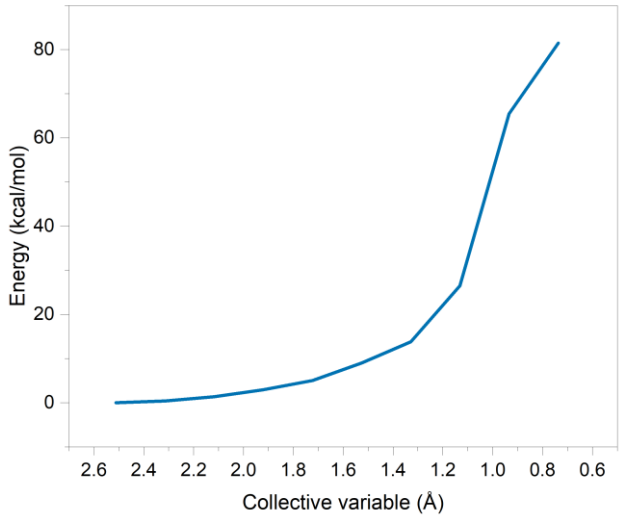

Figure C.40: PES energy profile of the dehydrogenation reaction of MeCTB across (B─C).

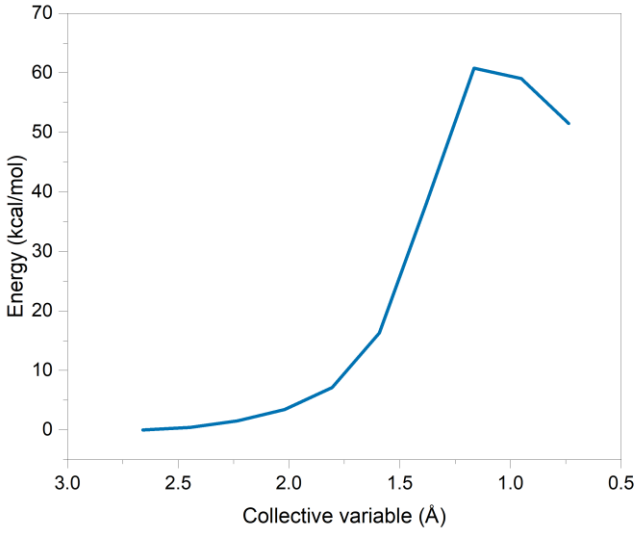

Figure C.41: PES energy profile of the dehydrogenation reaction of MeCTB across (N─N).

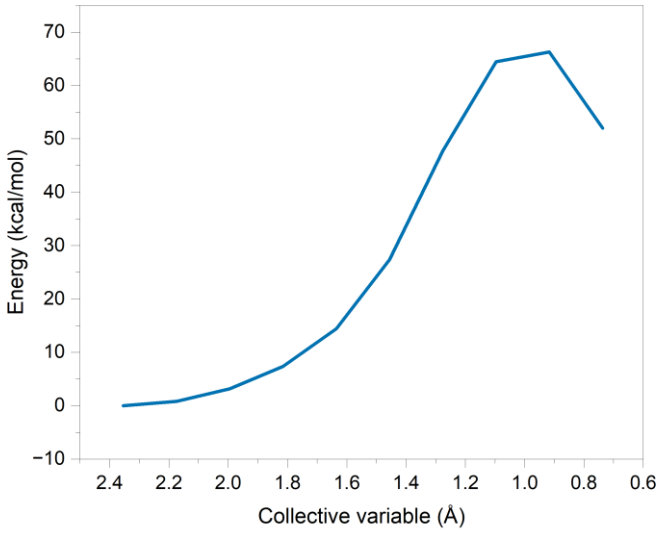

Figure C.42: PES energy profile of the dehydrogenation reaction of MeCTB across (N─C).

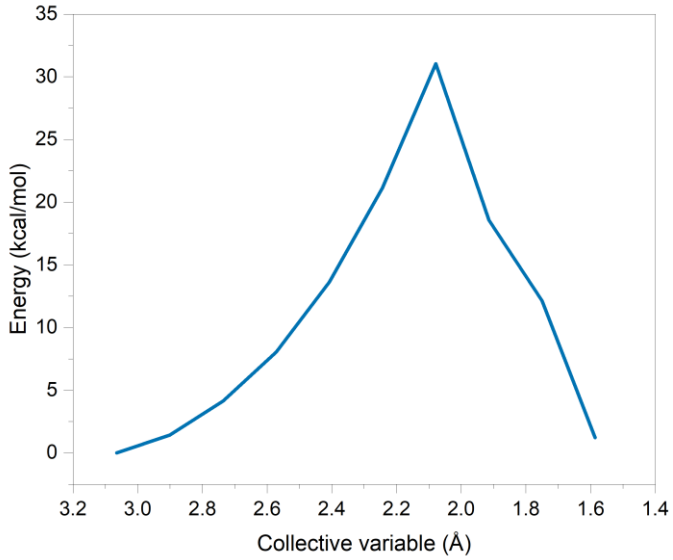

Figure C.43: PES energy profile of the addition reaction of MeCTB with BH_2.

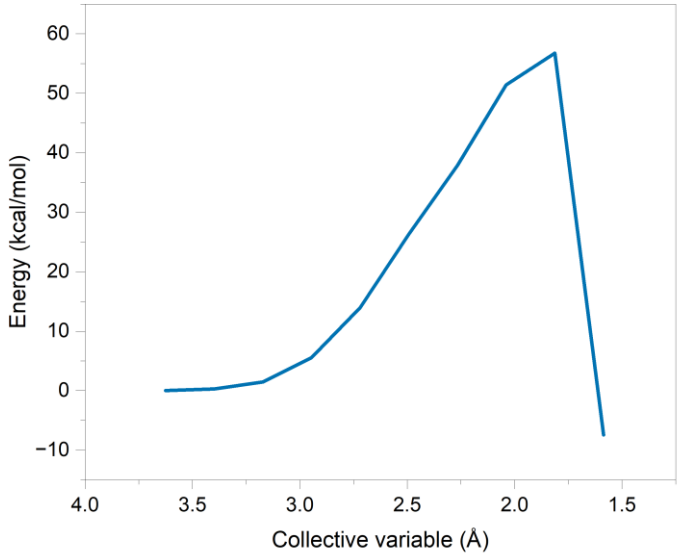

Figure C.44: PES energy profile of the addition/dehydrogenation reaction of MeCTB with BH_2.

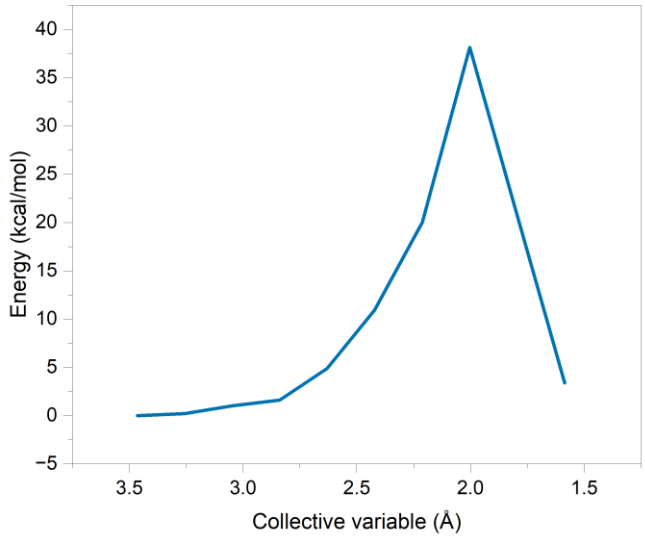

Figure C.45: PES energy profile of the addition reaction of MeCTB with BH_3.

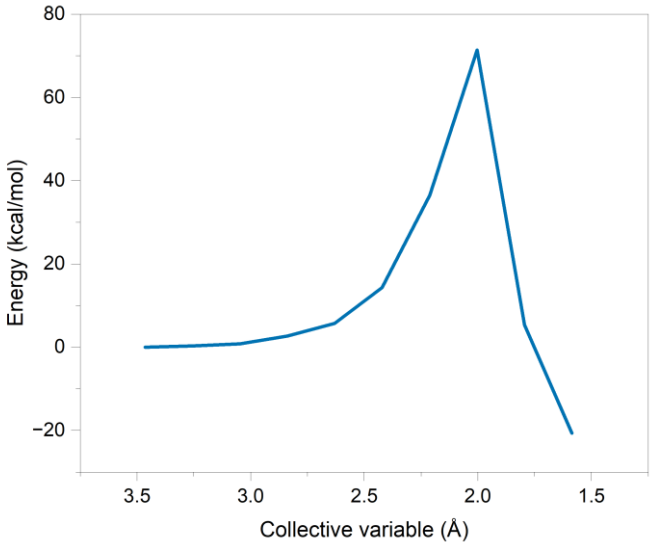

Figure C.46: PES energy profile of the addition/dehydrogenation reaction of MeCTB with BH_3.

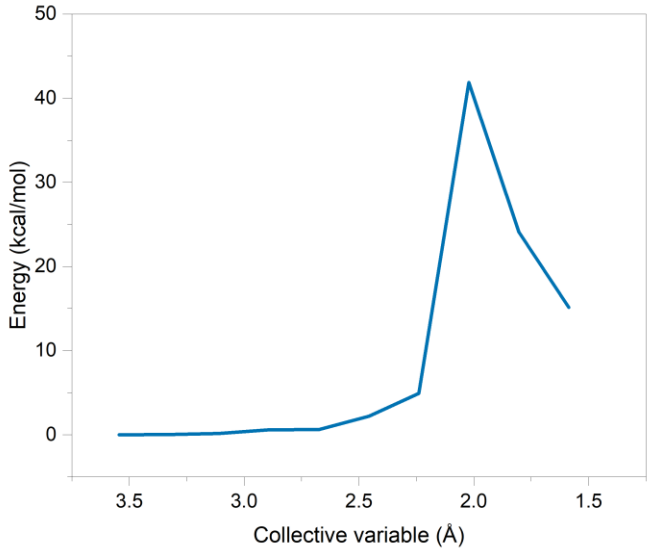

Figure C.47: PES energy profile of the addition reaction of MeCTB with MeIB.

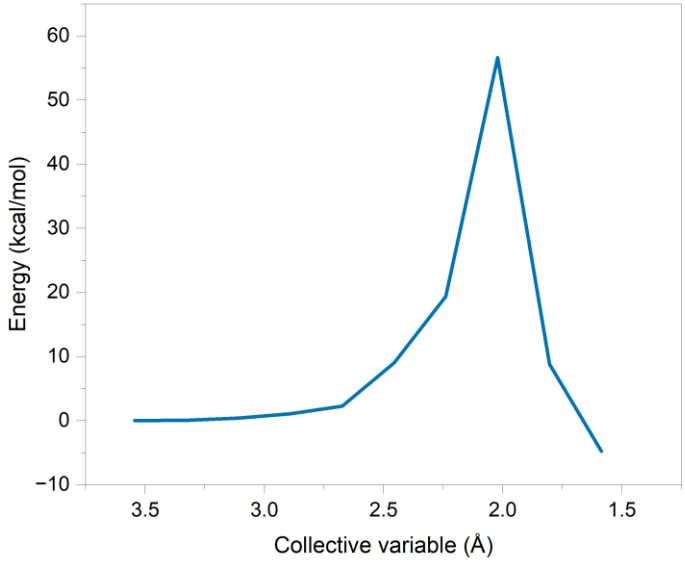

Figure C.48: PES energy profile of the addition/dehydrogenation reaction of MeCTB with MeIB.

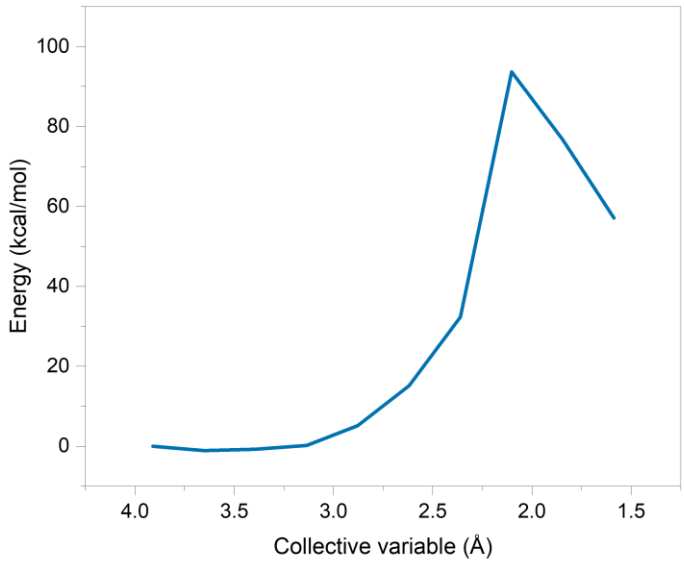

Figure C.49: PES energy profile of the addition reaction of MeCTB with PMeAB3-nocap.

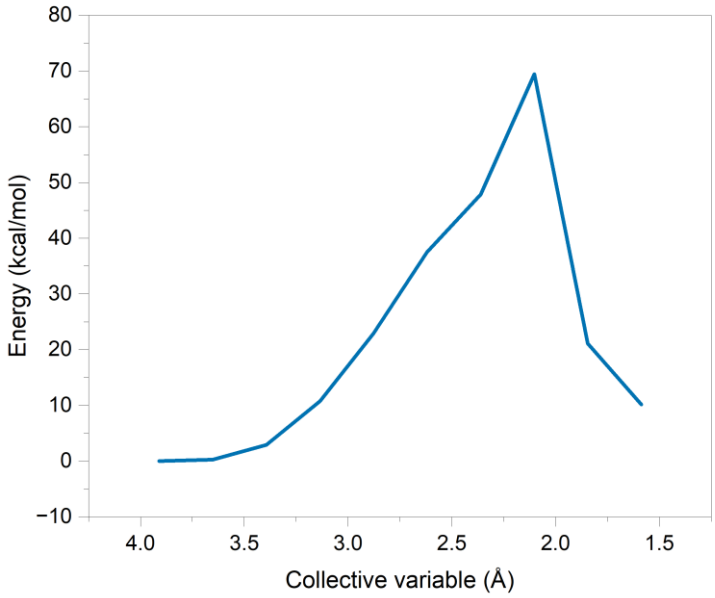

Figure C.50: PES energy profile of the addition/dehydrogenation reaction of MeCTB with PMeAB3-nocap.

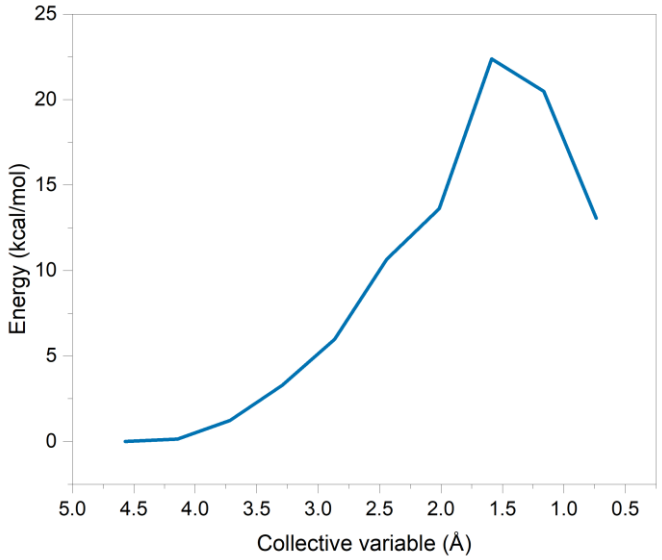

Figure C.51: PES energy profile of the dehydrogenation reaction of MeBZ across (B─B).

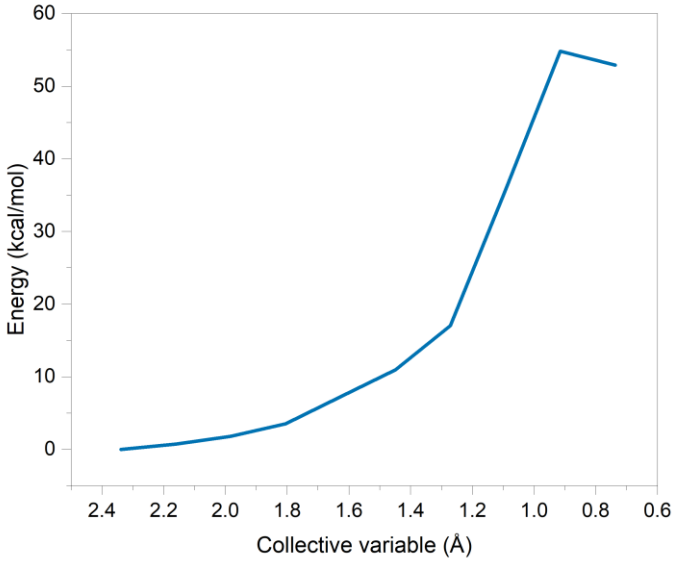

Figure C.52: PES energy profile of the dehydrogenation reaction of MeBZ across (B─C).

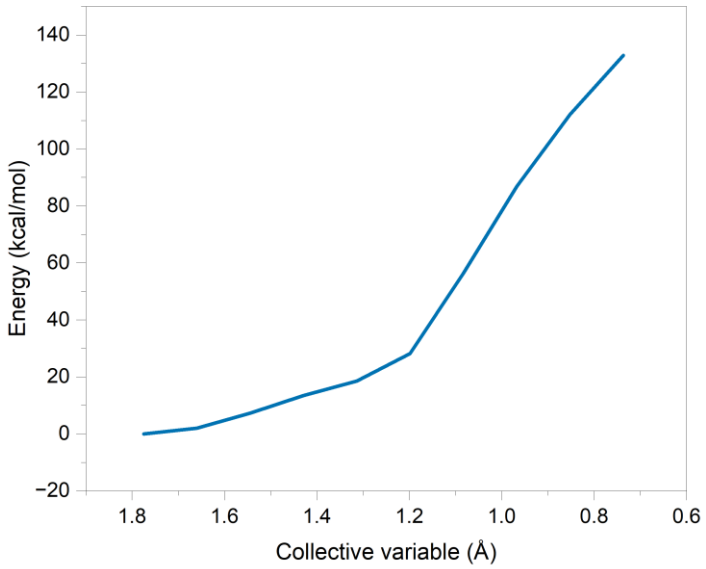

Figure C.53: PES energy profile of the dehydrogenation reaction of MeBZ across (C─C).

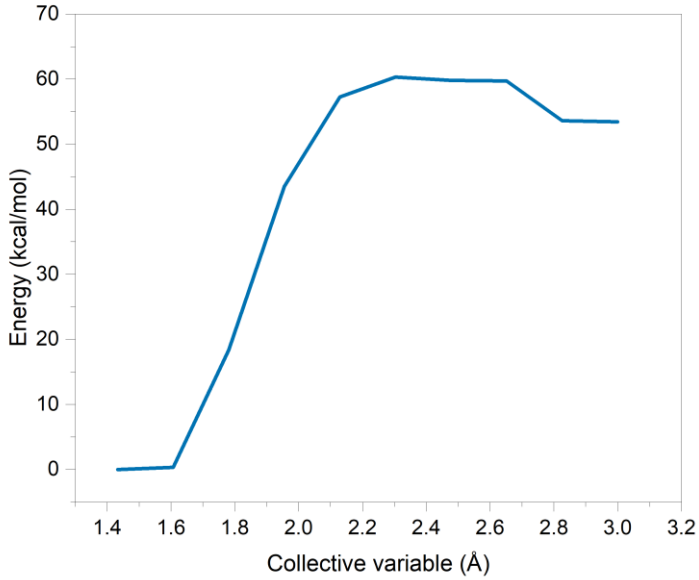

Figure C.54: PES energy profile of the dissociation reaction of MeBZ across (B─N).

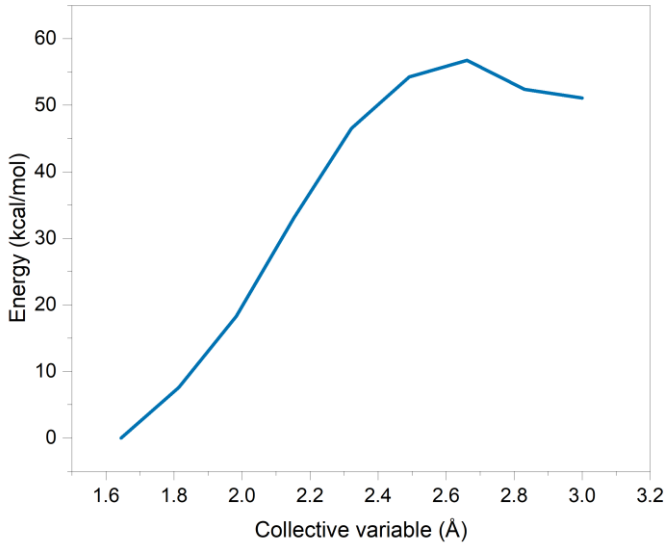

Figure C.55: PES energy profile of the dissociation reaction of PMeAB3-nocap to produce CH_3.

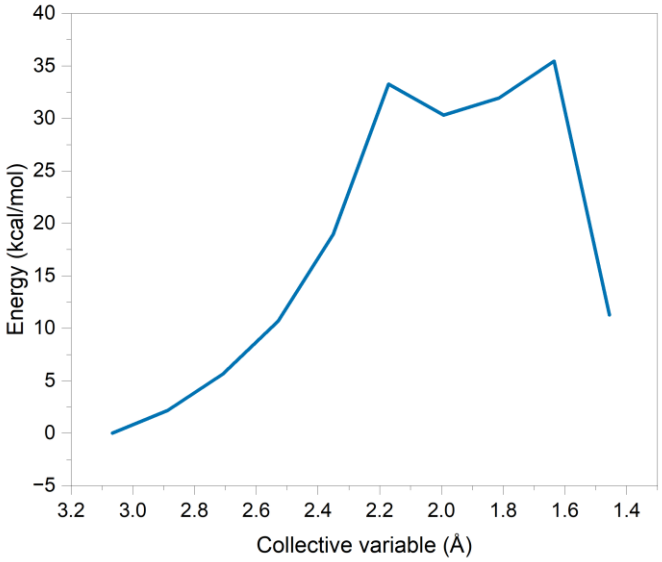

Figure C.56: PES energy profile of the addition reaction of PMeAB3-nocap with NH_3 (on C).

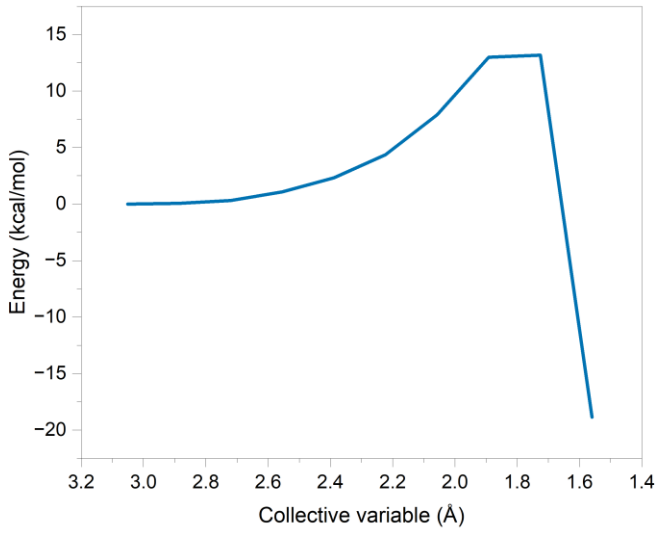

Figure C.57: PES energy profile of the addition reaction of PMeAB3-nocap with NH_3 (on B).

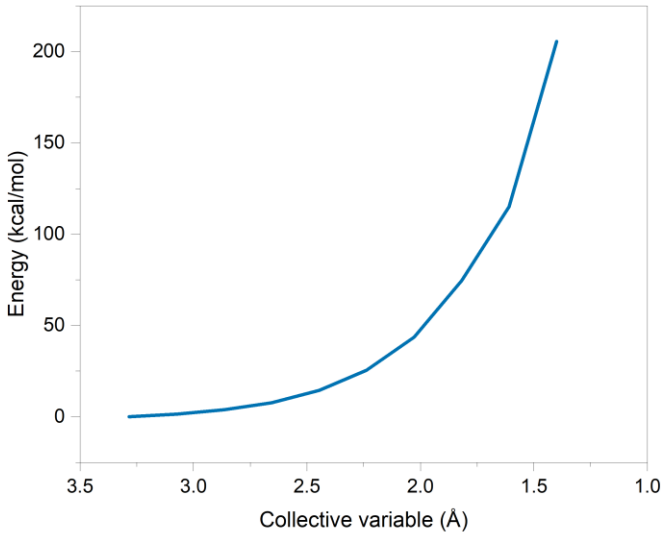

Figure C.58: PES energy profile of the addition reaction of PMeAB3-nocap with NH_3 (on N).

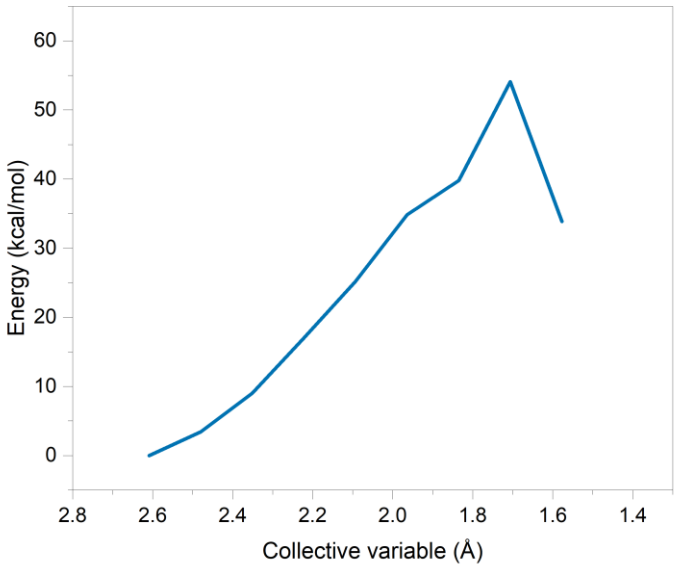

Figure C.59: PES energy profile of the addition reaction of MeIB with NH_3 (on C).

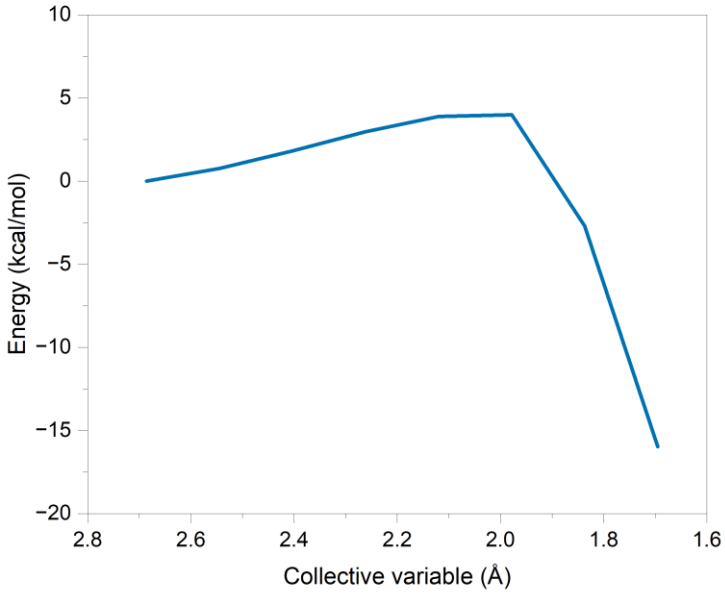

Figure C.60: PES energy profile of the addition reaction of MeIB with NH_3 (on B).

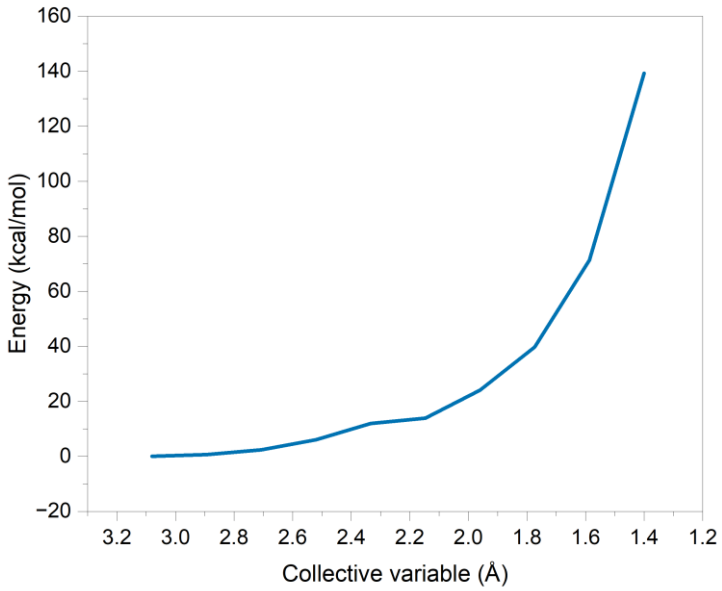

Figure C.61: PES energy profile of the addition reaction of MeIB with NH_3 (on N).

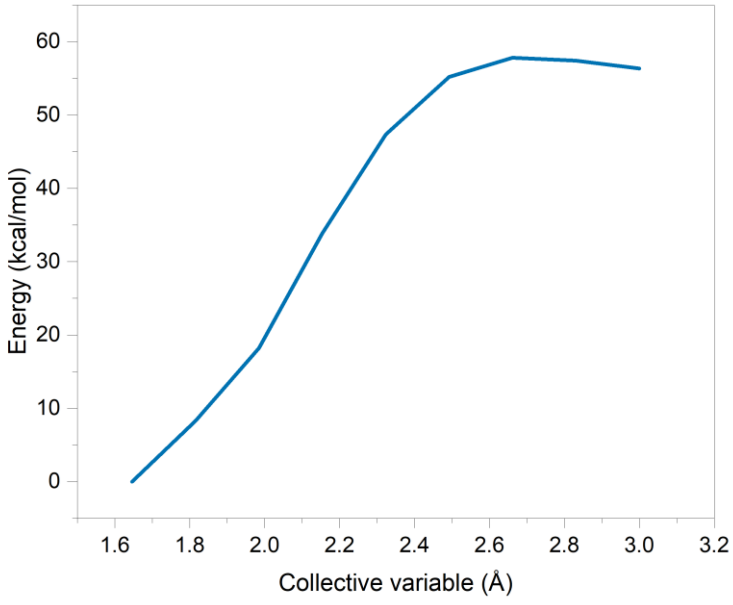

Figure C.62: PES energy profile of the dissociation reaction of MeCTB to produce CH_3.

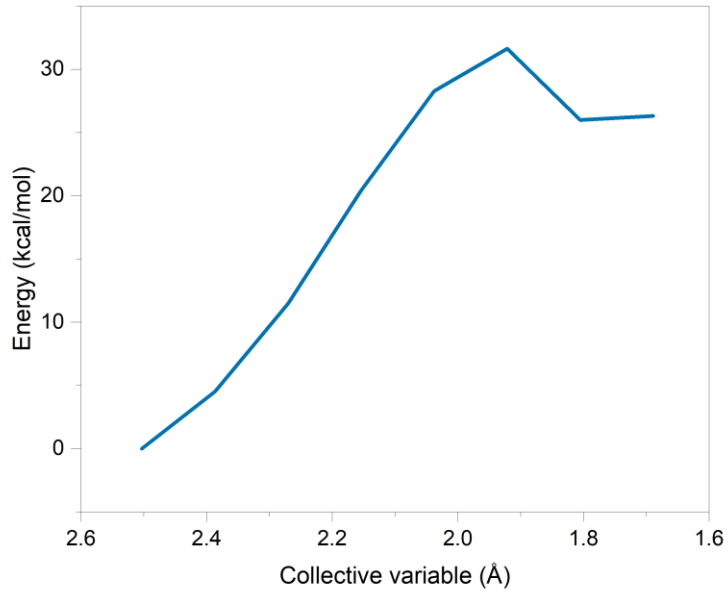

Figure C.63: PES energy profile of the addition reaction of MeCTB with NH_3 (on C).

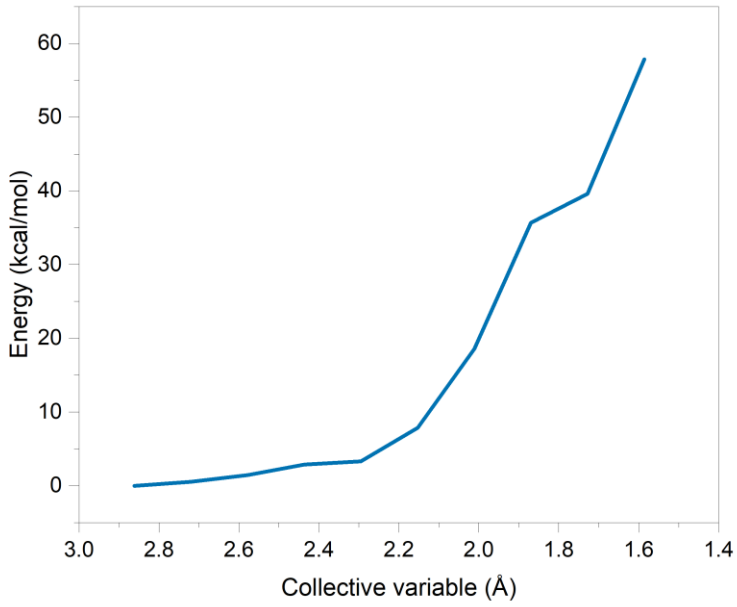

Figure C.64: PES energy profile of the addition reaction of MeCTB with NH_3 (on B).

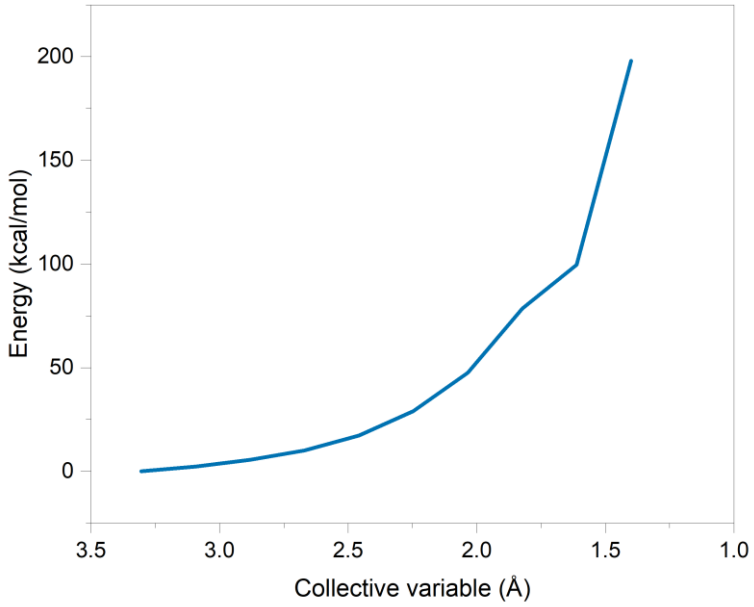

Figure C.65: PES energy profile of the addition reaction of MeCTB with NH_3 (on N).

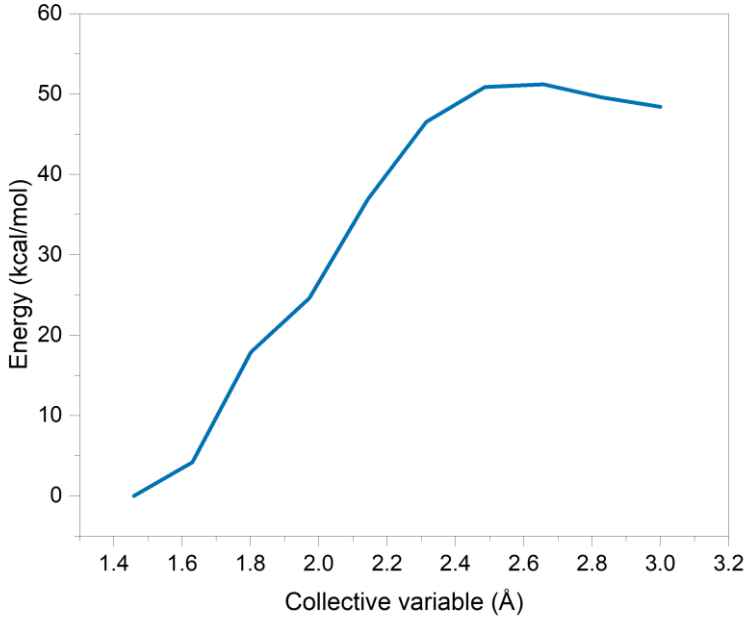

Figure C.66: PES energy profile of the dissociation reaction of MeBZ to produce CH_3.

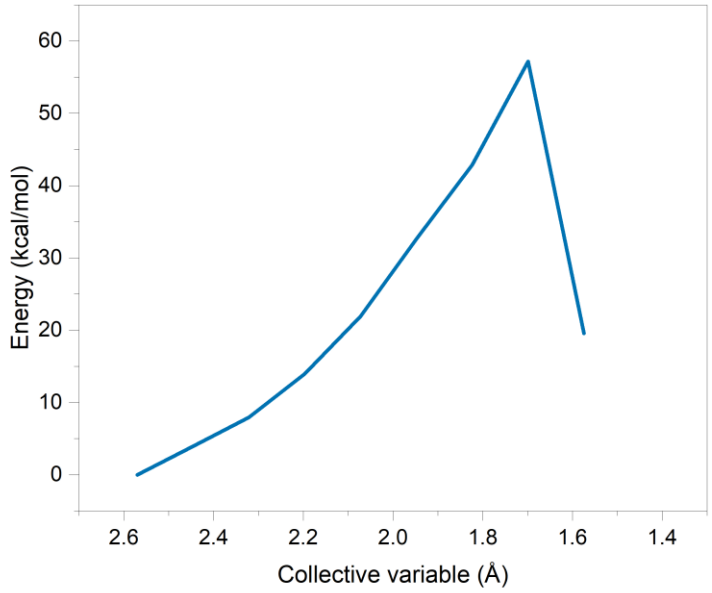

Figure C.67: PES energy profile of the addition reaction of MeBZ with NH_3 (on C).

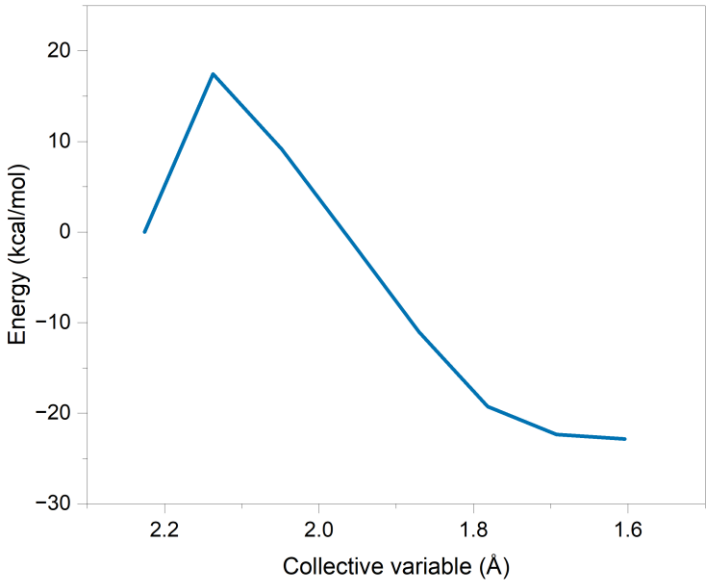

Figure C.68: PES energy profile of the addition reaction of MeBZ with NH_3 (on B).

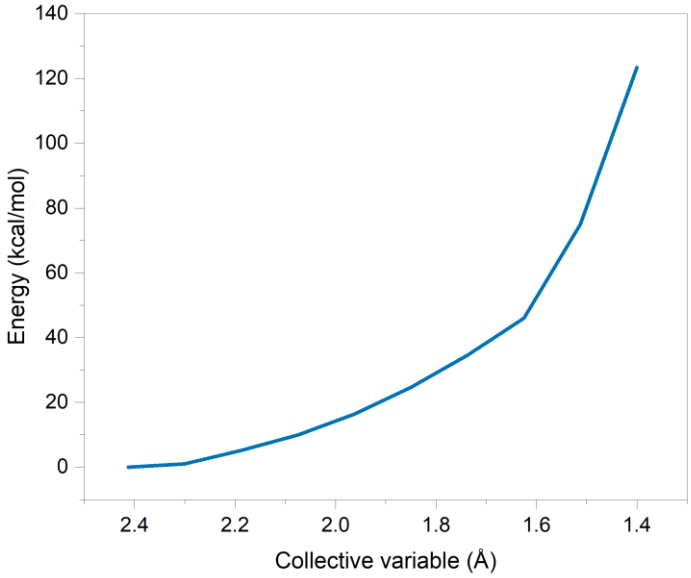

Figure C.69: PES energy profile of the addition reaction of MeBZ with NH_3 (on N).

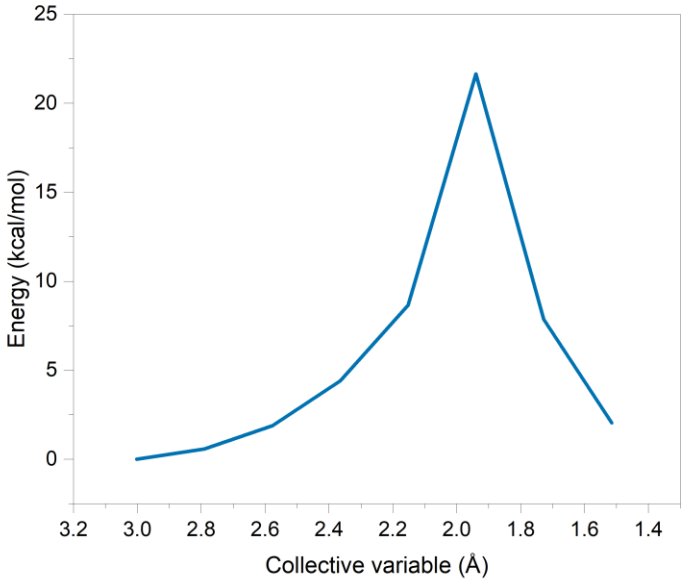

Figure C.69: PES energy profile of the addition reaction of PMeAB3-nocap with PMeAB3-nocap.

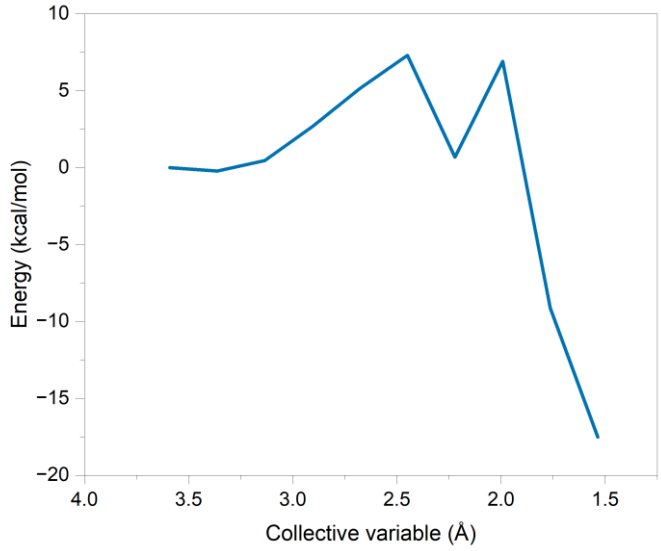

Figure C.70: PES energy profile of the addition reaction of PMeAB3-nocap-CH_3 with PMeAB3-nocap-CH_3.

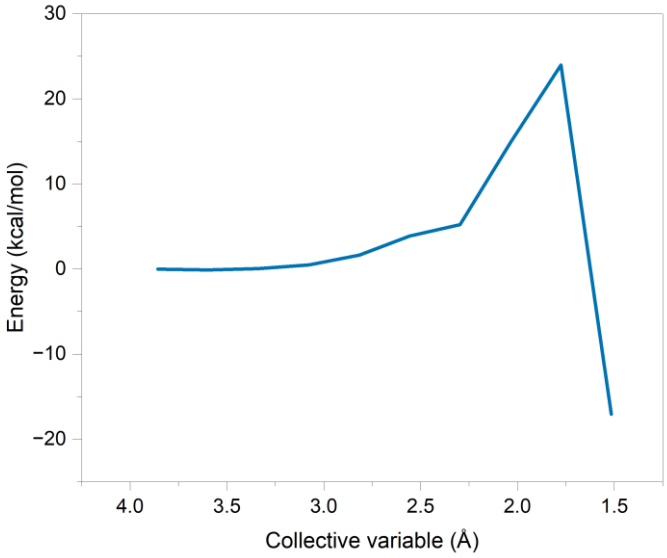

Figure C.71: PES energy profile of the addition reaction of PMeAB3-nocap with PMeAB3-nocap-CH_3.

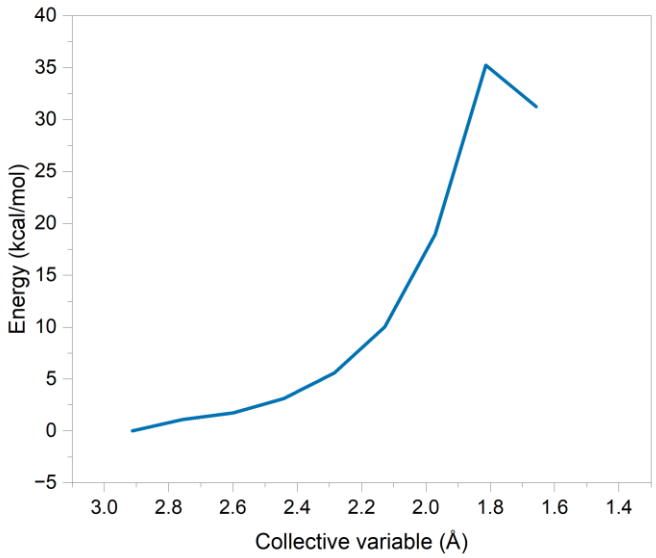

Figure C.72: PES energy profile of the addition reaction of PAB3-nocap with PAB3-nocap.

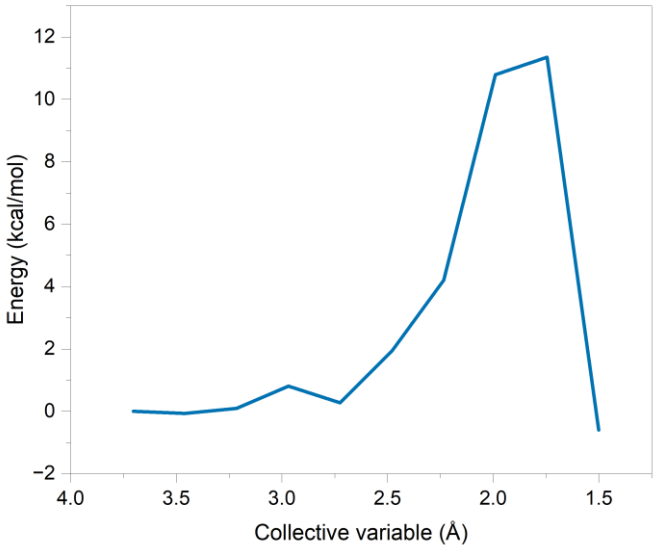

Figure C.73: PES energy profile of the addition reaction of PAB3-nocap with PMeAB3-nocap.

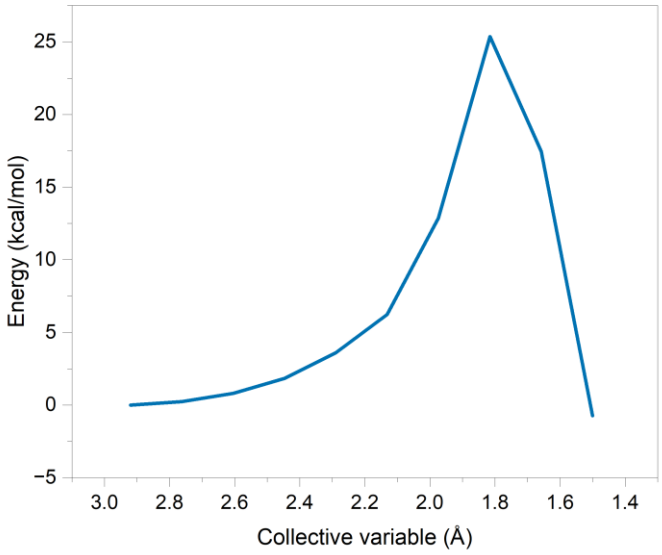

Figure C.74: PES energy profile of the addition reaction of PIB3 with PIB3.

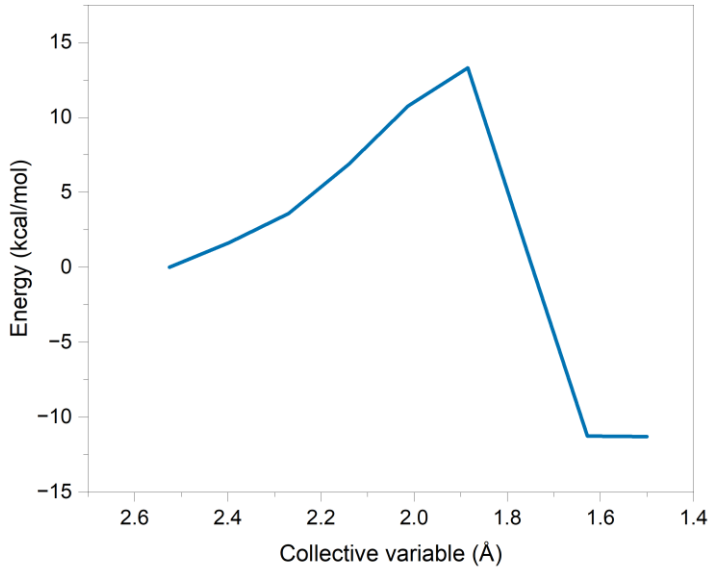

Figure C.75: PES energy profile of the addition reaction of PMeIB3 with PMeIB3.

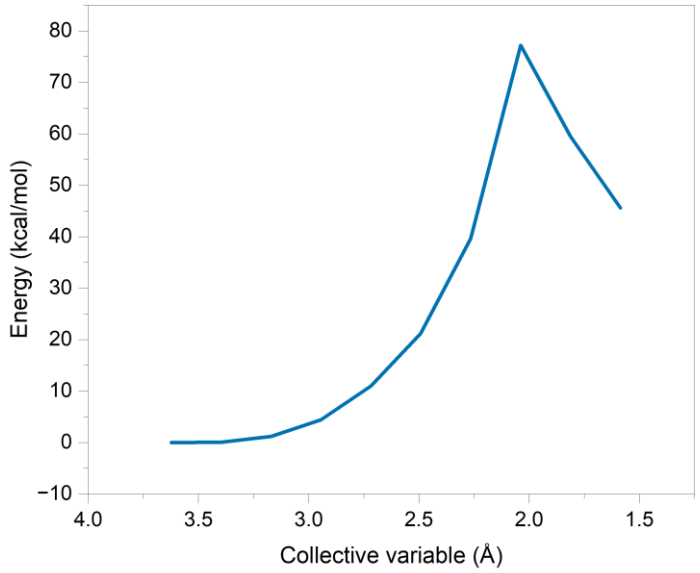

Figure C.76: PES energy profile of the addition reaction of MeCTB with MeCTB.

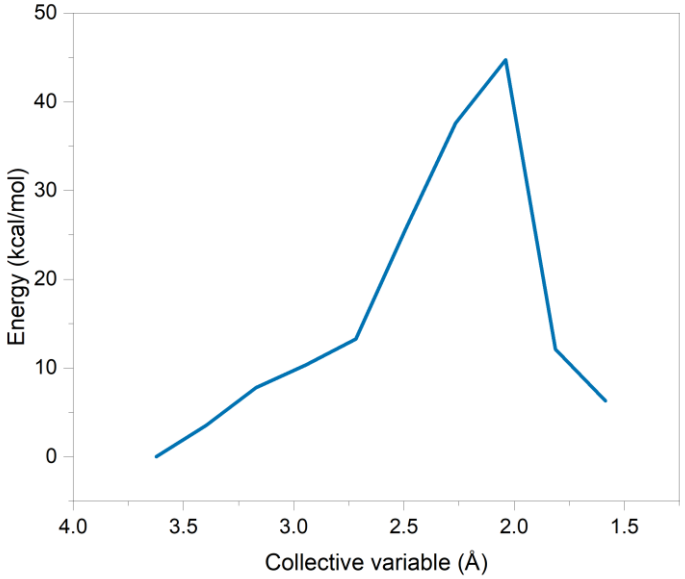

Figure C.77: PES energy profile of the addition/dehydrogenation reaction of MeCTB with MeCTB.

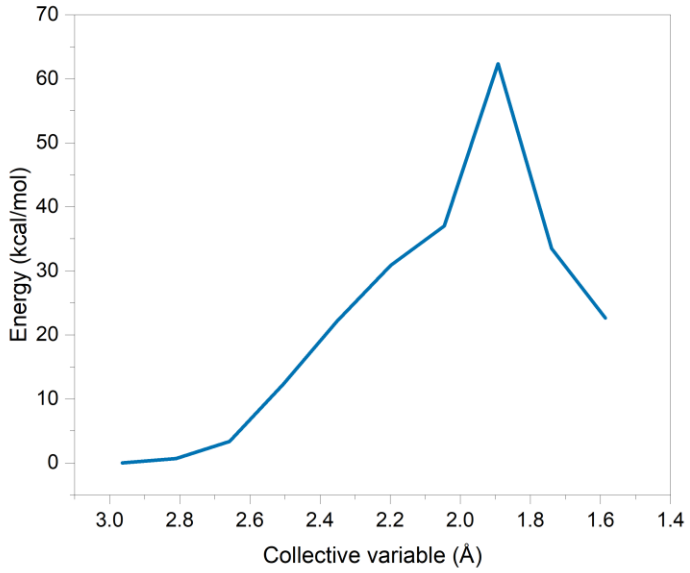

Figure C.78: PES energy profile of the addition/dehydrogenation reaction of MeCTB-CH_3 with MeCTB-CH_3.

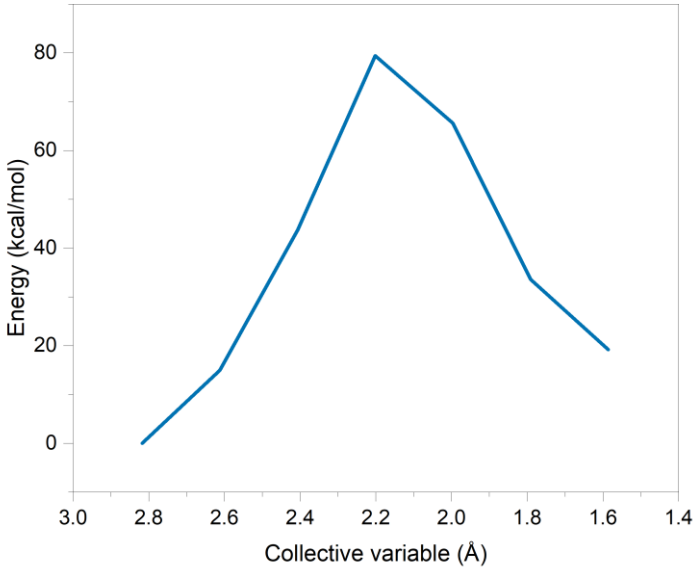

Figure C.79: PES energy profile of the addition/dehydrogenation reaction of MeCTB with MeCTB-CH_3.

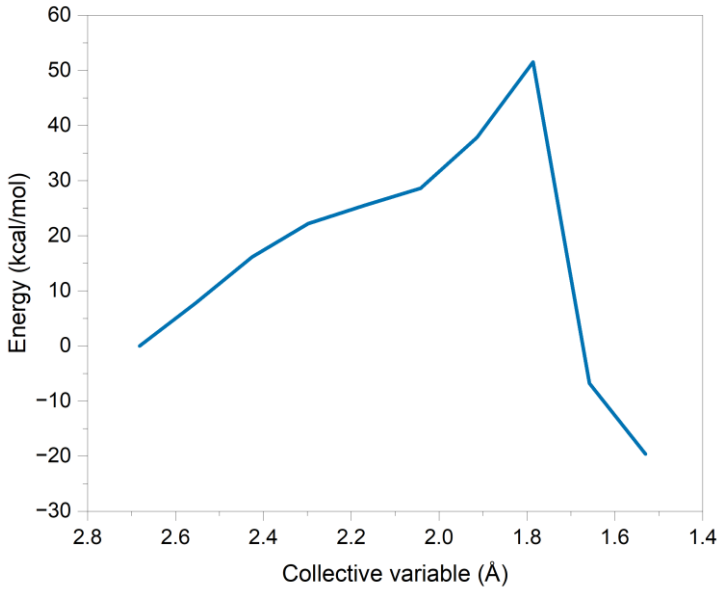

Figure C.80: PES energy profile of the addition/dehydrogenation reaction of CTB with CTB.

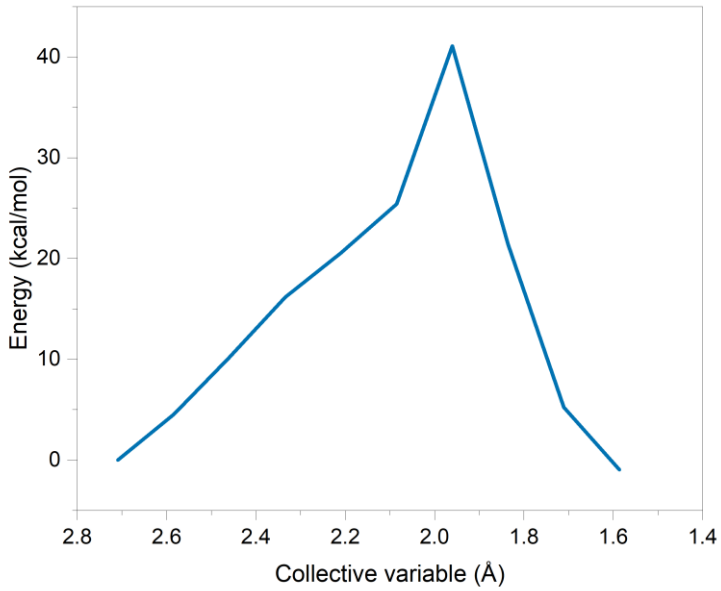

Figure C.81: PES energy profile of the addition/dehydrogenation reaction of CTB with MeCTB.

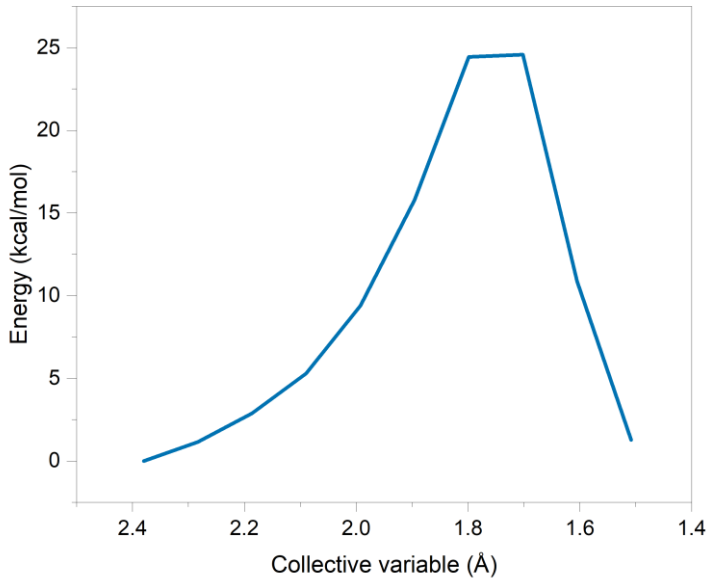

Figure C.82: PES energy profile of the addition/dehydrogenation reaction of BZ with BZ.

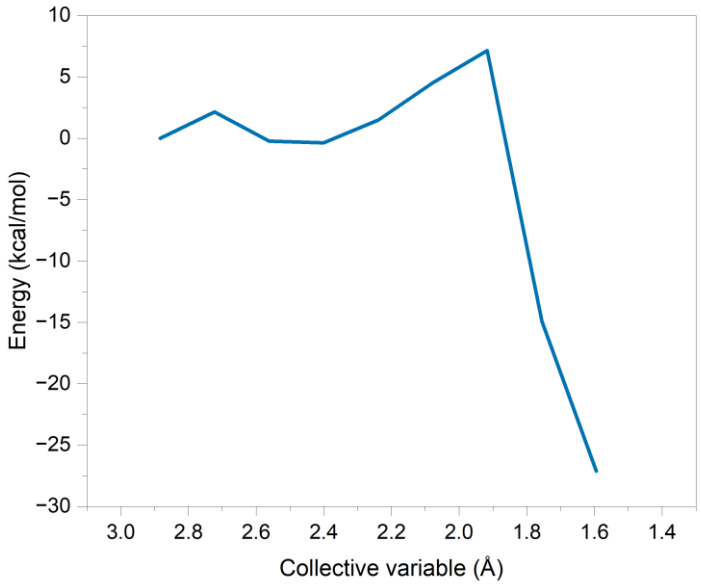

Figure C.83: PES energy profile of the addition/dehydrogenation reaction of MeBZ with MeBZ.

References

(1) Levchenko, I.; Xu, S.; Teel, G.; Mariotti, D.; Walker, M. L. R.; Keidar, M. Recent Progress and Perspectives of Space Electric Propulsion Systems Based on Smart Nanomaterials. *Nat Commun* **2018**, *9* (1), 879. https://doi.org/10.1038/s41467-017-02269-7.

(2) Scalia, T.; Bonventre, L. Nanomaterials in Space: Technology Innovation and Economic Trends. *Advances in Astronautics Science and Technology* **2020**, *3* (2), 145–155. https://doi.org/10.1007/s42423-020-00065-y.

(3) The National Aeronautics and Space Administration. *2015 NASA Technology Roadmaps TA 10: Nanotechnology*; 2015.

(4) Turhan, E. A.; Pazarçeviren, A. E.; Evis, Z.; Tezcaner, A. Properties and Applications of Boron Nitride Nanotubes. *Nanotechnology* **2022**, *33* (24), 242001. https://doi.org/10.1088/1361-6528/ac5839.

(5) American Elements. *Boron Nitride Nanotubes*. https://www.americanelements.com/boron-nitride-nanotubes-10043-11-5 (accessed 2025-05-08).

(6) American Elements. *Multi-Walled Carbon Nanotubes*. https://www.americanelements.com/multi-walled-carbon-nanotubes-308068-56-6 (accessed 2025-05-08).

(7) Chang, C. W.; Fennimore, A. M.; Afanasiev, A.; Okawa, D.; Ikuno, T.; Garcia, H.; Li, D.; Majumdar, A.; Zettl, A. Isotope Effect on the Thermal Conductivity of Boron Nitride Nanotubes. *Phys Rev Lett* **2006**, *97* (8), 85901. https://doi.org/10.1103/PhysRevLett.97.085901.

(8) Chopra, N. G.; Zettl, A. Measurement of the Elastic Modulus of a Multi-Wall Boron Nitride Nanotube. *Solid State Commun* **1998**, *105* (5), 297–300. https://doi.org/https://doi.org/10.1016/S0038-1098(97)10125-9.

(9) Hernández, E.; Goze, C.; Bernier, P.; Rubio, A. Elastic Properties of C and ${B}_{\mathit{x}}{C}_{\mathit{y}}{N}_{\mathit{z}}$ Composite Nanotubes. *Phys Rev Lett* **1998**, *80* (20), 4502–4505. https://doi.org/10.1103/PhysRevLett.80.4502.

(10) Citations-20250508T180402.

(11) Blase, X.; Rubio, A.; Louie, S. G.; Cohen, M. L. Stability and Band Gap Constancy of Boron Nitride Nanotubes. *Europhys Lett* **1994**, *28* (5), 335. https://doi.org/10.1209/0295-5075/28/5/007.

(12) Jones, R. S. Designing Boron Nitride Nanotubes and Their Macroscopic Assemblies via Sacrificial Templating. PhD thesis, University of Oxford, Oxford, 2021.
(13) Chen, Y.; Zou, J.; Campbell, S. J.; Le Caer, G. Boron Nitride Nanotubes: Pronounced Resistance to Oxidation. *Appl Phys Lett* **2004**, *84* (13), 2430–2432. https://doi.org/10.1063/1.1667278.
(14) Kim, K. S.; Jakubinek, M. B.; Martinez-Rubi, Y.; Ashrafi, B.; Guan, J.; O'Neill, K.; Plunkett, M.; Hrdina, A.; Lin, S.; Dénommée, S.; Kingston, C.; Simard, B. Polymer Nanocomposites from Free-Standing, Macroscopic Boron Nitride Nanotube Assemblies. *RSC Adv* **2015**, *5* (51), 41186–41192. https://doi.org/10.1039/C5RA02988K.
(15) McMullen, A. M. *Radiation Shielding Materials Containing Hydrogen, Boron, and Nitrogen: Systematic Computational and Experimental Study*; Rochester, 2012.
(16) Kim, J. H.; Pham, T. V.; Hwang, J. H.; Kim, C. S.; Kim, M. J. Boron Nitride Nanotubes: Synthesis and Applications. *Nano Converg* **2018**, *5* (1), 17. https://doi.org/10.1186/s40580-018-0149-y.
(17) Jones, R. S. Designing Boron Nitride Nanotubes and Their Macroscopic Assemblies via Sacrificial Templating. PhD thesis, University of Oxford, Oxford, 2021.
(18) Xue, J.; Wu, T.; Dai, Y.; Xia, Y. Electrospinning and Electrospun Nanofibers: Methods, Materials, and Applications. *Chemical Reviews*. American Chemical Society April 24, 2019, pp 5298–5415. https://doi.org/10.1021/acs.chemrev.8b00593.
(19) Diana Santiago; Maricela Lizcano; Thomas Sabo. *Fabrication of Boron Nitride Fibers by Force Spinning Method*; 2020. https://ntrs.nasa.gov/citations/20200001018.
(20) Kristina Vailonis; Diana Santiago; Maricela Lizcano; Thomas Sabo; Arko Roy. *Forcespun Polymers as Precursors to Boron Nitride Fibers*; 2023. https://ntrs.nasa.gov/citations/20230011556.
(21) Dong, S.; Maciejewska, B. M.; Lißner, M.; Thomson, D.; Townsend, D.; Millar, R.; Petrinic, N.; Grobert, N. Unveiling the Mechanism of the in Situ Formation of 3D Fiber Macroassemblies with Controlled Properties. *ACS Nano* **2023**, *17* (7), 6800–6810. https://doi.org/10.1021/acsnano.3c00289.
(22) Schofield, R. M.; Maciejewska, B. M.; Dong, S.; Tebbutt, G. T.; McGurty, D.; Bonilla, R. S.; Assender, H. E.; Grobert, N. Driving Fiber Diameters to the Limit: Nanoparticle-Induced Diameter Reductions in Electrospun Photoactive

Composite Nanofibers for Organic Photovoltaics. *Adv Compos Hybrid Mater* **2023**, *6* (6), 229. https://doi.org/10.1007/s42114-023-00788-0.

(23) Marchionni, D.; Basak, S.; Khodadadi, A. N.; Marrocchi, A.; Vaccaro, L. Synthesis and Applications of Organic Borazine Materials. *Adv Funct Mater* **2023**, *33* (49), 2303635. https://doi.org/https://doi.org/10.1002/adfm.202303635.

(24) Fazen, P. J.; Remsen, E. E.; Beck, J. S.; Carroll, P. J.; McGhie, A. R.; Sneddon, L. G. *Synthesis, Properties, and Ceramic Conversion Reactions of Polyborazylene. A High-Yield Polymeric Precursor to Boron Nitride*; 1995; Vol. 7. https://pubs.acs.org/sharingguidelines.

(25) Hwang, H. J.; Barakat, N. A. M.; Kanjwal, M. A.; Sheikh, F. A.; Kim, H. Y.; Abadir, M. F. Boron Nitride Nanofibers by the Electrospinning Technique. *Macromol Res* **2010**, *18* (6), 551–557. https://doi.org/10.1007/s13233-010-0601-2.

(26) Qiu, Y.; Yu, J.; Rafique, J.; Yin, J.; Bai, X.; Wang, E. Large-Scale Production of Aligned Long Boron Nitride Nanofibers by Multijet/Multicollector Electrospinning. *The Journal of Physical Chemistry C* **2009**, *113* (26), 11228–11234. https://doi.org/10.1021/jp901267k.

(27) Qiu, Y.; Yu, J.; Yin, J.; Tan, C.; Zhou, X.; Bai, X.; Wang, E. Synthesis of Continuous Boron Nitride Nanofibers by Solution Coating Electrospun Template. *Nanotechnology* **2009**, *20* (34), 345603. https://doi.org/10.1088/0957-4484/20/34/345603.

(28) Kimura, Y.; Kubo, Y.; Hayashi, N. High-Performance Boron-Nitride Fibers from Poly(Borazine) Preceramics. *Compos Sci Technol* **1994**, *51* (2), 173–179. https://doi.org/https://doi.org/10.1016/0266-3538(94)90188-0.

(29) Salles, V.; Bernard, S.; Brioude, A.; Cornu, D.; Miele, P. A New Class of Boron Nitride Fibers with Tunable Properties by Combining an Electrospinning Process and the Polymer-Derived Ceramics Route. *Nanoscale* **2010**, *2* (2), 215–217. https://doi.org/10.1039/B9NR00185A.

(30) Toury, B.; Bernard, S.; Cornu, D.; Chassagneux, F.; Létoffé, J. M.; Miele, P. High-Performance Boron Nitride Fibers Obtained from Asymmetric Alkylaminoborazine. *J Mater Chem* **2003**, *13* (2), 274–279. https://doi.org/10.1039/b207476a.

(31) Toury, B.; Miele, P.; Cornu, D.; Vincent, H.; Bouix, J. Boron Nitride Fibers Prepared from Symmetric and Asymmetric Alkylaminoborazines. *Adv Funct Mater* **2002**, *12* (3), 228–234. https://doi.org/https://doi.org/10.1002/1616-3028(200203)12:3<228::AID-ADFM228>3.0.CO;2-U.

(32) Cheng, T.; Bets, K. V.; Yakobson, B. I. Synthesis Landscapes for Ammonia Borane Chemical Vapor Deposition of H-BN and BNNT: Unraveling Reactions and Intermediates from First-Principles. *J Am Chem Soc* **2024**, *146* (13), 9318–9325. https://doi.org/10.1021/jacs.4c01354.

(33) Demirci, U. B. Mechanistic Insights into the Thermal Decomposition of Ammonia Borane, a Material Studied for Chemical Hydrogen Storage. *Inorg Chem Front* **2021**, *8* (7), 1900–1930. https://doi.org/10.1039/D0QI01366H.

(34) Haubner, R.; Wilhelm, M.; Weissenbacher, R.; Lux, B. Boron Nitrides — Properties, Synthesis and Applications. In *High Performance Non-Oxide Ceramics II*; Jansen, M., Ed.; Springer Berlin Heidelberg: Berlin, Heidelberg, 2002; pp 1–45. https://doi.org/10.1007/3-540-45623-6_1.

(35) Golberg, D.; Bando, Y.; Huang, Y.; Terao, T.; Mitome, M.; Tang, C.; Zhi, C. Boron Nitride Nanotubes and Nanosheets. *ACS Nano*. June 22, 2010, pp 2979–2993. https://doi.org/10.1021/nn1006495.

(36) Izyumskaya, N.; Demchenko, D. O.; Das, S.; Özgür, Ü.; Avrutin, V.; Morkoç, H. Recent Development of Boron Nitride towards Electronic Applications. *Adv Electron Mater* **2017**, *3* (5), 1600485. https://doi.org/https://doi.org/10.1002/aelm.201600485.

(37) Pakdel, A.; Bando, Y.; Golberg, D. Nano Boron Nitride Flatland. *Chem Soc Rev* **2014**, *43* (3), 934–959. https://doi.org/10.1039/C3CS60260E.

(38) Lee, K. H.; Shin, H.-J.; Lee, J.; Lee, I.; Kim, G.-H.; Choi, J.-Y.; Kim, S.-W. Large-Scale Synthesis of High-Quality Hexagonal Boron Nitride Nanosheets for Large-Area Graphene Electronics. *Nano Lett* **2012**, *12* (2), 714–718. https://doi.org/10.1021/nl203635v.

(39) Roy, S.; Zhang, X.; Puthirath, A. B.; Meiyazhagan, A.; Bhattacharyya, S.; Rahman, M. M.; Babu, G.; Susarla, S.; Saju, S. K.; Tran, M. K.; Sassi, L. M.; Saadi, M. A. S. R.; Lai, J.; Sahin, O.; Sajadi, S. M.; Dharmarajan, B.; Salpekar, D.; Chakingal, N.; Baburaj, A.; Shuai, X.; Adumbumkulath, A.; Miller, K. A.; Gayle, J. M.; Ajnsztajn, A.; Prasankumar, T.; Harikrishnan, V. V. J.; Ojha, V.; Kannan, H.; Khater, A. Z.; Zhu, Z.; Iyengar, S. A.; Autreto, P. A. da S.; Oliveira, E. F.; Gao, G.; Birdwell, A. G.; Neupane, M. R.; Ivanov, T. G.; Taha-Tijerina, J.; Yadav, R. M.; Arepalli, S.; Vajtai, R.; Ajayan, P. M. Structure, Properties and Applications of Two-Dimensional Hexagonal Boron Nitride. *Advanced Materials* **2021**, *33* (44), 2101589. https://doi.org/https://doi.org/10.1002/adma.202101589.

(40) Paine, R. T.; Narula, C. K. Synthetic Routes to Boron Nitride. *Chem Rev* **1990**, *90* (1), 73–91.

(41) Eichler, J.; Lesniak, C. Boron Nitride (BN) and BN Composites for High-Temperature Applications. *J Eur Ceram Soc* **2008**, *28* (5), 1105–1109. https://doi.org/https://doi.org/10.1016/j.jeurceramsoc.2007.09.005.

(42) Doll, G. L.; Speck, J. S.; Dresselhaus, G.; Dresselhaus, M. S.; Nakamura, K.; Tanuma, S. -I. Intercalation of Hexagonal Boron Nitride with Potassium. *J Appl Phys* **1989**, *66* (6), 2554–2558. https://doi.org/10.1063/1.344219.

(43) Jiang, H.; Cai, Q.; Mateti, S.; Yu, Y.; Zhi, C.; Chen, Y. Boron Nitride Nanosheet Dispersion at High Concentrations. *ACS Appl Mater Interfaces* **2021**, *13* (37), 44751–44759. https://doi.org/10.1021/acsami.1c11795.

(44) Smith McWilliams, A. D.; de los Reyes, C. A.; Liberman, L.; Ergülen, S.; Talmon, Y.; Pasquali, M.; Martí, A. A. Surfactant-Assisted Individualization and Dispersion of Boron Nitride Nanotubes. *Nanoscale Adv* **2019**, *1* (3), 1096–1103. https://doi.org/10.1039/C8NA00315G.

(45) Foroutan, M.; Fatemi, S. J.; Fatemi, S. M. A Mini-Review on Dispersion and Functionalization of Boron Nitride Nanotubes. *J Nanostructure Chem* **2020**, *10* (4), 265–274. https://doi.org/10.1007/s40097-020-00347-9.

(46) Li, Y.; Xiao-Yu, Y.; Yi, F.; Zhong-Yong, Y.; and Su, B.-L. One-Dimensional Metal Oxide Nanotubes, Nanowires, Nanoribbons, and Nanorods: Synthesis, Characterizations, Properties and Applications. *Critical Reviews in Solid State and Materials Sciences* **2012**, *37* (1), 1–74. https://doi.org/10.1080/10408436.2011.606512.

(47) Iijima, S. Helical Microtubules of Graphitic Carbon. *Nature* **1991**, *354* (6348), 56–58. https://doi.org/10.1038/354056a0.

(48) Gong, S.; Cheng, W. One-Dimensional Nanomaterials for Soft Electronics. *Adv Electron Mater* **2017**, *3* (3), 1600314. https://doi.org/https://doi.org/10.1002/aelm.201600314.

(49) Shi, L. Thermal and Thermoelectric Transport in Nanostructures and Low-Dimensional Systems. *Nanoscale and Microscale Thermophysical Engineering* **2012**, *16* (2), 79–116. https://doi.org/10.1080/15567265.2012.667514.

(50) Zhang, H.; Marwat, M. A.; Xie, B.; Ashtar, M.; Liu, K.; Zhu, Y.; Zhang, L.; Fan, P.; Samart, C.; Ye, Z. Polymer Matrix Nanocomposites with 1D Ceramic Nanofillers for Energy Storage Capacitor Applications. *ACS Appl Mater Interfaces* **2020**, *12* (1), 1–37. https://doi.org/10.1021/acsami.9b15005.

(51) Yu, L.; Ruan, S.; Xu, X.; Zou, R.; Hu, J. One-Dimensional Nanomaterial-Assembled Macroscopic Membranes for Water Treatment. *Nano Today* **2017**, *17*, 79–95. https://doi.org/https://doi.org/10.1016/j.nantod.2017.10.012.

(52) Akinwande, D.; Brennan, C. J.; Bunch, J. S.; Egberts, P.; Felts, J. R.; Gao, H.; Huang, R.; Kim, J.-S.; Li, T.; Li, Y.; Liechti, K. M.; Lu, N.; Park, H. S.; Reed,

E. J.; Wang, P.; Yakobson, B. I.; Zhang, T.; Zhang, Y.-W.; Zhou, Y.; Zhu, Y. A Review on Mechanics and Mechanical Properties of 2D Materials—Graphene and Beyond. *Extreme Mech Lett* **2017**, *13*, 42–77. https://doi.org/https://doi.org/10.1016/j.eml.2017.01.008.

(53) Kim, K. S.; Kim, M. J.; Park, C.; Fay, C. C.; Chu, S. H.; Kingston, C. T.; Simard, B. Scalable Manufacturing of Boron Nitride Nanotubes and Their Assemblies: A Review. *Semiconductor Science and Technology*. Institute of Physics Publishing January 1, 2017. https://doi.org/10.1088/0268-1242/32/1/013003.

(54) Kim, J. H.; Pham, T. V.; Hwang, J. H.; Kim, C. S.; Kim, M. J. Boron Nitride Nanotubes: Synthesis and Applications. *Nano Converg* **2018**, *5* (1), 17. https://doi.org/10.1186/s40580-018-0149-y.

(55) Zhou, X.; Liu, B.; Chen, Y.; Guo, L.; Wei, G. Carbon Nanofiber-Based Three-Dimensional Nanomaterials for Energy and Environmental Applications. *Mater Adv* **2020**, *1* (7), 2163–2181. https://doi.org/10.1039/D0MA00492H.

(56) Qiu, Y.; Yu, J.; Rafique, J.; Yin, J.; Bai, X.; Wang, E. Large-Scale Production of Aligned Long Boron Nitride Nanofibers by Multijet/Multicollector Electrospinning. *Journal of Physical Chemistry C* **2009**, *113* (26), 11228–11234. https://doi.org/10.1021/jp901267k.

(57) Cornu, D.; Bernard, S.; Duperrier, S.; Toury, B.; Miele, P. Alkylaminoborazine-Based Precursors for the Preparation of Boron Nitride Fibers by the Polymer-Derived Ceramics (PDCs) Route. *J Eur Ceram Soc* **2005**, *25* (2), 111–121. https://doi.org/https://doi.org/10.1016/j.jeurceramsoc.2004.07.016.

(58) Economy, J.; Anderson, R.V. Properties and Uses of Boron Nitride Fibers. *Textile Research Journal* **1966**, *36* (11), 994–1003. https://doi.org/10.1177/004051756603601108.

(59) Economy, J.; Anderson, R. V. Boron Nitride Fibers. *Journal of Polymer Science Part C: Polymer Symposia* **1967**, *19* (1), 283–297. https://doi.org/https://doi.org/10.1002/polc.5070190122.

(60) Tang, C.; Bando, Y.; Huang, Y.; Yue, S.; Gu, C.; Xu, F.; Golberg, D. Fluorination and Electrical Conductivity of BN Nanotubes. *J Am Chem Soc* **2005**, *127* (18), 6552–6553. https://doi.org/10.1021/ja042388u.

(61) Chen, H.; Chen, Y.; Liu, Y.; Fu, L.; Huang, C.; Llewellyn, D. Over 1.0mm-Long Boron Nitride Nanotubes. *Chem Phys Lett* **2008**, *463* (1), 130–133. https://doi.org/https://doi.org/10.1016/j.cplett.2008.08.007.

(62) Chopra, N. G.; Zettl, A. Measurement of the Elastic Modulus of a Multi-Wall Boron Nitride Nanotube. *Solid State Commun* **1998**, *105* (5), 297–300. https://doi.org/https://doi.org/10.1016/S0038-1098(97)10125-9.

(63) Chang, C. W.; Fennimore, A. M.; Afanasiev, A.; Okawa, D.; Ikuno, T.; Garcia, H.; Li, D.; Majumdar, A.; Zettl, A. Isotope Effect on the Thermal Conductivity of Boron Nitride Nanotubes. *Phys Rev Lett* **2006**, *97* (8), 85901. https://doi.org/10.1103/PhysRevLett.97.085901.

(64) Chen, Y.; Zou, J.; Campbell, S. J.; Le Caer, G. Boron Nitride Nanotubes: Pronounced Resistance to Oxidation. *Appl Phys Lett* **2004**, *84* (13), 2430–2432. https://doi.org/10.1063/1.1667278.

(65) Li, D.; Xia, Y. Electrospinning of Nanofibers: Reinventing the Wheel? *Advanced Materials* **2004**, *16* (14), 1151–1170. https://doi.org/https://doi.org/10.1002/adma.200400719.

(66) Wang, Y.; Serrano, S.; Santiago-Avilés, J. J. Raman Characterization of Carbon Nanofibers Prepared Using Electrospinning. *Synth Met* **2003**, *138* (3), 423–427. https://doi.org/https://doi.org/10.1016/S0379-6779(02)00472-1.

(67) Ye, H.; Titchenal, N.; Gogotsi, Y.; Ko, F. SiC Nanowires Synthesized from Electrospun Nanofiber Templates. *Advanced Materials* **2005**, *17* (12), 1531–1535. https://doi.org/https://doi.org/10.1002/adma.200500094.

(68) Li, D.; Wang, Y.; Xia, Y. Electrospinning of Polymeric and Ceramic Nanofibers as Uniaxially Aligned Arrays. *Nano Lett* **2003**, *3* (8), 1167–1171. https://doi.org/10.1021/nl0344256.

(69) Bernard, S.; Miele, P. Polymer-Derived Boron Nitride: A Review on the Chemistry, Shaping and Ceramic Conversion of Borazine Derivatives. *Materials* **2014**, *7* (11), 7436–7459. https://doi.org/10.3390/ma7117436.

(70) Hwang, H. J.; Barakat, N. A. M.; Kanjwal, M. A.; Sheikh, F. A.; Kim, H. Y.; Abadir, M. F. Boron Nitride Nanofibers by the Electrospinning Technique. *Macromol Res* **2010**, *18* (6), 551–557. https://doi.org/10.1007/s13233-010-0601-2.

(71) Liu, Z.; Zhao, K.; Luo, J.; Tang, Y. Electrospinning of Boron Nitride Nanofibers with High Temperature Stability. *Scr Mater* **2019**, *170*, 116–119. https://doi.org/https://doi.org/10.1016/j.scriptamat.2019.06.002.

(72) Duperrier, S.; Chiriac, R.; Sigala, C.; Gervais, C.; Bernard, S.; Cornu, D.; Miele, P. Thermal Behaviour of a Series of Poly[B-(Methylamino)Borazine] for the Preparation of Boron Nitride Fibers. *J Eur Ceram Soc* **2009**, *29* (5), 851–855. https://doi.org/https://doi.org/10.1016/j.jeurceramsoc.2008.07.012.

(73) Du, Y.; Wang, B.; Li, W.; Song, Q.; Shao, C.; Han, C.; Wang, Y. Design and Synthesis of a Novel Spinnable Polyborazine Precursor with High Ceramic Yield via One-Pot Copolymerization. *Journal of the American Ceramic Society* **2021**, *104* (11), 5509–5520. https://doi.org/https://doi.org/10.1111/jace.17950.

(74) Kimura, Y.; Kubo, Y.; Hayashi, N. High-Performance Boron-Nitride Fibers from Poly(Borazine) Preceramics. *Compos Sci Technol* **1994**, *51* (2), 173–179. https://doi.org/https://doi.org/10.1016/0266-3538(94)90188-0.

(75) Toury, B.; Bernard, S.; Cornu, D.; Chassagneux, F.; Létoffé, J.-M.; Miele, P. High-Performance Boron Nitride Fibers Obtained from Asymmetric Alkylaminoborazine. *J Mater Chem* **2003**, *13* (2), 274–279. https://doi.org/10.1039/B207476A.

(76) Chen, M.; Ge, M.; Zhang, W. Preparation and Properties of Hollow BN Fibers Derived from Polymeric Precursors. *J Eur Ceram Soc* **2012**, *32* (12), 3521–3529. https://doi.org/10.1016/j.jeurceramsoc.2012.04.012.

(77) Wang, Z.; Ge, M.; Yu, S.; Zhang, H.; Zhang, H.; Qi, X.; Xiao, W.; Zhao, H.; Zhang, W. Microstructures and Properties of Polymer-Derived Hexagonal Boron Nitride Fibers with Initial Gradient Oxygen Contents. *Mater Charact* **2024**, *207*, 113503. https://doi.org/https://doi.org/10.1016/j.matchar.2023.113503.

(78) Lei, Y.; Wang, Y.; Song, Y.; Deng, C.; Wang, H. Nearly Stoichiometric BN Fiber by Curing and Thermolysis of a Novel Poly[(Alkylamino)Borazine]. *Ceram Int* **2011**, *37* (6), 1795–1800. https://doi.org/https://doi.org/10.1016/j.ceramint.2011.03.007.

(79) Guilhon, F.; Bonnetot, B.; Cornu, D.; Mongeot, H. *CONVERSION OF TRIS(ISOPROPYLAMINO)BORANE TO POLYBORAZINES. THERMAL DEGRADATION TO BORON NITRIDE*; 1996; Vol. 15.

(80) Salles, V.; Bernard, S.; Brioude, A.; Cornu, D.; Miele, P. A New Class of Boron Nitride Fibers with Tunable Properties by Combining an Electrospinning Process and the Polymer-Derived Ceramics Route. *Nanoscale* **2010**, *2* (2), 215–217. https://doi.org/10.1039/b9nr00185a.

(81) Wu, C.; Wang, B.; Wu, N.; Han, C.; Zhang, X.; Shen, S.; Tian, Q.; Qin, C.; Li, P.; Wang, Y. Molecular-Scale Understanding on the Structure Evolution from Melamine Diborate Supramolecule to Boron Nitride Fibers. *Ceram Int* **2020**, *46* (1), 1083–1090. https://doi.org/10.1016/j.ceramint.2019.09.075.

(82) Mohajeri, N.; T-Raissi, A. Regeneration of Ammonia-Borane Complex for Hydrogen Storage. *MRS Online Proceedings Library* **2006**, *884* (1), 14. https://doi.org/10.1557/PROC-884-GG1.4.

(83) Jaska, C. A.; Temple, K.; Lough, A. J.; Manners, I. Rhodium-Catalyzed Formation of Boron–Nitrogen Bonds: A Mild Route to Cyclic Aminoboranes and Borazines. *Chemical Communications* **2001**, No. 11, 962–963. https://doi.org/10.1039/B102361F.

(84) Koski, A.; Yim, K.; Shivkumar, S. Effect of Molecular Weight on Fibrous PVA Produced by Electrospinning. *Mater Lett* **2004**, *58* (3–4), 493–497. https://doi.org/10.1016/S0167-577X(03)00532-9.

(85) Wang, T.-W.; Golder, M. R. Advancing Macromolecular Hoop Construction: Recent Developments in Synthetic Cyclic Polymer Chemistry. *Polym Chem* **2021**, *12* (7), 958–969. https://doi.org/10.1039/D0PY01655A.

(86) Yamamoto, T. Synthesis of Cyclic Polymers and Topology Effects on Their Diffusion and Thermal Properties. *Polym J* **2013**, *45* (7), 711–717. https://doi.org/10.1038/pj.2012.213.

(87) Yu, D.-G.; Branford-White, C.; White, K.; Li, X.-L.; Zhu, L.-M. Dissolution Improvement of Electrospun Nanofiber-Based Solid Dispersions for Acetaminophen. *AAPS PharmSciTech* **2010**, *11* (2), 809–817. https://doi.org/10.1208/s12249-010-9438-4.

(88) Shrivastava, A. 2 - Polymerization. In *Introduction to Plastics Engineering*; Shrivastava, A., Ed.; William Andrew Publishing, 2018; pp 17–48. https://doi.org/https://doi.org/10.1016/B978-0-323-39500-7.00002-2.

(89) Xu, Z.; Hadjichristidis, N.; Fetters, L. J.; Mays, J. W. Structure/Chain-Flexibility Relationships of Polymers. In *Physical Properties of Polymers*; Springer Berlin Heidelberg: Berlin, Heidelberg, 1995; pp 1–50. https://doi.org/10.1007/3-540-58704-7_1.

(90) Chen, H.; Chen, X.; Chen, H.; Liu, X.; Li, J.; Luo, J.; He, A.; Han, C. C.; Liu, Y.; Xu, S. Molecular Interaction, Chain Conformation, and Rheological Modification during Electrospinning of Hyaluronic Acid Aqueous Solution. *Membranes (Basel)* **2020**, *10* (9). https://doi.org/10.3390/membranes10090217.

(91) Shore, S. G.; Parry, R. W. THE CRYSTALLINE COMPOUND AMMONIA-BORANE,1 H3NBH3. *J Am Chem Soc* **1955**, *77* (22), 6084–6085. https://doi.org/10.1021/ja01627a103.

(92) Paine, R. T.; Narulat, C. K. *Synthetic Routes to Boron Nitride*; 1990; Vol. 90. https://pubs.acs.org/sharingguidelines.

(93) Bernard, S.; Miele, P. Nanostructured and Architectured Boron Nitride from Boron, Nitrogen and Hydrogen-Containing Molecular and Polymeric Precursors. *Materials Today*. Elsevier B.V. November 1, 2014, pp 443–450. https://doi.org/10.1016/j.mattod.2014.07.006.

(94) Bernard, S.; Miele, P. Nanostructured and Architectured Boron Nitride from Boron, Nitrogen and Hydrogen-Containing Molecular and Polymeric Precursors. *Materials Today*. Elsevier B.V. November 1, 2014, pp 443–450. https://doi.org/10.1016/j.mattod.2014.07.006.

(95) Zhang, K.; Feng, Y.; Wang, F.; Yang, Z.; Wang, J. Two Dimensional Hexagonal Boron Nitride (2D-HBN): Synthesis, Properties and Applications. *J Mater Chem C Mater* **2017**, *5* (46), 11992–12022. https://doi.org/10.1039/C7TC04300G.

(96) Demirci, U. B. Mechanistic Insights into the Thermal Decomposition of Ammonia Borane, a Material Studied for Chemical Hydrogen Storage. *Inorganic Chemistry Frontiers*. Royal Society of Chemistry April 7, 2021, pp 1900–1930. https://doi.org/10.1039/d0qi01366h.

(97) Beweries, T.; Helten, H. Poly(Aminoborane)s and Poly(Iminoborane)s. In *Encyclopedia of Inorganic and Bioinorganic Chemistry*; Wiley, 2020; pp 1–25. https://doi.org/10.1002/9781119951438.eibc2717.

(98) Dietrich, B. L.; Goldberg, K. I.; Heinekey, D. M.; Autrey, T.; Linehan, J. C. Iridium-Catalyzed Dehydrogenation of Substituted Amine Boranes: Kinetics, Thermodynamics, and Implications for Hydrogen Storage. *Inorg Chem* **2008**, *47* (19), 8583–8585. https://doi.org/10.1021/ic801161g.

(99) N. Brodie, C.; M. Boyd, T.; Sotorríos, L.; E. Ryan, D.; Magee, E.; Huband, S.; S. Town, J.; C. Lloyd-Jones, G.; M. Haddleton, D.; A. Macgregor, S.; S. Weller, A. Controlled Synthesis of Well-Defined Polyaminoboranes on Scale Using a Robust and Efficient Catalyst. *J Am Chem Soc* **2021**, *143* (49), 21010–21023. https://doi.org/10.1021/jacs.1c10888.

(100) Bowden, M. E.; Brown, I. W. M.; Gainsford, G. J.; Wong, H. Structure and Thermal Decomposition of Methylamine Borane. *Inorganica Chim Acta* **2008**, *361* (7), 2147–2153. https://doi.org/10.1016/j.ica.2007.10.034.

(101) Baumann, J.; Baitalow, F.; Wolf, G. Thermal Decomposition of Polymeric Aminoborane (H2BNH2)x under Hydrogen Release. *Thermochim Acta* **2005**, *430* (1), 9–14. https://doi.org/https://doi.org/10.1016/j.tca.2004.12.002.

(102) Du, V. A.; Jurca, T.; Whittell, G. R.; Manners, I. Aluminum Borate Nanowires from the Pyrolysis of Polyaminoborane Precursors. *Dalton Trans.* **2016**, *45* (3), 1055–1062. https://doi.org/10.1039/C5DT03324A.

(103) Pople, J. A. Nobel Lecture: Quantum Chemical Models. *Rev Mod Phys* **1999**, *71* (5), 1267–1274. https://doi.org/10.1103/RevModPhys.71.1267.

(104) Kohn, W. Nobel Lecture: Electronic Structure of Matter---Wave Functions and Density Functionals. *Rev Mod Phys* **1999**, *71* (5), 1253–1266. https://doi.org/10.1103/RevModPhys.71.1253.

(105) Mayo, S. L.; Olafson, B. D.; Goddard, W. A. DREIDING: A Generic Force Field for Molecular Simulations. *J Phys Chem* **1990**, *94* (26), 8897–8909. https://doi.org/10.1021/j100389a010.

(106) Rappe, A. K.; Casewit, C. J.; Colwell, K. S.; Goddard, W. A. I. I. I.; Skiff, W. M. UFF, a Full Periodic Table Force Field for Molecular Mechanics and Molecular Dynamics Simulations. *J Am Chem Soc* **1992**, *114* (25), 10024–10035. https://doi.org/10.1021/ja00051a040.

(107) Van Duin, A. C. T.; Dasgupta, S.; Lorant, F.; Goddard, W. A. ReaxFF: A Reactive Force Field for Hydrocarbons. *Journal of Physical Chemistry A* **2001**, *105* (41), 9396–9409. https://doi.org/10.1021/jp004368u.

(108) Al-Kukhun, A.; Hwang, H. T.; Varma, A. Mechanistic Studies of Ammonia Borane Dehydrogenation. *Int J Hydrogen Energy* **2013**, *38* (1), 169–179. https://doi.org/https://doi.org/10.1016/j.ijhydene.2012.09.161.

(109) Miranda, C. R.; Ceder, G. Ab Initio Investigation of Ammonia-Borane Complexes for Hydrogen Storage. *J Chem Phys* **2007**, *126* (18), 184703. https://doi.org/10.1063/1.2730785.

(110) Kumar, V.; Roy, B.; Sharma, P. Kinetics of Borazine Formation from Ammonia Borane Dehydrocoupling Reaction through Ab Initio Analysis. *Int J Hydrogen Energy* **2019**, *44* (39), 22022–22031. https://doi.org/10.1016/j.ijhydene.2019.06.172.

(111) Ayarde-Henríquez, L.; Guerra, C.; Duque-Noreña, M.; Chamorro, E. Revisiting the Bonding Evolution Theory: A Fresh Perspective on the Ammonia Pyramidal Inversion and Bond Dissociations in Ethane and Borazane. *Physical Chemistry Chemical Physics* **2023**, *25* (40), 27394–27408. https://doi.org/10.1039/D3CP03572G.

(112) Aldridge, S.; Downs, A. J.; Tang, C. Y.; Parsons, S.; Clarke, M. C.; Johnstone, R. D. L.; Robertson, H. E.; Rankin, D. W. H.; Wann, D. A. Structures and Aggregation of the Methylamine−Borane Molecules, MenH3−nN·BH3 (n = 1−3), Studied by X-Ray Diffraction, Gas-Phase Electron Diffraction, and Quantum Chemical Calculations. *J Am Chem Soc* **2009**, *131* (6), 2231–2243. https://doi.org/10.1021/ja807545p.

(113) Liu, B.; Yan, S. DFT Investigation on the Decomposition of Dihydrogen-Bonded Methylamine-Borane Octamer. *Comput Theor Chem* **2018**, *1127*, 1–7. https://doi.org/https://doi.org/10.1016/j.comptc.2018.01.018.

(114) Gilbert, T. M. Tests of the MP2 Model and Various DFT Models in Predicting the Structures and B−N Bond Dissociation Energies of Amine−Boranes (X3C)MH3-MB−N(CH3)NH3-n (X = H, F; m = 0−3; n = 0−3): Poor Performance of the B3LYP Approach for Dative B−N Bonds. *J Phys Chem A* **2004**, *108* (13), 2550–2554. https://doi.org/10.1021/jp031242z.

(115) Sun, C.-H.; Yao, X.-D.; Du, A.-J.; Li, L.; Smith, S.; Lu, G.-Q. Computational Study of Methyl Derivatives of Ammonia Borane for Hydrogen Storage.

Physical Chemistry Chemical Physics **2008**, *10* (40), 6104–6106. https://doi.org/10.1039/B807776B.

(116) Liu, B.; Yan, S. DFT Investigation on the Decomposition of Dihydrogen-Bonded Methylamine-Borane Octamer. *Comput Theor Chem* **2018**, *1127*, 1–7. https://doi.org/https://doi.org/10.1016/j.comptc.2018.01.018.

(117) Yaya, I.; Udofia, I. A.; Isyaku, Y.; Ja'o, A. M. Exploring the Hydrogen Storage Potential of Allylamine Borane Using Density Functional Theory. *ChemistrySelect* **2024**, *9* (38), e202401487. https://doi.org/https://doi.org/10.1002/slct.202401487.

(118) Matus, M. H.; Liu, S.-Y.; Dixon, D. A. Dehydrogenation Reactions of Cyclic C2B2N2H12 and C4BNH12 Isomers. *J Phys Chem A* **2010**, *114* (7), 2644–2654. https://doi.org/10.1021/jp9102838.

(119) Chenoweth, K.; C. T. van Duin, A.; A. Goddard, W. ReaxFF Reactive Force Field for Molecular Dynamics Simulations of Hydrocarbon Oxidation. *J Phys Chem A* **2008**, *112* (5), 1040–1053. https://doi.org/10.1021/jp709896w.

(120) Senftle, T. P.; Hong, S.; Islam, M. M.; Kylasa, S. B.; Zheng, Y.; Shin, Y. K.; Junkermeier, C.; Engel-Herbert, R.; Janik, M. J.; Aktulga, H. M.; Verstraelen, T.; Grama, A.; Van Duin, A. C. T. The ReaxFF Reactive Force-Field: Development, Applications and Future Directions. *npj Computational Materials*. Nature Publishing Group March 4, 2016. https://doi.org/10.1038/npjcompumats.2015.11.

(121) Castro-Marcano, F.; Kamat, A. M.; Russo, M. F.; van Duin, A. C. T.; Mathews, J. P. Combustion of an Illinois No. 6 Coal Char Simulated Using an Atomistic Char Representation and the ReaxFF Reactive Force Field. *Combust Flame* **2012**, *159* (3), 1272–1285. https://doi.org/https://doi.org/10.1016/j.combustflame.2011.10.022.

(122) te Velde, G.; Bickelhaupt, F. M.; Baerends, E. J.; Fonseca Guerra, C.; van Gisbergen, S. J. A.; Snijders, J. G.; Ziegler, T. Chemistry with ADF. *J Comput Chem* **2001**, *22* (9), 931–967. https://doi.org/https://doi.org/10.1002/jcc.1056.

(123) Weismiller, M. R.; Duin, A. C. T. V.; Lee, J.; Yetter, R. A. ReaxFF Reactive Force Field Development and Applications for Molecular Dynamics Simulations of Ammonia Borane Dehydrogenation and Combustion. *Journal of Physical Chemistry A* **2010**, *114* (17), 5485–5492. https://doi.org/10.1021/jp100136c.

(124) Kamat, A. M.; van Duin, A. C. T.; Yakovlev, A. Molecular Dynamics Simulations of Laser-Induced Incandescence of Soot Using an Extended ReaxFF Reactive Force Field. *J Phys Chem A* **2010**, *114* (48), 12561–12572. https://doi.org/10.1021/jp1080302.

(125) Ince, J. C.; Peerzada, M.; Mathews, L. D.; Pai, A. R.; Al-qatatsheh, A.; Abbasi, S.; Yin, Y.; Hameed, N.; Duffy, A. R.; Lau, A. K.; Salim, N. V. Overview of Emerging Hybrid and Composite Materials for Space Applications. *Adv Compos Hybrid Mater* **2023**, *6* (4), 130. https://doi.org/10.1007/s42114-023-00678-5.

(126) Chen, Y.; Zhang, J.; Li, Z.; Zhang, H.; Chen, J.; Yang, W.; Yu, T.; Liu, W.; Li, Y. Manufacturing Technology of Lightweight Fiber-Reinforced Composite Structures in Aerospace: Current Situation and toward Intellectualization. *Aerospace* **2023**, *10* (3). https://doi.org/10.3390/aerospace10030206.

(127) Zhang, W.; Xu, J. Advanced Lightweight Materials for Automobiles: A Review. *Mater Des* **2022**, *221*, 110994. https://doi.org/https://doi.org/10.1016/j.matdes.2022.110994.

(128) Economy, J.; Lin, R. Boron Nitride Fibers. In *Boron and Refractory Borides*; Matkovich, V. I., Ed.; Springer Berlin Heidelberg: Berlin, Heidelberg, 1977; pp 552–564. https://doi.org/10.1007/978-3-642-66620-9_29.

(129) Kostoglou, N.; Polychronopoulou, K.; Rebholz, C. Thermal and Chemical Stability of Hexagonal Boron Nitride (h-BN) Nanoplatelets. *Vacuum* **2015**, *112*, 42–45. https://doi.org/https://doi.org/10.1016/j.vacuum.2014.11.009.

(130) Falin, A.; Cai, Q.; Santos, E. J. G.; Scullion, D.; Qian, D.; Zhang, R.; Yang, Z.; Huang, S.; Watanabe, K.; Taniguchi, T.; Barnett, M. R.; Chen, Y.; Ruoff, R. S.; Li, L. H. Mechanical Properties of Atomically Thin Boron Nitride and the Role of Interlayer Interactions. *Nat Commun* **2017**, *8* (1), 15815. https://doi.org/10.1038/ncomms15815.

(131) Jones, R. S.; Gonzalez-Munoz, S.; Griffiths, I.; Holdway, P.; Evers, K.; Luanwuthi, S.; Maciejewska, B. M.; Kolosov, O.; Grobert, N. Thermal Conductivity of Carbon/Boron Nitride Heteronanotube and Boron Nitride Nanotube Buckypapers: Implications for Thermal Management Composites. *ACS Appl Nano Mater* **2023**, *6* (17), 15374–15384. https://doi.org/10.1021/acsanm.3c01147.

(132) Chen, J.; Huang, X.; Sun, B.; Jiang, P. Highly Thermally Conductive Yet Electrically Insulating Polymer/Boron Nitride Nanosheets Nanocomposite Films for Improved Thermal Management Capability. *ACS Nano* **2019**, *13* (1), 337–345. https://doi.org/10.1021/acsnano.8b06290.

(133) Tiano, A. L.; Park, C.; Lee, J. W.; Luong, H. H.; Gibbons, L. J.; Chu, S.-H.; Applin, S.; Gnoffo, P.; Lowther, S.; Kim, H. J.; Danehy, P. M.; Inman, J. A.; Jones, S. B.; Kang, J. H.; Sauti, G.; Thibeault, S. A.; Yamakov, V.; Wise, K. E.; Su, J.; Fay, C. C. Boron Nitride Nanotube: Synthesis and Applications. In *Proc.SPIE*; 2014; Vol. 9060, p 906006. https://doi.org/10.1117/12.2045396.

(134) Jones, R. S. Designing Boron Nitride Nanotubes and Their Macroscopic Assemblies via Sacrificial Templating, University of Oxford, 2021.
(135) Bernard, S.; Salameh, C.; Miele, P. Boron Nitride Ceramics from Molecular Precursors: Synthesis, Properties and Applications. *Dalton Transactions* **2016**, *45* (3), 861–873. https://doi.org/10.1039/C5DT03633J.
(136) Lindquist, D. A.; Janik, J. F.; Datye, A. K.; Paine, R. T.; Rothman, J. B. Boron Nitride Fibers Processed from Poly(Borazinylamine) Solutions. *Chemistry of Materials* **1992**, *4* (1), 17–19. https://doi.org/10.1021/cm00019a007.
(137) Duperrier, S.; Gervais, C.; Bernard, S.; Cornu, D.; Babonneau, F.; Balan, C.; Miele, P. Design of a Series of Preceramic B-Tri(Methylamino)Borazine-Based Polymers as Fiber Precursors: Architecture, Thermal Behavior, and Melt-Spinnability. *Macromolecules* **2007**, *40* (4), 1018–1027. https://doi.org/10.1021/ma0623035.
(138) Dong, S.; Maciejewska, B. M.; Lißner, M.; Thomson, D.; Townsend, D.; Millar, R.; Petrinic, N.; Grobert, N. Unveiling the Mechanism of the *in Situ* Formation of 3D Fiber Macroassemblies with Controlled Properties. *ACS Nano* **2023**. https://doi.org/10.1021/acsnano.3c00289.
(139) Vidal, F.; Jäkle, F. Functional Polymeric Materials Based on Main-Group Elements. *Angewandte Chemie International Edition* **2019**, *58* (18), 5846–5870. https://doi.org/https://doi.org/10.1002/anie.201810611.
(140) De Albuquerque Pinheiro, C. A.; Roiland, C.; Jehan, P.; Alcaraz, G. Solventless and Metal-Free Synthesis of High-Molecular-Mass Polyaminoboranes from Diisopropylaminoborane and Primary Amines. *Angewandte Chemie International Edition* **2018**, *57* (6), 1519–1522. https://doi.org/https://doi.org/10.1002/anie.201710293.
(141) Devillard, M.; De Albuquerque Pinheiro, C. A.; Caytan, E.; Roiland, C.; Dinoi, C.; Del Rosal, I.; Alcaraz, G. Uncatalyzed Formation of Polyaminoboranes from Diisopropylaminoborane and Primary Amines: A Kinetically Controlled Polymerization Reaction. *Adv Synth Catal* **2021**, *363* (9), 2417–2426. https://doi.org/https://doi.org/10.1002/adsc.202001458.
(142) Staubitz, A.; Presa Soto, A.; Manners, I. Iridium-Catalyzed Dehydrocoupling of Primary Amine–Borane Adducts: A Route to High Molecular Weight Polyaminoboranes, Boron–Nitrogen Analogues of Polyolefins. *Angewandte Chemie International Edition* **2008**, *47* (33), 6212–6215. https://doi.org/https://doi.org/10.1002/anie.200801197.
(143) Staubitz, A.; Sloan, M. E.; Robertson, A. P. M.; Friedrich, A.; Schneider, S.; Gates, P. J.; Schmedt auf der Günne, J.; Manners, I. Catalytic Dehydrocoupling/Dehydrogenation of N-Methylamine-Borane and Ammonia-

Borane: Synthesis and Characterization of High Molecular Weight Polyaminoboranes. *J Am Chem Soc* **2010**, *132* (38), 13332–13345. https://doi.org/10.1021/ja104607y.

(144) Stubbs, N. E.; Jurca, T.; Leitao, E. M.; Woodall, C. H.; Manners, I. Polyaminoborane Main Chain Scission Using N-Heterocyclic Carbenes; Formation of Donor-Stabilised Monomeric Aminoboranes. *Chemical Communications* **2013**, *49* (80), 9098–9100. https://doi.org/10.1039/C3CC44373F.

(145) Chen, E. Y.-X. Coordination Polymerization of Polar Vinyl Monomers by Single-Site Metal Catalysts. *Chem Rev* **2009**, *109* (11), 5157–5214. https://doi.org/10.1021/cr9000258.

(146) Jurca, T.; Dellermann, T.; Stubbs, N. E.; Resendiz-Lara, D. A.; Whittell, G. R.; Manners, I. Step-Growth Titanium-Catalysed Dehydropolymerisation of Amine–Boranes. *Chem Sci* **2018**, *9* (13), 3360–3366. https://doi.org/10.1039/C7SC05395A.

(147) Leitao, E. M.; Jurca, T.; Manners, I. Catalysis in Service of Main Group Chemistry Offers a Versatile Approach to P-Block Molecules and Materials. *Nat Chem* **2013**, *5* (10), 817–829. https://doi.org/10.1038/nchem.1749.

(148) Kim, D. P.; Moon, K. T.; Kho, J. G.; Economy, J.; Gervais, C.; Babonneau, F. Synthesis and Characterization of Poly-(Aminoborane) as a New Boron Nitride Precursor. *Polym Adv Technol* **1999**, *10* (12), 702–712. https://doi.org/10.1002/(SICI)1099-1581(199912)10:12<702::AID-PAT931>3.0.CO;2-Q.

(149) Oliver, W. C.; Pharr, G. M. Measurement of Hardness and Elastic Modulus by Instrumented Indentation: Advances in Understanding and Refinements to Methodology. *J Mater Res* **2004**, *19* (1), 3–20. https://doi.org/10.1557/jmr.2004.19.1.3.

(150) Shenoy, S. L.; Bates, W. D.; Frisch, H. L.; Wnek, G. E. Role of Chain Entanglements on Fiber Formation during Electrospinning of Polymer Solutions: Good Solvent, Non-Specific Polymer-Polymer Interaction Limit. *Polymer (Guildf)* **2005**, *46* (10), 3372–3384. https://doi.org/10.1016/j.polymer.2005.03.011.

(151) Lahann, J. Science and Technology of Polymer Nanofibers. *Macromol Chem Phys* **2010**, *211* (12), 1387–1387. https://doi.org/10.1002/macp.201000211.

(152) Okutan, N.; Terzi, P.; Altay, F. Affecting Parameters on Electrospinning Process and Characterization of Electrospun Gelatin Nanofibers. *Food Hydrocoll* **2014**, *39*, 19–26. https://doi.org/10.1016/j.foodhyd.2013.12.022.

(153) Amariei, N.; Manea, L. R.; Bertea, A. P.; Bertea, A.; Popa, A. The Influence of Polymer Solution on the Properties of Electrospun 3D Nanostructures. *IOP Conf Ser Mater Sci Eng* **2017**, *209* (1), 012092. https://doi.org/10.1088/1757-899X/209/1/012092.

(154) Han, D.; Joksch, M.; Klahn, M.; Spannenberg, A.; Drexler, H.-J.; Baumann, W.; Jiao, H.; Knitsch, R.; Hansen, M. R.; Eckert, H.; Beweries, T. Iridium(Iii) Hydrido Complexes for the Catalytic Dehydrogenation of Hydrazine Borane. *Dalton Transactions* **2016**, *45* (44), 17697–17704. https://doi.org/10.1039/C6DT03068H.

(155) Knitsch, R.; Han, D.; Anke, F.; Ibing, L.; Jiao, H.; Hansen, M. R.; Beweries, T. Fe(II) Hydride Complexes for the Homogeneous Dehydrocoupling of Hydrazine Borane: Catalytic Mechanism via DFT Calculations and Detailed Spectroscopic Characterization. *Organometallics* **2019**, *38* (14), 2714–2723. https://doi.org/10.1021/acs.organomet.9b00053.

(156) Wang, X.; Zhi, C.; Li, L.; Zeng, H.; Li, C.; Mitome, M.; Golberg, D.; Bando, Y. "Chemical Blowing" of Thin-Walled Bubbles: High-Throughput Fabrication of Large-Area, Few-Layered BN and Cx-BN Nanosheets. *Advanced Materials* **2011**, *23* (35), 4072–4076. https://doi.org/https://doi.org/10.1002/adma.201101788.

(157) Chrenko, R. M. Ultraviolet and Infrared Spectra of Cubic Boron Nitride. *Solid State Commun* **1974**, *14* (6), 511–515. https://doi.org/https://doi.org/10.1016/0038-1098(74)90978-8.

(158) Duperrier, S.; Gervais, C.; Bernard, S.; Cornu, D.; Babonneau, F.; Miele, P. Controlling the Chemistry, Morphology and Structure of Boron Nitride-Based Ceramic Fibers through a Comprehensive Mechanistic Study of the Reactivity of Spinnable Polymers with Ammonia. *J Mater Chem* **2006**, *16* (30), 3126–3138. https://doi.org/10.1039/B604482D.

(159) Lei, Y.; Wang, Y.; Song, Y. Boron Nitride by Pyrolysis of the Melt-Processable Poly[Tris(Methylamino)Borane]: Structure, Composition and Oxidation Resistance. *Ceram Int* **2012**, *38* (1), 271–276. https://doi.org/https://doi.org/10.1016/j.ceramint.2011.07.001.

(160) Cornu, D.; Miele, P.; Faure, R.; Bonnetot, B.; Mongeot, H.; Bouix, J. Conversion of B (NHCH3) 3 into Boron Nitride and Polyborazine Fibres and Tubular BN Structures Derived Therefrom. *J Mater Chem* **1999**, *9* (3), 757–761.

(161) Du, Y.; Wang, B.; Li, W.; Song, Q.; Shao, C.; Han, C.; Wang, Y. Design and Synthesis of a Novel Spinnable Polyborazine Precursor with High Ceramic Yield via One-Pot Copolymerization. *Journal of the American Ceramic Society* **2021**, *104* (11), 5509–5520. https://doi.org/10.1111/jace.17950.

(162) Bernard, S.; Chassagneux, F.; Berthet, M. P.; Cornu, D.; Miele, P. Crystallinity, Crystalline Quality, and Microstructural Ordering in Boron Nitride Fibers. *Journal of the American Ceramic Society* **2005**, *88* (6), 1607–1614. https://doi.org/10.1111/j.1551-2916.2005.00318.x.

(163) Duperrier, S.; Gervais, C.; Bernard, S.; Cornu, D.; Babonneau, F.; Miele, P. Controlling the Chemistry, Morphology and Structure of Boron Nitride-Based Ceramic Fibers through a Comprehensive Mechanistic Study of the Reactivity of Spinnable Polymers with Ammonia. *J Mater Chem* **2006**, 3126–3138. https://doi.org/10.1039/b604482d.

(164) Chassagneux, F.; Epicier, T.; Toutois, P.; Miele, P.; Vincent, C.; Vincent, H. Texture, Structure and Chemistry of a Boron Nitride Fibre Studied by High Resolution and Analytical TEM. *J Eur Ceram Soc* **2002**, *22* (13), 2415–2425. https://doi.org/https://doi.org/10.1016/S0955-2219(02)00002-X.

(165) Qiu, Y.; Yu, J.; Yin, J.; Zhou, X. Effects and Control of Polymer-Converted Carbon Impurity in Synthesizing Continuous Boron Nitride Nanofibers by Electrospinning. *Int J Appl Ceram Technol* **2012**, *9* (4), 823–832. https://doi.org/10.1111/j.1744-7402.2011.02697.x.

(166) Yuan, S.; Linas, S.; Journet, C.; Steyer, P.; Garnier, V.; Bonnefont, G.; Brioude, A.; Toury, B. Pure & Crystallized 2D Boron Nitride Sheets Synthesized via a Novel Process Coupling Both PDCs and SPS Methods. *Sci Rep* **2016**, *6* (1), 20388. https://doi.org/10.1038/srep20388.

(167) Zhang, C.; Zhao, S.; Jin, C.; Koh, A. L.; Zhou, Y.; Xu, W.; Li, Q.; Xiong, Q.; Peng, H.; Liu, Z. Direct Growth of Large-Area Graphene and Boron Nitride Heterostructures by a Co-Segregation Method. *Nat Commun* **2015**, *6* (1), 6519. https://doi.org/10.1038/ncomms7519.

(168) Pang, J.; Chao, Y.; Chang, H.; Li, H.; Xiong, J.; He, M.; Zhang, Q.; Li, H.; Zhu, W. Tuning Electronic Properties of Boron Nitride Nanoplate via Doping Carbon for Enhanced Adsorptive Performance. *J Colloid Interface Sci* **2017**, *508*, 121–128. https://doi.org/https://doi.org/10.1016/j.jcis.2017.08.012.

(169) Tay, R. Y.; Li, H.; Tsang, S. H.; Jing, L.; Tan, D.; Wei, M.; Teo, E. H. T. Facile Synthesis of Millimeter-Scale Vertically Aligned Boron Nitride Nanotube Forests by Template-Assisted Chemical Vapor Deposition. *Chemistry of Materials* **2015**, *27* (20), 7156–7163. https://doi.org/10.1021/acs.chemmater.5b03300.

(170) Fan, D.; Feng, J.; Liu, J.; Gao, T.; Ye, Z.; Chen, M.; Lv, X. Hexagonal Boron Nitride Nanosheets Exfoliated by Sodium Hypochlorite Ball Mill and Their Potential Application in Catalysis. *Ceram Int* **2016**, *42* (6), 7155–7163. https://doi.org/https://doi.org/10.1016/j.ceramint.2016.01.105.

(171) Du, M.; Wu, Y.; Hao, X. A Facile Chemical Exfoliation Method to Obtain Large Size Boron Nitride Nanosheets. *CrystEngComm* **2013**, *15* (9), 1782–1786. https://doi.org/10.1039/C2CE26446C.

(172) Kurakevych, O. O.; Solozhenko, V. L. Rhombohedral Boron Subnitride, B 13N 2, by X-Ray Powder Diffraction. *Acta Crystallographica Section C* **2007**, *63* (9), i80–i82. https://doi.org/10.1107/S0108270107037353.

(173) Xue, Y.; Zhou, X.; Zhan, T.; Jiang, B.; Guo, Q.; Fu, X.; Shimamura, K.; Xu, Y.; Mori, T.; Dai, P.; Bando, Y.; Tang, C.; Golberg, D. Densely Interconnected Porous BN Frameworks for Multifunctional and Isotropically Thermoconductive Polymer Composites. *Adv Funct Mater* **2018**, *28* (29). https://doi.org/10.1002/adfm.201801205.

(174) Maleki, M.; Beitollahi, A.; Shokouhimehr, M. Template-Free Synthesis of Porous Boron Nitride Using a Single Source Precursor. *RSC Adv* **2015**, *5* (58), 46823–46828. https://doi.org/10.1039/c5ra04636j.

(175) Monthioux, M. Describing Carbons. *Carbon Trends* **2024**, *14*. https://doi.org/10.1016/j.cartre.2024.100325.

(176) Simonsen Ginestra, C. J.; Martínez-Jiménez, C.; Matatyaho Ya'akobi, A.; Dewey, O. S.; Smith McWilliams, A. D.; Headrick, R. J.; Acapulco, J. A.; Scammell, L. R.; Smith, M. W.; Kosynkin, D. V; Marincel, D. M.; Park, C.; Chu, S.-H.; Talmon, Y.; Martí, A. A.; Pasquali, M. Liquid Crystals of Neat Boron Nitride Nanotubes and Their Assembly into Ordered Macroscopic Materials. *Nat Commun* **2022**, *13* (1), 3136. https://doi.org/10.1038/s41467-022-30378-5.

(177) Nautiyal, P.; Zhang, C.; Loganathan, A.; Boesl, B.; Agarwal, A. High-Temperature Mechanics of Boron Nitride Nanotube "Buckypaper" for Engineering Advanced Structural Materials. *ACS Appl Nano Mater* **2019**, *2* (7), 4402–4416. https://doi.org/10.1021/acsanm.9b00817.

(178) Jeong, G. H.; Sasikala, S. P.; Yun, T.; Lee, G. Y.; Lee, W. J.; Kim, S. O. Nanoscale Assembly of 2D Materials for Energy and Environmental Applications. *Advanced Materials* **2020**, *32* (35), 1907006. https://doi.org/https://doi.org/10.1002/adma.201907006.

(179) Kaiser, S. K.; Chen, Z.; Faust Akl, D.; Mitchell, S.; Pérez-Ramírez, J. Single-Atom Catalysts across the Periodic Table. *Chem Rev* **2020**, *120* (21), 11703–11809. https://doi.org/10.1021/acs.chemrev.0c00576.

(180) Duan, X.; Wang, C.; Pan, A.; Yu, R.; Duan, X. Two-Dimensional Transition Metal Dichalcogenides as Atomically Thin Semiconductors: Opportunities and Challenges. *Chem Soc Rev* **2015**, *44* (24), 8859–8876. https://doi.org/10.1039/C5CS00507H.

(181) Weng, Q.; Wang, X.; Wang, X.; Bando, Y.; Golberg, D. Functionalized Hexagonal Boron Nitride Nanomaterials: Emerging Properties and Applications. *Chem Soc Rev* **2016**, *45* (14), 3989–4012. https://doi.org/10.1039/C5CS00869G.

(182) Marchesini, S.; McGilvery, C. M.; Bailey, J.; Petit, C. Template-Free Synthesis of Highly Porous Boron Nitride: Insights into Pore Network Design and Impact on Gas Sorption. *ACS Nano* **2017**, *11* (10), 10003–10011. https://doi.org/10.1021/acsnano.7b04219.

(183) Lu, X.; Zhang, M.; Jin, D.; Dang, Y.; Zhou, S.; Wei, S.; Zhu, H.; Zhao, L. Competitive Adsorption of CO2/CH4 in Porous Boron Nitride Nanomaterials. *Mater Lett* **2015**, *161*, 545–548. https://doi.org/https://doi.org/10.1016/j.matlet.2015.09.036.

(184) Saha, D.; Orkoulas, G.; Yohannan, S.; Ho, H. C.; Cakmak, E.; Chen, J.; Ozcan, S. Nanoporous Boron Nitride as Exceptionally Thermally Stable Adsorbent: Role in Efficient Separation of Light Hydrocarbons. *ACS Appl Mater Interfaces* **2017**, *9* (16), 14506–14517. https://doi.org/10.1021/acsami.7b01889.

(185) Weng, Q.; Wang, X.; Zhi, C.; Bando, Y.; Golberg, D. Boron Nitride Porous Microbelts for Hydrogen Storage. *ACS Nano* **2013**, *7* (2), 1558–1565. https://doi.org/10.1021/nn305320v.

(186) Wang, X.; Pakdel, A.; Zhi, C.; Watanabe, K.; Sekiguchi, T.; Golberg, D.; Bando, Y. High-Yield Boron Nitride Nanosheets from “Chemical Blowing”: Towards Practical Applications in Polymer Composites. *Journal of Physics Condensed Matter* **2012**, *24* (31). https://doi.org/10.1088/0953-8984/24/31/314205.

(187) Maleki, M.; Beitollahi, A.; Shokouhimehr, M. Template-Free Synthesis of Porous Boron Nitride Using a Single Source Precursor. *RSC Adv* **2015**, *5* (58), 46823–46828. https://doi.org/10.1039/c5ra04636j.

(188) Li, J.; Bernard, S.; Salles, V.; Gervais, C.; Miele, P. Preparation of Polyborazylene-Derived Bulk Boron Nitride with Tunable Properties by Warm-Pressing and Pressureless Pyrolysis. *Chemistry of Materials* **2010**, *22* (6), 2010–2019. https://doi.org/10.1021/cm902972p.

(189) Cao, F.; Ding, Y.; Chen, L.; Chen, C.; Fang, Z. Fabrication and Characterization of Boron Nitride Bulk Foam from Borazine. *Mater Des* **2014**, *54*, 610–615. https://doi.org/10.1016/j.matdes.2013.08.089.

(190) Zou, C.; Guo, S.; Wang, S.; Shen, T.; Zhou, X.; Li, B.; Li, D.; Li, J. Dense Additive-Free Bulk Boron Nitride Ceramics Developed by Self-Densification of Borazine. *J Eur Ceram Soc* **2022**, *42* (6), 2640–2650. https://doi.org/10.1016/j.jeurceramsoc.2022.01.036.

(191) Lin, J.; Yuan, X.; Li, G.; Huang, Y.; Wang, W.; He, X.; Yu, C.; Fang, Y.; Liu, Z.; Tang, C. Self-Assembly of Porous Boron Nitride Microfibers into Ultralight Multifunctional Foams of Large Sizes. *ACS Appl Mater Interfaces* **2017**, *9* (51), 44732–44739. https://doi.org/10.1021/acsami.7b16198.

(192) Li, H.; Zhu, J.; Lin, J.; Wang, Q.; Yu, C.; Fang, Y.; Liu, Z.; Guo, Z.; Xue, Y.; Tang, C.; Cheng, C.; Huang, Y. Synthesis of Nanostructured Boron Nitride Aerogels by Rapid Pyrolysis of Melamine Diborate Aerogels via Induction Heating: From Composition Adjustment to Property Studies. *ACS Appl Nano Mater* **2021**, *4* (12), 13788–13797. https://doi.org/10.1021/acsanm.1c03183.

(193) Li, G.; Zhu, M.; Gong, W.; Du, R.; Eychmüller, A.; Li, T.; Lv, W.; Zhang, X. Boron Nitride Aerogels with Super-Flexibility Ranging from Liquid Nitrogen Temperature to 1000 °C. *Adv Funct Mater* **2019**, *29* (20), 1900188. https://doi.org/https://doi.org/10.1002/adfm.201900188.

(194) Zhang, X.; Lian, G.; Zhang, S.; Cui, D.; Wang, Q. Boron Nitride Nanocarpets: Controllable Synthesis and Their Adsorption Performance to Organic Pollutants. *CrystEngComm* **2012**, *14* (14), 4670–4676. https://doi.org/10.1039/C2CE06748J.

(195) Gautam, C.; Tiwary, C. S.; Jose, S.; Brunetto, G.; Ozden, S.; Vinod, S.; Raghavan, P.; Biradar, S.; Galvao, D. S.; Ajayan, P. M. Synthesis of Low-Density, Carbon-Doped, Porous Hexagonal Boron Nitride Solids. *ACS Nano* **2015**, *9* (12), 12088–12095. https://doi.org/10.1021/acsnano.5b05847.

(196) Zhao, Z.; Yang, Z.; Wen, Y.; Wang, Y. Facile Synthesis and Characterization of Hexagonal Boron Nitride Nanoplates by Two-Step Route. *Journal of the American Ceramic Society* **2011**, *94* (12), 4496–4501. https://doi.org/https://doi.org/10.1111/j.1551-2916.2011.04752.x.

(197) Xue, Y.; Dai, P.; Zhou, M.; Wang, X.; Pakdel, A.; Zhang, C.; Weng, Q.; Takei, T.; Fu, X.; Popov, Z. I.; Sorokin, P. B.; Tang, C.; Shimamura, K.; Bando, Y.; Golberg, D. Multifunctional Superelastic Foam-Like Boron Nitride Nanotubular Cellular-Network Architectures. *ACS Nano* **2017**, *11* (1), 558–568. https://doi.org/10.1021/acsnano.6b06601.

(198) Schlienger, S.; Alauzun, J.; Michaux, F.; Vidal, L.; Parmentier, J.; Gervais, C.; Babonneau, F.; Bernard, S.; Miele, P.; Parra, J. B. Micro-, Mesoporous Boron Nitride-Based Materials Templated from Zeolites. *Chemistry of Materials* **2012**, *24* (1), 88–96. https://doi.org/10.1021/cm201938h.

(199) Rushton, B.; Mokaya, R. Mesoporous Boron Nitride and Boron-Nitride-Carbon Materials from Mesoporous Silica Templates. *J Mater Chem* **2008**, *18* (2), 235–241. https://doi.org/10.1039/B713740K.

(200) Dibandjo, P.; Chassagneux, F.; Bois, L.; Sigala, C.; Miele, P. Comparison between SBA-15 Silica and CMK-3 Carbon Nanocasting for Mesoporous Boron Nitride Synthesis. *J Mater Chem* **2005**, *15* (19), 1917–1923. https://doi.org/10.1039/B417891B.

(201) Maleki, M.; Beitollahi, A.; Shokouhimehr, M. Simple Synthesis of Two-Dimensional Micro/Mesoporous Boron Nitride. *Eur J Inorg Chem* **2015**, *2015* (14), 2478–2485. https://doi.org/https://doi.org/10.1002/ejic.201500194.

(202) Dibandjo, P.; Bois, L.; Chassagneux, F.; Miele, P. Thermal Stability of Mesoporous Boron Nitride Templated with a Cationic Surfactant. *J Eur Ceram Soc* **2007**, *27* (1), 313–317. https://doi.org/https://doi.org/10.1016/j.jeurceramsoc.2006.04.178.

(203) Li, J.; Xiao, X.; Xu, X.; Lin, J.; Huang, Y.; Xue, Y.; Jin, P.; Zou, J.; Tang, C. Activated Boron Nitride as an Effective Adsorbent for Metal Ions and Organic Pollutants. *Sci Rep* **2013**, *3* (1), 3208. https://doi.org/10.1038/srep03208.

(204) Vinu, A.; Terrones, M.; Golberg, D.; Hishita, S.; Ariga, K.; Mori, T. Synthesis of Mesoporous BN and BCN Exhibiting Large Surface Areas via Templating Methods. *Chemistry of Materials* **2005**, *17* (24), 5887–5890. https://doi.org/10.1021/cm051780j.

(205) Zhang, N.; Liu, H.; Kan, H.; Wang, X.; Long, H.; Zhou, Y. The Preparation of High-Adsorption, Spherical, Hexagonal Boron Nitride by Template Method. *J Alloys Compd* **2014**, *613*, 74–79. https://doi.org/https://doi.org/10.1016/j.jallcom.2014.05.161.

(206) Han, W.-Q.; Brutchey, R.; Tilley, T. D.; Zettl, A. Activated Boron Nitride Derived from Activated Carbon. *Nano Lett* **2004**, *4* (1), 173–176. https://doi.org/10.1021/nl034843a.

(207) Cross, M. J.; Brodie, C. N.; Crivoi, D. G.; Goodall, J. C.; Ryan, D. E.; Martínez-Martínez, A. J.; Johnson, A.; Weller, A. S. Dehydropolymerization of Amine−Boranes Using Bis(Imino)Pyridine Rhodium Pre-Catalysis: σ-Amine−Borane Complexes, Nanoparticles, and Low Residual-Metal BN−Polymers That Can Be Chemically Repurposed. *Chemistry - A European Journal* **2023**, *29* (60). https://doi.org/10.1002/chem.202302110.

(208) Xue, Y.; Dai, P.; Zhou, M.; Wang, X.; Pakdel, A.; Zhang, C.; Weng, Q.; Takei, T.; Fu, X.; I. Popov, Z.; B. Sorokin, P.; Tang, C.; Shimamura, K.; Bando, Y.; Golberg, D. Multifunctional Superelastic Foam-Like Boron Nitride Nanotubular Cellular-Network Architectures. *ACS Nano* **2016**, *11* (1), 558–568. https://doi.org/10.1021/acsnano.6b06601.

(209) Maqbool, M.; Bashir, A.; Usman, A.; Khurram, M.; Aftab, W.; Li, Y.; Zou, R. 3D Interconnected Boron Nitride Macrostructures and Derived Composites for

Thermal Energy Regulation. *Adv Funct Mater* **2025**, *35* (9), 2414042. https://doi.org/https://doi.org/10.1002/adfm.202414042.

(210) Yuan, S.; Linas, S.; Journet, C.; Steyer, P.; Garnier, V.; Bonnefont, G.; Brioude, A.; Toury, B. Pure & Crystallized 2D Boron Nitride Sheets Synthesized via a Novel Process Coupling Both PDCs and SPS Methods. *Sci Rep* **2016**, *6* (1), 20388. https://doi.org/10.1038/srep20388.

(211) Lei, W.; Mochalin, V. N.; Liu, D.; Qin, S.; Gogotsi, Y.; Chen, Y. Boron Nitride Colloidal Solutions, Ultralight Aerogels and Freestanding Membranes through One-Step Exfoliation and Functionalization. *Nat Commun* **2015**, *6* (1), 8849. https://doi.org/10.1038/ncomms9849.

(212) Martin-Gullon, I.; Vera, J.; Conesa, J. A.; González, J. L.; Merino, C. Differences between Carbon Nanofibers Produced Using Fe and Ni Catalysts in a Floating Catalyst Reactor. *Carbon N Y* **2006**, *44* (8), 1572–1580. https://doi.org/https://doi.org/10.1016/j.carbon.2005.12.027.

(213) Teo, K. B. K.; Singh, C.; Chhowalla, M.; Milne, W. I. Catalytic Synthesis of Carbon Nanotubes and Nanofibers. *Encyclopedia of nanoscience and nanotechnology* **2003**, *10* (1).

(214) Yuan, S.; Journet, C.; Linas, S.; Garnier, V.; Steyer, P.; Benayoun, S.; Brioude, A.; Toury, B. How to Increase the H-BN Crystallinity of Microfilms and Self-Standing Nanosheets: A Review of the Different Strategies Using the PDCs Route. *Crystals (Basel)* **2016**, *6* (5). https://doi.org/10.3390/cryst6050055.

(215) Kubota, Y.; Watanabe, K.; Tsuda, O.; Taniguchi, T. Deep Ultraviolet Light-Emitting Hexagonal Boron Nitride Synthesized at Atmospheric Pressure. *Science (1979)* **2007**, *317* (5840), 932–934. https://doi.org/10.1126/science.1144216.

(216) Stowe, A. C.; Shaw, W. J.; Linehan, J. C.; Schmid, B.; Autrey, T. In Situ Solid State 11B MAS-NMR Studies of the Thermal Decomposition of Ammonia Borane: Mechanistic Studies of the Hydrogen Release Pathways from a Solid State Hydrogen Storage Material. *Physical Chemistry Chemical Physics* **2007**, *9* (15), 1831–1836. https://doi.org/10.1039/B617781F.

(217) Guilhon, F.; Bonnetot, B.; Cornu, D.; Mongeot, H. Conversion of Tris(Isopropylamino)Borane to Polyborazines. Thermal Degradation to Boron Nitride. *Polyhedron* **1996**, *15* (5), 851–859. https://doi.org/https://doi.org/10.1016/0277-5387(95)00336-6.

(218) Babenko, V.; Lane, G.; Koos, A. A.; Murdock, A. T.; So, K.; Britton, J.; Meysami, S. S.; Moffat, J.; Grobert, N. Time Dependent Decomposition of Ammonia Borane for the Controlled Production of 2D Hexagonal Boron Nitride. *Sci Rep* **2017**, *7* (1). https://doi.org/10.1038/s41598-017-14663-8.

(219) Frueh, S.; Kellett, R.; Mallery, C.; Molter, T.; Willis, W. S.; King'Ondu, C.; Suib, S. L. Pyrolytic Decomposition of Ammonia Borane to Boron Nitride. *Inorg Chem* **2011**, *50* (3), 783–792. https://doi.org/10.1021/ic101020k.

(220) Baitalow, F.; Baumann, J.; Wolf, G.; Jaenicke-Rößler, K.; Leitner, G. Thermal Decomposition of B–N–H Compounds Investigated by Using Combined Thermoanalytical Methods. *Thermochim Acta* **2002**, *391* (1), 159–168. https://doi.org/https://doi.org/10.1016/S0040-6031(02)00173-9.

(221) Paine, R. T.; Sodeck, G.; Stafford, F. E. Molecular Beam Mass Spectra and Pyrolyses of Fluorophosphine-Triborane(7) Complexes. Formation and Mass Spectrum of Triborane(7). *Inorg Chem* **1972**, *11* (11), 2593–2600. https://doi.org/10.1021/ic50117a005.

(222) Chen, X.; Zhao, J.-C.; Shore, S. G. Facile Synthesis of Aminodiborane and Inorganic Butane Analogue NH3BH2NH2BH3. *J Am Chem Soc* **2010**, *132* (31), 10658–10659. https://doi.org/10.1021/ja104938v.

(223) Schlesinger, H. I.; Ritter, D. M.; Burg, A. B. Hydrides of Boron. X. The Preparation and Preliminary Study of the New Compound B2H7N. *J Am Chem Soc* **1938**, *60* (10), 2297–2300. https://doi.org/10.1021/ja01277a006.

(224) Han, L.; Krstić, P. A Path for Synthesis of Boron-Nitride Nanostructures in Volume of Arc Plasma. *Nanotechnology* **2017**, *28* (7), 07LT01. https://doi.org/10.1088/1361-6528/aa5653.

(225) Khalilov, U.; Bogaerts, A.; Neyts, E. C. Atomic Scale Simulation of Carbon Nanotube Nucleation from Hydrocarbon Precursors. *Nat Commun* **2015**, *6*. https://doi.org/10.1038/ncomms10306.

(226) Rao, F.-B.; Li, T.; Wang, Y.-L. Effect of Hydrogen on the Growth of Single-Walled Carbon Nanotubes by Thermal Chemical Vapor Deposition. *Physica E Low Dimens Syst Nanostruct* **2008**, *40* (4), 779–784. https://doi.org/https://doi.org/10.1016/j.physe.2007.09.185.

(227) Zeng, Z. Y.; Lin, J. H. Metal-Catalyst-Free Growth of Carbon Nanotubes/Carbon Nanofibers on Carbon Blacks Using Chemical Vapor Deposition. *RSC Adv* **2014**, *4* (76), 40251–40258. https://doi.org/10.1039/c4ra03456b.

(228) McLean, B.; Webber, G. B.; Page, A. J. Boron Nitride Nanotube Nucleation via Network Fusion during Catalytic Chemical Vapor Deposition. *J Am Chem Soc* **2019**, *141* (34), 13385–13393. https://doi.org/10.1021/jacs.9b03484.

(229) Bae, D. S.; Kim, C.; Lee, H.; Khater, O.; Kim, K. S.; Shin, H.; Lee, K. H.; Kim, M. J. Spontaneous Formation of Boron Nitride Nanotube Fibers by Boron Impurity Reduction in Laser Ablation of Ammonia Borane. *Nano Converg* **2022**, *9* (1). https://doi.org/10.1186/s40580-022-00312-y.

(230) Angizi, S.; Akbar, M. A.; Darestani-Farahani, M.; Kruse, P. Review—Two-Dimensional Boron Carbon Nitride: A Comprehensive Review. *ECS Journal of Solid State Science and Technology* **2020**, *9* (8), 083004. https://doi.org/10.1149/2162-8777/abb8ef.

(231) Nehate, S. D.; Saikumar, A. K.; Prakash, A.; Sundaram, K. B. A Review of Boron Carbon Nitride Thin Films and Progress in Nanomaterials. *Materials Today Advances*. Elsevier Ltd December 1, 2020. https://doi.org/10.1016/j.mtadv.2020.100106.

(232) Mayo, D. W.; Miller, F. A.; Hannah, R. W. *Course Notes on the Interpretation of Infrared and Raman Spectra*; John Wiley & Sons, 2004.

(233) Gao, G.; Gao, W.; Cannuccia, E.; Taha-Tijerina, J.; Balicas, L.; Mathkar, A.; Narayanan, T. N.; Liu, Z.; Gupta, B. K.; Peng, J. Artificially Stacked Atomic Layers: Toward New van Der Waals Solids. *Nano Lett* **2012**, *12* (7), 3518–3525.

(234) Güler, S. H.; Güler, Ö.; Evin, E. The Production of Graphene Nano Layers by Using Milling—Exfoliation Hybrid Process. *Fullerenes, Nanotubes and Carbon Nanostructures* **2017**, *25* (1), 34–39.

(235) Lei, W.; Portehault, D.; Dimova, R.; Antonietti, M. Boron Carbon Nitride Nanostructures from Salt Melts: Tunable Water-Soluble Phosphors. *J Am Chem Soc* **2011**, *133* (18), 7121–7127.

(236) Xue, Y.; Yu, D.; Dai, L.; Wang, R.; Li, D.; Roy, A.; Lu, F.; Chen, H.; Liu, Y.; Qu, J. Three-Dimensional B, N-Doped Graphene Foam as a Metal-Free Catalyst for Oxygen Reduction Reaction. *Physical Chemistry Chemical Physics* **2013**, *15* (29), 12220–12226.

(237) Guo, F.; Yang, P.; Pan, Z.; Cao, X.; Xie, Z.; Wang, X. Carbon-doped BN Nanosheets for the Oxidative Dehydrogenation of Ethylbenzene. *Angewandte Chemie* **2017**, *129* (28), 8343–8347.

(238) Zagho, M. M.; Dawoud, H. D.; Bensalah, N.; Altahtamouni, T. M. A Brief Overview of RF Sputtering Deposition of Boron Carbon Nitride (BCN) Thin Films. *Emergent Mater* **2019**, *2*, 79–93.

(239) Kumar, R.; Gopalakrishnan, K.; Ahmad, I.; Rao, C. N. R. BN–Graphene Composites Generated by Covalent Cross-Linking with Organic Linkers. *Adv Funct Mater* **2015**, *25* (37), 5910–5917.

(240) Gong, Y.; Shi, G.; Zhang, Z.; Zhou, W.; Jung, J.; Gao, W.; Ma, L.; Yang, Y.; Yang, S.; You, G. Direct Chemical Conversion of Graphene to Boron-and Nitrogen-and Carbon-Containing Atomic Layers. *Nat Commun* **2014**, *5* (1), 3193.

(241) Wu, J.; Han, W.-Q.; Walukiewicz, W.; Ager, J. W.; Shan, W.; Haller, E. E.; Zettl, A. Raman Spectroscopy and Time-Resolved Photoluminescence of BN and B x C y N z Nanotubes. *Nano Lett* **2004**, *4* (4), 647–650.

(242) Attri, R.; Roychowdhury, S.; Biswas, K.; Rao, C. N. R. Low Thermal Conductivity of 2D Borocarbonitride Nanosheets. *J Solid State Chem* **2020**, *282*, 121105.

(243) Lee, C. H.; Wang, J.; Kayatsha, V. K.; Huang, J. Y.; Yap, Y. K. Effective Growth of Boron Nitride Nanotubes by Thermal Chemical Vapor Deposition. *Nanotechnology* **2008**, *19* (45). https://doi.org/10.1088/0957-4484/19/45/455605.

(244) Parker, J. H.; Feldman, D. W.; Ashkin, M. Raman Scattering by Silicon and Germanium. *Physical Review* **1967**, *155* (3), 712–714. https://doi.org/10.1103/PhysRev.155.712.

(245) Dillon, A. C.; Gupta, P.; Robinson, M. B.; George, S. M. *FTIR Studies of Water and Ammonia Decomposition on Silicon Surfaces*; Elsevier Science Publishers B.V, 1990; Vol. 54155.

(246) Li, L. H.; Chen, Y.; Glushenkov, A. M. Boron Nitride Nanotube Films Grown from Boron Ink Painting. *J Mater Chem* **2010**, *20* (43), 9679–9683. https://doi.org/10.1039/C0JM01414A.

(247) Coates, G. W.; Getzler, Y. D. Y. L. Chemical Recycling to Monomer for an Ideal, Circular Polymer Economy. *Nat Rev Mater* **2020**, *5* (7), 501–516.

(248) Ahmed, H. T.; Abdullah, O. Gh. Structural and Ionic Conductivity Characterization of PEO:MC-NH4I Proton-Conducting Polymer Blend Electrolytes Based Films. *Results Phys* **2020**, *16*, 102861. https://doi.org/https://doi.org/10.1016/j.rinp.2019.102861.

(249) Hanumantha Rao, M.; Muralidharan, K. Syntheses, Characterization and Energetic Properties of Closo-(B12H12)2− Salts of Imidazolium Derivatives. *Dalton Transactions* **2013**, *42* (24), 8854–8860. https://doi.org/10.1039/C3DT32834A.

(250) Su, L.; Niu, M.; Lu, D.; Cai, Z.; Li, M.; Wang, H. A Review on the Emerging Resilient and Multifunctional Ceramic Aerogels. *J Mater Sci Technol* **2021**, *75*, 1–13. https://doi.org/https://doi.org/10.1016/j.jmst.2020.10.018.

(251) Gonzalez Ortiz, D.; Pochat-Bohatier, C.; Cambedouzou, J.; Bechelany, M.; Miele, P. Exfoliation of Hexagonal Boron Nitride (h-BN) in Liquide Phase by Ion Intercalation. *Nanomaterials* **2018**, *8* (9). https://doi.org/10.3390/nano8090716.

(252) Tang, C.; Bando, Y.; Liu, C.; Fan, S.; Zhang, J.; Ding, X.; Golberg, D. Thermal Conductivity of Nanostructured Boron Nitride Materials. *J Phys Chem B* **2006**, *110* (21), 10354–10357. https://doi.org/10.1021/jp0607014.

(253) Chadderton, L. T.; Chen, Y. A Model for the Growth of Bamboo and Skeletal Nanotubes: Catalytic Capillarity. *J Cryst Growth* **2002**, *240* (1–2), 164–169.

(254) Ma, R.; Bando, Y.; Sato, T. Controlled Synthesis of BN Nanotubes, Nanobamboos, and Nanocables. *Advanced Materials* **2002**, *14* (5), 366–368. https://doi.org/10.1002/1521-4095(20020304)14:5<366::AID-ADMA366>3.0.CO;2-Q.

(255) Su, C.-Y.; Juang, Z.-Y.; Chen, K.-F.; Cheng, B.-M.; Chen, F.-R.; Leou, K.-C.; Tsai, C.-H. Selective Growth of Boron Nitride Nanotubes by the Plasma-Assisted and Iron-Catalytic CVD Methods. *The Journal of Physical Chemistry C* **2009**, *113* (33), 14681–14688.

(256) Zhi, C.; Bando, Y.; Tang, C.; Golberg, D. Immobilization of Proteins on Boron Nitride Nanotubes. *J Am Chem Soc* **2005**, *127* (49), 17144–17145.

(257) Zhang, L.; Wang, J.; Gu, Y.; Zhao, G.; Qian, Q.; Li, J.; Pan, X.; Zhang, Z. Catalytic Growth of Bamboo-like Boron Nitride Nanotubes Using Self-Propagation High Temperature Synthesized Porous Precursor. *Mater Lett* **2012**, *67* (1), 17–20. https://doi.org/https://doi.org/10.1016/j.matlet.2011.09.054.

(258) Sing, K. S. W. Reporting Physisorption Data for Gas/Solid Systems with Special Reference to the Determination of Surface Area and Porosity (Recommendations 1984). **1985**, *57* (4), 603–619. https://doi.org/doi:10.1351/pac198557040603.

(259) Thommes, M.; Kaneko, K.; Neimark, A. V; Olivier, J. P.; Rodriguez-Reinoso, F.; Rouquerol, J.; Sing, K. S. W. Physisorption of Gases, with Special Reference to the Evaluation of Surface Area and Pore Size Distribution (IUPAC Technical Report). **2015**, *87* (9–10), 1051–1069. https://doi.org/doi:10.1515/pac-2014-1117.

(260) C. T. van Duin, A.; Dasgupta, S.; Lorant, F.; A. Goddard, W. ReaxFF: A Reactive Force Field for Hydrocarbons. *J Phys Chem A* **2001**, *105* (41), 9396–9409. https://doi.org/10.1021/jp004368u.

(261) Stephens, F. H.; Pons, V.; Tom Baker, R. Ammonia–Borane: The Hydrogen Source Par Excellence? *Dalton Transactions* **2007**, No. 25, 2613–2626. https://doi.org/10.1039/B703053C.

(262) Stephens, P. J.; Devlin, F. J.; Chabalowski, C. F.; Frisch, M. J. Ab Initio Calculation of Vibrational Absorption and Circular Dichroism Spectra Using Density Functional Force Fields. *J Phys Chem* **1994**, *98* (45), 11623–11627.

(263) Becke, A. D. Density-functional Thermochemistry. III. The Role of Exact Exchange. *J Chem Phys* **1993**, *98* (7), 5648–5652.
(264) Schmalz, F.; Mudimu, E.; Chair, I.; Kopp, W.; Leonhard, K. Assessing Accelerated Reaction Network Exploration with ChemTraYzer-TAD and PESmapping. December 26, 2024. https://doi.org/10.26434/chemrxiv-2024-79drl-v2.
(265) Gonzalez, Carlos.; Schlegel, H. Bernhard. Reaction Path Following in Mass-Weighted Internal Coordinates. *J Phys Chem* **1990**, *94* (14), 5523–5527. https://doi.org/10.1021/j100377a021.
(266) Peng, C.; Bernhard Schlegel, H. Combining Synchronous Transit and Quasi-Newton Methods to Find Transition States. *Isr J Chem* **1993**, *33* (4), 449–454. https://doi.org/https://doi.org/10.1002/ijch.199300051.
(267) Vermeire, F. H.; Carstensen, H.-H.; Herbinet, O.; Battin-Leclerc, F.; Marin, G. B.; Van Geem, K. M. *The Thermal Decomposition of Furfural: Molecular Chemistry Unraveled*.
(268) Chen, X.; Franklin Goldsmith, C. Predictive Kinetics for the Thermal Decomposition of RDX. *Proceedings of the Combustion Institute* **2019**, *37* (3), 3167–3173. https://doi.org/10.1016/j.proci.2018.06.036.
(269) Golets, M.; Shimpi, M. R.; Wang, Y. L.; Antzutkin, O. N.; Glavatskih, S.; Laaksonen, A. Understanding the Thermal Decomposition Mechanism of a Halogen-Free Chelated Orthoborate-Based Ionic Liquid: A Combined Computational and Experimental Study. *Physical Chemistry Chemical Physics* **2016**, *18* (32), 22458–22466. https://doi.org/10.1039/c6cp03191a.
(270) Gao, P.; Zhang, J. Understanding the Dehydrogenation Pathways of Ammonium Octahydrotriborate (NH4B3H8) by Molecular Dynamics Simulations with the Reactive Force Field (ReaxFF). *Adv Theory Simul* **2020**, *3* (10). https://doi.org/10.1002/adts.202000139.
(271) Gao, P.; Huang, Z.; Yu, H. Exploration of the Dehydrogenation Pathways of Ammonia Diborane and Diammoniate of Diborane by Molecular Dynamics Simulations Using Reactive Force Fields. *Journal of Physical Chemistry A* **2020**, *124* (9), 1698–1704. https://doi.org/10.1021/acs.jpca.9b10441.
(272) Weismiller, M. R.; Russo, M. F.; Van Duin, A. C. T.; Yetter, R. A. Using Molecular Dynamics Simulations with a ReaxFF Reactive Force Field to Develop a Kinetic Mechanism for Ammonia Borane Oxidation. *Proceedings of the Combustion Institute* **2013**, *34* (2), 3489–3497. https://doi.org/10.1016/j.proci.2012.06.030.
(273) Pai, S. J.; Yeo, B. C.; Han, S. S. Development of the ReaxFFCBN Reactive Force Field for the Improved Design of Liquid CBN Hydrogen Storage Materials. *Physical*

Chemistry Chemical Physics **2016**, *18* (3), 1818–1827. https://doi.org/10.1039/c5cp05486a.

(274) Liu, S.; van Duin, A. C. T.; van Duin, D. M.; Liu, B.; Edgar, J. H. Atomistic Insights into Nucleation and Formation of Hexagonal Boron Nitride on Nickel from First-Principles-Based Reactive Molecular Dynamics Simulations. *ACS Nano* **2017**, *11* (4), 3585–3596. https://doi.org/10.1021/acsnano.6b06736.

(275) Lele, A.; Krstic, P.; Van Duin, A. C. T. ReaxFF Force Field Development for Gas-Phase HBN Nanostructure Synthesis. *Journal of Physical Chemistry A* **2022**, *126* (4), 568–582. https://doi.org/10.1021/acs.jpca.1c09648.

(276) te Velde, G.; Bickelhaupt, F. M.; Baerends, E. J.; Fonseca Guerra, C.; van Gisbergen, S. J. A.; Snijders, J. G.; Ziegler, T. Chemistry with ADF. *J Comput Chem* **2001**, *22* (9), 931–967. https://doi.org/https://doi.org/10.1002/jcc.1056.

(277) Berendsen, H. J. C.; Postma, J. P. M.; van Gunsteren, W. F.; DiNola, A.; Haak, J. R. Molecular Dynamics with Coupling to an External Bath. *J Chem Phys* **1984**, *81* (8), 3684–3690. https://doi.org/10.1063/1.448118.

(278) Döntgen, M.; Przybylski-Freund, M.-D.; Kröger, L. C.; Kopp, W. A.; Ismail, A. E.; Leonhard, K. Automated Discovery of Reaction Pathways, Rate Constants, and Transition States Using Reactive Molecular Dynamics Simulations. *J Chem Theory Comput* **2015**, *11* (6), 2517–2524. https://doi.org/10.1021/acs.jctc.5b00201.

(279) Döntgen, M.; Schmalz, F.; Kopp, W. A.; Kröger, L. C.; Leonhard, K. Automated Chemical Kinetic Modeling via Hybrid Reactive Molecular Dynamics and Quantum Chemistry Simulations. *J Chem Inf Model* **2018**, *58* (7), 1343–1355. https://doi.org/10.1021/acs.jcim.8b00078.

(280) Kröger, L. C.; Kopp, W. A.; Döntgen, M.; Leonhard, K. Assessing Statistical Uncertainties of Rare Events in Reactive Molecular Dynamics Simulations. *J Chem Theory Comput* **2017**, *13* (9), 3955–3960. https://doi.org/10.1021/acs.jctc.7b00524.

(281) Brown, C. M.; Jacques, T. L.; Hess, N. J.; Daemen, L. L.; Mamontov, E.; Linehan, J. C.; Stowe, A. C.; Autrey, T. Dynamics of Ammonia Borane Using Neutron Scattering. *Physica B Condens Matter* **2006**, *385*, 266–268.

(282) Domalski, E. S. Thermodynamics of Organic Compounds in the Gas State, Volumes I and II: Frenkel, M.; Kabo, G. J.; Marsh, K. N.; Roganov, G. N.; Wilhoit, R. C. TRC Data Series: College Station, Texas. 1994. Price: $250 (Each Volume, within U.S.A.); $280 (Each Volume, Outside U.S.A.). *J Chem Thermodyn* **1995**, *27* (7), 831–832. https://doi.org/https://doi.org/10.1006/jcht.1995.0087.

(283) Dumont, H.; Bayle, B.; Bonnetot, B.; Bouix, J. Deposition and Characterization of BN/Si(0 0 1) Using Tris(Dimethylamino)Borane. *Mater Res Bull* **2002**, *37* (9), 1565–1572. https://doi.org/https://doi.org/10.1016/S0025-5408(02)00844-9.

(284) Tay, R. Y.; Li, H.; Tsang, S. H.; Zhu, M.; Loeblein, M.; Jing, L.; Leong, F. N.; Teo, E. H. T. Trimethylamine Borane: A New Single-Source Precursor for Monolayer h-BN Single Crystals and h-BCN Thin Films. *Chemistry of Materials* **2016**, *28* (7), 2180–2190. https://doi.org/10.1021/acs.chemmater.6b00114.

(285) Luo, Y.-R. *Comprehensive Handbook of Chemical Bond Energies*; CRC press, 2007.

(286) Genisel, M. F.; Uddin, Md. N.; Say, Z.; Kulakci, M.; Turan, R.; Gulseren, O.; Bengu, E. Bias in Bonding Behavior among Boron, Carbon, and Nitrogen Atoms in Ion Implanted a-BN, a-BC, and Diamond like Carbon Films. *J Appl Phys* **2011**, *110* (7), 074906. https://doi.org/10.1063/1.3638129.

(287) Thompson, C. A.; Andrews, L.; Martin, J. M. L.; El-Yazal, J. *Infrared Spectra of Boron Atom-Ammonia Reaction Products in Solid Argon*; 1995; Vol. 99. https://pubs.acs.org/sharingguidelines.

(288) Anafcheh, M.; Ghazi Mir Saeed, S.; Zahedi, M. [2 + 2] Cycloaddition and Bond Cleavage of Boron Nitride Cages with Iminoborane: A DFT Study. *J Clust Sci* **2022**, *33* (1), 29–35. https://doi.org/10.1007/s10876-020-01933-1.

(289) Hsu, C.-M.; Shivkumar, S. N,N-Dimethylformamide Additions to the Solution for the Electrospinning of Poly(ε-Caprolactone) Nanofibers. *Macromol Mater Eng* **2004**, *289* (4), 334–340. https://doi.org/https://doi.org/10.1002/mame.200300224.

(290) Celebioglu, A.; Uyar, T. Electrospun Porous Cellulose Acetate Fibers from Volatile Solvent Mixture. *Mater Lett* **2011**, *65* (14), 2291–2294.

(291) Wang, S.; Shi, K.; Tripathi, A.; Chakraborty, U.; Parsons, G. N.; Khan, S. A. Designing Intrinsically Microporous Polymer (Pim-1) Microfibers with Tunable Morphology and Porosity via Controlling Solvent/Nonsolvent/Polymer Interactions. *ACS Appl Polym Mater* **2020**, *2* (6), 2434–2443.

(292) Lasseuguette, E.; Malpass-Evans, R.; Tobin, J. M.; McKeown, N. B.; Ferrari, M.-C. Control over the Morphology of Electrospun Microfibrous Mats of a Polymer of Intrinsic Microporosity. *Membranes (Basel)* **2021**, *11* (6), 422.

(293) Xiong, J.; Liu, Y.; Li, A.; Wei, L.; Wang, L.; Qin, X.; Yu, J. Mass Production of High-Quality Nanofibers via Constructing Pre-Taylor Cones with High Curvature on Needleless Electrospinning. *Mater Des* **2021**, *197*, 109247. https://doi.org/https://doi.org/10.1016/j.matdes.2020.109247.

(294) Snapp, P.; Cho, C.; Lee, D.; Haque, M. F.; Nam, S. W.; Park, C. Tunable Piezoelectricity of Multifunctional Boron Nitride Nanotube/Poly(Dimethylsiloxane) Stretchable Composites. *Advanced Materials* **2020**, *32* (43). https://doi.org/10.1002/adma.202004607.

(295) Leardini, F.; Flores, E.; Galvis, A. R. E.; Ferrer, I. J.; Ares, J. R.; Sánchez, C.; Molina, P.; Van Der Meulen, H. P.; Navarro, C. G.; Polin, G. L.; Urbanos, F. J.; Granados, D.; Garća-Garća, F. J.; Demirci, U. B.; Yot, P. G.; Mastrangelo, F.; Betti, M. G.; Mariani,

C. Chemical Vapor Deposition Growth of Boron-Carbon-Nitrogen Layers from Methylamine Borane Thermolysis Products. *Nanotechnology* **2018**, *29* (2). https://doi.org/10.1088/1361-6528/aa9c07.

(296) Gupta, R. K.; Dunderdale, G. J.; England, M. W.; Hozumi, A. Oil/Water Separation Techniques: A Review of Recent Progresses and Future Directions. *J Mater Chem A Mater* **2017**, *5* (31), 16025–16058. https://doi.org/10.1039/C7TA02070H.

(297) Nam, S.-N.; Park, C. M.; Jang, M.; Huang, Y.; Jang, A.; Son, A.; Yoon, Y. Review of Boron Nitride-Based Membranes in Liquid Purification/Separation Applications. *Chemical Engineering Journal* **2023**, *453*, 139740. https://doi.org/https://doi.org/10.1016/j.cej.2022.139740.

(298) Li, T.; Wang, L.; Zhang, K.; Xu, Y.; Long, X.; Gao, S.; Li, R.; Yao, Y. Freestanding Boron Nitride Nanosheet Films for Ultrafast Oil/Water Separation. *Small* **2016**, *12* (36), 4960–4965. https://doi.org/https://doi.org/10.1002/smll.201601298.

(299) Lei, W.; Portehault, D.; Liu, D.; Qin, S.; Chen, Y. Porous Boron Nitride Nanosheets for Effective Water Cleaning. *Nat Commun* **2013**, *4* (1). https://doi.org/10.1038/ncomms2818.

(300) Wu, C.; Wang, B.; Wang, Y. One-Step Fabrication of Boron Nitride Fibers Networks. *Ceram Int* **2018**, *44* (5), 5385–5391. https://doi.org/https://doi.org/10.1016/j.ceramint.2017.12.166.

(301) Hao, W.; Marichy, C.; Brioude, A. Promising Properties of ALD Boron Nitride Nanotube Mats for Water Purification. *Environ Sci Nano* **2017**, *4* (12), 2311–2320. https://doi.org/10.1039/c7en00811b.

(302) Wang, X.; Yu, J.; Sun, G.; Ding, B. Electrospun Nanofibrous Materials: A Versatile Medium for Effective Oil/Water Separation. *Materials Today* **2016**, *19* (7), 403–414. https://doi.org/https://doi.org/10.1016/j.mattod.2015.11.010.

(303) Rasouli, S.; Rezaei, N.; Hamedi, H.; Zendehboudi, S.; Duan, X. Superhydrophobic and Superoleophilic Membranes for Oil-Water Separation Application: A Comprehensive Review. *Mater Des* **2021**, *204*, 109599. https://doi.org/https://doi.org/10.1016/j.matdes.2021.109599.

(304) McLean, B.; Webber, G. B.; Page, A. J. Boron Nitride Nanotube Nucleation during Ni-Catalyzed Boron Oxide Chemical Vapor Deposition. *Journal of Physical Chemistry C* **2019**. https://doi.org/10.1021/acs.jpcc.9b07337.

(305) McLean, B.; Webber, G. B.; Page, A. J. Boron Nitride Nucleation Mechanism during Chemical Vapor Deposition. *Journal of Physical Chemistry C* **2018**, *122* (42), 24341–24349. https://doi.org/10.1021/acs.jpcc.8b05785.

(306) Swart, M. A New Family of Hybrid Density Functionals. *Chem Phys Lett* **2013**, *580*, 166–171. https://doi.org/https://doi.org/10.1016/j.cplett.2013.06.045.

(307) Keal, T. W.; Tozer, D. J. A Semiempirical Generalized Gradient Approximation Exchange-Correlation Functional. *J Chem Phys* **2004**, *121* (12), 5654–5660. https://doi.org/10.1063/1.1784777.
(308) Wrackmeyer, B. Nuclear Magnetic Resonance Spectroscopy of Boron Compounds Containing Two-, Three-and Four-Coordinate Boron. In *Annual Reports on NMR Spectroscopy*; Elsevier, 1988; Vol. 20, pp 61–203.
(309) Jefferson, R. , University of Sussex, 1967.
(310) Rzepa, H. S.; Arkhipenko, S.; Wan, E.; Sabatini, M. T.; Karaluka, V.; Whiting, A.; Sheppard, T. D. An Accessible Method for DFT Calculation of 11B Nmr Shifts of Organoboron Compounds. *J Org Chem* **2018**, *83* (15), 8020–8025.
(311) Heitsch, C. W. The Nuclear Magnetic Resonance Spectra of Some Boron Complexes. *Inorg Chem* **1965**, *4* (7), 1019–1024.
(312) ARKHIPENKO, S. Y. Approaches to Novel B-N Chemistry at the Boundary of Frustrated Lewis Pairs and Bifunctional Catalysis, Durham University, 2017.
(313) Wrackmeyer, B. Organoboranes and Tetraorganoborates Studied by 11B and 13C NMR Spectroscopy and DFT Calculations. **2015**, *70* (6), 421–424. https://doi.org/doi:10.1515/znb-2015-0040.
(314) Gellrich, U.; Diskin-Posner, Y.; Shimon, L. J. W.; Milstein, D. Reversible Aromaticity Transfer in a Bora-Cycle: Boron–Ligand Cooperation. *J Am Chem Soc* **2016**, *138* (40), 13307–13313.
(315) Wrackmeyer, B.; Schwarze, B.; Durran, D. M.; Webb, G. A. Multinuclear Magnetic Resonance Study of N, N′, N ″-tris (Trimethylsilyl) Borazine. *Magnetic resonance in chemistry* **1995**, *33* (7), 557–560.
(316) Jaska, C. A.; Temple, K.; Lough, A. J.; Manners, I. Transition Metal-Catalyzed Formation of Boron− Nitrogen Bonds: Catalytic Dehydrocoupling of Amine-Borane Adducts to Form Aminoboranes and Borazines. *J Am Chem Soc* **2003**, *125* (31), 9424–9434.
(317) Ramachandran, P. V.; Drolet, M. P.; Kulkarni, A. S. A Non-Dissociative Open-Flask Hydroboration with Ammonia Borane: Ready Synthesis of Ammonia–Trialkylboranes and Aminodialkylboranes. *Chemical Communications* **2016**, *52* (80), 11897–11900.
(318) Nöth, H.; Höllerer, G. Beiträge Zur Chemie Des Bors, XXXVI. Organylsilyl-Borane. *Chem Ber* **1966**, *99* (7), 2197–2205. https://doi.org/https://doi.org/10.1002/cber.19660990718.
(319) Lin, K.; Wang, Z. Multiscale Mechanics and Molecular Dynamics Simulations of the Durability of Fiber-Reinforced Polymer Composites. *Commun Mater* **2023**, *4* (1), 66. https://doi.org/10.1038/s43246-023-00391-2.

(320) Yang, R.; He, J.; Xu, L.; Yu, J. Bubble-Electrospinning for Fabricating Nanofibers. *Polymer (Guildf)* **2009**, *50* (24), 5846–5850. https://doi.org/https://doi.org/10.1016/j.polymer.2009.10.021.